A Study on Buoyancy Driven Turbulent Flow Associated with Radiation in Cavities Partially Filled with Blockages

Draco Aluya Iyi

Ph.D.

2013

A Study on Buoyancy Driven Turbulent Flow Associated with Radiation in Cavities Partially Filled with Blockages

Draco Aluya Iyi

A thesis submitted in partial fulfilment of the requirements for the award of

Doctor of Philosophy

University of Northumbria at Newcastle

Research undertaken in the

Department of Mechanical and Construction Engineering

Faculty of Engineering and Environment

October 2013

ABSTRACT

Fluid flow and heat transfer in cavities partially filled with disconnected blockages is important in the design of a wide range of industrial and engineering applications such as thermal management of indoor environments, cooling of electronic panels, drying of agricultural products, stacking of items in cold storage etc. The flows in such confined spaces develop as a result of temperature and concentration gradient which is further complicated by the interactive effects of turbulence and radiation. The aims of this research are to explore the detailed heat transfer and flow field inside cavities partially filled with solid blockages and, in particular, to address the uncertainties associated with turbulence models, to quantify the influence of double diffusion and to study the effect of surface properties.

To achieve the above aims, a systematic numerical investigation has been carried out by validating the computational results against reliable experimental data available in open literature. A selection of turbulence and radiation models has been employed to scrutinise the effects of the above flow physics. An experimental set up capable of establishing low Rayleigh number buoyancy driven flow in a rectangular cavity containing cylindrical blockages was designed and fabricated to obtain temperature data. A series of experiments was conducted to obtain reliable temperature distribution at various positions in the flow domain and on the surfaces of the blockages. This set up also allowed us to study the proximity effect of blockages which has not been reported elsewhere.

It has been found that the choice of turbulence model remains to be an important issue and should be given due consideration for natural convection flow with a high Rayleigh number. The results from the parametric study on the specification of passive thermal boundary conditions reveal that the experimental temperature profile is the most accurate boundary condition for passive walls in relation to the adiabatic and linear temperature profiles. Experimental benchmark temperature data evaluated at various positions in the cavity with and without blockages are presented and some of them are compared with CFD simulations.

Finally, as an example of the application of the research methodology, a detailed numerical modelling was conducted on a Double-Skin-Façade which is known to reduce energy consumption in building and has become popular in recent years. The

current methodology has been applied to establish a number of parameters in connection with the design and performance of DSF which are believed to be useful to practitioners.

TABLE OF CONTENTS

LIST OF FIGURES

LIST OF TABLE

NOMENCLATURE

A, Heat transfer area (m^2)

D, Depth of cavity (m)

g, Gravitational acceleration (m/s^2)

H, Height of the cavity (m)

L, Width of the cavity (m)

$\vec{r}$, Position vector

$\vec{s}$, Direction vector

s, Path length

n, Refractive index

σ_s, Scattering coefficient

σ, Stefan-Boltzmann constant (5.672×10^{-8} $W/m^2\text{-}K^4$)

T, Local temperature

Φ, Phase function

Ω', Solid angle

RH, Relative humidity

DSF, Double Skin Facade

ATP, Adiabatic Temperature Profile

LTP, Linear Temperature Profile

ETP, Experimental Temperature Profile

I, solar radiation, (W/m^2)

V_y, fluid velocity component in y-direction (m/s)

x, y, z Displacement in x, y and z directions

ρ, Density $(kg/m3)$

μ, Dynamic viscosity$(\mathrm{kg/ms})$

ΔT, temperature difference $(= T_h - T_c)$

C_p, Specific Heat capacity (J/kg-K)

k, Conductivity (W/m-K)

P_r, Prandtl number

β, Volumetric thermal expansion coefficient $(1/\mathrm{K})$

α, Absorption coefficient, thermal diffusivity $(= \mathrm{k}/\rho c_p)$ $(\mathrm{m}^2/\mathrm{s})$

K, Turbulent kinetic energy $(\mathrm{m}^2/\mathrm{s}^2)$

ε, Turbulent dissipation rate $(\mathrm{m}^2/\mathrm{s}^3)$

h, Average convective heat transfer coefficient, $(= q/A\Delta T)$ $(\mathrm{W/m^2K})$

P, Pressure (Pa)

$u, v\ and\ w$, Velocities in x, y and z direction $(\mathrm{m/s})$

T, Temperature (K, ℃)

V_o, buoyancy velocity $(= \sqrt{g\beta H\Delta T})$ (m/s)

u_τ, Shear velocity $\left(= \sqrt{\tau_w/\rho}\right)$ $(\mathrm{m/s^2})$

τ_w, Local wall shear stress, $(\mathrm{N/m^2})$

Φ, General variable for fluid equations,

σ, Turbulent Prandt number

f_μ, f_1 and f_2, The damping functions

q_{cond}, Conductive heat flux, $(= k\Delta T/L)$ $(\mathrm{W/m^2})$

q_{conv}, Convective heat flux $(\mathrm{W/m^2})$

q_{rad}, Radiative heat flux $(\mathrm{W/m^2})$

$\bar{q}_{conv}$, Average convective heat flux $(\mathrm{W/m^2})$

$\bar{q}_{rad}$, Average radiative heat flux $(\mathrm{W/m^2})$

$\bar{\varphi}$, Time-average quantity

B_i, Biot number

l, The turbulent length scale is $(= k^{3/2}/\varepsilon)$

ε, Emissivity

θ, Inclination angle

Ψ, Stream function (m²/s)

δ, Wall proximity

y^+, Non-dimensional wall distance

m, Mass fraction of vapour to dry air

S_p, Stratification parameter

M, molecular weight of vapour, (kg/kg-mol)

EVR, Eddy Viscosity Models

LRKE, Low Reynolds number k-ε models

LES, Large Eddy Simulation

B, Buoyancy flux, (m²/s³)

N, buoyancy number

S, Source term

D_{eff}, Effective diffusion coefficient, (m²/s)

ν_t, The turbulent viscosity ratio is $= C_\mu \left(k^{1/2}\right) l = C_\mu (k^2/\varepsilon)$

$\mu_t = \rho\, k/\omega \;\;,\qquad \varepsilon = \beta * \omega k,$

Dimensionless groups

$\boldsymbol{y^+}$ Dimensionless distance $= \rho\mu_\tau y/\mu$

Pr Prandtl number $= \mu c_p/k$

Gr Granhof number $= (g\beta\Delta T L^3\rho^2)/\mu^2$

Ra Rayleigh number $= (g\beta\Delta T L^3\rho)/\nu\alpha$

Ra_H Rayleigh number based on height, $= (g\beta\Delta T L^3\rho)/\nu\alpha$

Nu_{conc} Convective Nusselt number $= q_{conv}/q_{cond} = (hL/k)$

Nu_{rad} Radiative Nusselt number$= q_{rad}/q_{cond}$

Nu Total Nusselt number$= (q_{conv} + q_{rad})/q_{cond}$

$\overline{Nu}_{conv}$ Average convective Nusselt number $= \frac{\bar{q}_{conc}L}{\bar{k}\Delta T} = \int_0^H Nu_{conv}(y)\, dy$

$\overline{Nu}_{rad}$ Average radiative Nusselt number $= \frac{\bar{q}_{rad}L}{\bar{k}\Delta T} = \int_0^H Nu_{rad}(y)\, dy$

DEDICATION

To my beautiful wife, Mrs Jane Catherine Iyi and our children James and David, and to my lovely mother, Otiti Joy Iyi and my dear sister, Julie Iyi and to the memory of my father, Mr. Augustine Iyi.

ACKNOWLEDGEMENTS

I wish to express my thanks to God for his providential care on me and my family during the course of this research. My special thanks go to my supervisors Dr Reaz Hasan and Dr Roger Penlington for their guidance and advice at every step and stage of this research and a big thank you to my mother-in-law, Mrs Elizabeth Harrison for proof reading this thesis.

I would like to thank the laboratory technicians who have given me their valuable time and assistance for the experimental work.

I especially thank my in-laws and family for their constant support, patience, understanding and encouragement throughout the duration of this work.

Most importantly I would like to appreciate and thank Dr. Gillian Brooks and all my family in Nigeria; my mother, my father and my sisters.

DECLARATION

I declare that the work contained in this thesis has not been submitted for any other award and that it is all my own work. I also confirm that this work fully acknowledges opinions, ideals and contributions from the work of others.

Name: Draco Aluya Iyi

Signature: D.IYI

Date:

Chapter 1 - INTRODUCTION

1.1 Background

Heat transfer is energy in transit due to temperature difference. Conduction, convection and radiation are the three modes of heat transfer. Conduction heat transfer occurs by molecular excitation due to temperature gradient in a medium, usually solid. Convection heat transfer through gases and liquids from a solid boundary results from the fluid motion along the surface. Radiation heat transfer is concerned with the exchange of thermal energy between two or more bodies by electromagnetic waves and hence, does not need any medium. Convection heat transfer can be "forced" when movement of a fluid is by means of an external agent such as a fan or a pump. In many cases, natural buoyancy forces alone are responsible for fluid motion when the fluid is heated, and this process is called "free or natural" convection.

Natural convection flow is generated by density difference in different regions of the fluid. This density difference, along with the effect of the gravity, creates a buoyancy force which causes the heavier fluid to move downwards and the lighter fluid to move upwards, producing buoyancy driven flow. The density differences in natural convection flows may result from a temperature difference or from the differences in the concentration of chemical species, or from the presence of multiple phases in the fluid. One of the most common buoyant flows can be seen as air circulation around our rooms and offices, and other engineering applications [1-3].

In the case of a differentially heated rectangular cavity of height H and length L, shown in Fig.1-1, the natural convection heat transfer from hot to cold wall is characterised by the formation of a slow moving vortex. The fluid particles move up along the hot vertical wall (temperature T_{hot}) by absorbing heat from the 'source', which then flows downward along the cold wall, gradually losing the heat to the cold surface (temperature T_{cold}) which may be termed as the 'sink'.

The heat transfer inside enclosures depends strongly on the flow regimes. These flow regimes are usually characterised by the value of the Rayleigh number [4]. The Rayleigh number is defined as the product of the Grashof number, which describes the relationship between the ratio of buoyancy forces and viscous forces within a fluid, and the Prandtl number comprises some fluid properties, is defined as the ratio

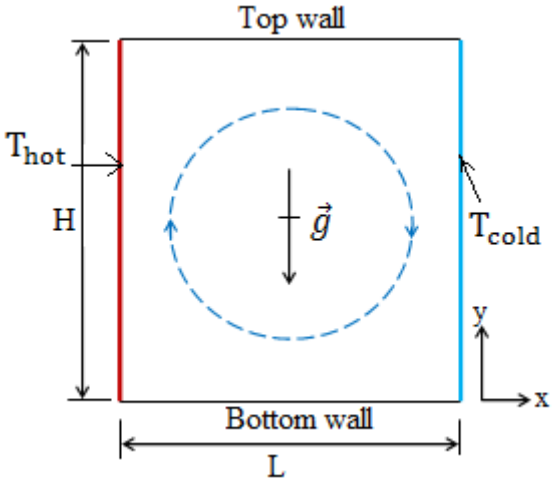

Figure 1-1: Physical model and coordinate system

of momentum diffusivity to thermal diffusivity. For a natural convection near a vertical wall, the strenght of the buoyancy-induced flow is measured by the Rayleigh number (Ra) which is defined mathematically as in Eq. (1-1)

$$Ra = Gr_L * Pr = \frac{g\beta\Delta T L^3 \rho}{\mu\alpha} \qquad (1-1)$$

Where, β is the thermal expansion coefficient:

$$\beta = -\frac{1}{\rho}\left(\frac{\partial\rho}{\partial T}\right)_p$$

and α is the thermal diffusivity:

$$\alpha = \frac{k}{\rho c_p}$$

$\Delta T = \mathrm{T_{hot}} - \mathrm{T_{cold}}$, g is the acceleration due to gravity and μ represent the viscosity of the fluid.

When the Rayleigh number is below the critical value for that fluid, the heat transfer is primarily in the form of conduction; when it exceeds the critical value, the heat transfer is primarily in the form of convection [5]. Rayleigh number plays a similar role in natural convection that the Reynolds number plays in forced fluid flow. The combined effects between free and forced convection must be considered when the ratio between Grashof and Reynolds numbers is of the same order, i.e., $(Gr_L/Re_L^2) \approx 1$. On the other hand, when $(Gr_L/Re_L^2) \ll 1$, the free convection

effects may be neglected and conversely, when $(Gr_L/Re_L^2) \gg 1$, the force convection effects may be neglected [6].

The convective heat transfer coefficient (which controls the rate at which heat is transported across enclosures) is the most important quantity that needs to be accurately predicted inside enclosures and is usually evaluated via the Nusselt number. The Nusselt number represents the enhancement of heat transfer by convection relative to conduction. That means the larger the Nusselt number the more effective is the convection heat transfer.

During the last three decades, there has been intensive research on such flows [7-10], due to the growing demand for detailed quantitative knowledge of the transfer processes and also due to its relevance in many practical applications [11-13]. Most of these past studies were for pure natural convection, whilst in reality heat transfer inside enclosed spaces is often determined by the presence of various obstacles. Examples of such situations can be seen in; thermal management of indoor environments [14], cooling devices for electronic packages [15, 16], solar collectors[17], gas-filled cavities around a nuclear reactor [18, 19], refrigeration units [20-22] etc., some of which are shown in Fig.1-2a-c.

In today's technological society most of our lifetime is spent in an indoor environment. The main objective of buildings has always been to provide shelter from sun, wind, cold and rain. In the past, designs were relatively simple and took into consideration the local environmental conditions. However, nowadays due to current energy saving procedures, indoor environment quality has tended to decrease. In fact, in the last two decades, the drive to produce more energy efficient buildings has led to the design of highly insulated buildings that are air tight. Therefore, the flows in most indoor environments use natural convection phenomenon for the improvement in the quality of life of the occupants, together with thermal comfort, air quality and energy conservation.

Refrigeration unit (Fig.1-2c) is an example of a study with blockages. The various products stored in the freezer influences the heat transfer, humidity and flow inside the unit whose performances are affected by the storage pattern. Similarly, the cooling

of modular network solution (Fig.1-2b) is also significantly dependent on the configuration.

Figure 1-2: Examples of natural convection systems: (a) Indoor environment [23], (b) Electronic devices [24], (c) refrigerator with food arrangement [25].

Indoor environment is also influenced by the concentration of moisture [26-28]. A humidity gradient will lead to the transfer of energy by desorption and adsorption which may be significant to the heat transfer by buoyancy. Therefore, the combined influence between temperature and concentration induced natural convection flow and heat transfer is important in understanding humidity control in domestic and industrial buildings, utilitarian buildings, drying of agriculture produce and cold storage.

In addition, most objects change size with changing relative humidity. Laminated materials, such as oil paintings and veneered furniture will therefore distort and suffer

shearing stresses with changing relative humidity. Also, at low humidity, organic materials become stiff and therefore less tolerant to the shearing stresses between layers. High relative humidity accelerates degradation as well as corrosion of metals.

1.2 **Research motivation and justification**

As will be shown in chapter two, there has been a significant number of experimental and theoretical works carried out in the past decade in an attempt to understand flow in enclosures due to buoyancy effects. These involve the following: laminar natural convection flow and heat transfer containing dry air [29, 30], turbulent natural convection flow in enclosures without blockages [31-33] and natural convection flow containing porous medium [34]. However, there appears to be limited studies on: combined influence of the interactions between turbulent natural convection and radiation heat transfers particularly in an indoor environment, influence of mass transfer on temperature induced buoyancy flow and natural convection in enclosures containing disconnected blockages or objects.

Also from the literature, a number of challenges have been identified and summarised.

- With a large number of turbulence models available in computational fluid dynamics, engineers, scientists and architects in the built environment are often puzzled with the choice of model for their predictions.
- Specification of passive horizontal thermal boundary layer functions for the numerical modelling of this kind of flow is still a major challenge even for near-ideal conditions of insulation. Since the upper and lower walls of the cavity are continually absorbing heat from the hot wall and supplying it to the fluid convectively and heat conduction within the adiabatic walls also alters the flow and temperature fields in the fluid and hence the net heat transfer rate.
- Influence of surface emissivity on double diffusive natural convection flow and heat transfer in confined space.
- Interaction influence between turbulent natural convection flow and blockages
- Limited experimental data are available for the validation of CFD codes for this kind of flow.

The works carried out in this thesis have carefully resolved the above limitations, and has provided us with the knowledge base for the design of our experimental test rig. The main objective of the rig is to provide highly reliable temperature data that will be made available for the validation of CFD codes for this kind of flow. Also, the results of this study are expected to contribute to the literature in this field of study and contribute to the understanding of natural convection in a cavity filled with solid objects.

1.3 **Research aims and objectives**

The aims of the research work are:

1. Detailed numerical investigations of the interaction between turbulent natural convection and thermal radiation in an enclosure partially filled with obstacles.
2. Detailed numerical investigations of the natural convection of heat and mass transfer in an enclosure partially filled with disconnected blockages.
3. Experimental investigation to provide reliable temperature data within an enclosed space containing disconnected blockages, with particular emphasis placed on quantifying the proximity to the active walls. These data will be used for the validation of numerical models for such flows.
4. Application of the research methodology to study the flow and heat transfer for Double Skin Facade (DSF).

In order to achieve these set research aims, the works undertaken are highlighted below.

- Performance evaluation of low-Re k-ε models for pure and double diffusive buoyancy driven turbulent flow in an enclosure with and without blockages, by validating computational results with existing experimental data. This will resolve the uncertainty in choosing turbulence models for this type of flow.
- Parametric study on a realistic thermal wall boundary condition in contrast to adiabatic wall specification which is normally used in the numerical study of natural convection flow and heat transfer.
- Evaluation of interaction of radiation with pure and double diffusive buoyancy driven turbulent flows in an enclosure, with and without blockages
- Design, fabrication and calibration of a flexible experimental set up to provide reliable temperature data for an enclosed cavity with and without

blockages. This experimental set up would allow validation of blockage proximity from the vertical active walls and grouping of blockages into various configurations.

- Conduct a detailed numerical study on the flow and heat transfer for a double-skin facade (DSF) in order to highlight the usefulness of the research methodology in the context of a practical application.

1.4 Thesis organization

In this thesis, the results of numerical and experimental study of natural convection flows and heat transfer with and without blockages inside differentially heated rectangular enclosures are discussed in detail. The analysis was carried out over a range of scenarios, which are presented in various chapters as follows:

Chapter 1 provides an introduction about natural convection flow and heat transfer and the importance of the study carried out in this thesis and it also includes the objectives and aims and roadmap showing the research contributions.

Chapter 2 discusses the literature review of the numerical and experimental natural convection heat transfer with and without blockages in a confined space. It also discusses the literature review of the uses of turbulent and radiation models on the flow and heat transfer by natural convection processes.

Chapter 3 explains the theoretical background of the natural convection flow and heat transfer process inside enclosures. It also discusses and explains the used numerical models, the governing equations and boundary conditions.

Chapter 4 discusses the numerical studies and analysis of turbulent natural convection flow and heat transfer in a rectangular enclosure without blockages. Also presented are the comparisons of results with experimental data from literature.

Chapter 5 presents a detailed experimental study of the flow and heat transfer in a rectangular enclosure without cylindrical blockages. Some details of the design procedure are presented and the analysis of the rig reliability is presented. Experimental studies were conducted to quantify the influence of blockage locations within the flow domain which are also reported in this chapter.

Chapter 6 reports the numerical analysis of the influence of blockage locations on turbulent natural convection flow and heat transfer. Different cases of these cylinder locations have been considered and analysed. It also reports the detailed validations of experimental data.

Chapter 7 analyses the interaction influence between turbulent natural convection and radiation heat transfer in an enclosure partially filled with disconnected cylindrical blockages. In addition, influence of these blockages on the heat and mass transfer is analysed.

Chapter 8 provides a detailed study on the application of the research methodologies on the influence of solar-blockages on turbulent natural convection flow and heat transfer in double-skin-facade, coupled with the indoor environment.

Chapter 9 summarizes the important findings and final conclusions from this study and proposes direction for future work.

1.5 **Original contributions**

During the course of this research, the author has:

1. Quantified the performance of low-Reynolds number k-ε models for natural convection and double diffusion flows in a cavity with and without disconnected blockages. This is to resolve the uncertainties associated with common viscous models.

2. Quantified the influence of surface emissivity on the heat and mass transfer within an enclosure partially filled with disconnected solid blockages. An understanding of these interactions is critical for the design of energy efficient electronic packages, ventilation inside buildings especially in a warm and humid environment or for humidity control in listed/utilitarian building applications.

3. Quantified the influence of three major wall boundary conditions on the flow and heat transfer in turbulent natural convection process. This is done to provide a comparative performance and to avoid the uncertainty associated with insufficient insulation for specifying adiabatic conditions for these walls.

4. Designed and built an experimental test rig for natural convection heat transfer in a rectangular enclosure partially filled with disconnected blockages. Temperature data were collected for configurations with and without blockages. These data will be useful for the validation of numerical and/or analytical predictions.

5. Conducted a detailed parametric study on Double-Skin-Facade, which is known to reduce energy consumption in building and has become popular in recent years. The findings from this research are based on fundamental transport processes compared with simplistic and trial and error method currently followed. It is believed that the results will be very valuable to the practitioner.

Generally, the study will add to enrich the knowledge on the phenomena which take place in confined space containing numerous solid objects. These contributions are summarised in Fig.1-4 on the following page and have led to a few publications listed in section 1.6.

1.6 **List of publications**

- Iyi, Draco, Hasan, Reaz and Penlington, Roger (2013) *Numerical simulation of 2D turbulent natural convection of humid air in a cavity filled with solid objects.* Procedia Engineering, 56. pp. 538-543. ISSN 1877-7058
- Iyi, Draco, Hasan, Reaz and Penlington, Roger (2012) *Interaction effects between surface radiation and double-diffusive turbulent natural convection in an enclosed cavity filled with solid obstacles.* In: International Symposium on Advances in Computational Heat Transfer ICHMT, 1-6 July 2012, Bath, England.
- Iyi, Draco, Hasan, Reaz and Penlington, Roger (2011) *Numerical analysis of the influence of thermal boundary condition and surface emissivity on the flow and heat transfer in turbulent buoyancy driven flow.* In: The Asian Symposium of Computational Heat Transfer and Fluid Flow, 22-26 September 2011, Kyoto University, Kyoto, Japan.
- Iyi, Draco, Hasan, Reaz and Penlington, Roger (2013), *Evaluation of various CFD modelling strategies in predicting air flow and heat transfer in forced and natural ventilated Double-Skin-Facade.* Submitted in Journal of Building Performance Simulation.

- Iyi, Draco, Hasan, Reaz and Penlington, Roger (2013), *CFD Analysis of Blockages Influence on the Heat and Mass Transfer for Double-Diffusive Buoyancy-Driven Flow*. Submitted in International Journal of Heat and Fluid Flow.
- Iyi, Draco, Hasan, Reaz and Penlington, Roger (2013) *Effect of Emissivity on Heat and Mass Transfer of Humid Air in a Cavity Filled with Solid Obstacles*. Submitted in International Journal of Numerical Heat Transfer, Part A: Application
- Iyi, Draco, Hasan, Reaz and Penlington, Roger (2013) *CFD Analysis of the Performance of Low-Reynolds number K-epsilon Models for Natural Convection Heat and Mass Transfer in Cavity Filled with Blockages*. Submitted in International Journal of Heat and Mass Transfer.
- Iyi, Draco, Hasan, Reaz and Penlington, Roger (2013) *Experimental study of heat transfer by natural convection in a compart cavity.* Submitted in International Journal of Experimental Heat Transfer.

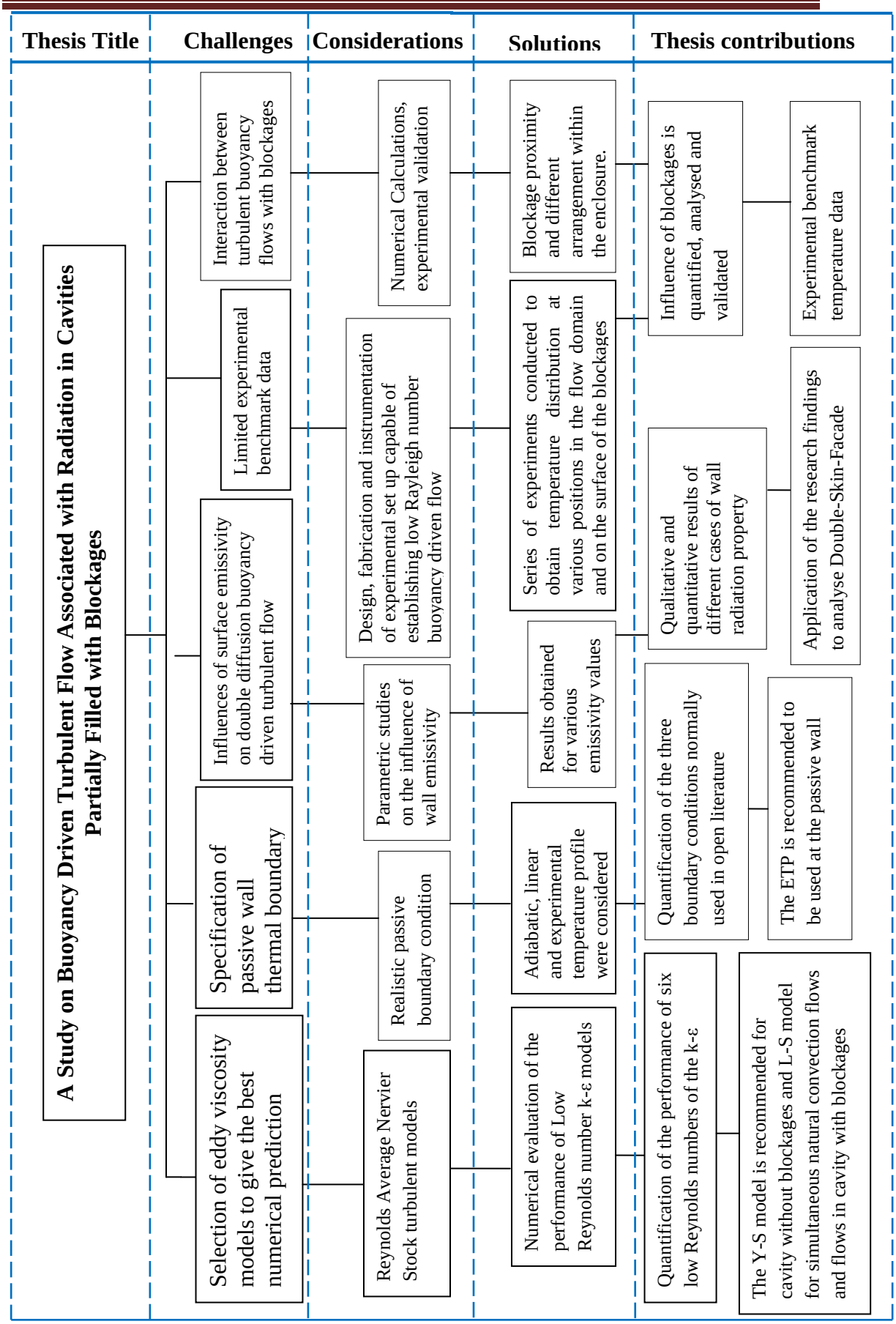

Figure 1-3 Project roadmap showing thesis contributions

Chapter 2 - LITERATURE REVIEW

2.1 Introduction

Buoyancy driven flow inside cavities has been the subject of extensive research for the last two decades due to the growing demand for detailed quantitative knowledge of the transfer processes and also because of its relevance in many practical applications [11, 13], such as heat transfer in buildings [35-40], electronic and other cooling processes [41-48] etc. The basic set up for such flows, which has also attracted most attention from researchers, is a rectangular cavity whose vertical walls are heated differentially [31, 49, 50]. Due to the fact that such a rig is relatively easy to fabricate, detailed data on the flow, turbulence and heat transfer have been collected through experiments [51-53].

Following on, numerical scientists have also been quick to respond to the experimental literature by conducting validation and exploratory studies on this very topic [52, 54-58]. The interest seems to be ongoing because more and more challenging situations are emerging with time [55, 59, 60]. Some of the important research conducted by various researchers in this field of study is briefly discussed in this chapter. The situation with and without blockages has also been considered including humidity. Also, the literature on the double-skin-facade will be discussed in the relevant chapter (chapter-8).

2.2 Experimental studies on natural convection flow in enclosures

Many researchers have experimentally studied the flow profiles inside cavities. Kutalela et al., [61] studied the turbulent natural convection on a vertical flat plate. They observed that the lateral position of the peak mean velocity increases with height. They also showed that increasing the cavity width will increase the boundary layer thickness and significantly decrease the velocity value. Giel and Schmidt [62], and Han and Kueln [63] studied the turbulent natural convection in an enclosure filled with water. They observed the flow reversals just outside of the boundary layer for about 60% upstream of each wall. They noticed that the peak of the velocity values start to decrease and move away from the wall (increasing the boundary layer thickness) after the enclosure mid-height. King [64] studied the turbulent natural convection in an air cavity. He observed that the boundary layer

thickness and the peak of the mean velocity were at its minimum near the bottom of the heated wall then starts to increase up to the mid-height, and then starts to decrease again.

Kirkpatrick and Bohn [65], investigated natural convection at a high Rayleigh number for a range of 0.1×10^{10} to 3×10^{10} in a cubical enclosure with various thermal boundary conditions. They have run experiments using four different configurations of differentially heated and cooled vertical and horizontal walls. In all the cases tested, the bottom wall was the heated wall. They made measurements of mean and fluctuating values of temperature and observed fluid flow patterns in the enclosure. It was concluded that heating from below would cause more mixing in the enclosure and consequently cause reduction of temperature stratification. As the Rayleigh number increased, the thermal stratification at the core of the cavity decreases. They observed that the thermal stratification changes suddenly at $Ra = 0.65 \times 10^{10}$. Also, the thermal stratification is not symmetric around the centreline. That is why increase of the bottom wall temperature leads to an increase of the temperature difference between the bottom wall and the core and produces thermal plumes which in turn cause mixing of the core.

Cheesewrite and King [66], Cheesewright and Ziai [67], Bowles and Cheesewright (1989), [68] carried out investigations on two-dimensional buoyant cavity flows. They studied rectangular cavities to produce experimental data for validation of two-dimensional computer codes. The working fluid was air and the Rayleigh number developed based on cavity height was 10^{10}. They produced a large amount of measurements of mean and fluctuating values of velocity and temperature. LDA and thermocouples were employed to carry out the measurements of velocity and temperature respectively. They observed that the flows on the hot and cold walls are not symmetrical to each other. Also they reported re-laminarization on the floor wall and then transition to turbulence at 20% of the way up the hot wall. The measurements of velocity fluctuations showed reduction at the bottom of the cavity which reconfirms the re-laminarization phenomena mentioned earlier.

Lankhorst et al. [69], conducted a study of buoyancy-induced flows in an enclosure at high Rayleigh numbers, using a differentially heated air filled square enclosure. The range of Rayleigh numbers covered in the experiment was from 1×10^{9} to 4×10^{9}.

Laser-Doppler velocimetry was used to obtain velocity profiles. The traversing of a thermocouple probe was employed to measure the vertical temperature distribution in the core. The vertical temperature distribution was slightly asymmetric. They suggested that the probable cause of this phenomenon is the mean temperature difference between the enclosure and the room. They observed that near the top and bottom walls, there is not a stable thermal stratification because of the existence of horizontal flow. They observed flow reversal outside the boundary layer. The reason for this reverse flow is that the fluid moves up the hot wall and then gets to a region at which the temperature at the core is higher. Because the free stream temperature is less than the core temperature, a slight reversal of flow occurs. This phenomenon is called "temperature defect".

DafaAlla and Betts [53] studied turbulent natural convection in a tall air cavity. They analyzed turbulent natural convection in an air cavity with an aspect ratio of 28.6. The experiment resulted in data for the velocities and temperatures at a Rayleigh number based on cavity width of 0.83×10^6 (representative of facades in a built environment application). The experimental data is useful for validating computational and theoretical studies. Velocity measurements were carried out by a Laser Doppler Anemometer. Fine thermocouples were employed for temperature measurements. Heat transfer rates and heat losses from the cell are evaluated. Their experimental data in the central portion of the tall cavity were averaged and used to simulate anti-symmetric fully developed flow in an infinitely tall air cavity. Causes of asymmetry of the data, including radiation absorption were assessed.

Betts and Bokhari [70] also studied turbulent natural convection in an enclosed tall cavity of 2.18m in height, 0.076m in width and 0.52m in depth. The temperature difference was imposed between vertical walls with isothermal temperature of 19.6ºC and 39.9ºC. This temperature difference created the Rayleigh number of 1.43×10^6 based on the width of the cavity as length scale. In this situation, the flow in the core of the cavity was fully turbulent and variation of property with temperature was relatively negligible. They modified a previously used experimental rig by fitting partially conducting top and bottom walls and outer guard channels to provide better adiabatic boundary conditions. This was done to avoid the inadequately defined sharp changes in temperature gradient and other problems associated with insufficient

insulation on the passive walls. Mean and turbulent temperature and velocity variations inside the cavity were obtained. Also heat fluxes and turbulent shear stresses were measured at various locations. The temperature and velocity distributions were shown to be nearly two-dimensional, except close to the front and back walls, and anti-symmetric across the diagonal of the cavity. The partially conducting top and bottom walls created local unstable thermal stratification in the wall impinging jet flows, which increases the turbulence as the flow moves toward the isothermal vertical plates.

Tian and Karayiannis [71] carried out an investigation on low turbulence natural convection in an air filled square cavity for a Rayleigh number of 1.58×10^9. The main focus in this work was analyzing turbulence quantities. The fluid flow resulting from natural convection was turbulent anisotropic wall shear flow. Turbulent frequencies of 0.1-0.2Hz were identified by analysing the power spectral density which is a function of frequency. Turbulence intensity was found to increase downstream of flow along hot and cold walls. The experimental results revealed that the temperature and velocity fluctuations were confined to the boundary layers along the solid walls and were not in Gaussian distribution. It was concluded that the temperature and velocity components were fluctuating independently of each other. The measurements were carried out in an unsteady state condition. Ampofo and Karayiannis, and Ampofo F., [51, 72] investigated turbulent natural convection in an air filled square cavity using similar conditions to that of Tian and Karayiannis [71]. They observed that thickness of boundary layer along hot and cold wall is 7% of thickness of the outer boundary layer. They also reported that thickness of viscous sub-layer is 3mm and thickness of conduction region is 2mm and that the maximum Nusselt number occurs at the bottom of the hot wall and top of the cold wall.

Chen and Liu [73] carried out an analysis of convection heat transfer in a passive solar heating room with greenhouse and heat storage. They investigated heat transfer and airflow in passive solar heating rooms with greenhouse and heat storage. They also studied the heat transfer and air flow on a rock bed. The rock bed was as a solar absorber and storage layer.

Calcagni et al. [49] studied natural convection heat transfer in a square cavity characterized by a discrete heater positioned over the lower wall and cooling taking

place from vertical walls of the cavity. The effect of heat source lengths on heat transfer and temperature distribution inside the cavity was investigated. In order to gather experimental data, measurements of temperature distribution in air were carried out by real-time and double-exposure holo-graphic interferometer. The commercial finite volume code Fluent was also used for a numerical study. The range of Rayleigh numbers covered by this experiment was from 10^3 to 10^6. The local Nusselt number was obtained on the heat source positions and it showed a symmetrical form increasing near the heat source borders. Finally, they presented graphs of the local Nusselt number on the heat sources and the average Nusselt number at several Rayleigh numbers. Thermocouples and data acquisition unit were employed to accomplish the measurements. For the Rayleigh numbers lower than 10^4, the conduction heat transfer is the most important heat transfer mechanism.

Xu and Li [74] investigated temperature gradient induced natural convection in molten gallium. The velocity and temperature field measurements were recorded simultaneously. A standard hot-film anemometer working under constant temperature mode was employed to measure the velocity profiles, and the temperature profiles were measured using a standard T-type thermocouple. The experimental velocity and temperature distributions were compared with previous numerical simulations and reasonably good agreement was achieved. The measurements were performed at steady state condition. The two side walls were rigid with constant temperature. The bottom wall was rigid and adiabatic. The numerical investigation was performed by a finite element model. The temperature measurements along horizontal lines revealed a nonlinear temperature distribution which in turn shows the significance of convection in this case. The total velocity along the horizontal line at the top and bottom of the geometry has a convex shape with maximum value located near the centre. The velocity along the line at the middle of geometry has two peak points near two vertical walls and zero at the core.

Laguerre et al., [75] studied heat transfer by natural convection in a closed cavity as a case relevant to domestic refrigerators. The experiment was carried out using a refrigerator model. In this model, heat was transferred by natural convection between a cold vertical wall and the other walls were exposed to heat losses. The air temperature distribution in the boundary layers and in the central space of the empty

refrigerator model was measured. In order to study the effect of existence of foods on temperature distributions, they filled the refrigerator model with 4 blocks of hollow spheres. Then they compared the experimental measurements in the case where there were blocks inside the model with the measurements from the case without blocks. The measurements were accomplished three-dimensionally and at steady state condition. The range of Rayleigh numbers covered in the study was from 1.92×10^8 to 3.02×10^8. The temperature measurements showed that in the case where there are blocks inside the refrigerator; the temperature is lower than for the case without blocks. They concluded that the heat transfer is augmented in the case with blocks. But those blocks cause increase of maximum temperature at the top of the refrigerator. This phenomenon can be explained by more stagnation because of the presence of blocks. The refrigerator model showed that there is a thermal stratification and is hotter at the top and colder at the bottom of it. From experimental data, they reported that the thickness of the boundary layer is 2cm and therefore they suggested that the food inside a refrigerator should be placed at a distance of more than 20mm from the walls.

Ampofo, F. [72] carried out an experimental investigation of turbulent natural convection of air in a non partitioned and partitioned cavities with differentially heated vertical and conducting horizontal walls. The experiments resulted in two-dimensional flow in the mid-plane of the cavity with dimensions of 0.75m high, 0.75m wide and 1.5m deep. The thermal boundary conditions of the experiment were isothermal vertical walls at 50ºC and 10ºC. This temperature difference created a Rayleigh number of 1.58×10^9. He installed five partitions with higher thermal conductivity material than that of the cavity material on the hot wall. The partitions' dimensions were 150 mm long, 3 mm thick and the same depth as the depth of the cavity. The local velocity and temperature were measured simultaneously at various locations in the cavities. Based on the experimental measurements, it was concluded that the average and local Nusselt number decreases because of the existence of partitions over the hot wall. The existence of partitions substantially modifies the dynamic and thermal fields compared to those in the empty cavity with the same dimensions and boundary conditions. Also partitions on the hot wall affect the cold wall and make the boundary layer thicker and give higher peak values.

Shu et al. [76] investigated natural convection in a cavity with imposed modulated thermal gradients or modulated gravity forces. The modulated thermal gradients mean that the imposed wall boundary condition changes periodically and consequently leads to a periodical change of buoyancy forces. A laser-based particle image velocimetry (PIV) system was employed to measure velocity fields. The comparison has been made between computed results and experimental measurements and they showed good agreement under various conditions. After validation of the numerical model, it was employed to investigate the effect of modulation frequency and Prandtl number on the fluid flow. The measurements were conducted at steady state condition. The numerical 2D computations were made to perform at steady state condition. They observed that the buoyancy driven flow follows the same pattern as oscillating driving temperature. The velocity induced as a result of natural convection has a phase difference with oscillating driving temperature. This conclusion is valid in both vertical cavity and tilted cavity. It was reported that the higher frequency of driving temperature creates weaker velocity field.

2.3 **Numerical studies on natural convection flow in cavity**

As mentioned before, the numerical prediction of natural or mixed convection can be an economical method to use for the design purposes in industrial applications. However, because of the complex nature of free convection flows, its numerical simulation is still a challenge for researchers. Some of the relevant issues are discussed in the following paragraphs.

Ince and Launder [77] numerically studied buoyancy-driven flows in rectangular enclosures. In the numerical study, air was the working fluid. They investigated two different aspect ratios, 30:1 and 5:1, which showed different flow structure in the two cases. It was concluded that the version of Jones-Launder low-Reynolds-number k-ε model [78] performed satisfactorily in these cases. There was good agreement with reported experimental data. The generalized gradient diffusion hypothesis (GGDH) was employed to compute turbulent heat fluxes and eventually calculate buoyancy turbulence generation term. In the GGDH, cross flow gradients were taken into account which might be important in buoyancy driven flows. Henkes et al. [79] investigations natural convection flow in a cavity using low-Reynolds-number turbulence models. Their computations covered Rayleigh numbers, ranging up to 10^{15}

for water. Three turbulence models of the standard k-ε model with logarithmic wall function, the low-Reynolds-number of Chein [80], and Jones and Launder were used. They found that the standard wall function gave too high predictions regarding the average Nusselt number over the hot vertical wall. The low-Reynolds-number models gave Nusselt number results in better agreement with the experimental data.

The importance of surface radiation with natural convection in square and rectangular enclosures has also been studied and investigated by many researchers. Balaji and Venkateshan [81, 82], numerically investigated the interaction of surface radiation with laminar free convection in a square cavity. They elucidated the importance of surface radiation even at low emissivity and provided some reasons for the discrepancies noted between the experimental and theoretical correlations. They derived correlation equations to calculate convection and radiation Nusselt numbers in square enclosures.

Sen and Sarkar [83], have considered the effects of variable properties on the interaction of laminar natural convection and surface radiation in a differentially heated square cavity. They discovered that, the presence of both radiation at low emissivity (ε=0.1) and variable properties, affect intensively, the thermal stratification of the core and the symmetry of the mid-plane vertical velocity as well as temperature profiles. Akiyama and Chong [84], analysed the interaction of laminar natural convection with surface thermal radiation in a square enclosure filled with air. They found that the presence of surface radiation significantly altered the temperature distribution and the flow patterns and affected the values of average convective and radiation Nusselt numbers.

Velusamy et al., [85], studied the turbulent natural convection with the effect of surface radiation in square and rectangular enclosures. They pointed out that, the radiation heat transfer is significant even at low temperatures and low emissivity. Colomer et al., [86] looked at the three-dimensional numerical simulation of the interaction between the laminar natural convection and the radiation in a differentially heated cavity for both transparent and participating media. Their work reveals that in a transparent fluid, the radiation significantly increases the total heat flux across the enclosure.

Ridouane and Hasnaui [87] investigated the effect of surface radiation on multiple natural convection solutions in a square cavity partially heated from below. They found that, the surface radiation alters significantly the existence ranges of the resultant solutions. Sharma et al., [88] studied the turbulent natural convection with surface radiation in air filled rectangular enclosures heated from below and cooled from other walls. Their results emphasise the need for coupling radiation and convection to get an accurate prediction of heat transfer in enclosures.

2.4 Simultaneous temperature and mass transfer induced buoyancy driven flow in enclosures

The Simultaneous heat and mass transfer in enclosures containing solid objects is important for many practical flows such as indoor environments [89-95], drying/cooling of agricultural products [96] and other engineering applications [97-105]. The basic set up for such flows, which has also attracted attention from both experimental and numerical scientists, is a rectangular cavity whose vertical walls are heated differentially [50, 106, 107].

In the last decade or so the trend in buoyancy driven flow research has shifted to the examination of cavity flow coupled with heat and mass transfer. Most of the studies in this category are concentrated on steady state laminar flow of Rayleigh number ranging from 10^4 to 10^6. Moshkin et al., [108] and McBrain [109] investigated temperature and mass concentration gradient induced laminar flow in an enclosure. They used a single phase modeling approach for the transport of fluid mixture.

It is fairly recently that a number of works have appeared on buoyancy driven flows in enclosures filled with varying numbers of solid objects. Unlike porous medium, these objects are not in contact with each other, but are close enough to influence the transfer processes significantly [110, 111]. Most of these works are limited to steady state two dimensional laminar flow of Rayleigh number ranging from 10^5 to 10^9, although the higher values of Rayleigh number are likely to be turbulent. The flow development is further complicated by the evidence that radiation also plays an important role [107, 112-121] in establishing the flow.

An important aspect of the above type of flow which has not been investigated in detail is the effect on heat and mass transfer due to the wall proximity of blockages. This issue has many practical engineering applications such as natural drying of wood

stacks [122, 123], cold storage stacking [124-130] or location of venetian blinds in double facade [131, 132]. The objectives of this paper are hence, to look at typical features of the heat and mass transfer for variable proximity of the solid objects. The issue of emissivity for radiation simulation has also been explored.

Catalin et al. [133] and Laguerre et al. [111] investigated temperature and mass concentration gradient induced laminar flow in an enclosure. They used the single phase modelling approach for the transport of fluid mixture. Saturation condition with fluid mixture in thermal equilibrium was assumed for the fluid domain and the ideal gas law was used for density. However, the numerical work carried out by Catalin et al. [133] and Close [134] assumed a two-phase laminar flow for the transport of fluid mixture.

2.5 **Natural convection in confined space partially filled by solid products**

Published works in this category are fairly recent where the focus of research is on buoyancy driven flows in an enclosure filled with varying numbers of solid obstacles. Unlike porous medium, these obstacles are not in contact with each other but are close enough to influence the transfer processes significantly. Typical examples in this category are the works by Das and Reddy [110], Desrayaud and Lauriat [135], Laaroussi and Lauriat [136] and Yoon et al. [56], all of which are limited to steady state two dimensional laminar natural convection flow of Rayleigh number ranging from 10^5 to 10^8.

Das and Reddy [110] and Yoon et al., [56] have reported the fluid flow and heat transfer in a differentially heated rectangular cavity containing just one disconnected solid product, and Bragas and de Lemos [137] and Hooman and Merrikh [138] investigated the cavity filled with several. The findings from these research works show that when a limited number of solid products are involved, the fluid flow is predominantly confined between the vertical walls and the first column of the objects. Also, an increase in the number of solid products results in greater fluid flow in some areas especially close to the product surfaces.

Another important characteristic of this kind of flow is the importance of radiation between surfaces. It is well known [131, 132, 139-148] that the effect of radiation is fairly significant and comparable with the convective heat transfer even for moderately low temperature difference in naturally ventilated spaces. In this context,

the surface emissivity plays a very important role in establishing the total heat transfer. Laguerre et al., [13] have reported a study for a Rayleigh number of 1.45 x 10^9. The numerical calculations were based on the assumption that the flow is laminar but in reality the above Ra is more towards the turbulent regime. Also, the effect of radiation has been analysed only for a specific emissivity.

2.6 **Summary of key literatures**

Authors	Fluid and Ra	Method/ Highlights
Kutatelaze et at., [149].	Dry air Ra unspecified	Experimental study of the hydrodynamics of a turbulent free convection boundary layer on a vertical plate. The lateral position of the peak mean velocity increases with height and increasing the cavity width leads to a corresponding increase of the boundary layer thickness but significantly decrease the velocity value.
Fillis and Poulikakos, [150].	Water $10^{10}<Ra<5\times10^{10}$	The experimental study of natural convection in a parallelepipedal enclosure induced by a single vertical wall. The findings support the view that the use of more realistic temperature boundary conditions in enclosure natural convection needs careful examination.
Han et al., [151].	Water Pr=8, Sc=2000 $10^5<Ra<10^6$	Experimental study of double diffusive natural convection flows in a 2D rectangular enclosure, were investigated using an electrochemical technique with the vertical electrodes maintained at different temperatures. They noticed that the peak of the velocity values starts to decrease and move away from the wall after the enclosure mid-height.
King K. J., [152].	Dry air Pr = 0.7 $Ra = 4.5\times10^{10}$	The experimental study of natural convection in a rectangular cavity with the vertical walls maintained at different temperatures. The boundary layer thickness and the peak of the mean velocity were at its minimum near the bottom of the heated wall then starts to increase up to the mid-height, and then starts to decrease again.
Kirkpatrick and Bohn, [153].	Dry air $0.1 \times10^{10} \leq Ra \geq 3 \times 10^{10}$	The experimental study of natural convection using four different configurations of differently heated and cooled vertical and horizontal surfaces in a cubical enclosure at high Rayleigh numbers were conducted. For the boundary conditions of the experiment, the heat transfer from the horizontal surfaces was not strongly affected by the presence of a horizontal temperature gradient.

Cheesewright et al., [154].	Dry air $Ra = 10^{10}$	Carried out experimental investigations on 2D buoyant cavity flows. They studied rectangular cavities to produce experimental data for validation of two-dimensional CFD codes. They also produced a large amount of measurements of mean and fluctuating values of velocity and temperature.
Lankhorst et al., [69].	Dry air $1\times10^9 \leq Ra \geq 4\times10^9$	Conducted experimental studies on buoyancy-induced flows in a differentially heated air filled square enclosure. Core stratification was found to have a profound influence on the regimes and the characteristics of the flow. They also observed flow reversal outside the boundary layer.
Dafa Alla and Betts, [155].	Dry air $Ra = 0.83 \times 10^6$	Carried out an experimental investigation on turbulent natural convection in an air cavity with an aspect ratio of 28.6. The experimental data in the central portion of the tall cavity have been averaged to simulate an antisymmetric, Boussinesq, fully developed flow in an infinitely tall air cavity. Causes of asymmetry of the data, including radiation absorption, were also assessed.
Betts and Bokhari, [156].	Dry air 0.86×10^6 and 1.43×10^6	Experiments were undertaken to investigate the natural convection of air in a tall differently heated rectangular cavity, by fitting partially conducting top and bottom walls and outer guard channels. It was observed that the partially conducting roof and floor provide locally unstable thermal stratification in the wall jet flows there, which enhances the turbulence as the flow moves towards the temperature controlled plates.
Ampofo, F., [72].	Dry air $Ra = 1.58 \times 10^9$	Conducted an experimental study of low level turbulence natural convection in an air filled vertical partitioned square cavity. The main focus of this work was analysing turbulence quantities. The experimental results revealed that the temperature and velocity fluctuations were confined to the boundary layers along the solid walls. It was also concluded that the temperature and velocity components were fluctuating independently of each other.
Ampofo and Karayiannis, [157].	Dry air $Ra = 1.58 \times 10^9$	Carried out an experimental study of low-level turbulence natural convection in an air filled vertical square cavity. The experiments were conducted with very high accuracy and as such the results can form experimental benchmark data and will be useful for validation of computational fluid dynamics codes.
Tian and Karayiannis	Dry air	An experimental study of two-dimensional low level turbulence natural convection in an air filled vertical

[158]	Ra = 1.58×10^9	square cavity was conducted. It was in the low turbulence region with a base frequency of about 0.1–0.2 Hz. The temperature and velocity fluctuations were limited in the boundary layers along the solid walls and were not in Gaussian distribution. The results indicate that the temperature and the velocity components fluctuate separately.
Calcagni and Paroncini, [49].	Dry air Ra = 10^3 to 10^6	Experimental and numerical study was performed on free convective heat transfer in a square enclosure characterized by a discrete heater located on the lower wall and cooled from the lateral walls. The study analysed how the heat transfer develops inside the cavity at the increasing of the heat source length. It was observed that for low Rayleigh numbers ($\leq 10^4$); the conduction heat transfer is the most important heat transfer mechanism.
Xu and Li, [159].	Molten gallium Ra unspecified	An experimental study on the temperature gradient induced natural convection in molten gallium was conducted. The temperature measurements along horizontal lines revealed a nonlinear temperature distribution which in turn shows the significance of convection in this case. The velocity along the line in the middle of geometry has two peak points near two vertical walls and zero at the core.
Laguerre et al., [13].	Dry air $1.92 \times 10^8 \leq Ra \geq 3.04 \times 10^8$	An experiment was carried out using a refrigerator model in which heat is transferred by natural convection between a cold vertical wall and the other walls, which are exposed to heat losses. Their aim was to study the effect of obstacles on temperature profiles. The air temperatures were lower almost everywhere in the model containing blocks. The presence of the blocks seems to enhance heat transfer particularly near the cold wall.
Shu et al., [160].	Dr air, and Molten metal Pr = 0.7 to 0.01	An investigation of natural convection in a cavity with imposed modulated thermal gradients or modulated gravity force was carried out. It was also found that for a fluid with a small Prandtl number typical of molten metal and semiconductor melts, modulated gravity and thermal gradients produce almost the same flow field both in structure and in magnitude.
Ince and Launder, [77].	Dry air Ra unspecified	Numerical computations were reported of turbulent natural convection of air in two tall rectangular enclosures with heated and cooled vertical walls. The very different aspect ratios considered, 30:1 and 5:1, lead to appreciable differences in flow structure in the two cases.

		The standard form of the k-ε predicts length scales too large at locations near to separation points and consequently gives wrong prediction of wall heat transfer.
Henkes and Hoogendoom, [161].	Dry air, Water $Ra=10^{14}$ for air $Ra=10^{15}$ for water	Numerical investigation was performed for laminar and turbulent natural-convection flow in a two-dimensional square cavity heated from the vertical side. Three different turbulence models are compared. Comparison of the averaged wall-heat transfer with experiments for the hot vertical plate and for tall vertical cavities shows that the standard *k-ε* model gives a too high prediction, whereas the low-Reynolds-number models were reasonably close to the experiment.
Balaji and Venkateshan, [162].	Dry air Ra unspecified	A numerical investigation of free convection in a rectangular enclosure has been carried. Their study has thrown light onto the importance of surface radiation even at low emissivity and temperature levels and provides an explanation of the discrepancies between the experimental and theoretical correlations.
Swarnendu and Sarkar, [83].	Dry air $5x10^3 \leq Ra \geq 10^6$	The interaction of variable property convection and surface radiation in a differentially heated square cavity was reported. It was observed that the effect of radiation is to suppress the formation of multi-cells within the core, as well as the separation cells at the top and bottom plates. From the numerical viewpoint, the presence of radiation considerably delays the convergence.
Akiyama and Chong, [84].	Dry air Ra unspecified	The interaction of natural convection with thermal radiation of gray surfaces in a square enclosure filled with air was numerically investigated. The effect of radiation on the flow field, temperature distribution, and heat transfer are predicted. The result shows that surface radiation significantly altered the temperature distribution and the flow patterns, especially at higher Rayleigh numbers.
Velusamy et al., [163].	Dry air $10^9 \leq Ra \geq 10^{12}$	The interaction effects between surface radiations with turbulent natural convection of a transparent medium in rectangular enclosures were numerically analysed, for a wide range of Rayleigh number and aspect ratio from 1 to 200. The interaction with surface radiation results in larger velocity magnitudes and turbulence levels in the vertical as well as horizontal boundary layers, leading to an increase in the convective heat transfer.

Ridouane and Hasnaoui, [164].	Dry air $10^3 \leq Ra \geq 4\times10^6$	A numerical study of natural convection with surface radiation in an air filled square enclosure with a centrally heated bottom wall and cooled upper wall is presented. The vertical walls and the rest of the bottom wall are assumed to be insulated. The problem was studied for surfaces emissivity ε, varying from 0 to 1. It was found that the surface radiation alters significantly the existing range of the solutions.
Sharma et al., [165].	Dry air $10^8 \leq Ra \geq 10^{12}$	Conjugate turbulent natural convection and surface radiation in rectangular enclosures heated from below and cooled from other walls, typically encountered in Liquid Metal Fast Breeder Reactor subsystems, was investigated by a finite volume method for various aspect ratios. The influence of the wall emissivity and the external heat transfer coefficient on the heat transfer from the enclosure has also been investigated.
McBain G.D., [109]. Sparrow et al., [166].	Multi-component fluids $10^4 \leq Ra \geq 10^6$	An investigation of temperature and mass concentration gradient induced laminar flow in an enclosure was reported. They used a single phase modelling approach for the transport of fluid mixture. The heat transfer formula agrees well with published data for the square cavity with zero humidity gradients.
Laguerre et al., [167].	Moist air $Ra = 10^9$	The work zone was arranged in such a way that 2D transfer and flow were established. At steady state, temperature, velocity and humidity fields on the symmetry plane were measured in un-humidified and humidified cavity. The influence of radiation near the cold and warm walls was found to be significant
Catalin et al., [168].	Moist air Ra unspecified	A numerical investigation was conducted to assess the thermal comfort taking into account the indoor air moisture and its transport by the airflow within an enclosure. Their results revealed a good potential to ameliorate the combined modelling of heat, moisture and air transport, and that the effect due to water vapour should not be neglected.
Laaroussi and Lauriat, [136].	Moist air $10^6 \leq Ra \geq 10^7$	Heat transfer by natural convection and surface condensation in two-dimensional enclosures in contact with a cold external ambient through a wall of finite thickness was studied numerically. Special attention was given on the modelling of the flow of a binary mixture consisting of humid air. The decrease in the average density of the mixture leads to significant variable's reductions at steady-state which, in turn, causes lower overall heat transfer rate

		than in dry air.
Yoom et al., [169].	Dry air $10^3 \leq Ra \geq 10^6$	Numerical calculations were carried out for the three-dimensional natural convection induced by a temperature difference between a cold outer cubic enclosure and a hot inner sphere. The study investigated the effect of the inner sphere location on the heat transfer and fluid flow. For the highest Rayleigh number, the local peaks of the Nusselt number on the top wall of the enclosure shows sinusoidal distribution along the circumferential direction.
Braga and Lemos, [137].	Dry air $Ra = 10^4$	Their work compared heat transfer characteristics across a square cavity partially filled with a fixed amount of conducting solid material. Comparisons were obtained by numerically solving a conjugate heat transfer problem that considers both the solid and the fluid space. Their results show that the average Nusselt number of cylindrical rods is slightly lower than those for square rods.

2.7 **Concluding remarks**

From the literature reviewed presented in this chapter, it has been found that natural convection flows have been extensively studied during the past few decades both experimentally and numerically. Even a two-dimensional natural convection in rectangular cavity which seems simple, however, still poses a great numerical challenge, although great progress has been made. However, several issues are still unresolved and need further attention. For example, the treatments of the sub-layer near the wall, uncertainty of boundary conditions, influence of radiation properties etc.

There seems to be very limited work reported for cavities partially filled with disconnected blockages, in particular, no work on the influences of blockage proximity and group location within the enclosed space can be found. Furthermore, there appears to be limited experimental data for the blockage interaction with flow and heat transfer. Therefore, this study is focused on resolving the various unresolved issues specified in the literature, which will further enhance the understanding of the subject. This will be achieved by providing reliable experimental benchmark data and

performing a number of parametric studies on various issues associated with the resolved issues.

Chapter 3 - THEORETICAL BACKGROUND

3.1 Introduction

A study of considerable importance in areas concerned with the physical processes involved in energy generation and utilization is that of heat transfer. Heat transfer is thermal energy in transit due to a spatial temperature difference. Whenever a temperature difference exists in a medium or between media, heat transfer must occur. Conduction, convection and radiation are the three modes of heat transfer; the former occurs if a temperature difference exists in a material due to the motion of the microscopic particles that comprise the material. When the conduction heat transfer processes are coupled with the motion of the fluid it is termed convection heat transfer. Thermal radiation heat transfer is caused by energy emission in the form of electromagnetic waves or stream of photons.

In the diversity of studies related to heat transfer, considerable effort has been directed at the convective mode, in which the relative motion of the fluid provides an additional mechanism for the transfer of energy and of material, the latter being a more important consideration in cases where mass transfer, due to a concentration or composition difference, occurs. Besides the importance of natural convection in many areas of interest in technology and in nature, a study of natural convection processes is also important because of heat rejection and removal in many devices, processes and systems. Natural convection represents a limit on the heat transfer rates and this becomes a very important consideration for problems in which other modes of heat transfer are either not possible or not practical [170, 171].

It is also relevant for safety considerations under conditions when the usual mode fails and the system has to depend on natural convection to get rid of the generated heat. This is particularly significant in many electronic devices and systems and in power, where such considerations in design are essential to avoid overheating. The growth of interest over the recent past has also been largely due to its relevance to thermal management of indoor environments. Theoretical background of natural convection flow and heat and mass transfer mechanisms is the subject of this chapter.

3.2 The nature of coupled fluid dynamics and heat transfer

In natural convection process the flow results from an interaction of the density difference with the gravitational field and is dependent on the temperature and concentration fields. As such the motion that arises is not known at the onset and has to be determined from a consideration of the heat and mass transfer processes coupled with fluid flow mechanisms. The schematic and the boundary layer flow are shown in Fig. 3-1.

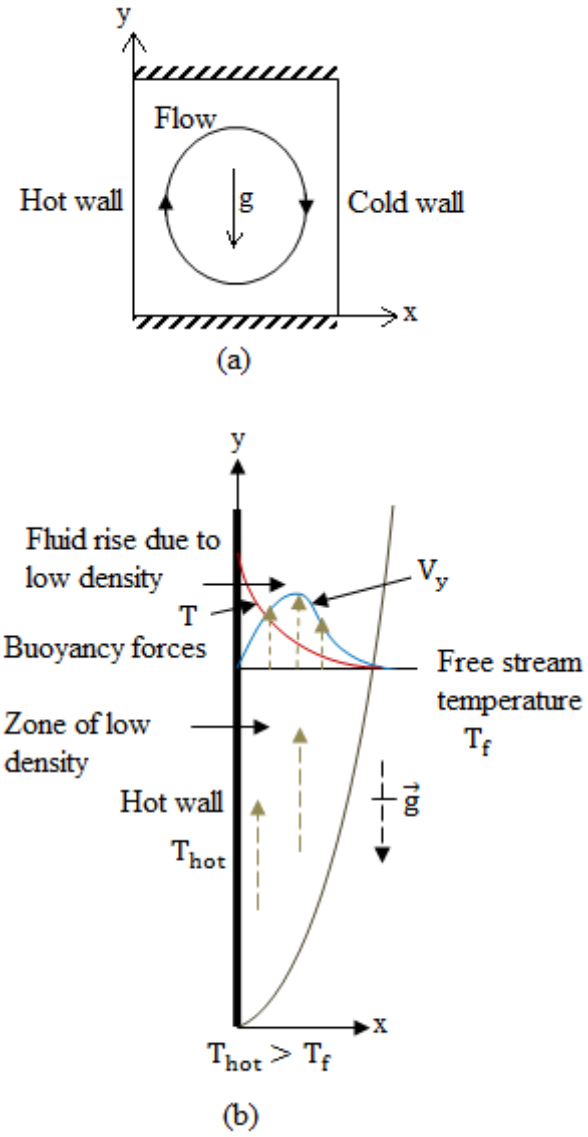

Figure 3-1: Schematic of natural convection flow (a) rectangular enclosure (b) along a heated vertical surface

Convection is also inevitably coupled with the conductive mechanisms, since, though the fluid motion modifies the transport process, the eventual transfer of energy from

one fluid element to another in its neighbourhood is through conduction. Also, at the solid surface, the process is predominantly conduction due to the no-slip condition at the boundary. A study of convective heat transfer, therefore, involves the mechanisms of conduction and, sometimes, of radiation coupled with fluid flow. Hence the study of this mode of heat transfer is a very complex one [4, 172].

Natural convection processes are a multi-dimensional problem involving conduction, convection and radiation heat transfer and can be solved using computational fluid dynamics (CFD). CFD is a branch of fluid mechanics that uses numerical methods and algorithms to solve and analyze problems involving fluid flow. Conduction-only problems can be simply dealt with by solving the heat conduction equation (diffusion equation). When fluid flow is involved the resulting convective heat transfer problem is solved by tackling the enthalpy equation, alongside the Navier-Stokes equation and the continuity equation. These equations can be found in most fluid dynamics text books [4, 173-176]. The boundary conditions for the enthalpy equation take the case of heat transfer into and out of the computational domain across its boundaries. The internal distribution of heat source and sink processes and the transport of heat by means of diffusion and convection determine the enthalpy distribution due to fluid flow.

In naturally ventilated spaces in building and offices, temperatures are low so radiative heat fluxes are comparable in size with convective heat fluxes since buoyancy-driven flow velocities are often small [4, 173, 177]. Also, there is no direct coupling between radiation and the flow field, since radiation or radiation properties of fluids and boundaries do not depend directly on the fluid velocity. However, the fluid flow influences the spatial distribution of temperature and species concentration. These determine the intensity of radiation emitted by boundary surfaces and participating fluids as well as the radiation properties of a participating medium. This ensures that there is strong indirect coupling between the flow field and radiation environment. Therefore, radiation effects will cause changes in the boundary equations of the energy equation.

3.3 Natural convection correlation and dimensionless numbers

In natural convection processes the flow is usually wall bounded and develops as a result of density difference due to temperature gradient in the presence of gravitational field. Therefore Reynolds number has no place in natural convection definition. The dimensionless numbers associated with natural convection flow are:

- Grashof number (Gr) describes the relationship between natural convection buoyancy and viscosity within a fluid. $Gr = \frac{g\beta\Delta TL^3}{v^2}$

  Where, L=length, v=kinematic viscosity and β=volumetric thermal expansion coefficient.

- Prandtl number describes the relationship between momentum diffusivity and thermal diffusivity. $Pr = \frac{v}{\alpha}$

- Rayleigh number is the product of Grashof and Prandtl number. $Ra = Gr.Pr$

  The Rayleigh number represent the ratio of buoyancy and viscosity forces times the ratio of momentum and thermal diffusivities.

- Nusselt number is the ratio between total heat transfers by convection to that by conduction in the fluid. $Nu = \frac{hL}{k_f}$

3.4 Turbulent natural convection

Some of the numerical approaches for solving turbulent flows are highlighted here. The main focus is on the low-Reynolds number version of the k-ε model which is adopted in all simulations of this research. The modeling code that has been used is a state-of-the-art general purpose commercial package FLUENT 14 which is a part of the ANSYS software. The solvers are based on finite volume method where the flow domain is discretized onto a finite set of control volume or cells, and the general transport equations for mass, momentum, energy, species, etc., are solved on this set of control volumes shown in equation (3-1) for a general variable ϕ.

$$\frac{\partial}{\partial t}\int_V \rho\phi dV + \oint_A \rho\phi V.dA = \oint_A \Gamma_\phi \bar{\nabla}\phi.dA + \int_V S_\phi dV \qquad (3-1)$$

Then, the partial differential equations are discretized into a system of algebraic equations. Finally, all the algebraic equations are then solved numerically to render the solution field.

3.4.1 **Mean flow equations and their solution**

There are three major numerical methods for predicting turbulent flows in:

i. Direct Numerical Simulation (DNS): This is the most accurate approach for solving the Navier-Stokes equations. Also it can be mentioned that it is the simplest method regarding implementation concept [173]. The DNS result is valid like measurements from experimental data and is in principle, capable of resolving all motions in the flow. DNS produces very detailed data for the flow but it is computationally too expensive and hence is hardly used for practical flows.

ii. Large eddy simulation (LES): In this approach, the largest scale motions of the flow are solved but approximations are used to predict the small scale motions. LES is less accurate than DNS but is numerically more economic. However, for practical engineering flows of complex flow field, LES is still computationally too expensive [178-180].

iii. Reynolds averaged Navier-Stokes (RANS): This method is based on time averaging the governing equations of motion. Typical examples of such models are the k-ε or the k-ω models in their different forms. These models simplify the problem to the solution of two additional transport equations and introduce an Eddy-Viscosity (turbulent viscosity) to compute the Reynolds Stresses. More complex RANS models are available which solve an individual equation for each of the six independent Reynolds Stresses directly (Reynolds Stress Models – RSM) plus a scale equation (ε-equation or ω-equation).

We have restricted ourselves to the eddy viscosity models (EVM) due to the fact that other advanced turbulence modelling such as DNS and LES are still very demanding from computation point of view and it is unlikely that it can be applied to practical flows [181, 182].

A set of differential equations result from averaging the equations of motion. The set of differential equations are called Reynolds averaged Navier-Stokes (RANS) equations. The ensemble-averaged governing equations for a conservation of the

mass, momentum and energy can be written as follows: (Eq. 3-2 to 3-5) [79, 183-185].

The continuity equation:

$$\frac{\partial \rho}{\partial t} + \frac{\partial \left(\rho u_j\right)}{\partial x_j} = 0 \qquad (3-2)$$

Momentum equation:

$$\frac{\partial (\rho u_i)}{\partial t} + \frac{\partial \left(\rho u_i u_j\right)}{\partial x_j} = -\frac{\partial p}{\partial x_i} + \frac{\partial}{\partial x_j}\left(\mu\left[\frac{\partial u_i}{\partial x_j} + \frac{\partial u_j}{\partial x_i}\right] - \rho\overline{u_\iota u_j}\right) + B_{T_i} \qquad (3-3)$$

B_{T_i} is the buoyancy term and is equal to $g_i(\rho - \rho_o)$. The fluid properties change with temperature, and in the case where the density change with temperature is not high, it is possible to assume the density in the unsteady and convection terms is constant and density only varies in the buoyancy term. This is called the Boussinesq approximation [173]. The buoyancy term is given in Eq. (3-4),

$$(\rho - \rho_o) \approx -\rho_o g_i \beta (T - T_o) \qquad (3-4)$$

Where, ρ_o is the (constant) density of the flow, T_o is the operating temperature,

β is the thermal expansion coefficient, and is represented as: $\beta = \frac{1}{\rho}\left(\frac{\partial \rho}{\partial T}\right)_p$

The mean temperature *T* is obtained from the enthalpy transport equation presented in equation (3-5),

$$\frac{\partial (\rho T)}{\partial t} + \frac{\partial \left(\rho u_j T\right)}{\partial x_j} = \frac{\partial}{\partial x_j}\left(\frac{\mu}{Pr}\frac{\partial T}{\partial x_j} - \rho\overline{u_\iota T}\right) \qquad (3-5)$$

The RANS turbulence models approach is adopted to solve the buoyancy flow in this research. These models are not closed set of equations due to the presence of $-\rho\overline{u_\iota u_j}$ and $-\rho\overline{u_\iota T}$ in equation 3-3 and 3.5 and in order to close the set of equations it is required to use turbulence models [186]. Different turbulence model means different treatment of the Reynolds stresses or turbulence heat fluxes.

3.4.2 **Treatment of Reynolds Stresses**

3.4.2.1 **Two-layer k-ε model**

The k-ε model is among the category of two-equation models in which the turbulence kinetic energy, k and dissipation, ε are solved. These two quantities allow evaluating turbulence data such as length scale, time scale, turbulence viscosity ratio etc. In the most commonly used two-equation turbulence models the Reynolds stresses in Eq. (3-3) are modelled by the following Bousinesque assumption:

$$\overline{u_i u_j} = -\nu_T \left(\frac{\partial U_j}{\partial x_i} + \frac{\partial U_i}{\partial x_j}\right) + \frac{2}{3} k \delta_{ij} \qquad (3-6)$$

Where the turbulent eddy viscosity is given by

$$\nu_T = C_\mu \frac{k^2}{\varepsilon} \qquad (3-7)$$

The kinetic energy k and its dissipation rate ε in Eq. (3-7) are computed by the following partial differential equations:

$$\frac{D}{Dt}(k) = \frac{\partial}{\partial x_j}\left[\left(\nu + \frac{\nu_T}{\sigma_k}\right)\frac{\partial k}{\partial x_j}\right] + (P_k + G_k) - \varepsilon \qquad (3-8)$$

$$\frac{D}{Dt}(\varepsilon) = \frac{\partial}{\partial x_i}\left[\left(\nu + \frac{\nu_T}{\sigma_\varepsilon}\right)\frac{\partial \varepsilon}{\partial x_j}\right] + \frac{\varepsilon}{k}[C_{\varepsilon 1}(P_k + G_k) - C_{\varepsilon 2}\varepsilon] \qquad (3-9)$$

In the two-layer model by Chen and Patel [187], the eddy viscosity and the rate of dissipation of turbulent kinetic energy in the near wall region are specified as follows employing the one-equation model:

$$\nu_T = C_\mu \sqrt{k}\, l_\mu, \qquad \varepsilon = \frac{k^{3/2}}{l_\varepsilon} \qquad (3-10)$$

Where

$$l_\varepsilon = C_L y\left[1. - e^{-(R_y/A_\varepsilon)}\right], \;\; l_\varepsilon = C_L y\left[1. - e^{-(R_y/A_\mu)}\right] \;\; and \;\; R_y = y\rho \sqrt{k}/\mu \qquad (3-11)$$

In this model the equation of turbulence kinetic energy, Eq. (3-8), is solved all the way to the wall while the equation of the turbulence kinetic energy dissipation rate, Eq. (3-9), is solved in the outer region. It is noted that the length scales in Eq. (3-10)

and constants in Eq. (3-11) is based on the forced convection turbulent boundary layer and it is questionable whether this model works well in the natural convection flows.

The high-Reynolds-number k-ε model cannot be integrated right across the wall sub-layer. Therefore, for the wall-bounded flows, the high Reynolds number version of the k-ε model cannot be applied in the immediate vicinity of the wall since it does not take into account the effects of viscosity. In order to avoid modelling these viscous effects, empirical wall functions are often employed to bridge the gap between the solid boundary and the turbulent zone. However, the universality of the high Reynolds number model breaks down for complex flows. Near-wall k-ε turbulence models or low Reynolds number k-ε models, which attempt to model the direct influence of viscosity, have been developed.

3.4.2.2 **Shear stress transport (SST) model**

In the SST model by Menter [188] the governing equations for the k and ω are solved as follows:

$$\frac{D}{Dt}(\rho k) = \frac{\partial}{\partial x_j}\left[(\mu + \sigma_{k3}\mu_T)\frac{\partial k}{\partial x_j}\right] + \rho(P_k + G_k) - \beta^*\rho\omega k \qquad (3-12)$$

$$\frac{D}{Dt}(\rho\omega) = \frac{\partial}{\partial x_j}\left[(\mu + \sigma_{\omega 3}\mu_T)\frac{\partial \omega}{\partial x_j}\right] + \rho\frac{\gamma_3}{\mu_T}(P_k + G_k) + 2\rho(1-F_1)\frac{\sigma_{\omega 2}}{\omega}\frac{\partial k}{\partial x_j}\frac{\partial \omega}{\partial x_j} - \rho\beta_3\omega^2 \qquad (3-13)$$

In this model the turbulence eddy viscosity in Eq. (3-6) is expressed by the following equations:

$$\nu_T = \frac{a_1 k}{\max(a_1\omega, SF_2)} \qquad (3-14)$$

where

$$F_1 = tanh\,(arg\,1^4), \qquad F_2 = tanh\,(arg\,2^2), \qquad (3-15)$$

$$\arg 1 = min\left[max\left(\frac{\sqrt{k}}{\beta^*\omega y}, \frac{500\nu}{y^2\omega}\right), \frac{4\rho k\sigma_{\omega 2}}{CD_{k\omega}y^2}\right] \qquad (3-16)$$

$$\arg 2 = max\left(\frac{2\sqrt{k}}{\beta^*\omega y}, \frac{500\nu}{y^2\omega}\right) \qquad (3-17)$$

$$CD_{k\omega} = max\left(\frac{2\rho\sigma_{\omega 2}}{\omega}\frac{\partial k}{\partial x_j}\frac{\partial \omega}{\partial x_j}, 10^{-10}\right) \quad (3-18)$$

The coefficient of SST model are a linear combination of the corresponding coefficients such that

$$\varphi_3 = F_1\varphi_1 + (1-F_1)\varphi_2 \quad (3-19)$$

Where F_1 is a blending function defined by Eq. (3-15), and the σ_{k3}, $\sigma_{\omega 2}$, β_3, and γ_3 are calculated by Eq. (3-19). This model is also based on the Bousinesque assumption, Eq. (3-6), in the expression of the Reynolds stresses.

3.4.3 Treatment of turbulent heat fluxes

3.4.3.1 Simple gradient diffusion hypothesis (SGDH)

In the SGDH, the turbulent heat fluxes $\left(\overline{\theta u_j}\right)$ in Eq. (3-5) are treated by the following equation:

$$(\overline{\theta u_\iota}) = -\frac{\nu_t}{Pr_t}\frac{\partial T}{\partial x_i} \quad (3-20)$$

In this equation Pr_t is the turbulent Prandtl number. It is well known that this assumption is not adequate for natural convection flows although it is widely used in forced convection flows.

3.4.3.2 Generalized gradient diffusion hypothesis (GGDH)

In the GGDH by Ince and Launder [77], the turbulent heat fluxes $\left(\overline{\theta u_j}\right)$ in Eq. (3-5) are approximated by the following equation.

$$\overline{\theta u_\iota} = -C_\theta\frac{k}{\varepsilon}\left(\overline{u_\iota u_k}\frac{\partial T}{\partial x_k}\right) \quad (3-21)$$

As shown in the above equation, the accuracy of this assumption depends on the accuracy of the computed Reynolds stresses. Ince and Launder [77] and Choi and Kim [189] used the GGDH for natural convection in a rectangular cavity with success. However, it is known that this assumption is not adequate for a natural convection with a strong stratification.

3.4.3.3 **Algebraic flux model (AFM)**

In the AFM by Kenjeres and Hanjalic [190] the turbulent heat fluxes are computed by the following algebraic equation:

$$\overline{\theta u_\iota} = -C_\theta \frac{k}{\varepsilon}\left(\overline{u_\iota u_j}\frac{\partial T}{\partial x_j} + \xi\overline{\theta u_j}\ \frac{\partial U_i}{\partial x_j} + \eta\beta g_i\overline{\theta^2}\right) \qquad (3-22)$$

When compared with the GGDH model, the last term with a temperature variance has a positive effect on the gravitational generation term G_k and it prevents G_k from being negative value. This effect stabilizes the overall solution procedures, especially for strong stratified flows

3.4.4 **Low Reynolds number RANS models**

In natural convection heat transfer the flow near the boundary is very important for establishing the temperature field in the whole domain [191]. When the wall functions are not used, sufficient grid lines near solid boundaries are desirable so that the boundary layer can be adequately resolved. However, when the wall is approached the viscous effects become more important and for $y^+ < 5$ the flow is viscous dominating, i.e. the viscous diffusion is much larger than the turbulent one. Thus, the high-Re k-ε turbulence model may not be very accurate.

The low-Re k-ε models are the modifications of high-Re k-ε models so that they can be used all the way down the wall. These low Reynolds number models allow integration of the transport equations for the turbulent kinetic energy and its dissipation rate to the wall. The constants and coefficients in the high-Re k-ε model are adjusted so that it is capable of resolving flows near the wall.

The selection of the low Reynolds number models used in this work was guided by the investigation carried out by Martinuzzi and Pollard [192]. Their study compared the ability of the four turbulence models mentioned above (high-Re k-ε model, low-Re k-ε model, algebraic stress model, and Reynolds stress model) to predict developing, turbulent pipe flow. Several versions of the low Reynolds number k-ε models were reviewed and evaluated by Patel, V.C., et al.[193]. Hrenya C. M., et al. [194] extended the numerical study of Patel, V.C., et al. [193] on Turbulence models for near-wall and low Reynolds number flows in pipes. Wang S. J., et al. [195] tested

the predictive capability of the low Reynolds number k-ε models for the case of impingement heat transfer.

In general, analyses of turbulence modelling for low speed turbulent natural convection flow and heat transfer applications are notably lacking in literature. However, differences do exist between the flow in a pipe and natural convection heat transfer, therefore the purpose of the current investigation is to test the predictive capabilities of these models for the cases of natural convection flow and heat transfer.

3.4.5 **Low-Reynolds-number k-ε models**

In the low-Reynolds-number k-ε model, the transport equations can be integrated up to the wall. The constants and coefficients are adjusted in the k-ε model so that it is capable of resolving flows near the wall. Low local Reynolds number damping is applied in order to capture the effect of the wall.

Based on the Bousinesq approximation, the Reynolds stress is related to the local velocity gradients by an eddy viscosity ν_t. The turbulence scalar quantities (k and ε) used to calculate ν_t are determined from the transport equation of turbulent kinetic energy and its dissipation rate, presented in Eq. (3-23) and (3-24) respectively:

$$\frac{\partial(\rho k)}{\partial t}+\frac{\partial\left(\rho U_j k\right)}{\partial x_j}=\frac{\partial}{\partial x_j}\left[\left(\mu+\frac{\mu_t}{\sigma_k}\right)\frac{\partial k}{\partial x_j}\right]+P_k+G_k-\rho\varepsilon+D \qquad (3-23)$$

$$\frac{\partial(\rho\varepsilon)}{\partial t}+\frac{\partial\left(\rho U_j \varepsilon\right)}{\partial x_j}=\frac{\partial}{\partial x_j}\left[\left(\mu+\frac{\mu_t}{\sigma_\varepsilon}\right)\frac{\partial \varepsilon}{\partial x_j}\right]+C_{\varepsilon 1}f_1\frac{\varepsilon}{k}(P_k+G_k)-C_{\varepsilon 2}f_2\rho\frac{\varepsilon^2}{k}+E \qquad (3-24)$$

The eddy viscosity is: $\mu_t=\rho C_\mu f_\mu \frac{k^2}{\varepsilon}$

The constants $C_\mu, C_{\varepsilon 1}$ and $C_{\varepsilon 2}$ in the high-Reynolds-number k-ε model are respectively multiplied by, $f_{\varepsilon 1}\ and\ f_{\varepsilon 2}$. These wall damping functions are in turn functions of turbulent Reynolds number Re_t,

Where $Re_t=\frac{\rho k^2}{\mu\varepsilon}$, $P=\tau_{ij}^{turb}\frac{\partial u_i}{\partial x_j}$ and $Re_\varepsilon=\frac{\rho\left(\mu\varepsilon/\rho\right)^{1/4}y}{\mu}$

Where C_μ, C_1, C_2, σ_μ and σ_ε are the same empirical turbulence model constants to those conventionally used in the high Reynolds number k-ε model. The damping

functions f_μ, f_1 and f_2, and in some models the terms *D* and *E* are used to make the low Reynolds numbers valid in the near wall region.

These leads to the formulation of low Reynolds number k-ε models. The six low Reynolds k-ε models available in FLUENT are those developed by Abid - AB [196]; Lam and Bremhorst - LB [197]; Launder and Sharma - LS [198]; Yang-Shih -YS [199]; Abe, Kondoh and Nagano - AKN [200]; and Change, Hsieh and Chen - CHC [201], respectively.

3.4.6 **Low-Reynolds number k-ε Models Constants**

Table 3-1 summarizes the numerical values assigned to the constants of the six different low Reynolds number models. The value of C_μ is fixed (0.09) by the requirement that for local equilibrium shear layers, the production of the *k* equals its dissipation. The value of C_1 is estimated from a constraint relation resulting from consistency with the law of the wall region, where the molecular viscosity effects are negligible.

The value for the model constant C_2, in all six models lies between 1.8 and 2.0. This range of values is based on experiments of decaying homogenous grid turbulence. This value is determined directly from measurements of the decay of k behind a grid at high-Re numbers. The constants σ_k and σ_ε are obtained by computer optimization.

Table 3-1: Numerical values for the Low-Re k-ε number models constants

Model	Researcher	C_μ	C_1	C_2	σ_k	σ_ε
AB	Abid (1993)	0.09	1.45	1.83	1.0	1.4
LB	Lam and Bremhorst (1981)	0.09	1.44	1.92	1.0	1.3
LS	Launder - Sharma (1974)	0.09	1.44	1.92	1.0	1.3
YS	Yang – Shih (1993)	0.09	1.44	1.92	1.0	1.3
AKN	Abe-Kondoh-Nagano (1994)	0.09	1.50	1.90	1.4	1.4
CHC	Chang-Hsieh-Chen (1995)	0.09	1.44	1.92	1.0	1.3

3.4.7 **Low-Reynolds number k-ε model functions**

Table 3-2 outlines the different functions f_μ, f_1 and f_2 for the six models. The main implication of these functions is to modify the models constants C_μ, C_1, C_2 to account for low Reynolds number effects. The Table (3-2) presents a summary of the

motivation for the choices of the different model functions descriptions and, in some cases, includes comments on how these descriptions affect the production of k.

The summary of the wall boundary conditions for k and ε are shown in Table 3-3. Also shown in table 3-4 are the expressions for the terms D and E. D term is needed to balance the molecular diffusion of k in order to satify the k transport equation in the near wall region. In several of the models (LS and YS) the term has no physical justification. But, it was included to increase the predicted dissipation rate in order to obtain a realistic k profile in the near-wall region.

Table 3-2: Summary of the low-Re k-ε model functions

Model	f_μ	f_1	f_2
AB	$tanh(0.008Re_y)(1+4{Re_T}^{-3/4})$	1.0	$[1-2/9\,exp\,(-Re_T^2)/36]^2[1-(Re_y/12)]$
LB	$[1-exp(-0.0165Re_T)]^2[1+(20.5/Re_y)]$	$1+(0.005/f_\mu)^3$	$1-exp(-Re_T^2)$
LS	$exp[-3.4/(1+Re_T/50)^2]$	1.0	$1-0.3exp(-Re_T^2)$
YS	$(1+1/\sqrt{Re_T})[1-exp(-1.5\times10^{-4}Re-5.0\times10^{-7}Re^3-1.0\times10^{-10}Re^5)]^{1/2}$	$\frac{\sqrt{Re_T}}{1+\sqrt{Re_T}}$	$\frac{\sqrt{Re_T}}{1+\sqrt{Re_T}}$
AKN	$\{(1+5.0/Re_T^{3/4})exp[-(Re_T/200)^2]\}[1-exp(-Re_\varepsilon/14)]^2$	1.0	$\{1-0.3exp[(-Re_T/6.5)^2]\}[1-(Re_\varepsilon/3.1)]^2$
CHC	$[1-exp(-0.0215Re_y)]^2(1+31.66/Re_T^{5/4})$	1.0	$[1-0.01exp(-Re_T^2)][1-exp(-0.0631Re_y)]$

Table 3-3: Basis for choice and origin of the low-Re k-ε model functions

Model	f_μ	f_1	f_2
AB	Obtained by fitting DNS data of Kim *et al*. [202] for the flow between flat plates	Did not modify ε production since near-wall effects result in a net destruction of ε	Derived from evaluation of the terms in the exact ε equation using DNS data of Kim et al. [202] for flow between flat plates
LB	Derived by combining the eddy viscosity and dissipation rate equations of a one-equation model by Hassid and Poreh [203]	Augmented to match experimental data as no E term was included in the model which solves the true dissipation rate	Tends to zero as Re_T tends to zero; does not correctly satisfy the asymptotic behaviour of the ε equation
LS	From the predictions of constant stress Couette flow; υ_T was obtained using a mixing length model and Van Driest's damping function and not the turbulent kinetic viscosity in the low Reynolds number turbulence models $\upsilon_T = C_\mu f_\mu \frac{k^2}{\varepsilon}$	Found no advantage in making f_1 a function of Re_T	Determined from measurements of isotropic grid turbulence at high and low turbulence intensities
YS	Based on characteristic time scale which approaches the Kolmogorov time scale in the near-wall region	Form obtained from the ε equation which was developed based on characteristic time scale	Form obtained from the ε equation which was developed based on characteristic time scale
AKN	Rigorous derivation; developed a characteristic length scale expression for ε valid over the entire turbulent length Re range	Followed LS	Proportional to y^2 near the wall
CHC	Direct wall effect through y^+	Enhanced generation of ε near the wall	Followed Hanjalic and Launder [204]; based on the lowest Re decay pattern data of Batchelor and Townsend (1948) [205, 206]

Table 3-4: Summary of D and E terms, and wall boundary conditions for k and ε

Model	D	E	Wall boundary condition
AB	0	0	$k = 0, \varepsilon_w = \nu\left(\frac{\partial^2 k}{\partial y^2}\right)$
LB	0	0	$\frac{\partial k}{\partial y} = 0, \left(\frac{\partial \varepsilon_w}{\partial y}\right)_w = 0$
LS	$2\nu\left(\frac{\partial \sqrt{k}}{\partial y}\right)^2$	$2\mu\nu_t\left(\frac{\partial^2 U}{\partial y^2}\right)^2$	$k = \varepsilon_w = 0$
YS	0	$\nu\nu_t\left(\frac{\partial^2 U}{\partial y^2}\right)^2$	$k = 0,\ \varepsilon_w = 2\nu\left(\frac{\partial \sqrt{k}}{\partial y}\right)^2$
AKN	0	0	$k = 0, \varepsilon_w = \nu\left(\frac{\partial^2 k}{\partial y^2}\right)$
CHC	0	0	$k = 0, \varepsilon_w = \nu\left(\frac{\partial^2 k}{\partial y^2}\right)$

3.5 **Thermal radiation modeling**

FLUENT provides five radiation models which allow radiation to be included in heat transfer simulations, with or without a participating medium [207]. The models are: Rosseland radiation model, discrete ordinates (DO) radiation model, Surface-to-Surface (S2S) radiation model, P-1 radiation model and discrete transfer radiation model (DTRM).

Numerous studies have been conducted [208] earlier to evaluate the performances of these models in evaluating the surface radiation heat transfer during natural convection and the analysis shows that Surface-to-surface radiation model is suitable for modelling enclosure radiative transfer with non-participating media. These include Surface-to-surface radiant heating or cooling, coupled radiation, convection, and/or conduction heat transfer, radiation through windows in HVAC applications, cabin heat transfer analysis in automotive application etc. The discrete ordinate radiation model gives interesting results. The advantage of the DO model over the S2S model is its ability to model enclosure radiative transfer with non-participating and participating media including radiation properties of the participating fluid.

3.5.1 **Surface emissivity thermal radiation heat transfer equation**

The emissive power of an ideal black surface is given by $E_s = \sigma T_s^4$, where T_s is the surface temperature. Surface emissivity, ε is the ratio of heat flux emitted by real surface to the heat flux emitted by a black surface. Real surface usually emits less radiative heat. Therefore, the emissive power of a real surface with emissivity ε is given by: $E_s = \varepsilon\sigma T_s^4$

Radiation transfer equation for absorbing, emitting, and scattering medium at position $\vec{r}$ in the direction $\vec{s}$ is [186, 209]:

$$\frac{dI(\vec{r},\vec{s}\,)}{ds} + (\alpha + \sigma_s)I(\vec{r},\vec{s}\,) = \alpha n^2 \frac{\sigma T^4}{\pi} + \frac{\sigma_s}{4\pi}\int_0^{4\pi} I(\vec{r},\vec{s}\,')\,\Phi(\vec{s},\vec{s}\,')d\Omega' \qquad (3-25)$$

Where $(\alpha + \sigma_s)s$ is the optical thickness of the medium.

FLUENT also allows the modelling of non-gray radiation using a gray-band model. The radiation transfer equation for the spectral intensity $I_\lambda(\vec{r},\vec{s})$ can be written as:

$$\frac{dI_\lambda(\vec{r},\vec{s}\,)}{ds} + (\alpha_\lambda + \sigma_s)I_\lambda(\vec{r},\vec{s}\,) = \alpha_\lambda n^2 I_{b\lambda} + \frac{\sigma_s}{4\pi}\int_0^{4\pi} I_\lambda(\vec{r},\vec{s}\,')\,\Phi(\vec{s},\vec{s}\,')d\Omega' \qquad (3-26)$$

λ is the wavelength, α_λ is the spectral absorption coefficient, and $I_{b\lambda}$ is the black body intensity. The non-gray DO model divides the radiation spectrum into N wavelength bands, which need not be contiguous or equal in extent.

3.6 **Mass transfer modelling**

Mass transfer is modelled using the species transport in FLUENT [207]. The model predicts the local mass fraction of each species, Y_i, through the solution of a convection-diffusion equation for the i^{th} species. This conservation equation takes the following general form:

$$\frac{\partial}{\partial t}(\rho Y_i) + \nabla.(\rho\vec{v}Y_i) = -\nabla.\vec{J_i} + R_i + S_i \qquad (3-27)$$

Where R_i the net is rate of production of species i and S_i is the rate of creation by addition from the dispersed phase plus any user-defined sources. $\vec{J_i}$ is the diffusion flux of species i, which arises due to concentration gradients. Mass diffusion in turbulent flows is

$$\vec{J_\iota} = -\left(\rho D_{i,m} + \frac{\mu_t}{Sc_t}\right)\nabla \mathrm{Y_i} \qquad (3-28)$$

where $Sc_t = \rho D_t$, is the turbulent Schmidt number, μ_t is the turbulent viscosity and D_t is the turbulent diffusivity. The convection-diffusion equation

$$\frac{\partial}{\partial x_i}(\rho u_i m_{i'}) + \frac{\partial}{\partial x_i} J_{i',i} = S_{i'} \qquad (3-29)$$

Where, $\frac{\partial}{\partial x_i}(\rho u_i m_{i'})$ = Convective term.

The convection-diffusion equation is added to airflow turbulent model to take into account the distribution of water vapour mass fraction within the square cavity.

3.7 **Conclusion**

This chapter has discussed some of the theoretical background associated with turbulent natural convection heat and mass transfer. It is understood that conduction as well as radiation may be coupled with convection during natural convection in an enclosed cavity.

The low Reynolds number k-ε model has been proposed for this study because it allows integration through the viscous sublayer and up to the wall. To scrutinize the performances of the low Reynolds number k-ε models available in FLUENT, six version have been considered and a summary of their damping functions, constants and basic choice have been presented.

One of the objectives of this thesis was to scrutinize and quantify the performance of the low Reynolds number k-ε model for natural convection heat and mass transfer in an enclosed cavity and a cavity partially filled with disconnected solid blockages

Chapter 4 - NUMERICAL STUDY OF TURBULENT NATURAL CONVECTION IN AN ENCLOSURE WITHOUT BLOCKAGES

4.1 Introduction

This chapter is focused on establishing accuracy and resolving uncertainties in relation to numerical calculations. From a computational point of view, the accuracy is affected by the choice of grids, turbulence models and other numerical issues such as convection term discretization and convergence, and these have been the major concern for numerical scientists[193, 210]. One apparently obvious point which causes differences in results is due to the choice of thermal boundary conditions for the walls [211]. While the vertical surfaces have well defined boundaries namely, isothermal walls, the boundary conditions for the horizontal walls are highly variable.

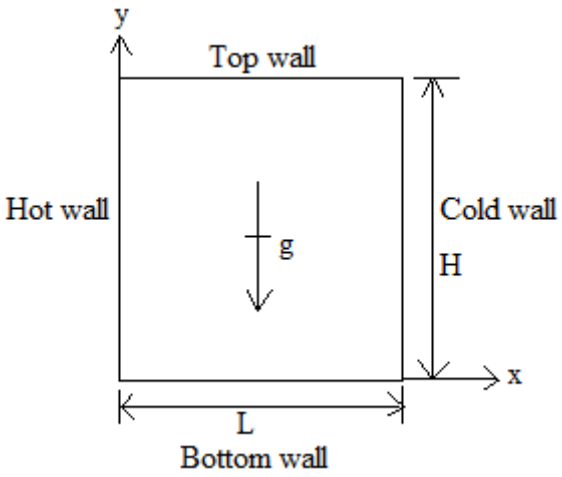

Figure 4-1 Geometry and the coordinates

The most common one that the numerical codes employ is adiabatic condition. However, due to practical problems this is not usually achievable. In this study, we investigate the two dimensional natural convection for a square cavity with particular attention given on the choice of boundary condition for the horizontal walls. Another aspect which is focused on in this work is the importance of radiation for this simple geometry. By changing the value of surface emissivity we had been able to quantify the effects of radiation on the overall heat transfer. This issue may be particularly relevant for situations where high emissivity surface properties are encountered. A number of parametric studies have been reported in this chapter, which include the following:

- Performance of low Reynolds number k-epsilon (Low-Re k-ε) models for quantifying the flow and heat transfer in coupled turbulent natural convection flow and thermal radiation heat transfer in an enclosure.
- Influence of the specification of thermal boundary condition for the passive walls (horizontal surfaces).
- Effects of surface emissivity on the flow, turbulence and heat transfer during natural convection in an enclosed cavity.

4.2 **Problem description**

The problem under investigation is shown schematically in Fig. 4-1 above. This case study is similar to that modelled experimentally by Ampofo and Karayiannis [51], and the experimental benchmark data was produced and made available in open literature for a pure natural convection in a rectangular cavity, whose flow domain of height H and length L aspect ratio =1. Vertical walls of the enclosure are isothermal and are kept at 50.15^0 C and 10.15^0 C for the hot wall and cold wall respectively. This gives a vertical wall temperature difference of 40^0 C. Temperature of the dry air is controlled at 30.15^0 C which is equal to the average of the hot and cold wall temperature. This gives buoyancy driven flow of Rayleigh number 1.5×10^9 based on the vertical wall temperature difference. Therefore, this situation is characterised by low-level turbulence in the near-wall region and a stable thermal stratification in the core fluid region.

All calculations reported herein have been performed with the general-purpose computational fluid dynamics (CFD) code, FLUENT, based on the finite volume method. Convection of mean-flow as well as turbulence quantities was approximated by second-order-upwind spatial discretization scheme, except for pressure where the PRESTO was used. The fluid is initially motionless and at a uniform temperature equal to the average of the vertical active walls temperatures. Thermo-physical properties of the dry-air are estimated at this mean temperature of the isothermal vertical walls.

Table 4-1 summarizes the physical properties of the air used. Boussinesq approximation [212] was used to describe air density variation due to temperature. No slip condition applies for all cavity walls.

Table 4-1: Physical properties of air used in the simulations

Air (at 30.15^0 C)	Value	Unit
Density (ρ)	1.16	kg/m^3
Dynamic viscosity (μ)	$1.87x10^{-5}$	kg/m.s
Kinematic viscosity (ν)	$1.61x10^{-5}$	m^2/s
Specific heat (C_p)	$1.01x10^3$	J/kg.K
Conductivity (k)	0.0264	W/m.K
Prandtl number (P_r)	0.714	-
Thermal diffusivity (α)	$2.25x10^{-5}$	m^2/s
Thermal expansion coefficient (β)	$3.30x10^{-3}$	1/K

4.3 **Grid independence study**

It is important to consider the near-wall y^+ distribution on each of the walls in the mesh. The y^+ value is a non-dimensional distance (based on local cell fluid velocity) from the wall to the first mesh node. Accurate presentation of the flow in the near-wall region determines successful prediction of wall-bounded turbulent flows. Values of $y^+ \approx 1$ are most desirable for near-wall modelling. In the present study, non-uniform grids with grid clustering near the walls, as shown in Fig. 4-2, were employed to better capture the sharp gradients near the wall. The clustering was accomplished by the use of a geometric progression in both the 'x' and 'y' coordinates.

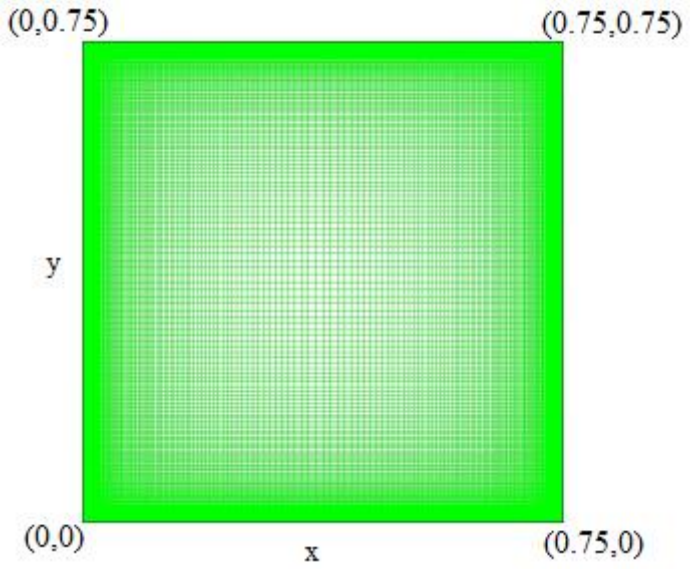

Figure 4-2 Computational grid, wall clustering

Systematic investigation was carried out using various grid densities 100X100, 140X140, 180X180, 200X200 and 220X220 were analyzed for grid independence test. Flow solution at steady state conditions are compared using low-Re k-ε model of Yang-Shih [199]. Some details of the results on the walls y^+ are shown in Fig. 4-3 (a-d). They illustrate the mean flow and heat transfer result for the grid independence study. The process for computing a steady-state solution for the refined meshes has been difficult due to the oscillation of the flows when higher-order discretization schemes are used. The less refined meshes seem to reproduce the stationary flow behaviour in the core fluid region and the flows in the corners is well-behaved.

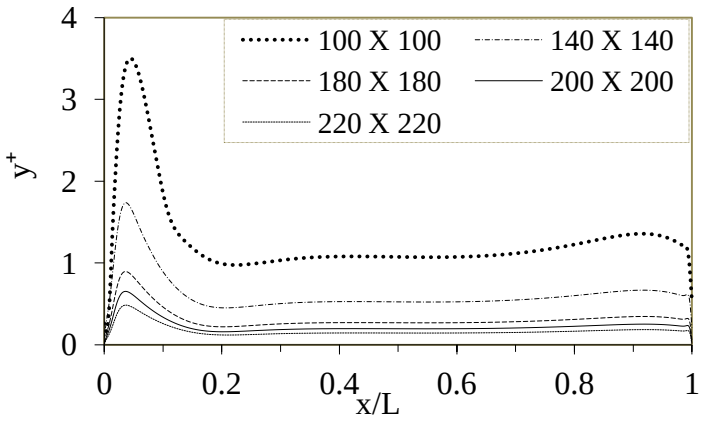

(4-3a)

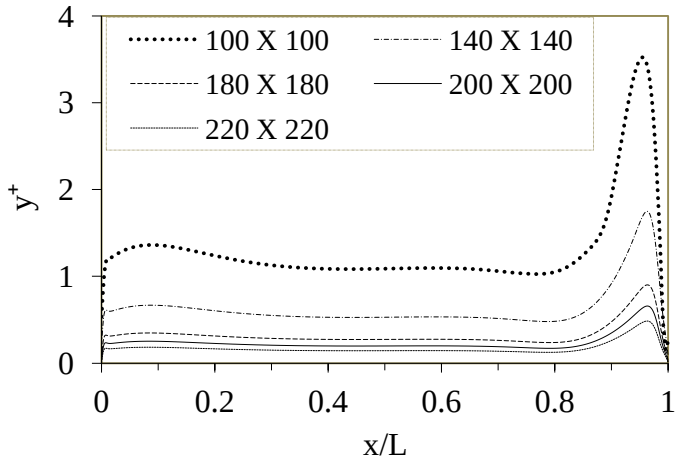

(4-3b)

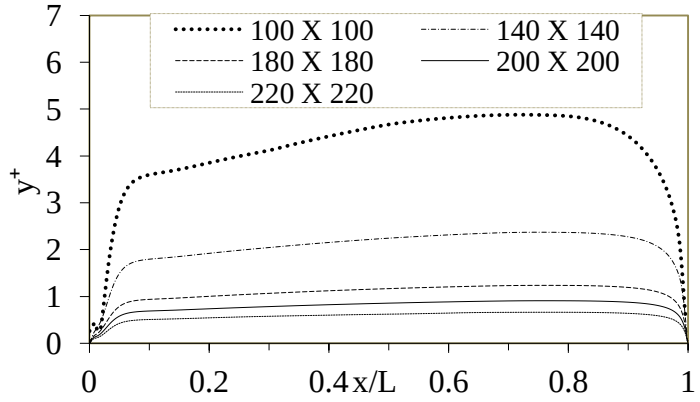

(4-3c)

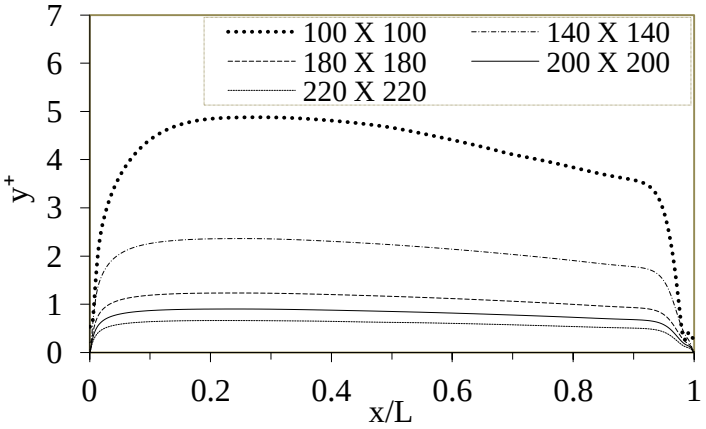

(4-3d)

Figure 4-3: Non-dimensional normal distance (y-plus); (a) top wall (b) bottom wall (c) cold wall (d) hot wall

With increasing mesh resolution, there are locations where the values of y^+ are higher. This suggests a rather different flow field is being predicted which supports increased scale capturing that is fundamental to the flow physics. A mesh density that displays a wall y^+ of about 1 is acceptable for this kind of boundary layer flow [213]. Therefore, for $y^+ \approx 1$ adequate mesh density is specified to capture the physics occurring within the inner layer.

Table 4-2: Comparison of Walls average Nusselt numbers

Mesh	100X100	140X140	180X180	200X200	220X220	Data [214]
Bottom	15.03	14.67	14.40	14.32	13.95	14.40
Cold	72.40	63.68	62.60	62.42	62.04	62.60
Hot	72.67	63.90	62.83	62.65	62.53	62.90
Top	14.53	14.20	13.92	13.84	13.39	13.90

Table 4-2 further highlight the influence of grid on the wall heat transfer for all meshes used and comparison with the experimental data of Ampofo and Karayiannis [214]. The extra fine meshes of 200X200 and 220X220 shows relatively small reduction in the wall heat transfer and y^+ value less than 1. While the coarse meshes (100X100 and 140X140) show relatively higher heat transfer, the moderately fine mesh (180X180) gives the best comparison for the wall heat transfer. Therefore the 180x180 mesh density is used for all calculations reported in this chapter.

4.4 **Low Reynolds number comparative performances**

It is well known that turbulence models play an important role in the predictions of fluid flows. A total of six eddy-viscosity (EVM) turbulence models have been tested to quantify the natural convection flow and heat transfer in an enclosed space. The reason that we restricted ourselves to the EVM is due to the fact that other advanced turbulence modeling such as LES is still very demanding.

The Reynolds Stress Models (RSMs) are much more complex than eddy-viscosity models, but are physically most complete model (history, transport, and anisotropy of turbulent stresses are all accounted for) [186]. They are computationally more expensive and less stable. Hence it is much more important to scrutinize the models (Low-Re k-ε models) that are likely to be used from the viewpoint of practitioners.

The relative performance of all six versions of the low-Re k-ε models this kind of flow and heat transfer characteristics have not been reported in literature. The results of the flow and heat transfer were analyzed by comparison with the available experimental data of Ampofo and Karayiannis [214]. The numerical modelling was performed using a commercial CFD code FLUENT 13.0 [215].

The predictions obtained from the High-Reynolds number two-equation k-ε models (Launder and Spalding,[216] Shih et al, [217], and Yakhot and Orszag [218]) will not be shown since the Low-Re number two-equation k-ε models performed considerably better. The models result comparisons are shown in Fig.4-4 for stream function plots. To further highlight the influence of these models, Fig.4-5 to Fig.4-11d show the typical mean quantity profiles predicted by various turbulence models. A careful look at the plots reveal that while the core region had been predicted well by most of the models, the situation is very different for the near wall region. For both cases

(velocity and temperature), it is clear that the Yang-Shih model [199] return the best results. Hence this model has been used for the subsequent calculations reported in this work.

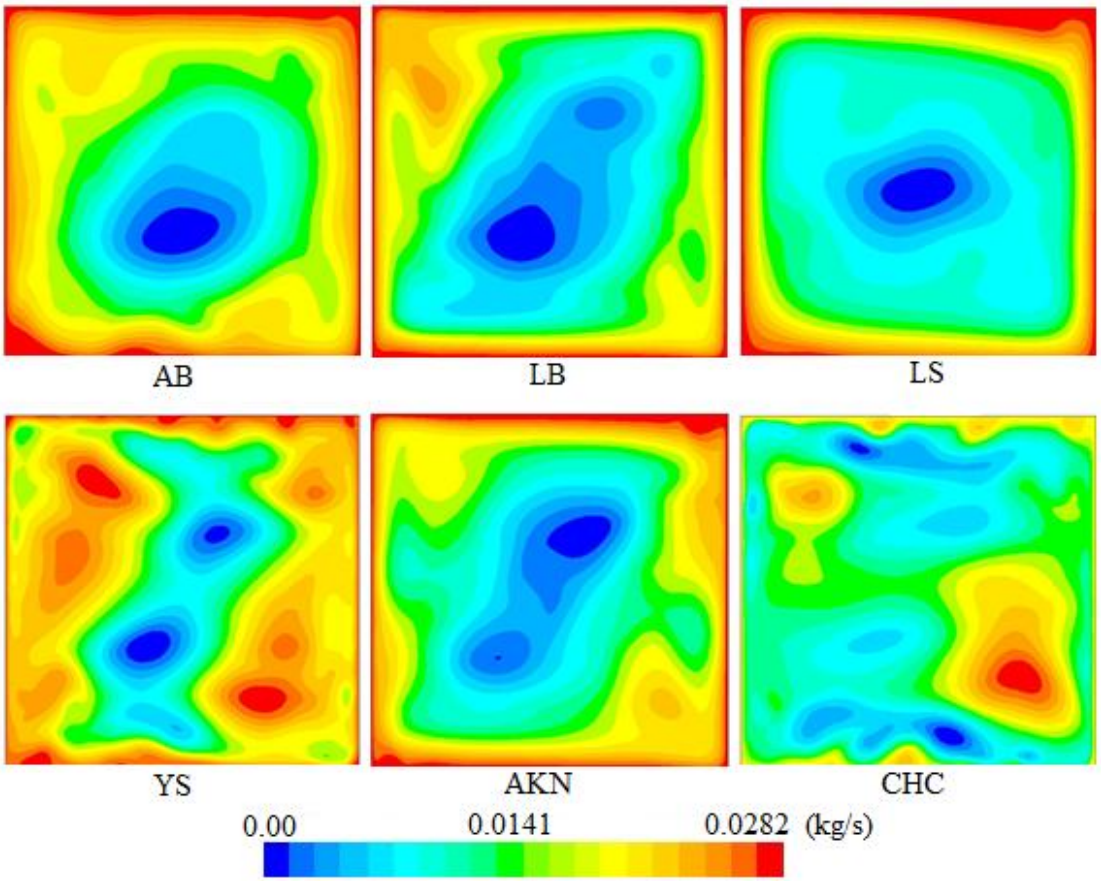

Figure 4-4: Stream function contours

This observation is in line with the mean horizontal velocity component V_x, prediction of which is shown in Fig.4-6. V_o is the reference velocity defined as $V_o = \sqrt{g\beta H\Delta T}$ and in our case is equal to 1 m/s.

The total heat transfer across the glass wall is given by the Nusselt numbers. The total heat transfer involves the contribution of the convective and radiative Nusselt numbers which can be expressed as:

$$Nu_{total} = Nu_{conv} + Nu_{rad}$$

The convective and radiative average heat transfer data are compared in terms of an average Nusselt number computed at each wall. The average Nusselt numbers for the convective and radiation components are given below:

$$\overline{Nu}_{conv} = \frac{\bar{q}_{conc} L}{\bar{k}\Delta T} = \int_0^H Nu_{conv}(y)\, dy$$

$$\overline{Nu}_{rad} = \frac{\bar{q}_{rad} L}{\bar{k}\Delta T} = \int_0^H Nu_{rad}(y)\, dy$$

Where $\bar{q}_{conv}$ and $\bar{q}_{rad}$ are the integral average wall heat flux for the convective and radiative component respectively, these values are obtained from FLUENT post-processing. L is the width of the cavity, $\bar{k}$ is the average fluid thermal conductivity, and ΔT is the temperature difference, $(= T_{hot} - T_{cold})$. The local heat transfer Nusselt number is given below:

$$Nu_{conv} = \frac{q_{conv} L}{\bar{k}\Delta T}$$

$$Nu_{rad} = \frac{q_{rad} L}{\bar{k}\Delta T}$$

Where $q_{conv} = hA(T_w - T_\infty)$ and $q_{rad} = \varepsilon\sigma A(T_h^4 - T_c^4)$ are the local heat transfer rate by convective and radiative components respectively, between a surface of area A at a temperature of T_w and a fluid of temperature T_∞. T_h and T_c represents the temperature of the hot and cold wall respectively and are evaluated at each node along a given wall. h is the average convective heat transfer coefficient, ε and σ represents the emissivity of the surface and the Stefan-Boltzmann constant $(= 5.67 \times 10^{-8}\ W/m^2K^4)$ respectively.

The data from the experimental benchmark study of Ampofo and Karayiannis were used for the results comparison (DATA) [51].

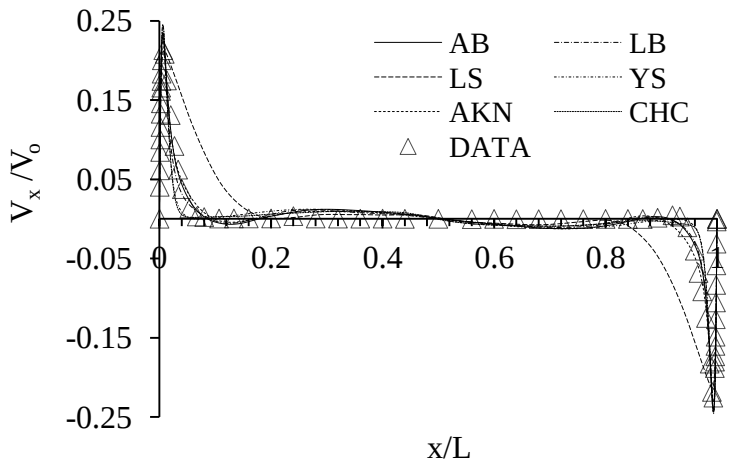

(4-5a)

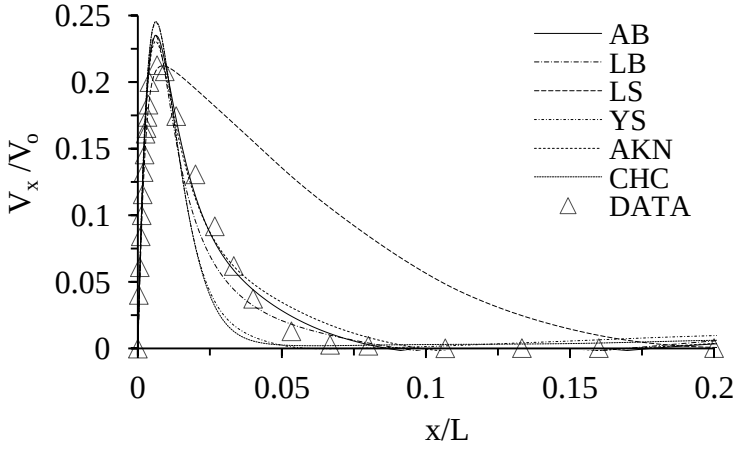

(4-5b)

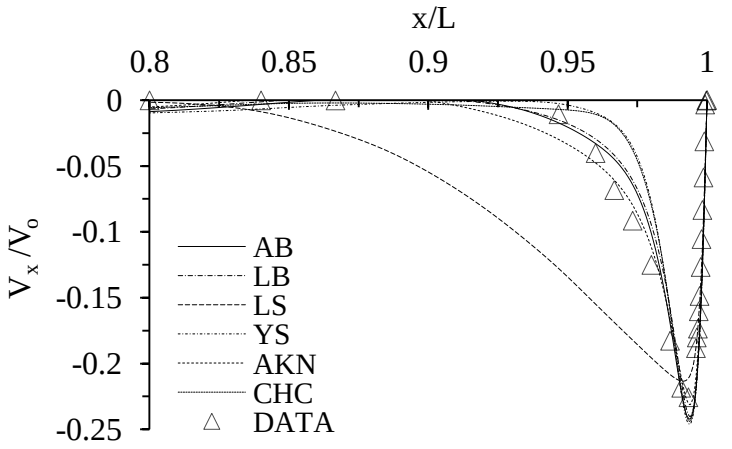

(4-5c)

Figure 4-5: Non-dimensional horizontal velocity profile (a) at mid-height (b) near hot wall (c) near cold wall at mid-height of the cavity.

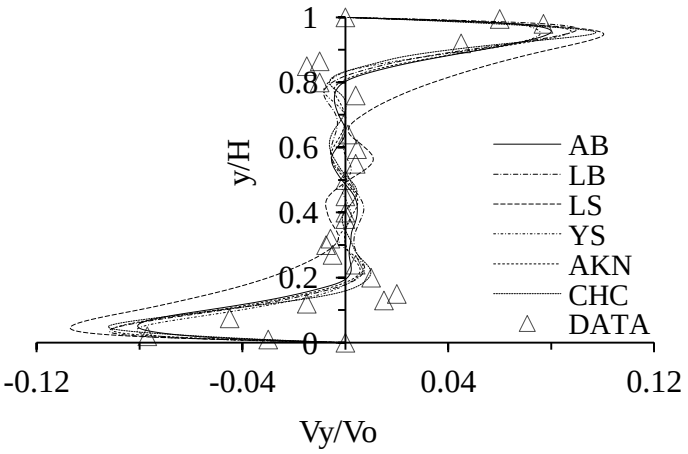

Figure 4-6: Non-dimensional Vertical velocity profile at mid-width of the cavity

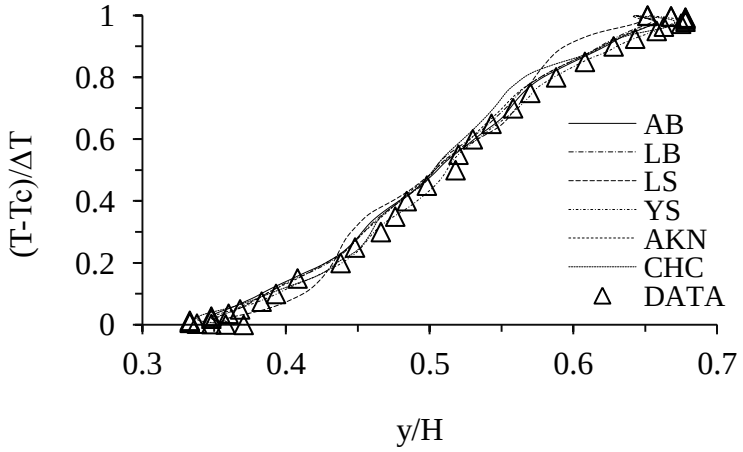

Figure 4-7: Non-dimensional mean temperature at mid-width of the cavity

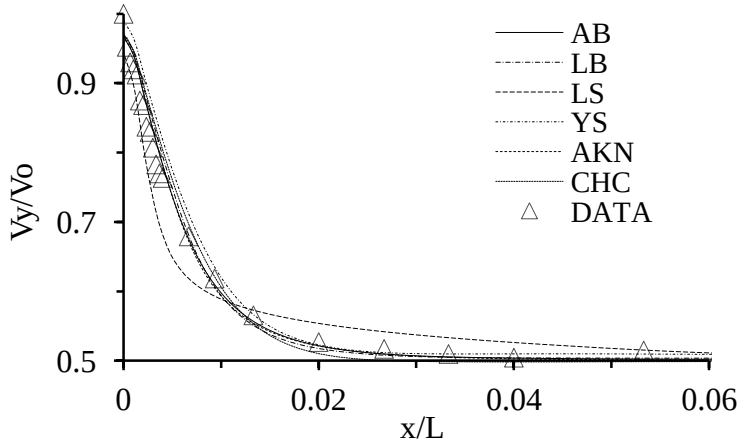

(4-8a)

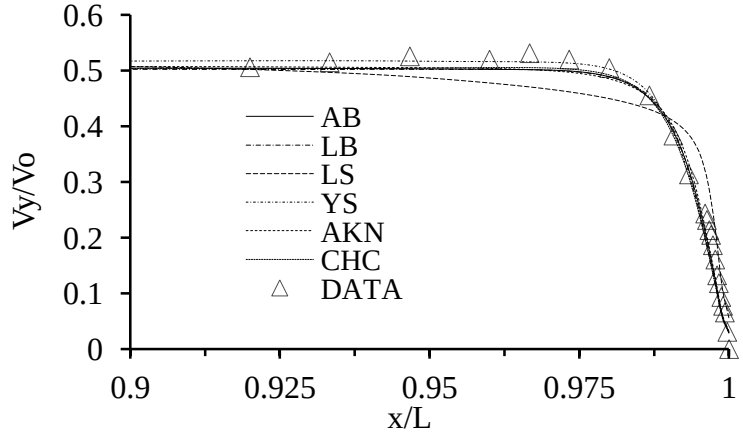

(4-8b)

Figure 4-8: Non-dimensional velocity profile (a) near hot wall (b) near cold wall

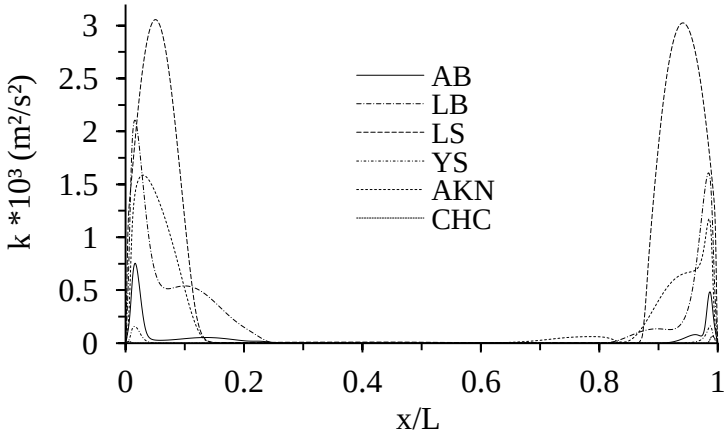

(4-9a)

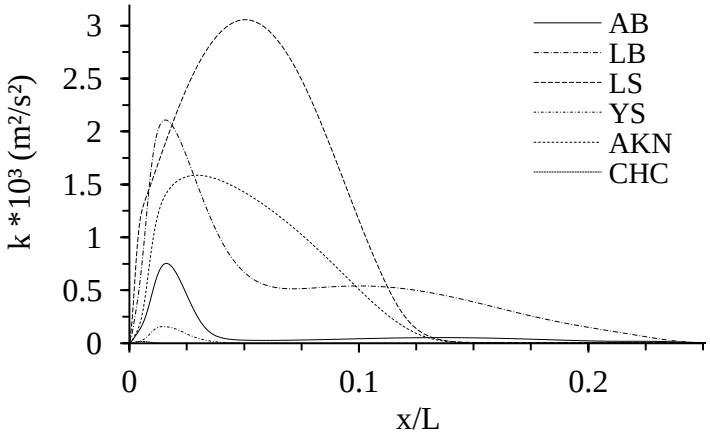

(4-9b)

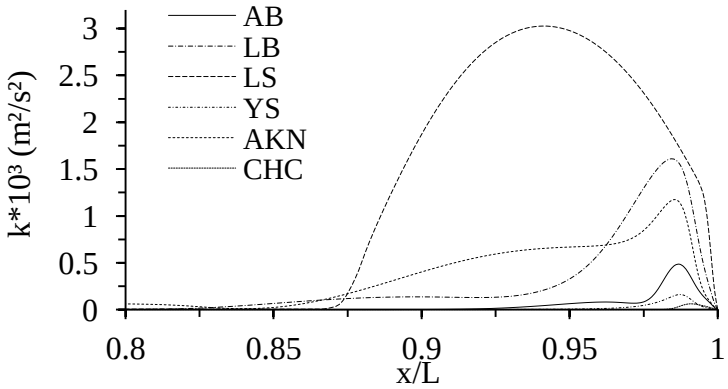

(4-9c)

Figure 4-9: Turbulent kinetic energy profile; (a) at mid-height (b) near hot wall (c) near cold wall at mid-height

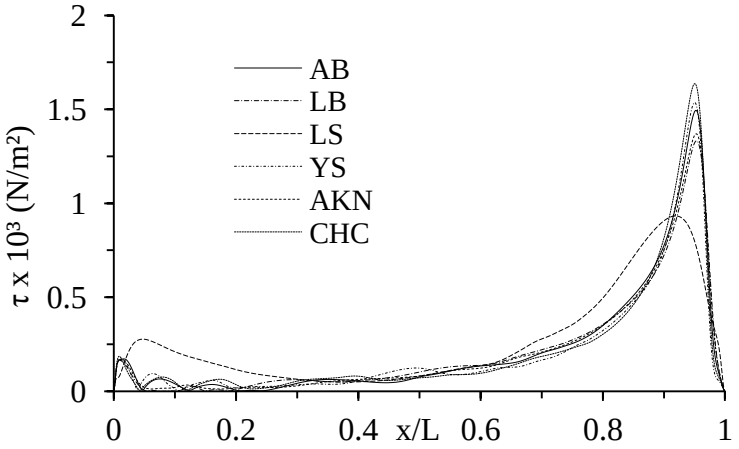

(4-10a)

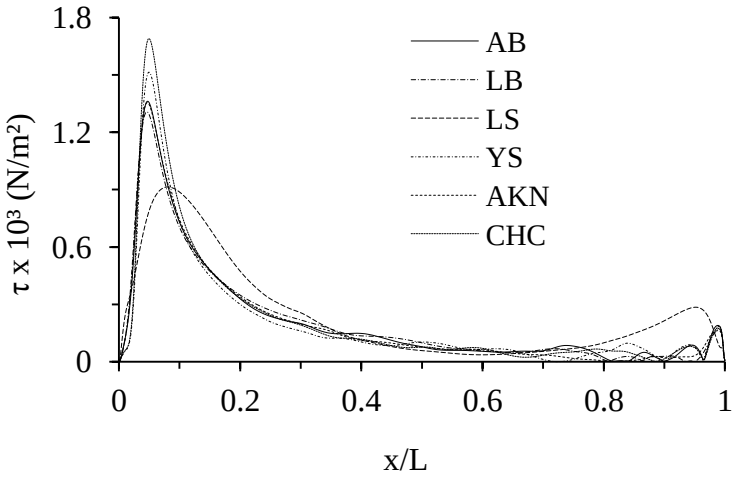

(4-10b)

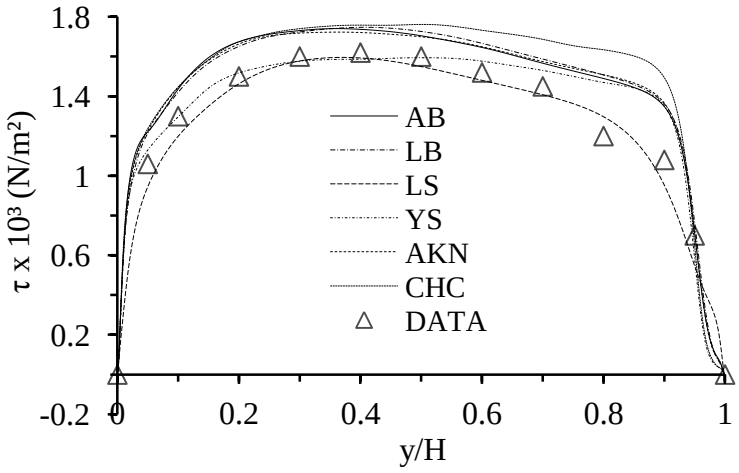

(4-10c)

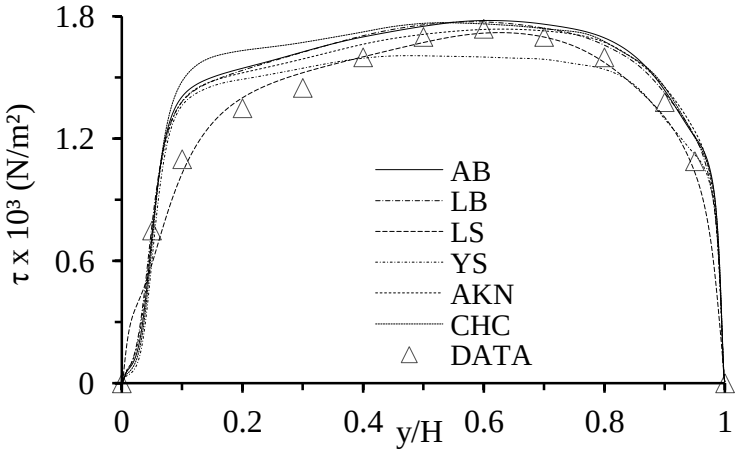

(4-10d)

Figure 4-10: Wall shear; (a) bottom wall (b) top wall (c) hot wall (d) cold wall

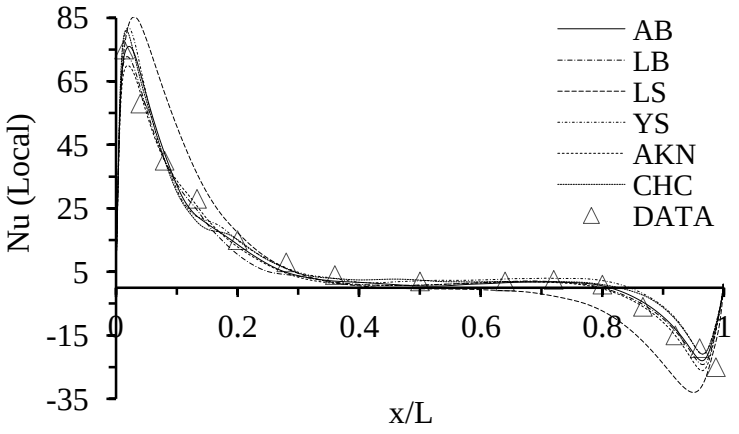

(4-11a)

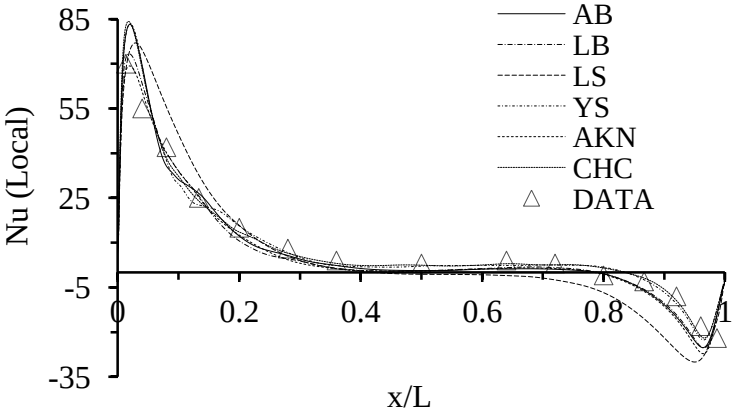

(4-11b)

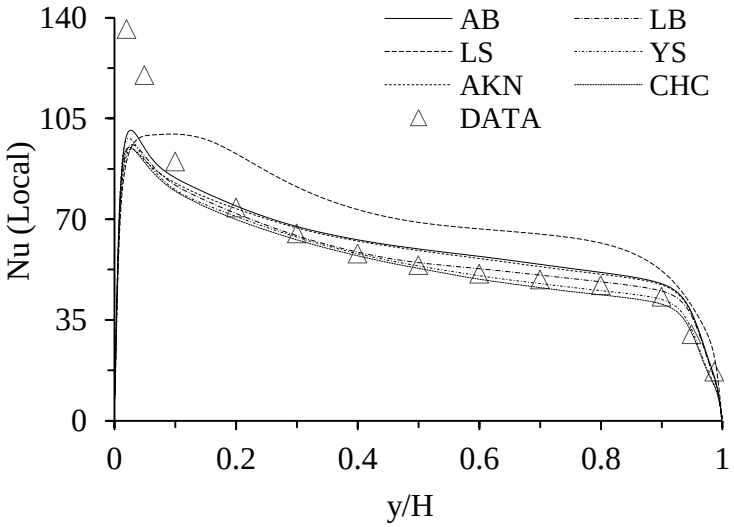

(4-11c)

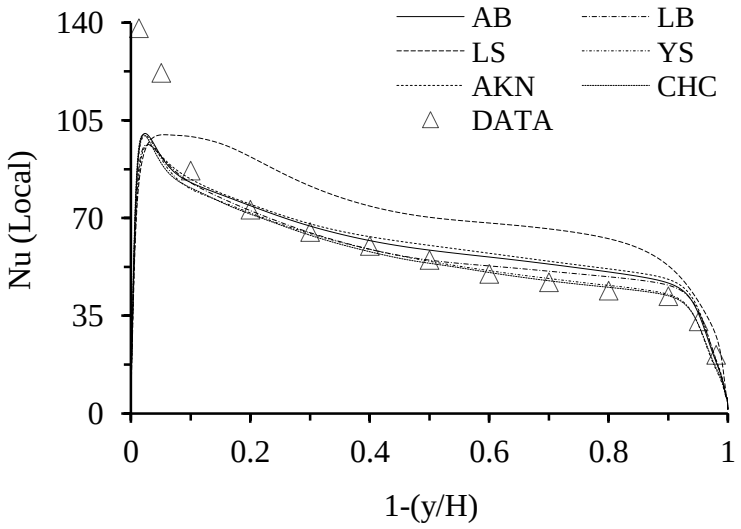

(4-11d)

Figure 4-11: Wall local Nusselt number; (a) bottom wall (b) top wall (c) hot wall (d) cold wall

Table 4-3, presents the average wall heat transfer comparison with Ampofo and Karayiannis experimental data [51], it is clear that the YS model [199] compared relatively well with the experimental data of Ampofo and Karayiannis [51]. Table 4-4 further highlights the performance by presenting the percentage change in average wall Nusselt number for each model. Relatively the YS model has shown less

deviation from the experimental data, while the AKN [219] gives the most percentage deviation.

Table 4-3: Comparison of average Nusselt numbers

Models	Bottom	Top	Hot	Cold
AB	12.07	11.54	68.55	66.40
LB	10.95	10.96	64.80	64.18
LS	14.99	14.61	59.80	59.31
YS	14.25	13.89	62.87	62.60
AKN	10.80	10.27	67.44	67.35
CHC	13.42	14.27	61.68	61.98
Data [51]	14.40	13.9	62.9	62.6

Table 4-4: Comparison of percentage change in walls average Nusselt numbers (%)

Models	Bottom	Top	Hot	Cold
AB	19.30	20.45	-8.24	-5.72
LB	31.51	26.82	-2.93	-2.46
LS	-3.94	-4.86	5.18	5.55
YS	1.053	0.072	0.05	0
AKN	33.33	35.35	-6.73	-7.05
CHC	7.30	-2.59	1.98	1.00

Further evaluation on the performance of the six low-Re k-ε models in predicting low turbulent buoyancy driven air flow and heat transfer is summarised in Table 4-5, while the computation efforts is presented in Table 4-6. The results show that some models perform better in one case but more poorly in another. The YS model gives stable results and always agrees with the experimental data, but with relatively greater computation efforts to other models in this category. The AB and CHC models give relatively good results and similar computation efforts, although the predictions do not always agree with the experimental data. The LS model is the most stable of the six models and offers a relatively good performance for the heat transfer and the mean temperature profiles, but performs fairly poorly for the prediction of the boundaries heat transfer.

Table 4-5: Summary of the performance of the low-Re k-ε models for predicting low turbulent buoyancy driven air flow in enclosure without blockages

Low-Re k-ε models	Mean temperature	Mean velocity	Heat transfer
AB	B	B	C
LB	A	B	D
LS	A	D	B
YS	A	A	A
AKN	B	B	D
CHC	B	B	C

A=excellent, B=good, C=fair and D=poor

Table 4-6: Number of iteration and CPU time normalized by those of standard k-ε model

Models	Number of iterations	CPU time	CPU time/iteration
AB	1.15	1.21	1.052
LB	1.11	1.17	1.054
LS	1.04	1.1	1.058
YS	1.01	1.07	1.059
AKN	1.06	1.12	1.057
CHC	1.15	1.21	1.052

All turbulence models tested are insensitive in the core region. The validated results show that the Yang-Shih model is the most accurate in predicting the flow and especially the heat transfer close to the walls of the cavity. The performance of the YS model might be linked to the wall boundary condition specification that account for the effects of damped turbulence by approximation, $f_\varepsilon = \frac{1}{\left(1+\frac{C_k}{\sqrt{R_T}}\right)}$.

4.5 **Influence of boundary condition**

A comprehensive analysis of the effects of thermal boundary conditions on the flows and heat transfer applied at the horizontal walls for natural convection in an air filled rectangular cavity are investigated here. Constant thermal boundary conditions have been imposed on the active vertical walls (Hot wall = 50^0C, cold wall = 10^0C). Three different thermal boundary conditions have been tested for the horizontal walls. These are abbreviated as ATP, LTP and ETP as explained below. ATP represents Adiabatic Temperature Profile i.e., the walls are perfectly insulated; LTP is a Linear Temperature Profile and corresponds to a perfect conduction and ETP represents

Experimental Temperature Profile from the experimental paper [51]. The mathematical meanings are shown in Table 4-7.

Table 4-7: The three thermal boundary conditions

Boundary conditions	Temperature functions
ATP	$\partial T/\partial x = 0$
LTP	$T_L = T_c + \Delta T(x/L - 1)$
ETP	$T_E = T_c + \Delta T(X_{ETP})$

Where T_L and T_E represent the linear and experimental function of temperature distributions along the horizontal walls, and T_c is the constant temperature specified at the cold wall.

The experimental temperature profile (ETP) is a best-fit polynomial based on the experimental data of Ampofo and Karayiannis [51].

X_{ETP} is defined by the polynomial presented in equation (4-1) and the coefficients are given in Table 4-8.

$$X_{ETP} = a\left(\frac{x}{L}\right)^4 + b\left(\frac{x}{L}\right)^3 + c\left(\frac{x}{L}\right)^2 + d\left(\frac{x}{L}\right) + e \qquad (4-1)$$

Table 4-8: Coefficients for the polynomial of Equation (4-1)

Walls	a	b	c	d	e
Top	-2.458	1.686	1.211	-1.440	1.00
Bottom	2.458	-8.146	8.477	-3.789	1.00

The above boundary conditions were implemented with a User-Define-Function (UDF) in FLUENT (see Appendix A for the UDF). The temperature profiles are shown in Fig.4-12.

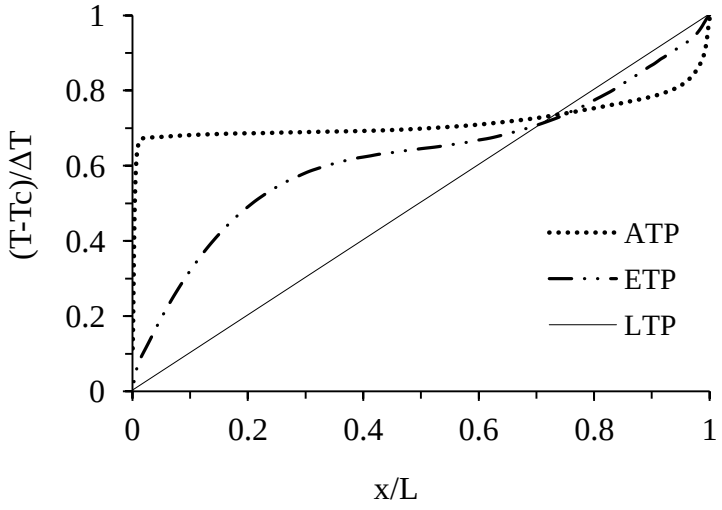

(4-12a)

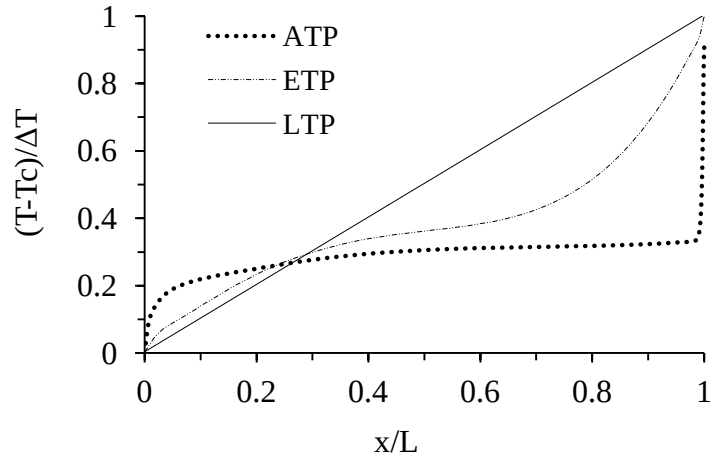

(4-12b)

Figure 4-12: Mean Temperature profiles; (a) top wall (b) bottom wall

Figs. 4-12 (a-b) has shown the profiles of local temperature distribution at the centre-line of the top and bottom walls respectively.

Fig. 4-13 shows the stream function plots for the three different boundary conditions. The flow field is characterized by a stable stratified flow with a core region in the middle. However, the adiabatic temperature profile on the horizontal walls shows more uniform velocity as the core region is rather squeezed towards the centre plane. On the other hand, the linear temperature profile and the experimental temperature profile boundary conditions display very similar stream functions with the former showing higher velocity gradient near the vertical walls.

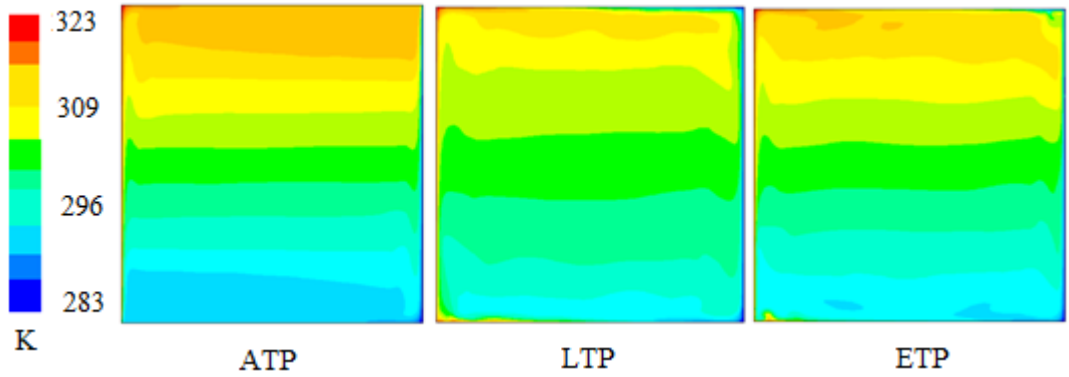

(4-13a)

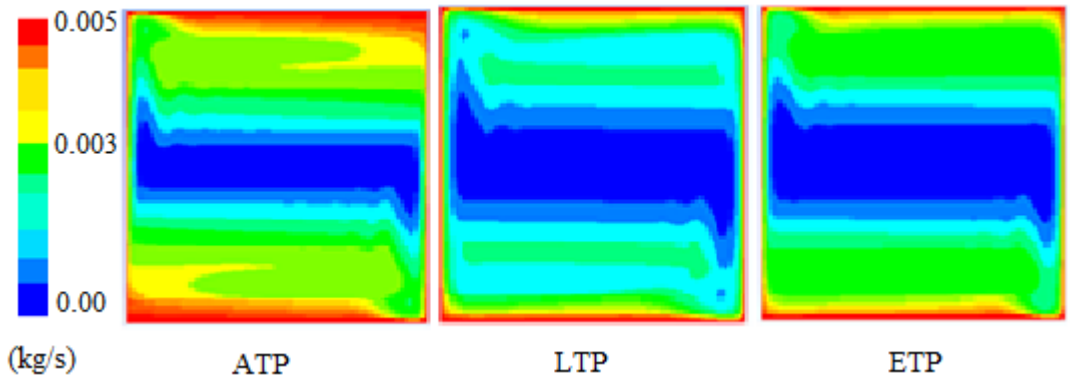

(4-13b)

Figure 4-13: Flow contours comparison; (a) temperature (b) stream function

The accuracy of the ETP boundary condition can be clearly seen from the plots presented in Fig.4-14 to 17. It can be argued that the ETP profiles display slightly higher discrepancies at a distance of one quarter from the vertical walls, however, it should be recognised that the magnitude of the velocity in this region is very small. As a matter of interest, the numerical result of Nicholas [220] , is also included in the figure which clearly demonstrates the improvement in our calculations. A similar set of results is presented in Fig.4-14 and 16, where we compare the horizontal and vertical component of the velocity, V, along the mid-height and mid-width of the square cavity respectively.

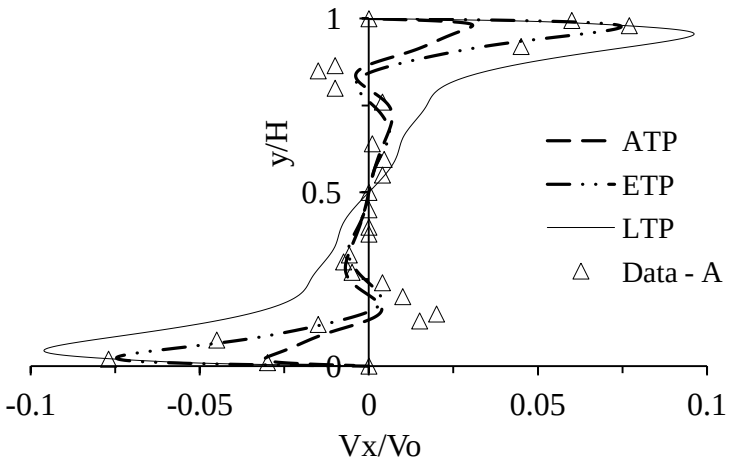

Figure 4-14: Mean horizontal component of velocity at x/L=0.5

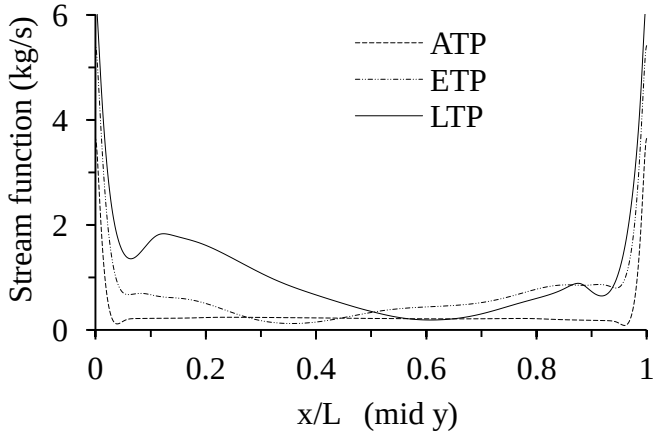

Figure 4-15: Stream function at mid-height

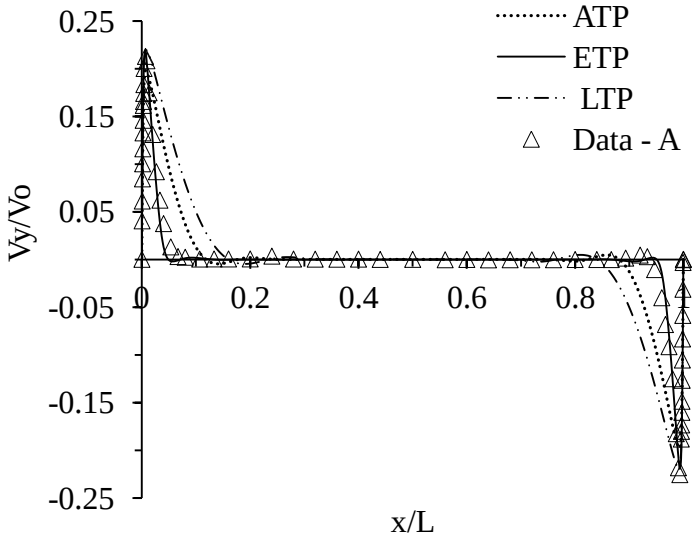

Figure 4-16: Non-dimensional mean vertical component of velocity at y/L=0.5

Figs. 4-17(a-c) shows the turbulence intensity comparison for the three cases for three locations y/L=0.125, 0.25 and 0.5. In these plots, k represents the turbulence intensity. It can be seen from y/L=0.5 location, that the ETP can predict the maximum turbulence near the walls more accurately than the other two boundary conditions. One limitation is that the asymmetry, as evidenced in the experimental data, in the maximum magnitude of turbulence intensity is not well predicted by any of the boundary conditions. However, the turbulence intensity asymmetry is better predicted at two other locations.

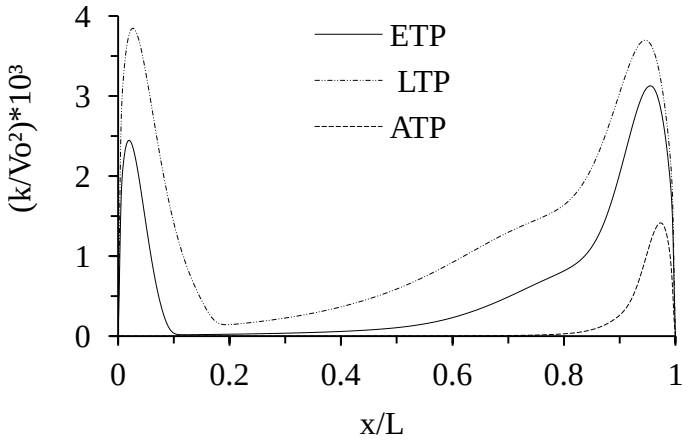

(4-17a)

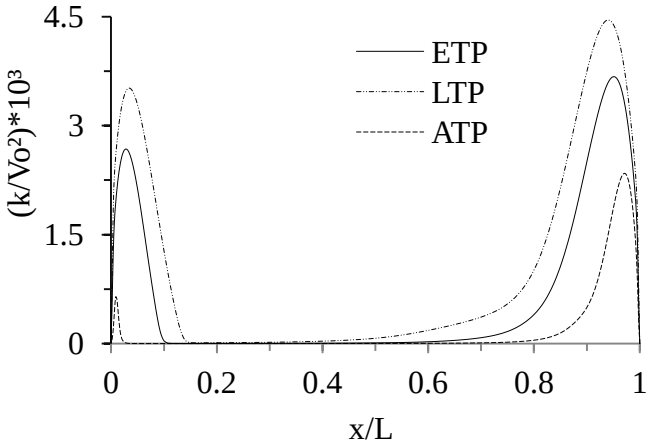

(4-17b)

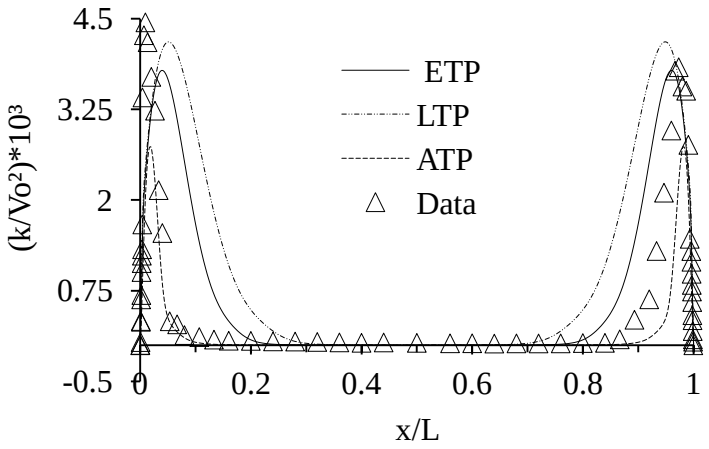

(4-17c)

Figure 4-17: Comparison of turbulence kinetic energy; (a) y/L=0.125 (b) y/L=0.25 (c) y/L= 0.5

The turbulence intensity contours shown in Fig. 4-18 demonstrates that the shear layer in the case of ATP is concentrated only in the two diagonally opposite corners whereas for the other two boundary conditions, very similar contours can be observed. In all cases, the flow field is seen to be dominated by turbulence only in the near wall regions and the core area is essentially a bulk mean flow with a rather stagnating condition. This observation further highlights the importance of using a low Reynolds number model.

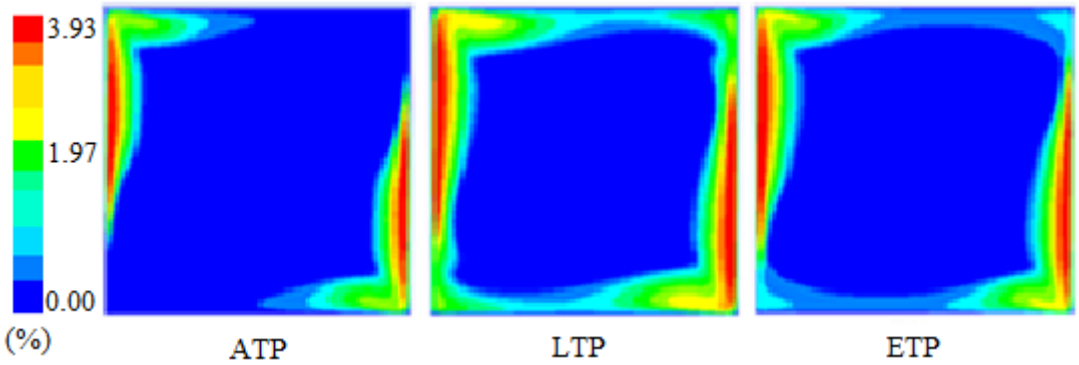

Figure 4-18: Contours of turbulence intensity for three boundary conditions

The plots related to the mean temperature profile along the mid-width (x/L=0.5) of the cavity is shown in Fig.4-19, the ETP shows the best agreement while the ATP over- or under-predict the temperature at the passive horizontal walls. The importance of an appropriate boundary condition has been emphasized by these plots. In fact, the temperature distribution is the most critical mean quantity due to the fact that this may be interpreted as both ‘cause’ and ‘effect’ and vice versa. The flow develops due to

the buoyancy which is directly dependent on temperature and at the same time temperature is also affected by the flow field.

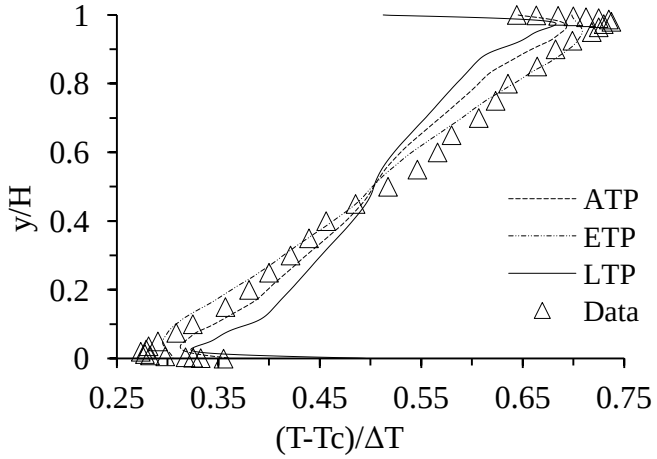

Figure 4-19: Mean temperature at x/L=0.5

Figs.4-20 presents the local Nusselt numbers comparisons with experimental and/or numerical results are also included wherever possible. Although there are discrepancies between the various predictions, overall, the ETP boundary conditions appear to be better. The ATP boundary condition fails to mimic the qualitative trends observed in experiments.

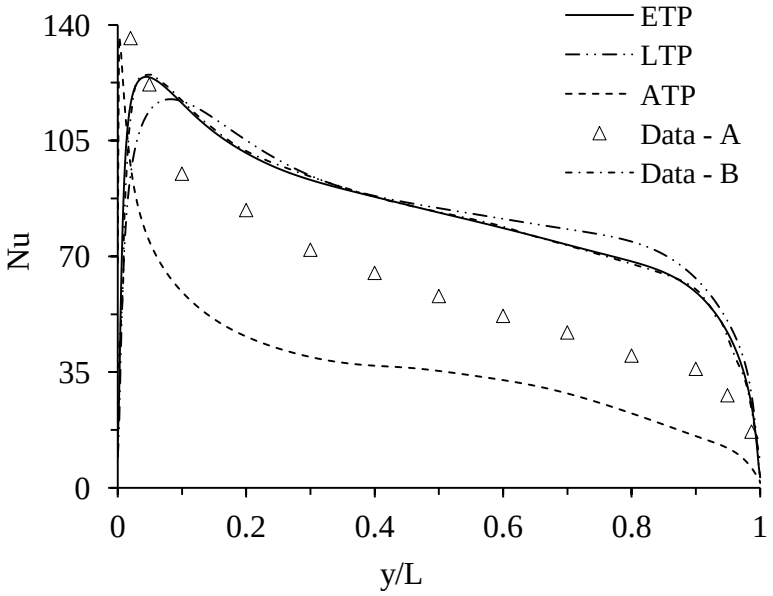

(4-20a)

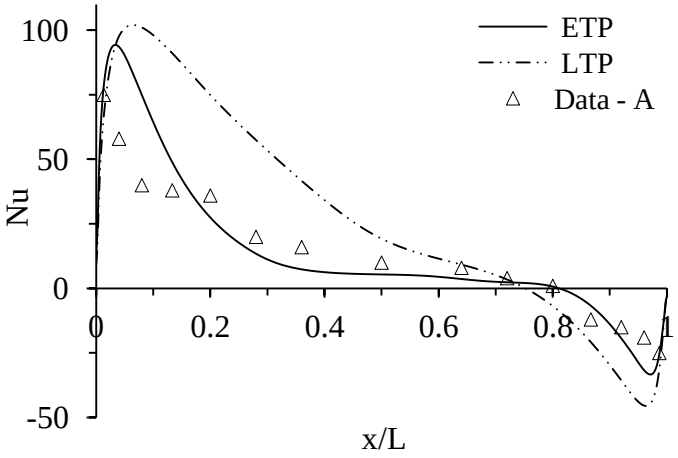

(4-20b)

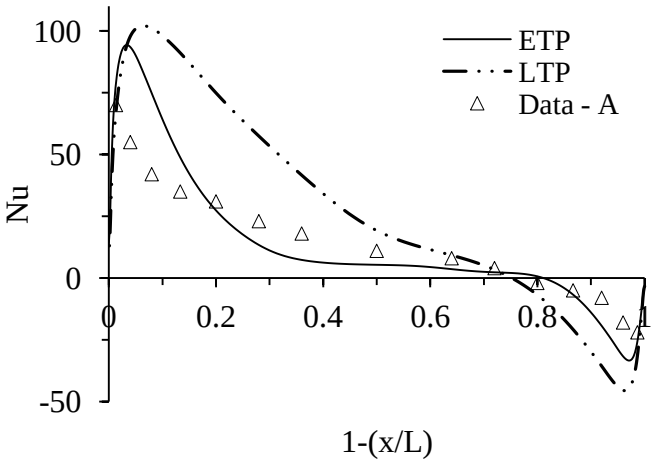

(4-20c)

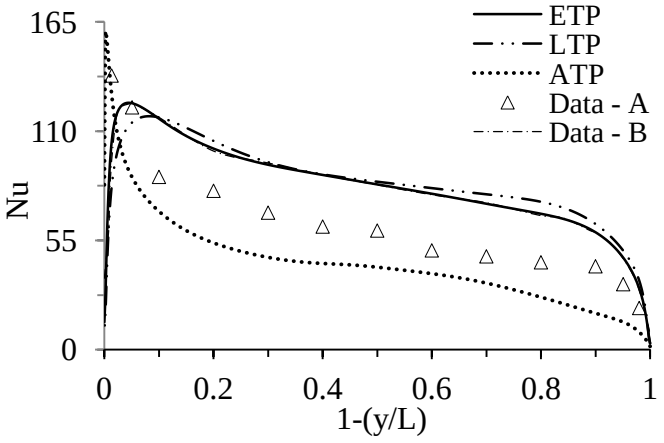

(4-20d)

Figure 4-20: Local Nusselt number; (a) hot wall (b) bottom wall (c) top wall (d) cold wall (Data –A [214] , Data -B [220])

Finally, the predicted values of the average Nusselt numbers and percentage deviation from experimental data are shown in Tables 4-9 and 4-10 respectively. Again, the values returned by the ETP are very close (less than 1% difference) to the experimental values for the active wall and the ATP is furthest.

Table 4-9: Comparison of average Nusselt numbers

Case	Bottom	Cold	Hot	Top
ETP	14.40	62.60	62.90	13.90
LTP	29.74	60.99	61.22	29.30
ATP	0.00	66.86	67.42	0.00
Data- B [214]	14.40	62.60	62.90	13.90

Table 4-10: Table 4-9: Comparison of average Nusselt number percentage change

Case	Bottom	Cold	Hot	Top
ETP	-0.0012	0.00	0.00	-0.0014
LTP	18.123	-1.586	-1.655	18.2029
ATP	-12.587	4.445	4.7303	-12.2037

4.6 **Influence of wall radiation property**

Further calculations were carried out for the above flow geometry to explore the influence of surface emissivity on the heat transfer. The wall boundary conditions for the vertical walls were isothermal and the horizontal walls were specified by the ETP boundary condition as described before. Numerical analysis of coupled thermal radiation and natural convection in an enclosed square cavity whose vertical surfaces are maintained at constant differential temperatures is reported in this section. The objective is to ascertain the effects of surface emissivity on the flow and heat transfer characteristics of the square cavity. This surface emissivity value of all surfaces was kept the same for this study.

Three different parametric studies of the influence of surface emissivity have been reported here. These studies are;

- 2D and 3D numerical analysis of coupled thermal radiation and natural convection in an air filled enclosed square cavity were scrutinised.
- Influence of constant wall emissivity on the heat transfer

- Influence of varying wall emissivity on the heat transfer

In all cases studied, turbulence is modelled using the low-Re k-epsilon RANS model of YS model. Simulations were performed by varying the emissivity values of the surfaces to investigate the effects of radiation boundary conditions. Analysis of the flow and heat transfer is carried out by plotting the turbulence quantities and the local average Nusselt numbers, and quantified the wall heat transfer in tables. To model radiation heat exchange between surfaces, the DO radiation model was adopted in FLUENT. The reason for the choice of the DO model was that it is found to give better results [221].

4.6.1 **2D Vs 3D radiation modeling**

The effect of 2D simplification of inherently 3D radiation modelling of the flow field is scrutinised for an air filled cavity without blockages in the flow domain. Table 4-11 to 4-13 present the relative percentage difference between the wall heat transfer using the benchmark experimental study of Ampofo and Karayannis [51]. This issue of 2D simplification of 3D radiation is very prominent when there are obstacles due to multiple radiations. These aspects are dealt with more rigorously in section 7.3.3.

Table 4-11: Percentage error on wall surface heat transfer for a case without radiation

Surfaces	Nu_{2D}	Nu_{3D}
Bottom	0.370	-0.54
Top	0.86	-0.20
Hot	2.19	1.63
Cold	1.63	0.24

Table 4-12: Average Nusselt number for $\boldsymbol{\varepsilon = 0.9}$

Surfaces	Nu_{2D}	Nu_{3D}	$\mathrm{Nu}_{3D} - \mathrm{Nu}_{2D}$
Bottom	18.15	19.06	0.91
Top	11.87	12.81	0.94
Hot	173.5	174.81	1.31
Cold	166.68	168.43	1.75

Table 4-13: Average Nusselt number for $\boldsymbol{\varepsilon = 0.5}$

Surfaces	Nu_{2D}	Nu_{3D}	$Nu_{3D} - Nu_{2D}$
Bottom	16.00	16.77	0.77
Top	12.5	13.37	0.87
Hot	118. 35	118.82	0.47
Cold	113.68	115.44	1.76

Tables 4-12 and 4.13 show relative walls average Nusselt number for the two wall emissivity values (ε=0.9 and ε=0.5). It has been observed that an increase in wall emissivity value will lead to an increase of the average Nusselt number. However, for the 2D and 3D modelling approaches this will only have limited influence (< 2%) on the wall heat transfer across the cavity. Therefore, modelling the flow domain with radiation as a two-dimensional configuration will have a negligible influence on the heat transfer. This has a particular advantage in the numerical modelling approach of such geometry, which will limit the cost of computation considerately by 95%.

4.6.2 **Influence of surface emissivity on turbulence quantities**

Three different cases of constant wall emissivity values (ε=0, ε=0.2, ε=0.5 and ε=0.7) were tested and the results of their influence on the turbulence quantities are presented in Figs.4-21a-c. The turbulence Reynolds stress (Fig.4.21a) shows a relative increase in the turbulence level in the flow domain for correspond increase value of emissivity. This behavior is further supported by the results of the turbulent kinetic energy presented in Fig.4-21b, where the kinetic energy per unit mass associated with the eddies increases slightly with increase in the emissivity value of the wall. Fig. 4-21c shows the eddy viscosity ratios at mid-height of the cavity. In the plot, three values of wall emissivity were shown.

Turbulent viscosity ratio is described as the ratio between the turbulent viscosity and the molecular dynamic viscosity. Although all curves indicate similar maximum value of μ^*, the presence of a radiation and surface emissivity significantly reduces its value at the core.

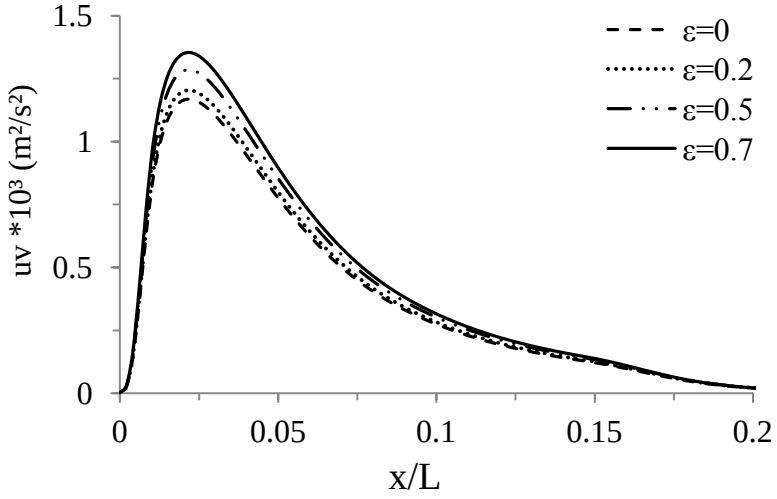

(4-21a)

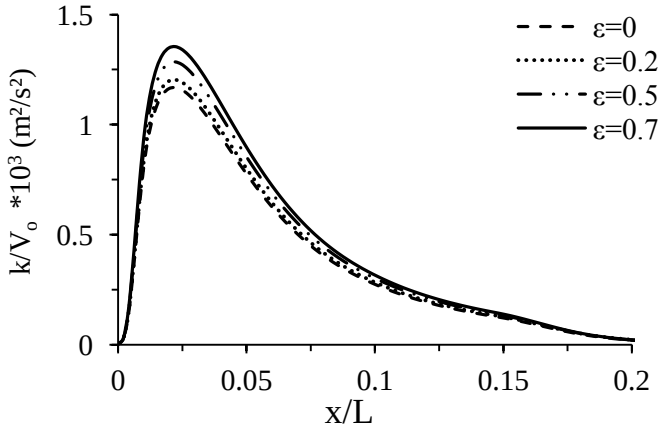

(4-21b)

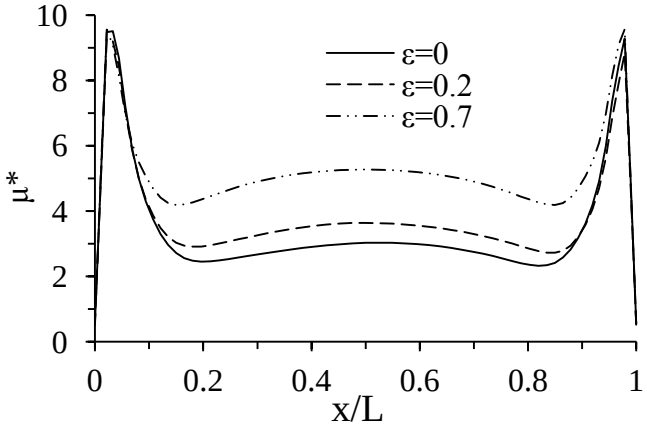

(4-21c)

Figure 4-21: Turbulent quantities profiles (a) $\overline{uv}$ Reynolds stress near hot wall (b) kinetic energy near hot wall (c)viscosity ratio at mid-height

4.6.3 **Influence of surface emissivity on wall heat transfer**

Further calculations were carried out for the above flow geometry to explore the influence of surface emissivity on the heat transfer. Figs. 4-22(a-c) show the local Nusselt number for a range of wall emissivity, with average values shown in Table 4-14. The plots of wall local heat transfer as a function of wall emissivity are shown in Figs.4-23a-d for the active vertical and passive horizontal walls respectively. It is observed that, the local heat transfer increases linearly with corresponding increase of the wall emissivity values for both the vertical and top wall. However, the bottom wall average heat transfer decreases with increasing values of the wall emissivity. Similar behaviour can be observed in Figs.4-23c-d for the local wall radiative heat transfer. Fig.4-23e shows the profile of the average convective component along the vertical walls. It can be seen that the values decrease with increasing values of wall emissivity. Therefore it can be concluded that radiation suppresses the convective heat transfer along the walls. Hence, changes in the surface emissivity value can influence the heat transfer process. The bottom wall shows an increase in the value of the wall heat transfer with increasing value of the wall emissivity.

Table 4-14: Average Nusselt number

Surfaces	ε_0	$\varepsilon_{0.2}$	$\varepsilon_{0.5}$	$\varepsilon_{0.7}$
Bottom	10.31	10.57	20.75	37.01
Cold	56.16	65.55	56.16	56.16
Hot	56.16	80.75	94.33	113.6
Top	10.31	10.80	16.92	20.35

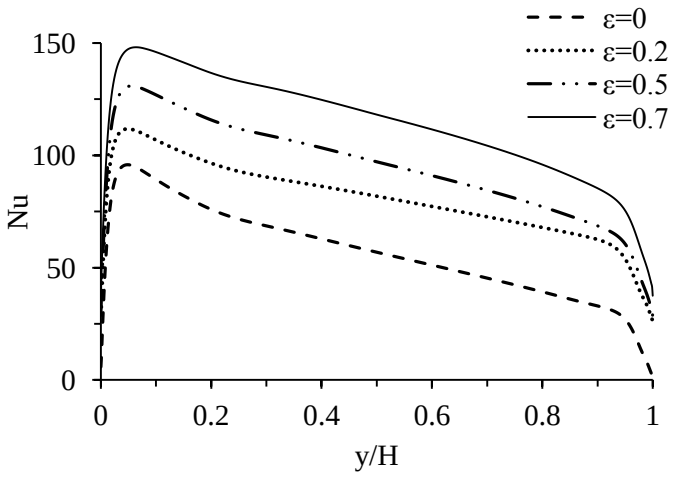

(4-22a)

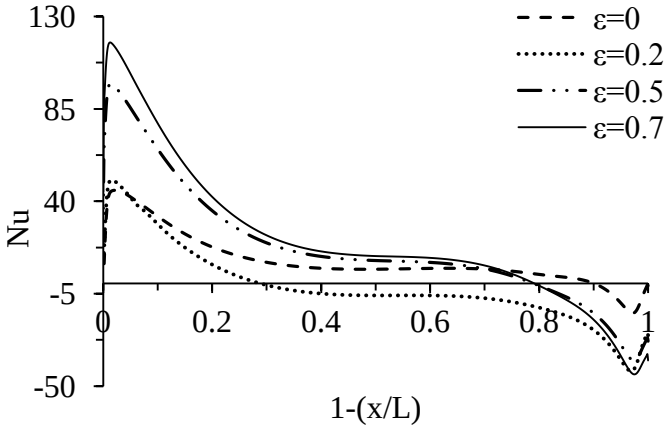

(4-22b)

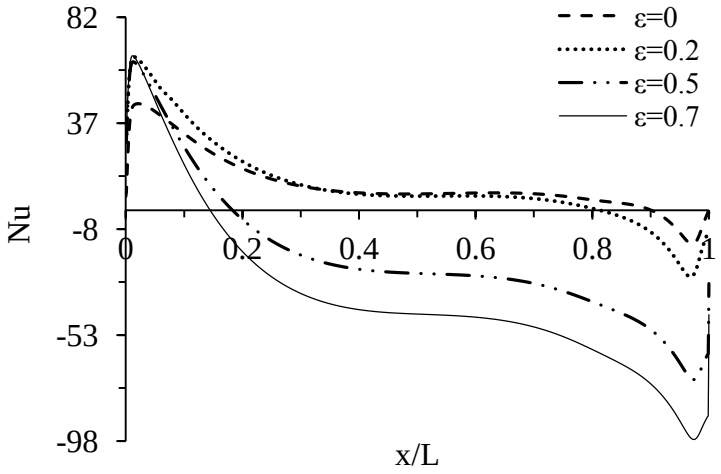

(4-22c)

Figure 4-22: Local Nusselt number comparison; (a) hot wall (b) top wall (c) bottom wall

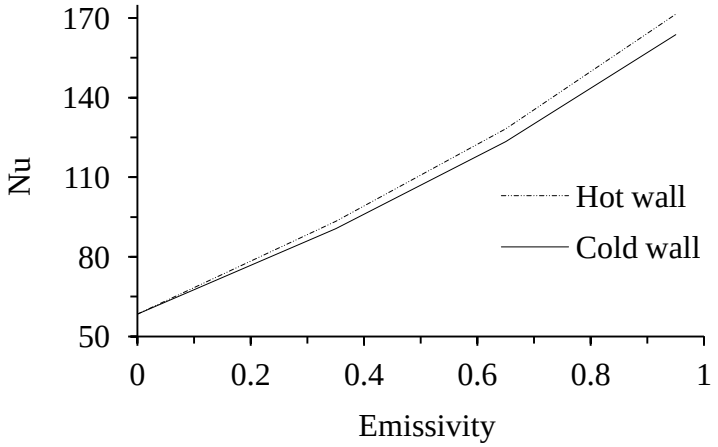

(4-23a)

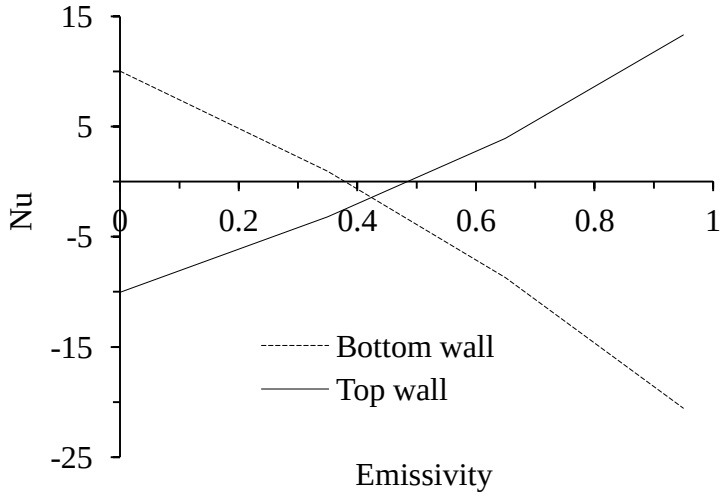

(4-23b)

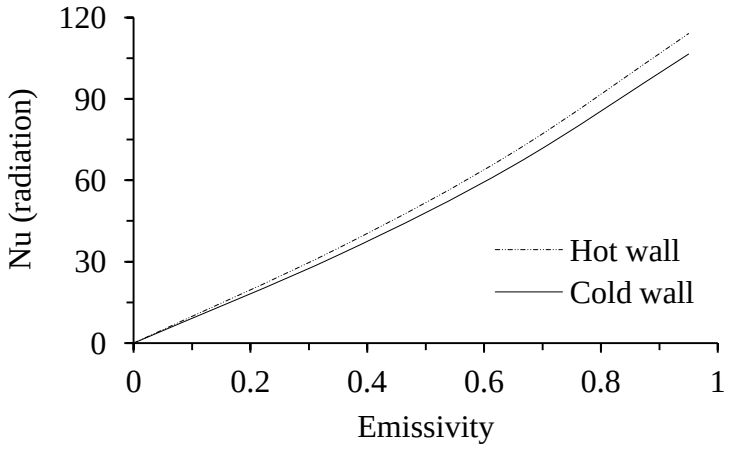

(4-23c)

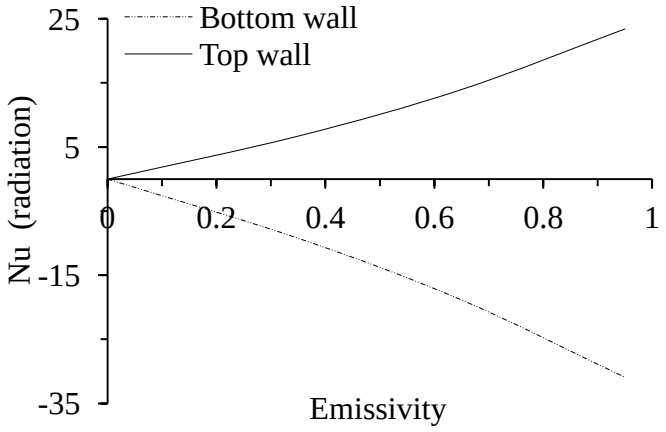

(4-23d)

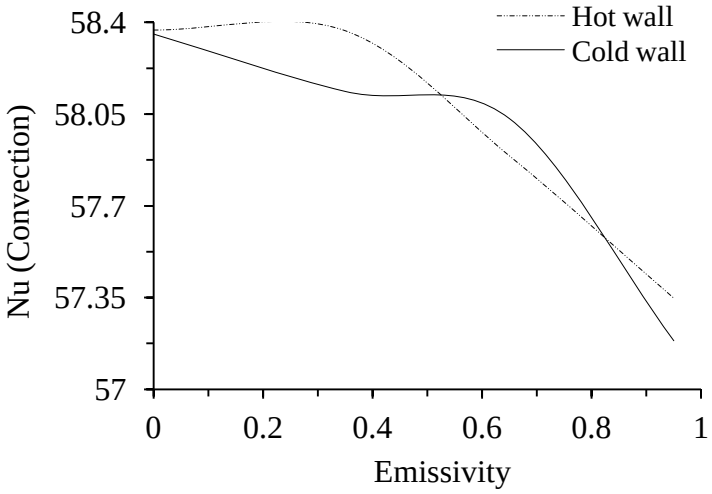

(4-23e)

Figure 4-23: Average heat transfer as function of emissivity (a) hot and cold walls total Nu (b) top and bottom walls total Nu (c) hot and cold walls radiative Nu (d) top and bottom walls radiative Nu (e) hot and cold walls convective Nu

4.7 **Influence of wall emissivity configuration on the flow and heat transfer**

Further exploratory investigation was carried out by changing the emissivity values in pairs for four different cases as shown in Table 4-15. Fig. 4-24 shows the stream function for all cases. The variations of local Nusselt number are plotted in Figs. 4-31(a-d), while the average wall heat transfer is displayed in Table 4-16. It can be seen that the local and average Nusselt numbers are influenced by the configuration of surface emissivity. Selection of high values of emissivity for the passive walls also shows significant influence on the heat transfer within the cavity.

Air mixing rate varied significantly with varying surface emissivity as represented by the air stream function in Fig.4-30. It can be observed that case-1 displays a more even mixing within the cavity, while case 4 shows less mixing and a prominent wall bounded convection currents close to the top and bottom zones of the cavity. This phenomena influence the local and average heat transfer across the boundaries of the cavity. Case-2 gives the highest heat transfer across the boundaries of the active vertical walls compared to Case-4 which gives the lowest heat transfer for all the cases studied.

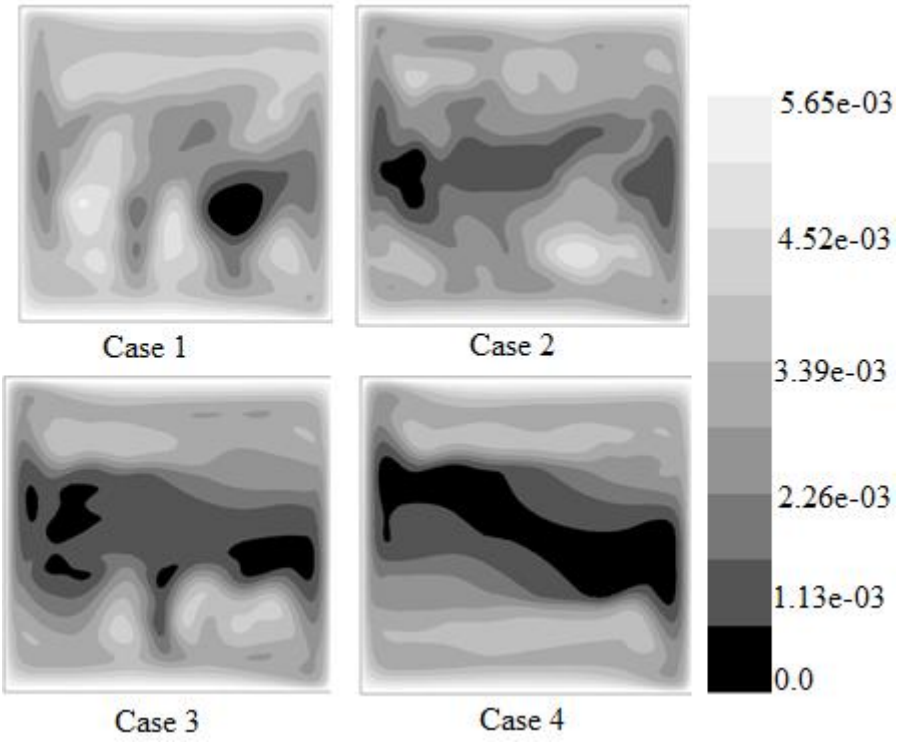

Figure 4-24: Stream function (kg/s) contours

Table 4-15: Wall emissivity for all case

Cases	Top wall	Bottom wall	Cold wall	Hot wall
1	0.2	0.7	0.7	0.2
2	0.2	0.2	0.7	0.7
3	0.7	0.7	0.2	0.2
4	0.7	0.7	0.2	0.7

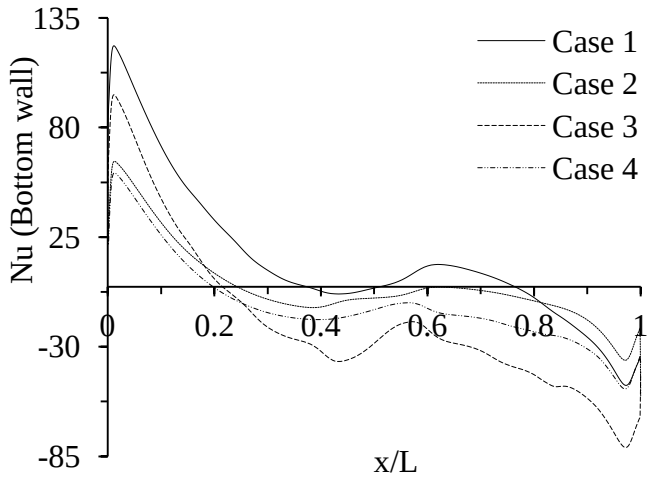

(4-31a)

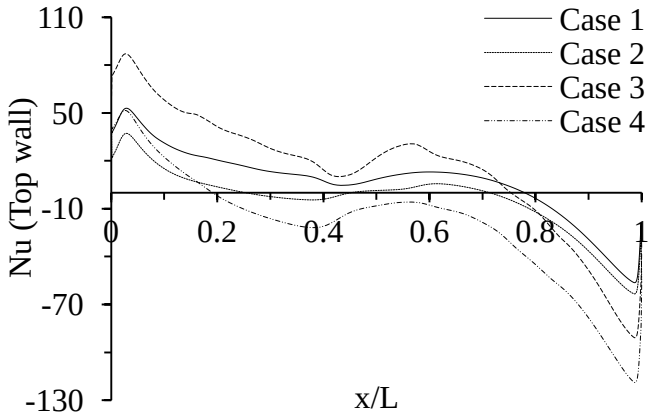

(4-31b)

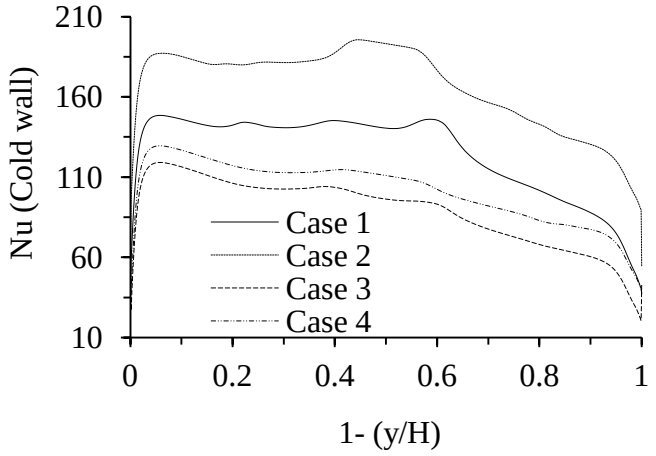

(4-31c)

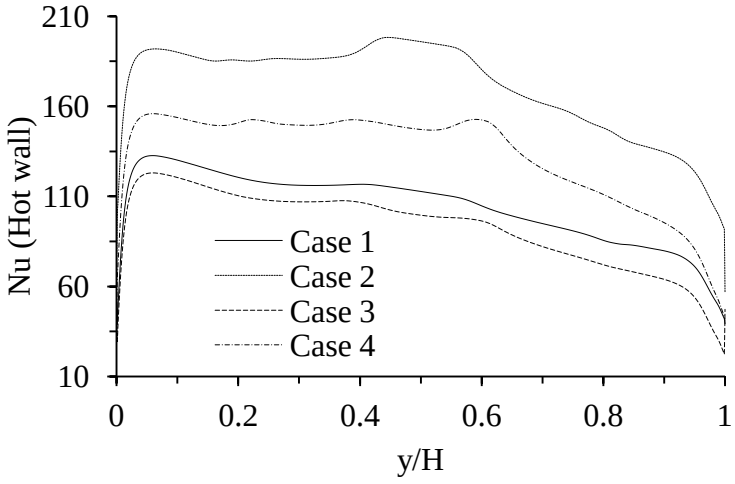

(4-31c)

Figure 4-25: Local Nusselt number; (a) bottom wall (b) top wall (c) cold wall (d) hot wall

Table 4-16: Average Nusselt number comparison

	Total Nu		Radiative Nu	
	Cold	Hot	Cold	Hot
Case 1	125.07	104.25	66.57	46.18
Case 2	166.64	170.9	109.03	112.81
Case 3	88.71	92.54	30.55	34.26
Case 4	101.65	133.06	43.74	74.30

4.8 **Conclusions**

The work presented in this chapter highlights the fact that turbulent natural convection flow is very sensitive to the appropriate choice of boundary specification. At the same time since the flow is dominated by turbulence mainly near the walls, it is also important to resolve the flow variables in this region very carefully. A detailed understanding of the performance of EVM is essential. The numerical results for the surface emissivity used in this study indicate that the effect of radiation is very significant and influences the weak natural convection flows.

A very good agreement is obtained between this study and the experimental data from literature [51] as shown in the validated results. It is noted from the qualitative result that the highest velocities are located close to the hot wall near the higher corner and the lowest velocities are close to the cold wall near the lower corner. The flow close to the active walls is similar to the turbulent flow over a vertical flat plate, where there is formation of thermal and hydrodynamic turbulent boundary layers.

The numerical results of the three boundary conditions are characterized by stable thermal stratification in the core fluid region and low-level turbulence in the near-wall region. The effects of the temperature conduction along the horizontal walls on heat transfer in the enclosure on pure natural convection are brought out and the numerical results showed good agreement between calculated and measured values at mid-height of the cavity. Detailed analysis of the flow and heat transfer were carried out by plotting the local and average Nusselt numbers, and percentage heat transfer contributions for the three boundary conditions used was evaluated. Excellent agreement with benchmark experimental data and ETP boundary condition was observed.

Performance of the six low Reynolds number k-ε models was quantified. A comparative study using the models was conducted to investigate their relative performance on the flow and heat transfer during natural convection processes. The results show that, some of these models over predict or under predict the flow physics and heat transfer near the walls and that the Yang-Shih model [199] gives a more approximate prediction of the mean velocity measured at the mid-width, the mean temperature measure at the mid-width and the walls average and local Nusselt numbers.

The presence of radiation influences the enclosure wall temperature and the wall temperature in turn influences the weak natural convection flows. Detailed investigations show that the top surface is cooled down as net radiative flux is positive. The bottom wall is heated up as net radiative flux is negative. It was also observed that surface radiation has limited influence on the vertical flows along the active walls but reinforces horizontal flow along the horizontal walls. Thus, the interaction of natural convection and surface radiation is of practical interest. The next chapter will detail the design procedure for producing a novel experimental study of turbulent natural convection heat transfer in a rectangular enclosure with and without blockages.

Chapter 5 - TEST RIG AND TEMPERATURE MEASUREMENT FOR VARIOUS ARRANGEMENT OF BLOCKAGES

5.1 Introduction

This chapter presents the design and fabrication processes of the test rig for the experimental study of turbulent natural convection in a rectangular enclosure with and without blockages. One objective of the test rig is to provide high quality temperature data for the validation of numerical method. To achieve this, rigorous attempts were made to scrutinize the two-dimensionality of the flow domain, detailed energy balance to calculate the heat loss, uniformity of temperature on the thermally active vertical walls, and air temperature profiles at different locations in the fluid domain and on the surface of the cavity walls and on the surface of the cylinders.

After satisfactory temperature data were obtained for steady state situation, blockages were systematically positioned within the enclosure and temperature readings were gathered. The experimental findings presented in this chapter are complementary to the numerical investigation by allowing necessary validation to be carried out later in the thesis.

5.2 Experimental facility and procedure

The schematic of the thermal rig fabricated for this study is depicted in Fig.5-1. The major components of the rig are the enclosure, hot and cold wall temperature control systems and the facilities for measuring temperature. A detailed description of the experimental test rig and the results are divided into two sections. The first section deals with the cavity design which includes the description of the hot and cold walls and their temperature controls. The second section describes the temperature results which were collected using thermocouples at various positions in the fluid domain and at the solid wall surfaces. These wall temperature data were used in the calculations of the heat transfer from the hot to the cold walls and the heat losses through the walls for different temperature gradients.

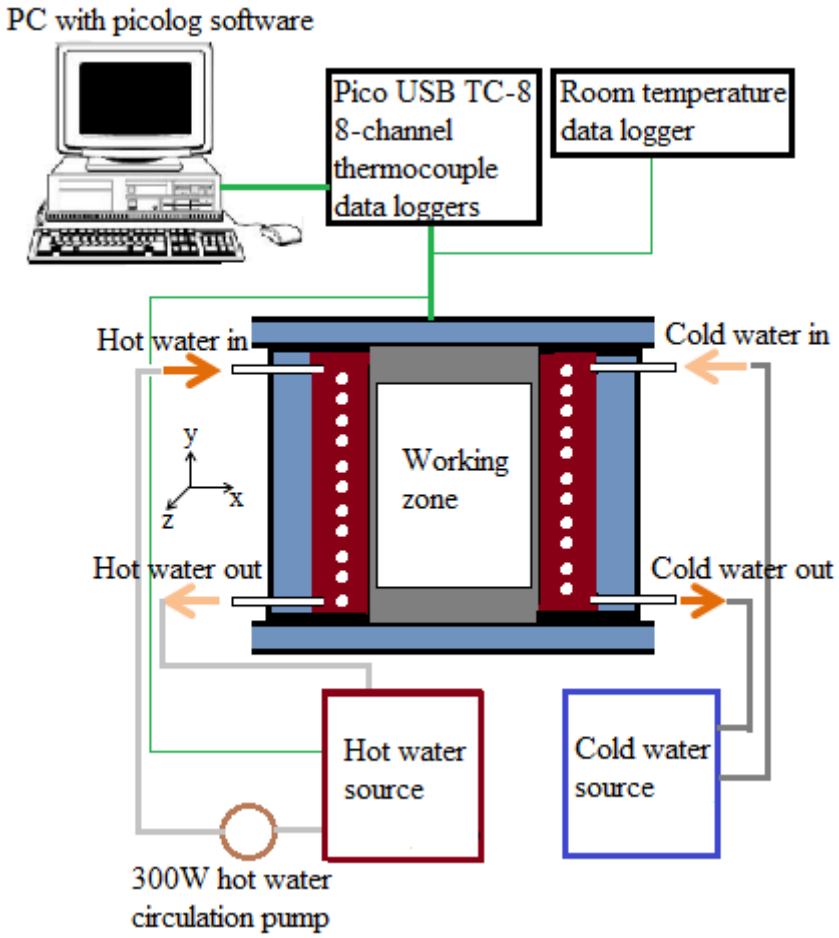

Figure 5-1: Schematic diagram of the experimental facility and test cavity

The enclosure consisted of six sides: a hot wall, a cold wall and four side walls. The cavity air domain has two configurations. The first configuration is an empty enclosure, while the second configuration is that partially filled with cylindrical blockages. Fig.5-2 shows the schematic diagram of the vertical section of the test cavity. The enclosure is designed using xtratherm boards of thickness 85mm. These boards were cut to different sizes to form the cavity shapes, guided using plywood (6.35mm) and supported on a steel frame. The two side walls and the top and bottom walls are adjustable and are connected to a fixed steel base.

The passive horizontal (top and bottom) and active vertical walls are fitted with polished aluminium plate to get a low emissivity on the inside surfaces of the enclosure. To fix tightly and remove the gaps between them the four side walls were clamped from a fixed steel frame. This was done to ensure that the losses through the gaps are kept to a minimum.

The enclosure size is fixed to H=0.97m, L=0.4m, depth is the z-direction of D=1m. The geometrical aspect ratios are AR_x=H/L (2.425) and AR_y=D/L (2.5). The Rayleigh number, $Ra = (g\beta\Delta TH^3)/(\nu\alpha)$ based on the temperature differential ($\Delta T=42.2^0C$) between the active vertical walls is equal to 4.04 x 10^9. Therefore, a weak turbulent air flow in the cavity is established within the cavity and the intensity of the flow is largely dependent on ΔT.

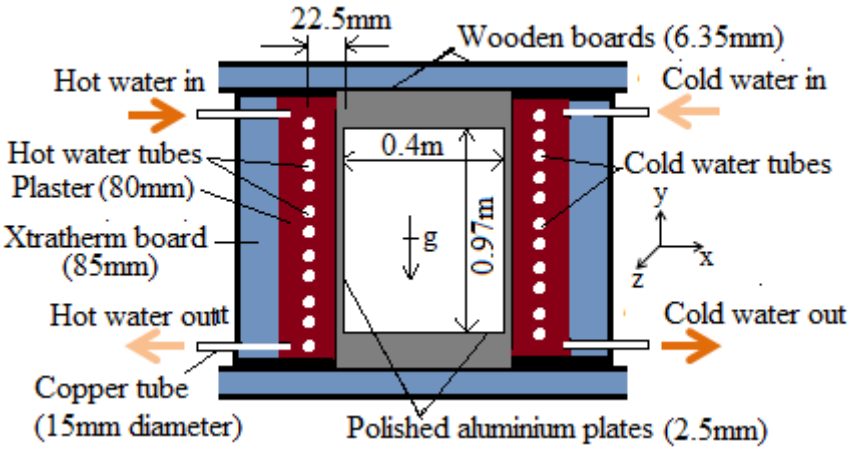

Figure 5-2: Vertical section of test cavity arrangement

The vertical walls are near isothermal with one wall hot and the other wall cold. Hot water from a constant hot water bath and cold water from a chiller were pumped through the two vertical walls respectively. The desired temperatures at these walls were achieved by regulating them externally and kept constant throughout the period of the experiment which was typically over a 20hrs period.

A lab-calibrated, 75µm Chromel-Alumel, K-type thermocouples were used to measured all temperature data. The sampling rate was 20Hz, and at each location data were collected for a minimum time of one minute (the majority of data were collected for 5 minutes). The K-type thermocouples with data logger are connected to a PC with PICOLOG software. PICO USB TC-8 data acquisition software was used to measure and save the collected data at each sampling rate. The thermocouples were fitted in position accurately using a precision height gauge to an accuracy of about 1mm.

Fig.5-3 shows the pictures of the experimental test rig components and facilities. During all measurements, the experimental conditions were kept steady and

experimental repeatability was also verified. The maximum deviation between readings obtained during experiments performed at different times was 0.8^0C.

Figure 5-3: (a) radiator for active wall (b) hot water tank fitted with circulation pump (c) cold water chillers

Air temperature distributions within the cavity working zone are measured on the symmetry planes. The temperature of the hot and cold walls, top and bottom walls are also measured at a chosen location. A total number of 54 thermocouples were employed for the measurement of the air temperature, and 60 thermocouples were used for wall surfaces. The initial tests carried out on the rig before conducting the experiments have showed that the temperatures of the cold and hot water sources are kept constant to within 0.1^0 C and deviations from temperature uniformity are also of a similar magnitude. This implies that the rig is capable of giving steady and isothermal boundary conditions.

5.2.1 **Design of active walls (hot & cold)**

The hot and cold sides of the cavity are a radiator embedded in plaster (20mm thick). The side facing the fluid domain is fitted with aluminum plate, while the other face is insulated with 89mm thick polystyrene (xtratherm) boards. The xtratherm boards are gas tight foil facers, this makes the insulator air tight, vapour resistant and the foil low emissivity gives its high thermal performance. All arrangements are guarded with wooden plates of thickness 6.35mm. One of the two radiators is shown in Fig.5.3a; these had been designed and fabricated locally using 13mm internal diameter copper tubes and fittings. A total length of 0.8m was needed for each radiator.

A hot water heating system was connected to the radiator for the hot wall side and a cold water system was connected to the cold wall. The heat input device was a 2KW

immersion heater. Hence, the hot water tank has the capacity to supply the required energy for this wall. To keep the temperature steady ($\pm 0.1^0$C), a PID temperature controller was fitted to the heater, this maintained the temperature of the hot water at the set value, with the heat being taken from the tank and dissipated to the fluid from the hot radiator (wall). The PID controller provided proportional, integral and derivative control and has been adjusted to automatically compensate for the temperature changes in the system.

The cold wall system is similar to that of the hot wall in terms of design. The inlet and outlet of the radiator was connected to a recirculation chiller (KT 1 chiller). The plumbing connections are located on the rear of the unit and labelled as SUPPLY and RETURN. The KT 1 chiller is designed to provide a continuous supply of cooling water at a constant temperature and flow rate. The cooling capacity of the unit is 1KW at 20^0C set point, with a temperature range of $+4^0$C to $+35^0$C. The water temperature of the inlet and the outlet of the radiator were measured using three k-type thermocouples each for the inlet and outlet copper tubes. The six thermocouples were connected to a PC through a USB based data acquisition system to monitor and record the temperatures at the selected sampling rate, which was set at every five seconds. A similar technique was used for the hot water system.

5.2.2 **Heat loss measurement**

Tests were carried out to measure and compare the total heat transfer from the hot side to that from the cold wall side inside the enclosure. The total heat transfer from the hot wall side of the cavity (radiator) was calculated using equation (5-1);

$$\dot{Q}_{h-Total} = \dot{m}_h C_p (T_{h-in} - T_{c-out}) \qquad (5-1)$$

Where $\dot{Q}_{h-Total}$ is the total heat transfer rate from the hot side of the enclosure; C_p is the specific heat of the hot water side; T_{h-in} is the water inlet hot wall temperature and T_{c-out} represents the water outlet wall temperature; $\dot{m}_h$ is the hot water mass flow rate which is calculated using equation (5-2);

$$\dot{m}_h = \rho_h \dot{Q}_h \qquad (5-2)$$

Where $\dot{Q}_h$, is the volumetric flow rate of the hot water and ρ_h is the density of the hot water. Water flow rate was measured manually using the bucket method. This method requires a stopwatch and a large bucket. The measurement was done at the flow outlet

of both radiators through the use of a bypass. With a stopwatch we recorded the time taken to completely fill a bucket with water. The stopwatch was started simultaneously with the start of the bucket being filled and then stopped when the bucket is completely filled. The process was repeated for 5 consecutive times and the average time was calculated. The flow rate Q, is the volume of the bucket divided by the average time it took to completely fill the bucket.

Six different hot wall temperatures ranging from 45^0C to 85^0C were imposed on the hot wall. For each hot wall temperature, the heat losses were calculated using the relationship presented in equation (5-3);

$$\dot{Q}_{loss} = \dot{Q}_{h-Total} - \dot{Q}_{c-Total} \qquad (5-3)$$

Which is the heat transferred through the walls or the gaps in the walls to the surroundings and equal to the difference between the heat transferred to the medium from the hot side to the heat removed by the cold side. In comparison with the total amount of heat transferred from hot wall to cold wall, the amount of heat loss represented less than 3.2%.

For each temperature the error of the heat losses were calculated from equation (5-4)

$$Error\ (\%) = \frac{\dot{Q}_{h-Total} - \dot{Q}_{c-Total}}{\dot{Q}_{h-Total}} \times 100 \qquad (5-4)$$

The heat losses are the heat transfer to the enclosure structure and then through the cavity walls or gaps to the surrounding air. The heat loss through the hot wall is less than 3.5%. Therefore, this rig was able to give reliable temperature data.

5.3 **Thermocouple calibration and measurement uncertainty**

Thermocouples used for all measurements were calibrated using digital reference thermometer (model: CIS-640P, accuracy: $\pm 0.1^0$ C, resolution: 0.01^0 C, range -50 + 200^0 C and stability 0.01^0 C) [222] which has a resolution of 0.01^0 C with an uncertainty of $\pm 0.05^0$ C. The calibrations of these thermocouples were done using the hot water tank with stirring devices to keep the temperature of the water uniform. Three reference temperatures of 18^0 C, 45^0 C and 70^0 C were used for calibration. Any temperature difference was constant for all three reference temperatures used and the initial offset was equalised through the conversion equation based on type K thermocouple within the data logging software.

The uncertainties in the determination of the temperature data of the air within the cavity have been estimated. As mentioned above, a hand-held digital reference thermometer has been used as a reference temperature for the thermocouple calibrations. The uncertainty in this reference thermometer reading is $\pm 0.1^0$ C. Throughout the calibration, the temperature of the thermocouple and that of the reference thermometer are assumed to be the same. However, there was always going to be some difference; no matter how well controlled the calibration medium. In our calibration experiments, the thermocouple and the thermometer are immersed in a stirred water bath close to each other. The water is also manually stirred to ensure a constant temperature of the bath. Therefore, the uncertainty coming from this source should be about 0.5^0 C. Following Chunovkina and Chursin [223], the uncertainty in the measured experimental temperature data is 0.51^0 C. (See Appendix E for more details)

5.4 Temperature data repeatability and two-dimensionality validation

In this set-up, temperature data repeatability and two-dimensionality of the flow was thoroughly examined and verified. The number of samples chosen was considered to be sufficient to give statistically significant results at all points measured. The mean temperature profile was measured across different sections of the cavity along the central plane between the active walls. The number and location of these sections depends on the case being studied. Furthermore, one of the temperature measurements has typically been repeated to ascertain steady state conditions and repeatable data. Figure 4.1 illustrates an example of one of the repeated measurements and it clearly shows that the experimental results are repeatable.

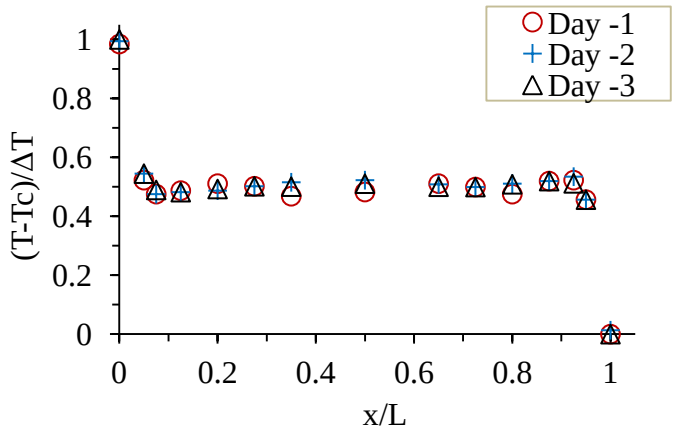

Figure 5-4: Temperature distribution repeatability, y=H/2

The two dimensionality of the flow was verified by comparing the temperature distributions at three different sections of cavity depth, *z/D* = 0.15, 0.5 and 0.85 and for three different horizontal planes, namely y/H = 0.05, y/H = 0.5, and y/H = 0.95. The similarity of the profiles at these three sections, as shown in Figure 4.10, suggested that the temperature field is almost two dimensional across the cavity, since there is no obvious dissimilarities in the temperature profiles at the different sections. Therefore, the three profiles differed only by 2.5%, which indicates that the cavity depth can provide a 2D field. This condition was pointed out earlier by Penot and N'Dame [224], that the 2D approximation of experimental natural convection in cavities should be valid if the horizontal aspect ratio (*D/L*) of the cavity is greater than 1.8. In our study, this aspect ratio is 2.5.

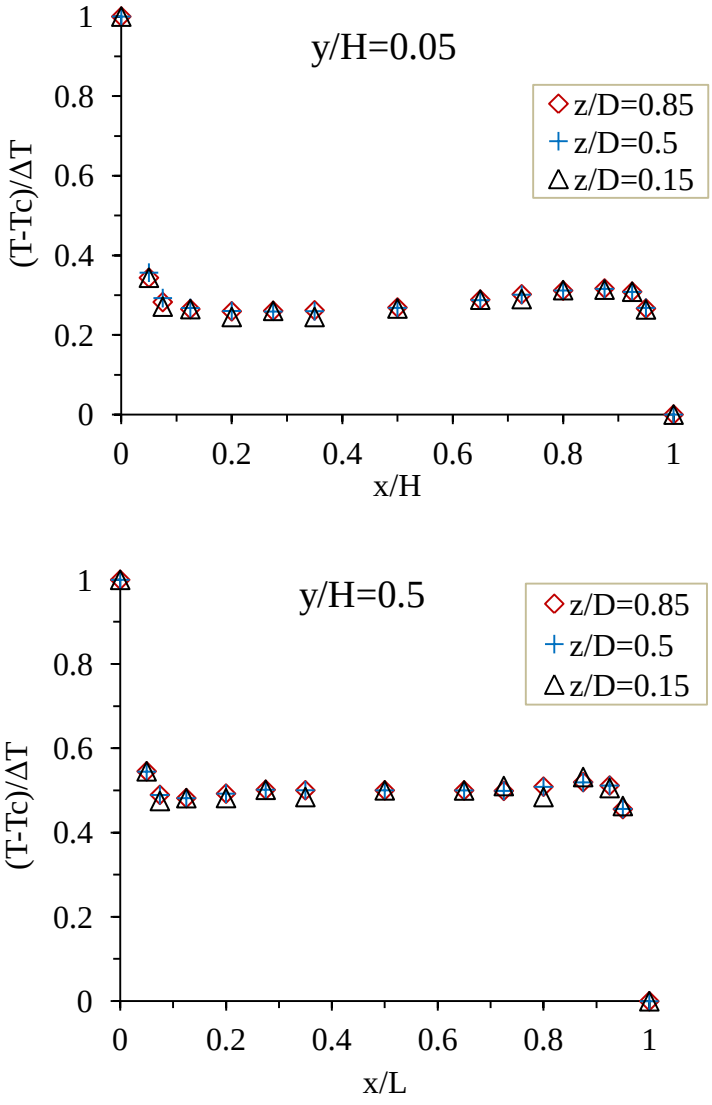

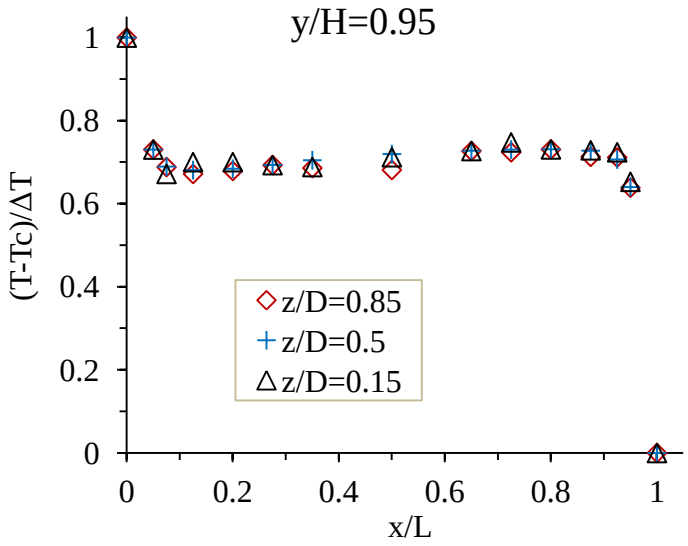

Figure 5-5: Two-dimensionality comparison for the thermal field across different heights of the vertical cavity at different depths

5.5 Vertical walls temperature distributions

Surface temperatures of the hot and cold walls at steady state are shown in Fig.5-6 (a-b) respectively. The average temperature of the hot wall is 65.5^{0}C, and that of the cold wall is 23.3^{0}C. The surface emissivity value was measured using a thermal imaging camera (E60bx model) and was found to be 0.07, and the thermal conductivity of the material is 202.4W/m-K.

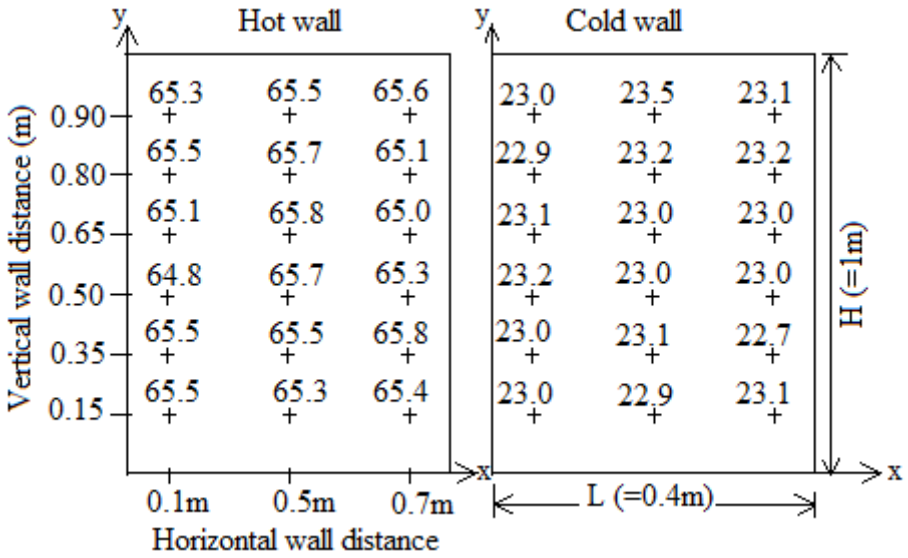

(5-6a) (5-6b)

Figure 5-6: Active vertical wall temperature distributions (a) hot wall (b) cold wall

5.6 Horizontal wall temperature profiles data

The temperature profiles for the highly conductive top and bottom wall of the rectangular enclosure was initially examined. The normalized temperature profiles measured along the horizontal centre-line starting from the heated vertical wall of the enclosure are shown in Fig.5-7. It was expected that these walls would conduct heat from the hot wall to the cold wall and dissipate or absorb some of the heat from the fluid near the surface due to conduction, convection and radiation.

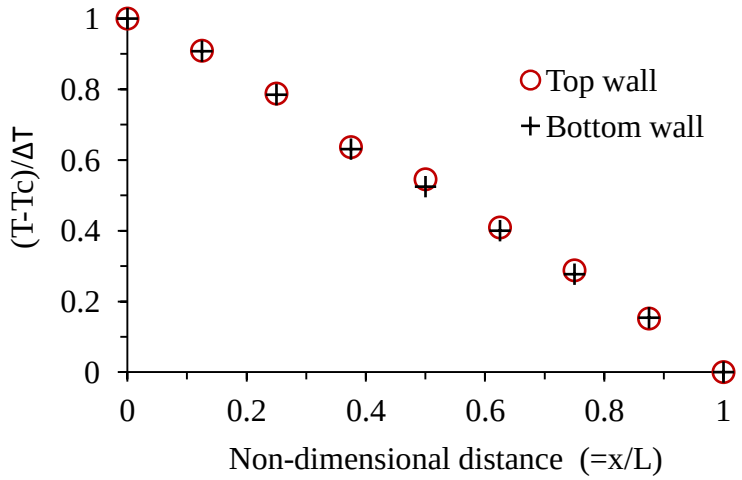

Figure 5-7: Temperature profile on horizontal walls

The horizontal wall temperature variation can be represented by a best-fit linear expression as shown below:

$T_{top\text{-}wal} = 296.45 - 42.2(1.03 – x/L)$

$T_{bottom\text{-}wall} = 296.45 - 42.2(1.02 – x/L)$

These temperature expressions will be used as the thermal boundary condition for the inactive walls in our numerical calculations to be presented in later chapter.

5.7 Air temperature data for cavity without blockage

The key parameter measured in the experiments is limited to mean temperature only. This is because the temperature distribution is the most critical quantity due to the fact that this may be interpreted as both the ‘cause’ and ‘effect’ and vice versa. The flow development due to buoyancy is directly dependent on temperature and at the same time temperature is also affected by the flow field.

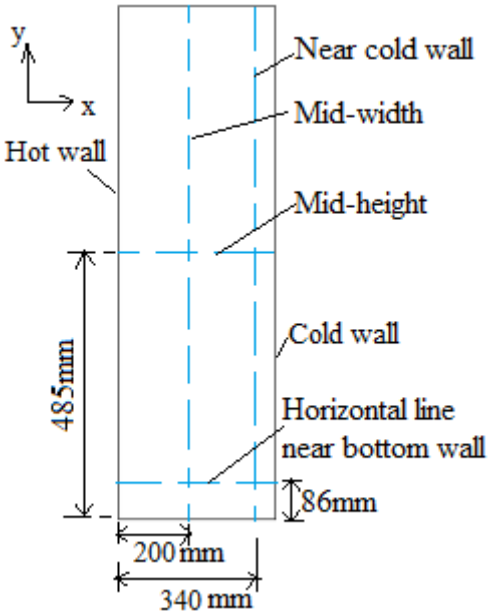

Figure 5-8: Schematic of cavity showing planes of temperature data for air

The centre-lines for which air temperature data was measured are shown in Fig.5-8. Temperature profiles near the cold wall and at the mid-width of the cavity are displayed in Figs.5-9a and 5-9b respectively. The horizontal temperature profiles near the bottom wall and at the mid-height of the cavity are also shown in Figs. 5-9c and 5-9d respectively.

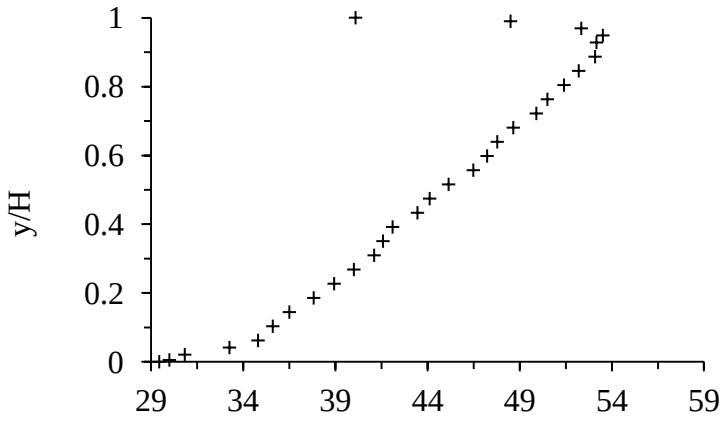

(5-9a)

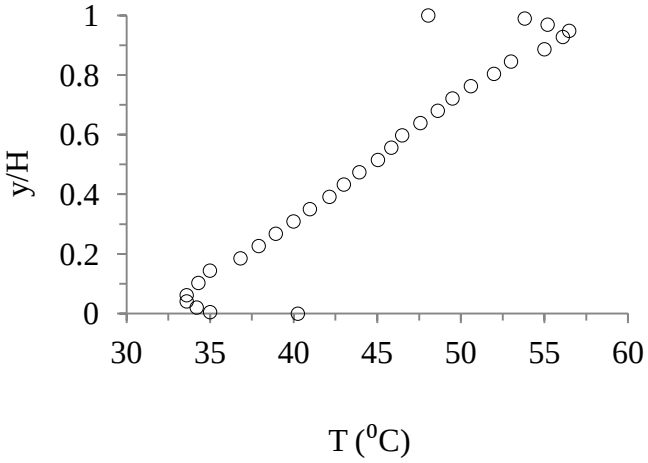

(5-9b)

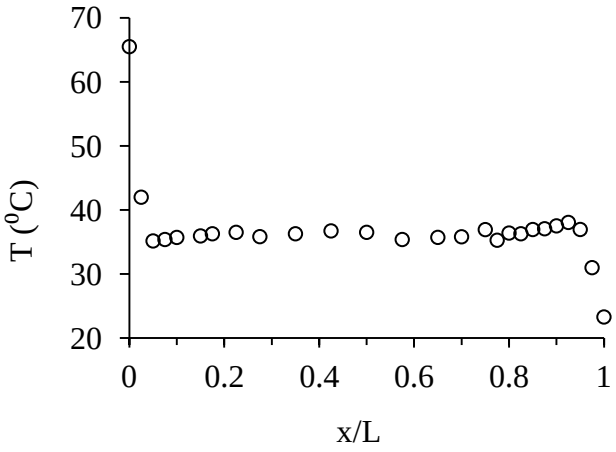

(5-9c)

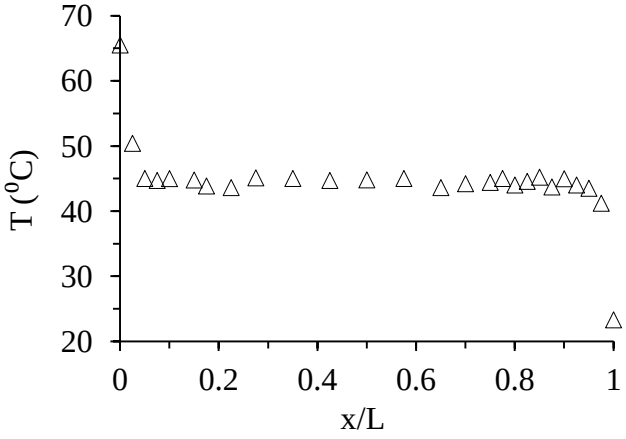

(5-9d)

Figure 5-9: (a) vertical temperature profile near cold wall at 340mm from hot wall (b) vertical temperature profile at mid-width (c) horizontal temperature profile near bottom wall at 0.86mm from bottom wall (d) horizontal temperature mid-height

It may be observed that the temperature profiles outside of the boundary layer are approximately uniform indicating that there is no significant natural convection in the core region. Therefore, conduction and radiation are likely to dominate which is indicated by the linear variation as can be seen in Figs.5-9a and 5-9b. In other words, most of the air in the cavity is stably stratified reducing the local buoyancy force acting on the flow in the boundary layer as it travelled upward along the heated vertical wall. This observation is true for all cases reported in published literature [225, 226].

Temperature profile measured at the mid-width near the cold wall as shown in Fig.5-9a, had undershoot at the walls, where the local temperature fell below the local temperature in the core region of the rectangular cavity. Also, temperature profile measured along a vertical line near hot wall and from bottom wall is similar but showed an overshoot at the walls. A similar undershoot was also observed by Tian and Karayiannis and others [51, 227, 228] in their temperature profiles measured for the natural convection in a square cavity. There is an overshoot near the edge of the boundary layer as the fluid travels up the heated vertical wall.

5.8 **Cavity partially filled with blockages**

In this section, experimental study of turbulent natural convection in a confined space containing arrays of disconnected cylinders is conducted. The test rig used in the experimental investigation without blockages is modified to contain arrays of disconnected cylindrical objects. The working zone is partially filled with cylindrical blockages and occupied about 34.3% of the total cavity volume. The vertical walls of the cavity were isothermal with a temperature differential of 42.2^0C, giving a Rayleigh number of 2.5×10^9. In this study, particular emphasis was played on quantifying the temperature distribution at various positions within the flow domain due to the proximity of these blockages to the thermally active vertical walls.

This work aims to provide high quality temperature data that can be used for the validation of computational fluid dynamics CFD codes. It is believed that a CFD code, which can predict the fluid flow and heat transfer in such a “congested” cavity, can be used with confidence in indoor environment and electronic equipment cooling

studies and design optimisation. Also, the collected data will enrich the knowledge on the flow on the phenomena that take place in a confined space containing numerous solid objects. The schematic of the thermal rig used in this study is shown in Fig.5-10a- b.

The rig is loaded with disconnected ABS pipes of diameter 33.7mm and 1m long. Three different blockages densities were studied. They are: 10(rows) x 5(column) representing 34.3% blockage; 10x3 representing 20.6% blockage and 5x5 representing 17.2% blockage. This material was chosen because of its light weight, cost effectiveness, rigidity, and its suitability for use over a wide temperature range from -40^0C to $+80^0$C and up to 15 bar pressure. The thermal coefficient of linear expansion is 10.1 x 10^{-5} ($/^0$C) and its thermal conductivity is 0.33 (W/m-k). The emissivity of the surface is 0.9.

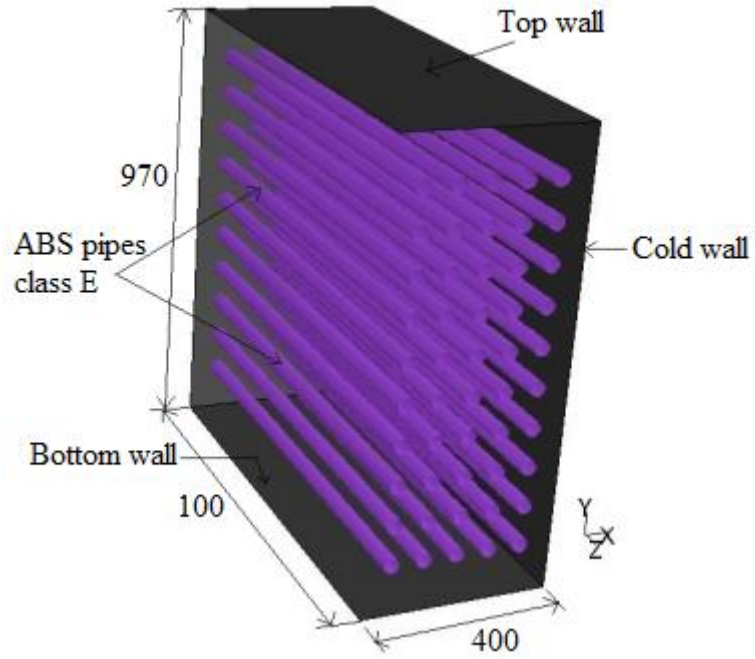

(a)

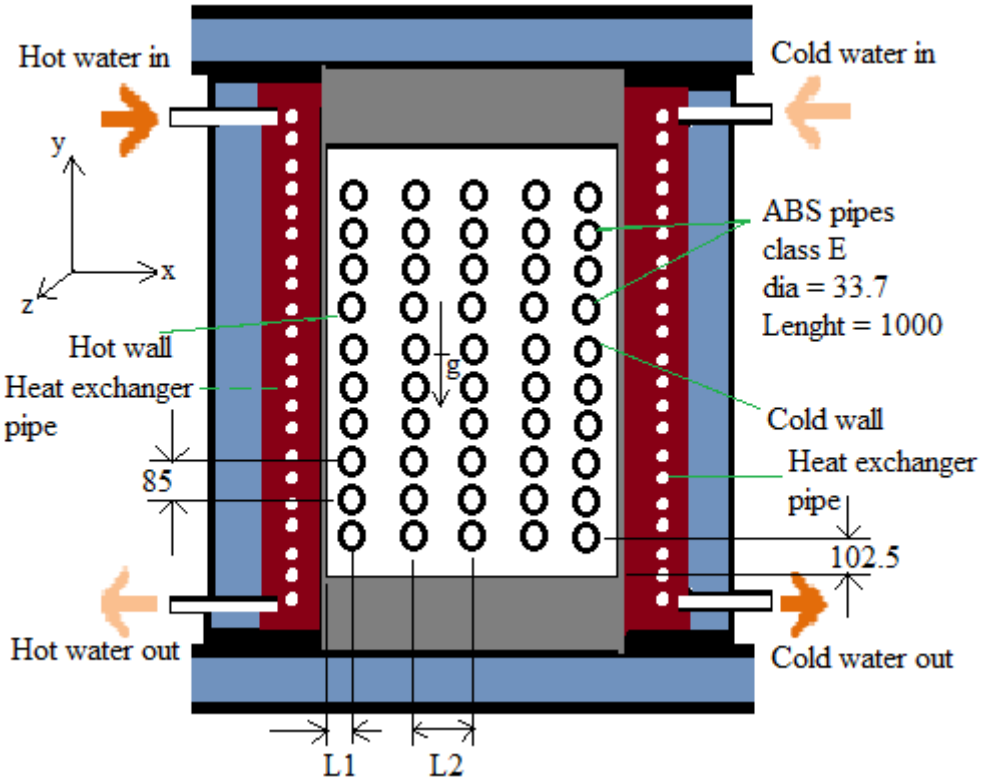

(b)

Figure 5-10: Schematic of the experimental facility for 5x10 blockage (a) 3D arrangement (b) test cavity showing details of construction (all dimensions are in mm)

ABS pipes have low thermal conductance which help to maintain more uniform temperature when interacting with fluids. In addition, low thermal conductivity of the pipe walls help to eliminate or reduce greatly the need for pipe insulation to control sweating. The pipes were positioned linearly near the side walls using specially designed guide rails fitted to these walls. These guide rails were accurately fitted to these walls using a precision height gauge.

Air temperature distributions within the cavity working zone were measured on the symmetry planes. Also measured were the temperatures of the hot and cold walls and top and bottom walls along the symmetry planes A total of 166 thermocouples were fitted inside the cavity of which 52 were on pipe surfaces, 60 on walls and 54 for measuring air temperature.

5.9 **Blockage proximity study for 10x5 arrangement**

In this set of experiments, temperature data at various positions in the fluid zone for the case of cavity with cylindrical blockages are presented. Measured data along the

vertical planes of the enclosure are presented first, followed by data close to the cold wall and finally along the horizontal planes are presented. As before, measurements were done at steady state condition. Fig.5-11 shows the locations of temperature data along vertical planes. The vertical temperature lines are shown by L1 (Near hot wall), L2 (location at mid-width) and L3 (Near cold wall) respectively. The proximity of the first row of cylinders is given by δ, which is variable, and is equal to L1. Also shown in Fig.5-11 are thermocouple positions P-1 and P-2 which correspond to the top and bottom surface position of the pipes respectively.

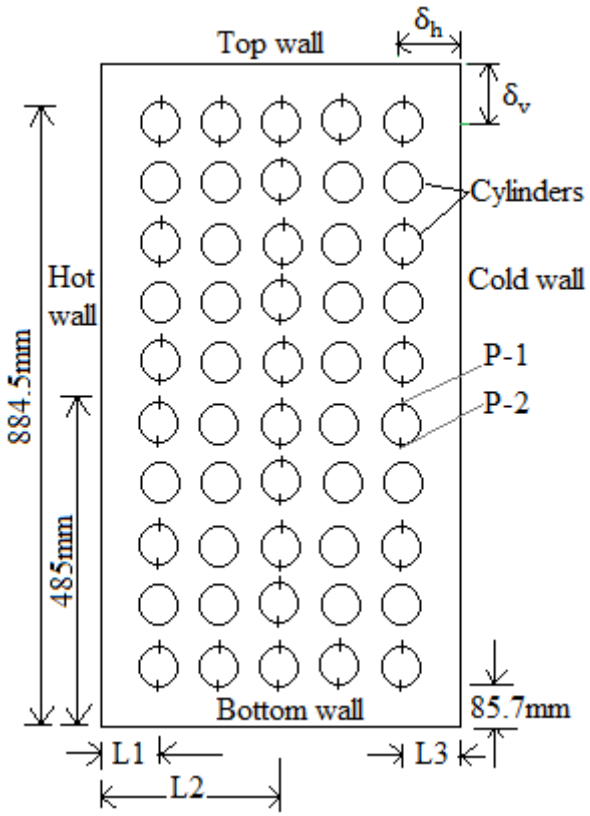

Figure 5-11: Thermocouple position on the cylinder walls at symmetry plane of the cavity

5.9.1 **Temperature profile**

Air temperature data measured at the mid-height of the cavity for all cases is shown in Figs.5-12a-c. Figs.5-13 and 5-14 showing cylinder wall temperature data measured at positions near the hot wall and near the cold wall respectively. Plots of temperature profiles along mid-height of the cavity (485mm from bottom wall) are shown in Figs.5-15a-d.

The temperature distribution along the vertical mid-plane centreline, x/L =0.5(L2) in the y-direction is shown in Fig.5-12a-c. The temperature profiles are nearly asymmetric about the centreline region, unlike the temperature profile plot without blockages shown earlier in Fig.5-9b, which is almost symmetrical measured along similar centreline. The variations may be due to the multiple radiations from the surface of blockages. Also, there seems to be a slight variation of temperature profile for the three cases of blockages arrangements as shown in Fig.5-9b. The trend in temperatures variation between the air and region near the walls and cylinders may be linked to the blockage proximity which damped the horizontal convection flow and turbulence, hence causing the temperature to vary.

Figs.5-15a-d show the temperature profiles measured at mid-height of the cavity. The mean temperature variation shows a sharp linear change in the regions near the two active walls. The profiles have almost a linear variation near the centre region of the cavity. The slight deviations are due to multiple radiations from the cylinders, and as the blockages are closer to the centre of the cavity, the deviation increase. The core region flows due to blockages proximity effects which also contribute to the overall flow in the cavity, and is a further indication that the fluid motion is a low turbulent natural convection flow. Near the wall regions, the temperature also varies almost linearly with the horizontal distance, but with a much larger slope. This indicates that only a small portion of heat is transferred by molecular conduction across the core of the cavity. It is also observed that temperature profiles overshoot near the edge of the boundary layer as the fluid travels up the heated vertical wall, and it can be seen from works done by various researchers [51, 111, 229]. Temperature data at the surface of the cylinders measured at different horizontal planes of the enclosure are shown in Appendix D.

Furthermore, experimental temperature data at the surface of the cylinders near the hot and cold walls are depicted in Figs.5-13 and 5-14 respectively. The positions for the temperature profiles of the cylinder surface measurements are near the hot wall (L1) and cold wall (L3) as shown in Fig.5-11, P-1 represents cylinder walls facing upward and P-2 is that facing downward. All plots show steady temperature stratification along the vertical axes of the cavity

The experimental results also show that the cylinder temperatures increase with height. It is believed that the heat exchange by radiation between the cold wall and cylinder surface contribute to cool down the cylinder. In the same manner, heat exchange by radiation between the hot wall and cylinder surface leads to increase the cylinders temperature. In our studies, radiation is not negligible compared to convection so that a cylinder located near the wall is at an intermediated temperature between the surrounding air, with which it exchanges heat by convection, and wall, with which it exchanges heat by radiation.

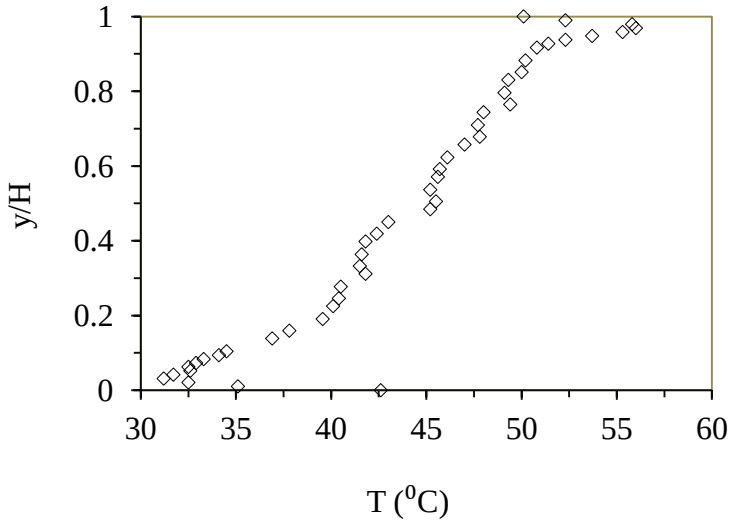

(5-12a)

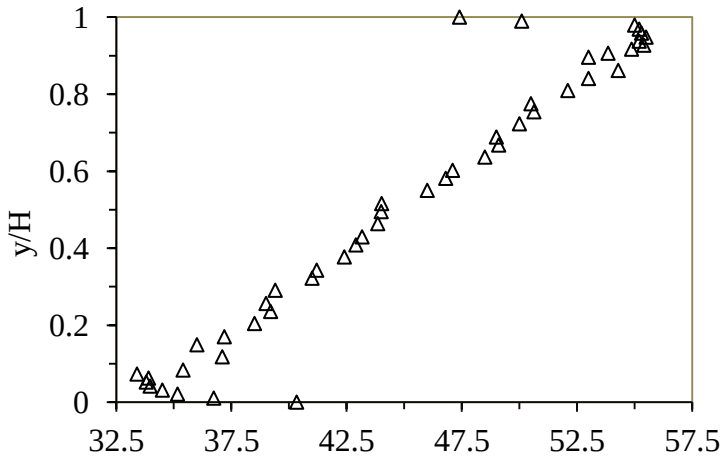

(5-12b)

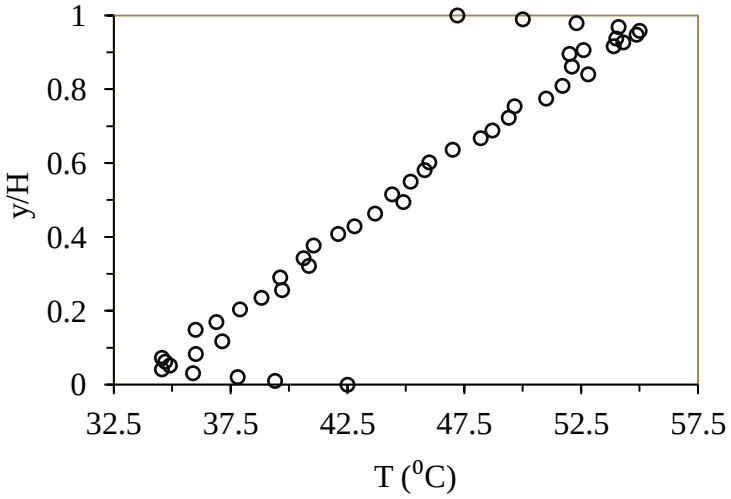

(5-12c)

Figure 5-12: Temperature profile at mid-width (a) δ = 25mm (b) δ = 58mm (c) δ = 108mm

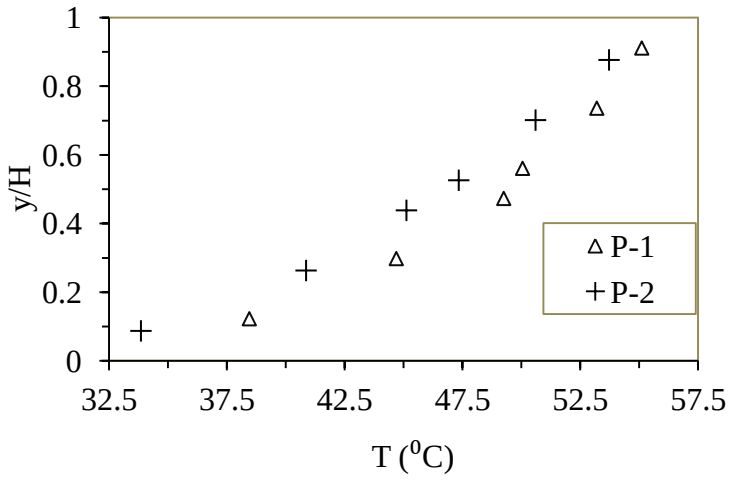

(5-12a)

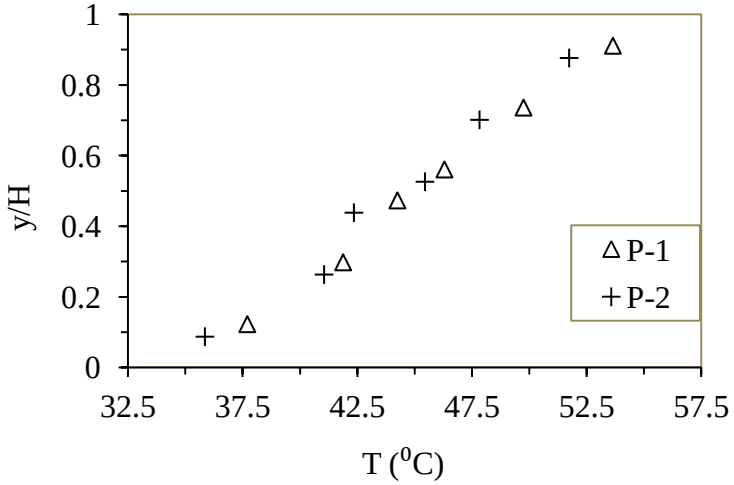

(5-12b)

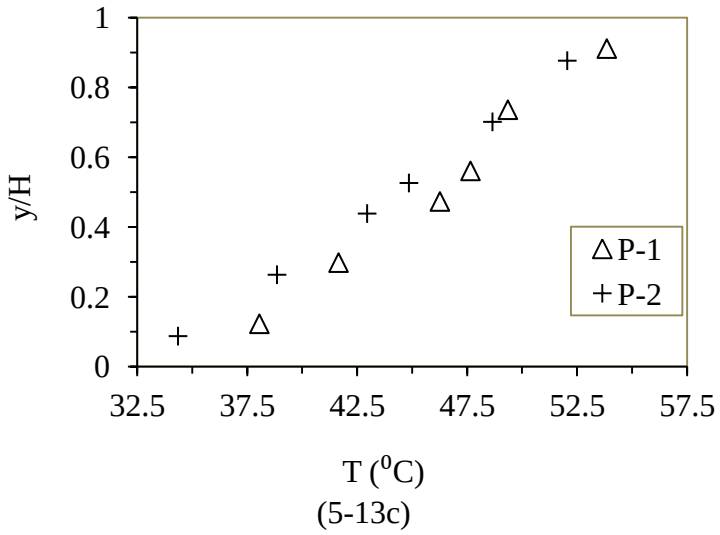

(5-13c)

Figure 5-13: Cylinders wall temperature profiles near hot wall (a) δ_h=25 mm (b) δ_h=58 mm (c) δ_h=108 mm from hot wall

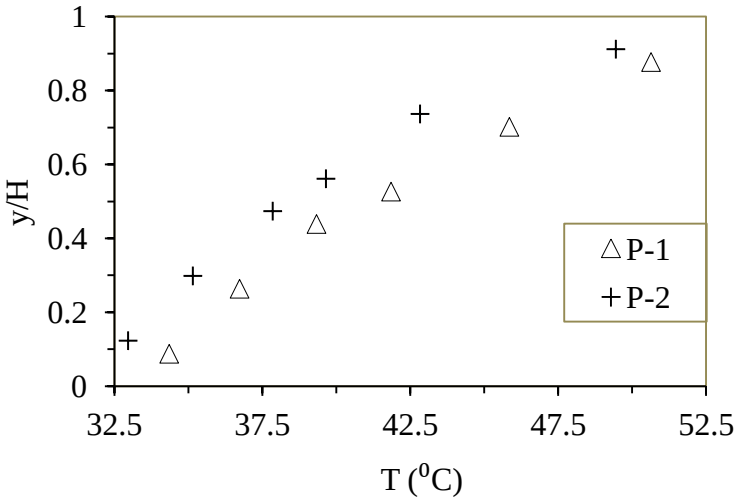

(5-14a)

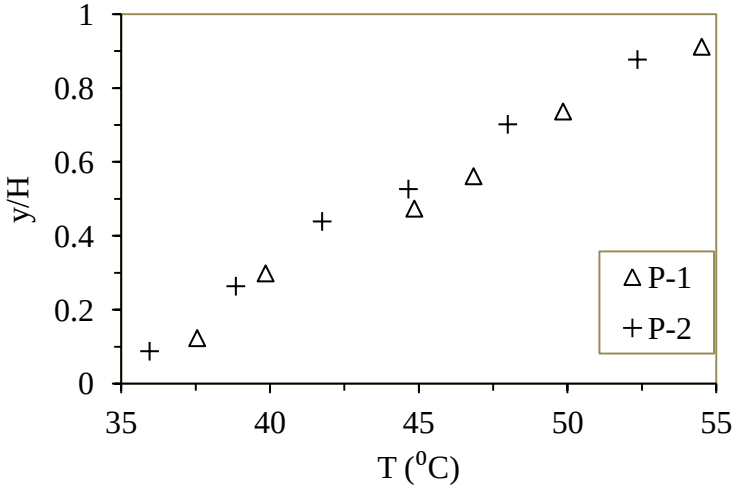

(5-14b)

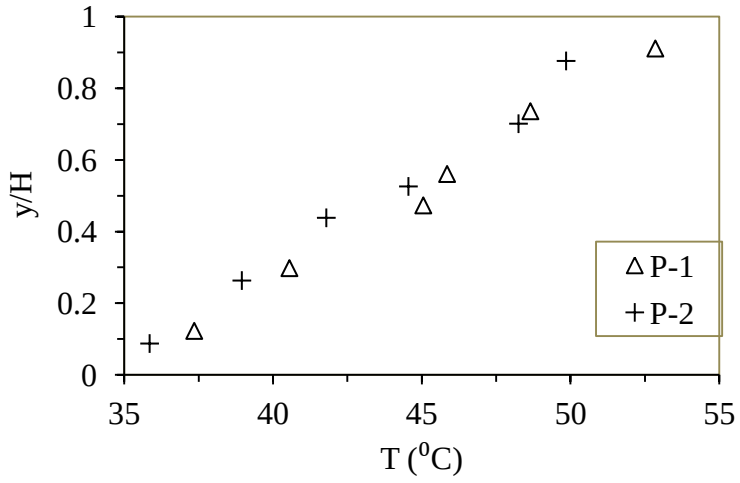

(5-14c)

Figure 5-14: Cylinders wall temperature profiles near cold wall (a) δ_h=25 mm (b) δ_h=58 mm (c) δ_h=108 mm from cold wall

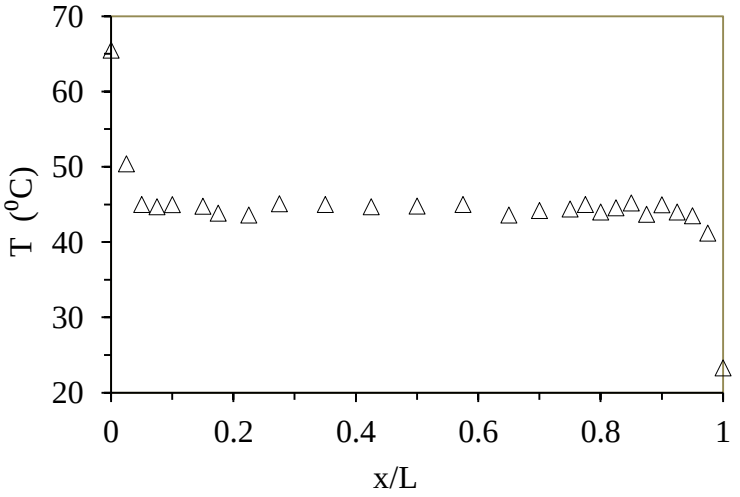

(5-15a)

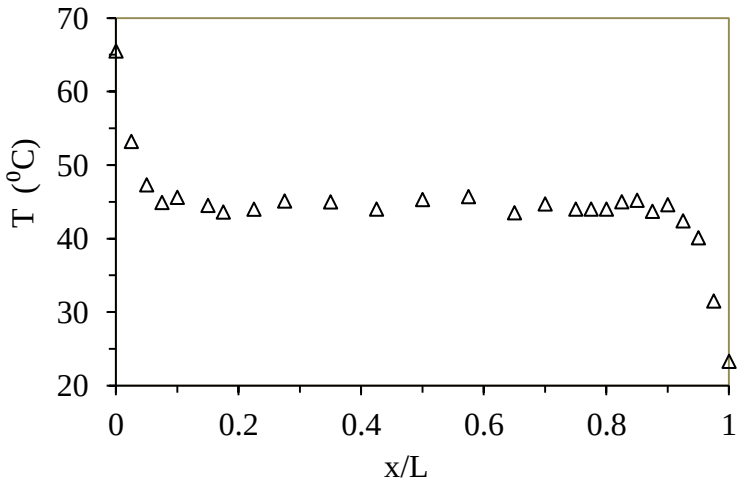

(5-15b)

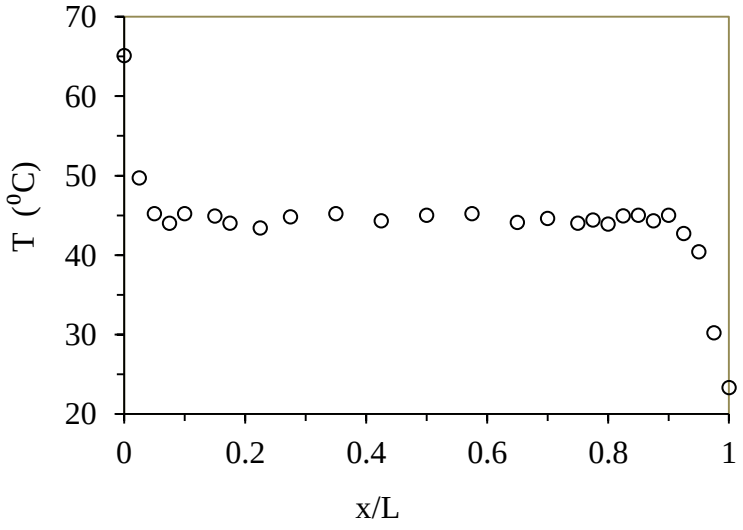

(5-15c)

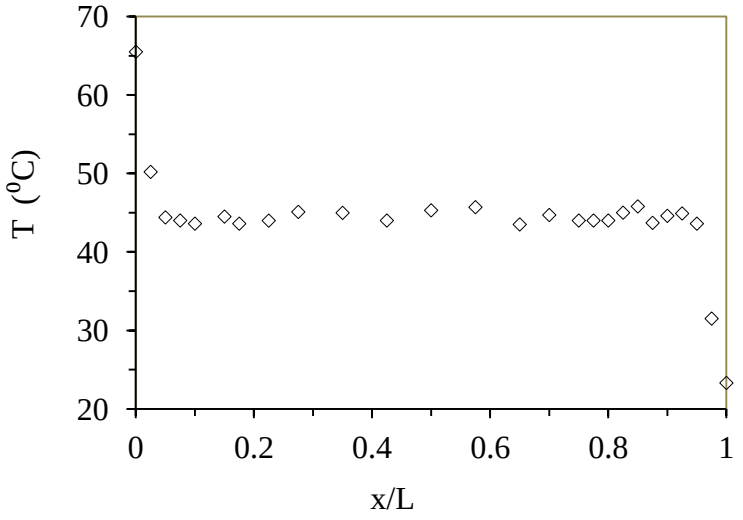

(5-15d)

Figure 5-15: Temperature profile at (a) mid-height, without blockages (b) mid-height, δ = 25mm (c) mid-height, δ = 58mm (d) mid-height, δ = 108mm

5.10 **Experimental data for 10x3 blockage arrangement**

The configuration for the fluid zone arrangement is shown in Fig.5-16; the blockages are in arrays of 10 rows and 3 columns representing a blockage of 20.6% of the cavity. The cases considered are: case 1 (near hot wall), case 2 (near cold wall) and case 3 (at the middle).

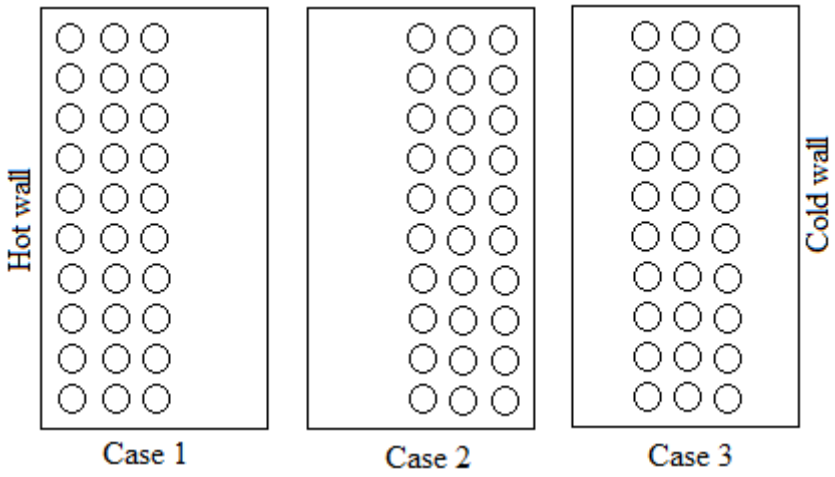

Figure 5-16: Schematic of the flow domain arrangement for all three cases

At steady state, temperature profiles along the mid-height and mid-width were collected and the compared results are presented in Figs.5-17a-b. Temperature data for the mid-height and mid-width displays a stable core region; the average core temperature for Case-1, 2 and 3 are shown in Fig.5-17a and Table 5-1. It is observed that the temperature profile at the core region measured along the mid-height of the cavity is strongly influenced by the blockages arrangement along the horizontal direction from hot wall to cold wall. Using 44.5^0 C as a reference temperature evaluated at the mid-height of the cavity without blockages, the percentage change in average temperature measured along the same height for the three cases of arrangement gives an increment in temperature of 5.1% for Case-2 arrangement, 0.2% for Case-3, and Case-1 shows a average value of -5.7% in the average temperature. Similar variations are observed in the temperature profile measured along the mid-width of the cavity as shown in Fig.5-17b, the mean values at the core region are shown in Table 5-1. Percentage change in temperature along the mid-height of the cavity using 44.4% as the reference temperature for cavity without blockage show that, Case-2 shows 3.2% of temperature increment, Case-3 shows -0.2% and Case-1 is -2.4%. Therefore, products arrangement near the hot wall significantly reduced the temperature and hence the heat transfer.

Table 5-1: Average core temperature for all cases (^{0} C)

Cases	Mid-height profile	Mid-width profile
Case 1	42.1	43.39
Case 2	46.9	45.89
Case 3	44.6	44.33

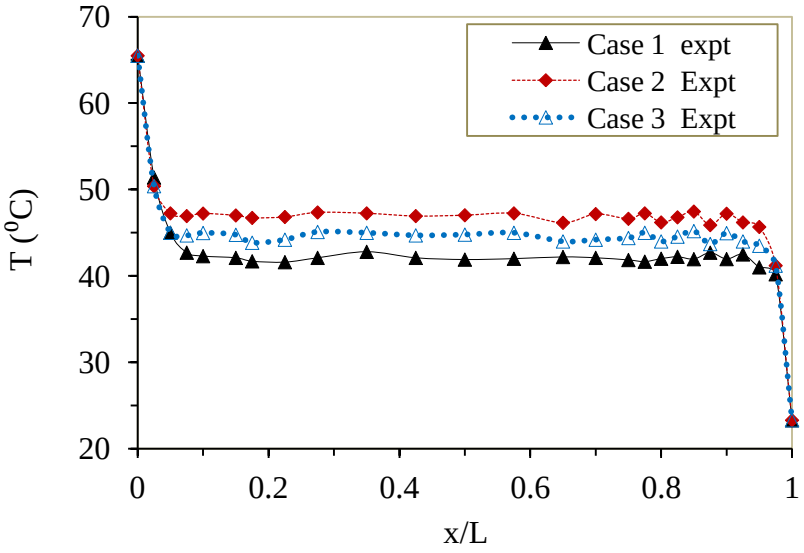

(5-17a)

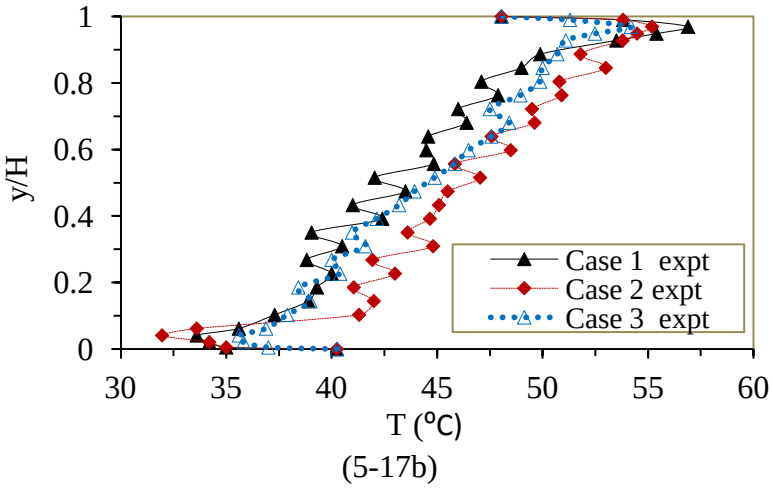

(5-17b)

Figure 5-17: Temperature profiles for all three cases at (a) mid-height (b) mid-width

5.11 **Experimental data for 5x5 arrangement**

The blockages arrangement is shown in Fig.5-18. Two different configurations were studied. These cases involve the arrays of (5 rows and 5 column) blockages group location near the top (NTW: Near Top Wall) and bottom walls (NBW: Near Bottom

Wall) of the rectangular enclosure. Fig.5-19 shows the temperature distribution comparison at the mid-height of the enclosure for the two cases considered. The two blockages configuration gives an average of 2.1^0 C temperature difference. Using the average temperature (44.4^0 C) measured along mid-height and at the core region for a cavity without blockage to evaluate the percentage temperature change, shows an increment of 4.1% for NTW and -0.5% for NBW. Therefore, products arrangement near the top wall influences the heat transfer positively.

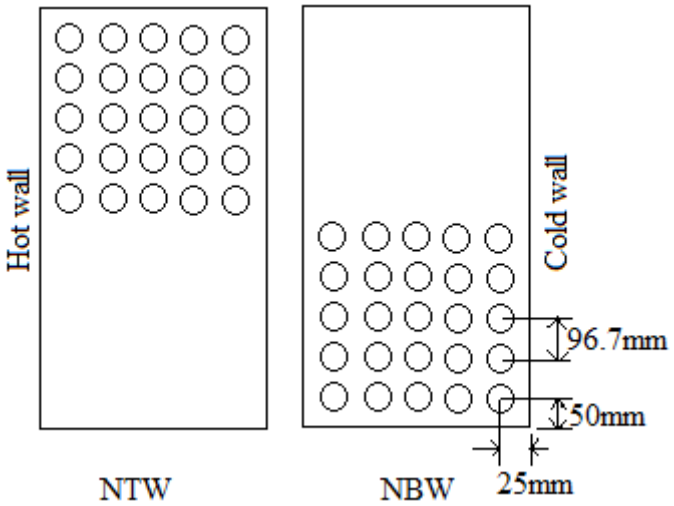

Figure 5-18: Schematic of the flow domain arrangement

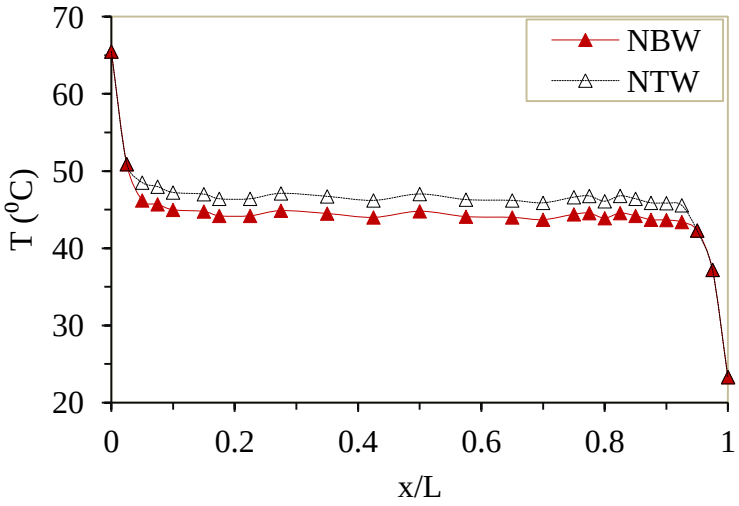

Figure 5-19: Temperature profile comparison at mid-height of the cavity

5.12 **Conclusion**

This study was carried out in order to obtain experimental temperature data which allows the understanding of two-dimensional heat flow in an enclosure partially

loaded with disconnected cylindrical objects. Additional experimental results are given in Appendix C. Some general conclusions from the different parametric cases studied are highlighted below;

- Temperature stratification was observed in all cases
- High temperature at the top and low temperature at the bottom region of the enclosure.
- The thickness of thermal boundary layer is greatly suppressed as the gap between the walls and the solid objects become smaller.
- The fact that the variation of the proximity of solid objects from the vertical walls influences the scenario drastically is a vindication that proximity of objects near vertical walls does plays a significant role in apparently low temperature applications. This may have an important implication in thermal management in built environment, cooling of electronic panel and other engineering applications.

Chapter 6 - NUMERICAL INVESTIGATION OF FLOW AND HEAT TRANSFER FOR DIFFERENT ARRANGEMENT OF BLOCKAGES

6.1 Introduction

Three-dimensional numerical study of low turbulence natural convection flow in a confined space containing solid objects is conducted. Since our experimental data presented in the previous chapter were limited to temperature only, particular emphasis was placed on quantifying the airflow, turbulence quantities and heat transfer due to various arrangements of blockages. The experimental data were validated by computational results to provide confidence in exploring the flow fields.

The test zone is similar to the one used in our experimental rig with blockages. Cylindrical objects were arranged in 10 rows and 5 columns in such a way that 2D flow was established. The vertical walls of the cavity were isothermal with a temperature differential of 42.2^0C, giving Rayleigh number of 4.04×10^9. Therefore, airflow in the cavity involved low turbulence and is a function of the temperature gradient between the vertical walls.

The parametric studies reported are the analysis of the influence of blockage proximity and arrangement from the vertical and horizontal walls. The schematic of the fluid domain and blockage arrangements is depicted in Fig.6-1. The enclosure is a rectangular box with internal dimension of 0.97m x 0.4m and depth of 1m. L1 and h1 represent the proximity from active vertical walls and passive horizontal wall respectively.

This investigation aims to provide accurate and detailed numerical results for the airflow, turbulence quantities and heat transfer due to the influence of these blockages. Also, the results will be used to compare with experimental temperature data for validation. It is found that the results will provide insight into the flow and thermal fields in an enclosure partially filled with disconnected cylinders.

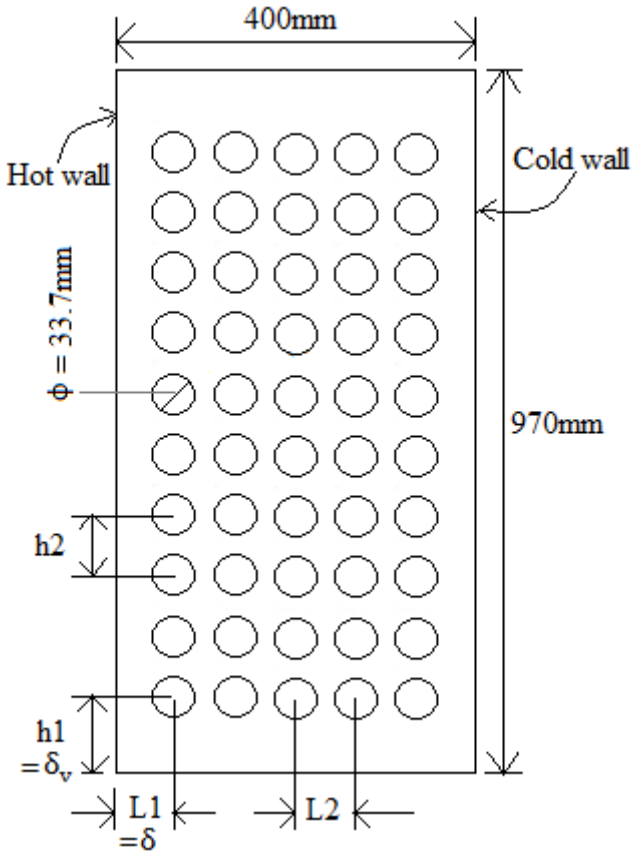

Figure 6-1: Schematic of the flow domain and blockages arrangement

6.2 **Numerical Method**

Three-dimensional CFD simulation was performed for all test cases used in the experiment using the commercial CFD package of ANSYS FLUENT 14. Turbulent fluxes of momentum, heat and mass were modelled by low Reynolds number k-ε eddy viscosity model of Launder-Sharma with the inclusion of the buoyancy terms in the energy equation. The L-S model was incorporated through the User Define Interface (UDI). This model has been used for greater stability and superior results for blockage flow as will be shown in chapter 7.

Systematic grid dependency test were carried out for all three cases and the final results were obtained with about 4.5million cells with $y^+ \approx 5$. It is worthwhile to note that the process of computing a steady-state solution using very fine mesh has been quite challenging because of the oscillations associated with higher-order discretization schemes. As a result, a number of steps were taken to achieve a steady-state solution. Initially, low value of Rayleigh number (10^6) was adopted to state the solution using an incompressible unsteady solver with a time step of 0.002s, with the

first-order scheme and the solution was allowed to run to convergence which was typically three orders of magnitude lower than the residual at the start.

The resulting data files for the three cases were then used as an initial guess for the higher Rayleigh number simulation using the higher-order discretization schemes. This method helped to create a more realistic initial field for the LRKE runs. All simulations were performed using a single Intel core 2Duo E6600 2.4 GHZ processor and a typical run took about 4 days of computing time. Thermal properties of the working air were estimated at the mean temperature of the isothermal walls (44.4^0C) of the cavity as presented in Table 6-1.

Table 6-1: Thermo-physical properties of dry air used in the simulations

Thermal properties	Air (at 44.4^0C)
Density (kg/m³)	1.110
Dynamic viscosity (kg/m-s)	1.94×10^{-5}
Specific heat (J/kg-K)	1.01×10^{3}
Thermal conductivity (W/m-K)	0.0274
Prandtl number	0.711
Thermal diffusivity (m^2/s)	2.45×10^{-5}
Thermal expansion coefficient (1/K)	3.15×10^{-3}

The Under-Relaxation parameters and the discretization scheme used in the simulations are presented in Table 6-2.

Table 6-2: Solver parameters

Spatial discretization	Under-relaxation coefficient	Type of discretization
Gradient	-	Least square cell based
Pressure	0.3	PRESTO!
Momentum	0.2	Second order upwind
Turbulent kinetic energy	0.5	Second order upwind
Turbulent dissipation rate	0.5	Second order upwind
Turbulent viscosity	0.7	Second order upwind
Energy	0.9	Second order upwind
Discrete ordinates	0.9	Second order upwind

Wall thermal conditions used in the calculation are the same as those in the experimental study of this work, and are summarised in Table 6-3. No slip shear condition has been applied to all surfaces. The horizontal wall temperature profiles are a best-fit based on the experimental result of our earlier study given in section 5.6. This experimental thermal boundary condition has been used for the top and the

bottom walls and was incorporated into FLUENT through the User-Defined-Function (see Appendix A for the UDF). The rational for using experimental boundary condition has been strongly established in chapter 4.

Table 6-3: Physical properties of the materials involve in the simulations

Surfaces	Material	Temperature (^{0}C)	Emissivity	Conductivity (W/m-K)
Hot wall	Aluminium	65.5	0.07	202.4
Cold wall	Aluminium	23.3	0.07	202.4
Top wall	Aluminium	ETP (Top wall)	0.07	202.4
Bottom wall	Aluminium	ETP (Bottom wall)	0.07	202.4
Blockages	ABS pipe	-	0.9	0.33
Side walls	Plywood	-	0.83	0.13

Finally, to simulate the heat transfer due to radiation, the Discrete Ordinate (DO) method has been chosen due to its proven superiority in predicting radiative heat transfer involving a participating medium. The angular discretization parameters used in the simulation are: Theta and Phi divisions are specified as 2 and 6 each for Theta and Phi pixels.

6.3 **Blockage proximity from vertical active walls for 10x5 arrangement**

In this study, we present the detailed results from numerical calculation on the 10x5 arrangement of cylinders as shown in Fig.6-2. The proximity of the nearest column of cylinders, δ (=L1), is varied for three values of 25, 58 and 108mm. The following four sections will show the results for flow field, turbulence quantities, heat transfer and finally validation with experimental data.

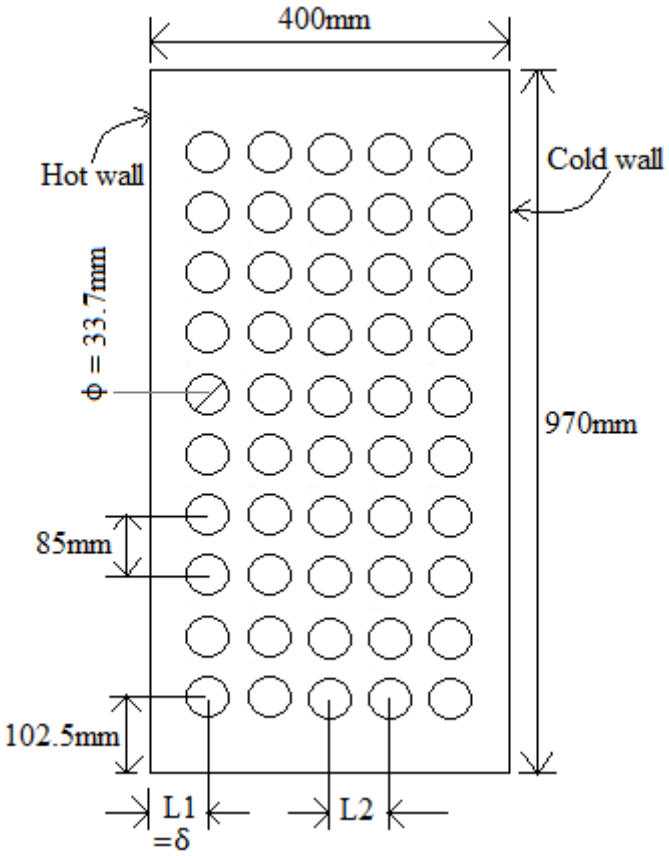

Figure 6-2: 2D schematic showing the arrangement of the blockages from the walls

6.3.1 **Flow fields (10x5 arrangement)**

Fig.6-3a-c show the mean velocity results for different blockage proximity values. The contour (Fig.6-3a) highlight the expected wall – confined boundary layer flows and the typical primary vortex can be observed. A closer look reveals that for δ=25mm, the blockages are inside the boundary layer and hence the flows are highly perturbed. The maximum velocity is at the boundary layer and reaches a value of 0.25m/s and is found to decrease as the value of δ decrease. The thickness of the boundary layer is about 100mm. Fig.6-3c shows the peak of the velocity profile near the hot wall, the main circular air flow near the cavity walls occurs in a boundary layer whose thickness λ (=0.00492m to 0.00324m) is small compared to cavity dimension (typically λ/L=0.0123 to 0.0081) and even compared to the cylinder (λ/d≈0.1562 to 0.097) so that the cylinder interacts slightly with this boundary layer.

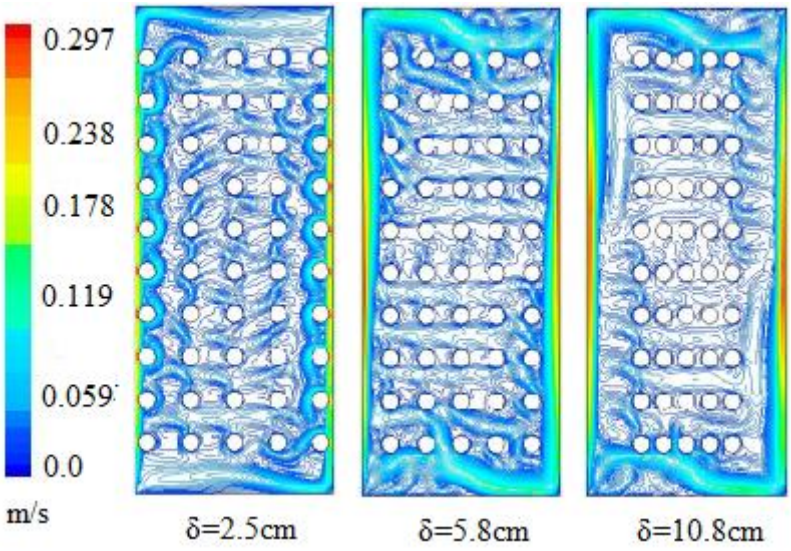

(6-3a)

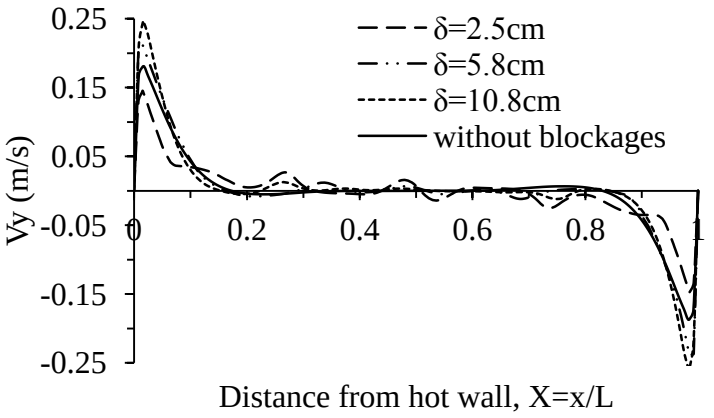

(6-3b)

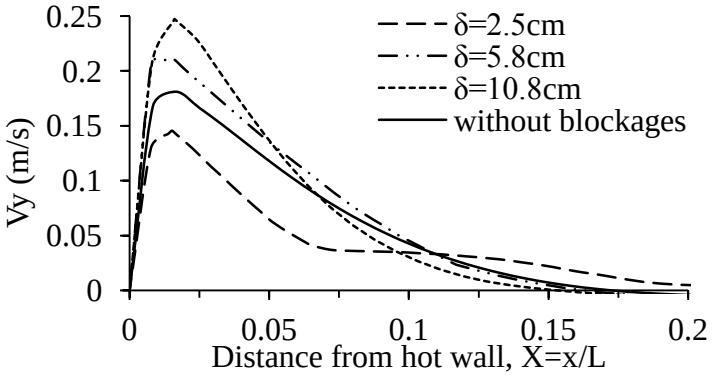

(6-3c)

Figure 6-3: (a) mean velocity filed (m/s), (b) velocity profile at mid-height, (c) same as (b), but on an exaggerated scale.

Figs.6-4a-b show the contours of the temperature field. Stratifications can be clearly seen, with high temperature at the top and low temperature near the bottom of the

cavity. Fig.6-4b shows that the cylinder located nearer the wall is at intermediate temperature between the surrounding air, with which it exchanges heat by convection and the wall with which it exchanges heat by radiation. In addition to the primary natural convection flow near the walls due to temperature difference between the vertical walls and the adjacent air, secondary natural convection flows around the surface of the cylinders is due to the temperature difference between the surface of the cylinders and the surrounding air. This is in agreement with our experimental results presented in section 5.9.1.

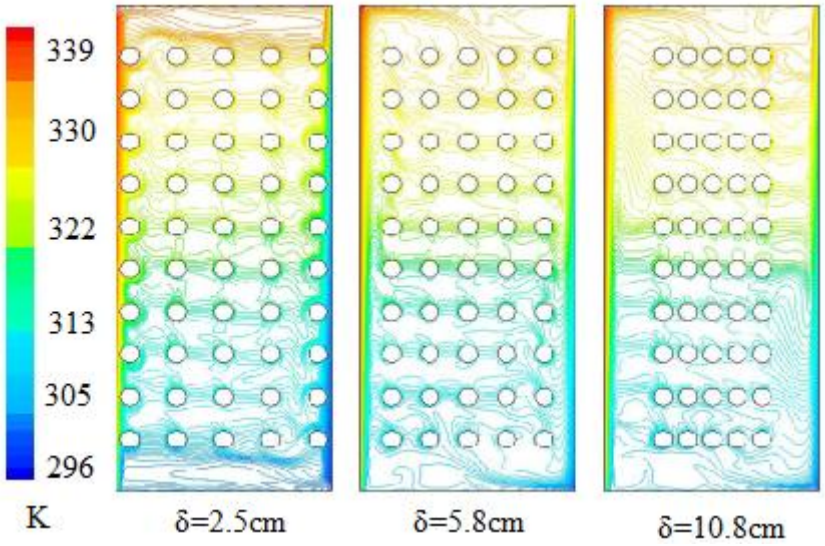

(6-4a)

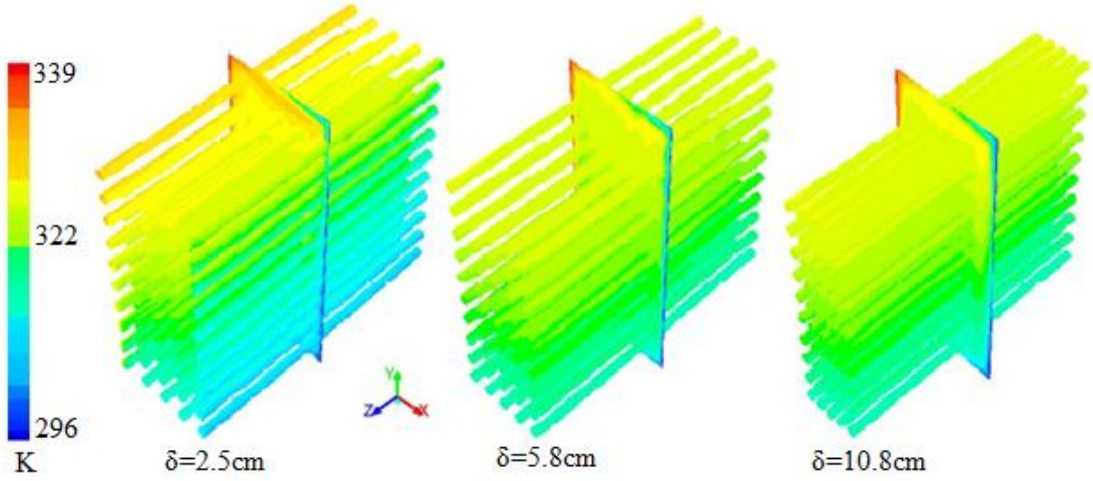

(6-4b)

Figure 6-4: Temperature contours on the (a) symmetry plane of the enclosure (b) cylinders and symmetry plane of the enclosure

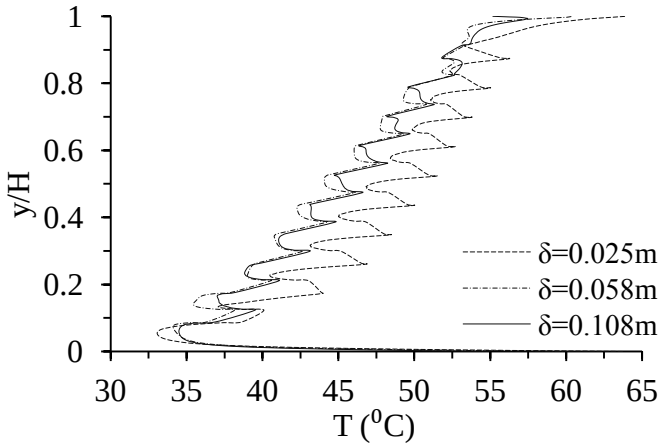

(6-5a)

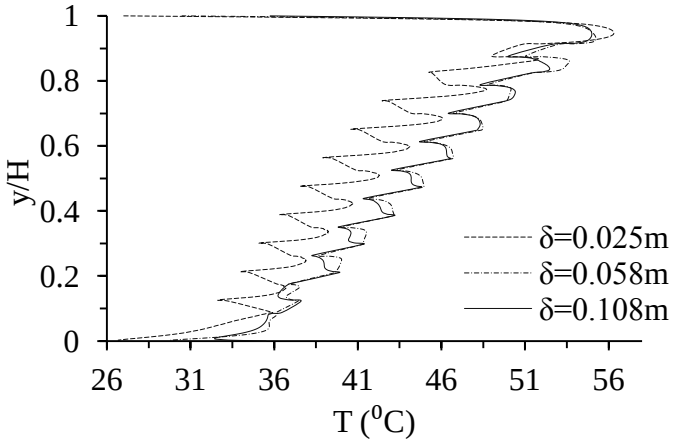

(6-5b)

Figure 6-5: Relative comparison of temperature profiles at (a) 0.025, 0.058 and 0.108m from hot wall, (b) 0.025, 0.058 and 0.108m from cold wall

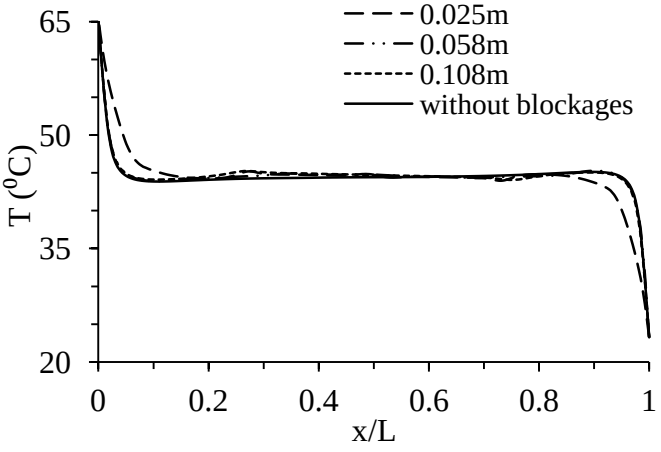

(6-6a)

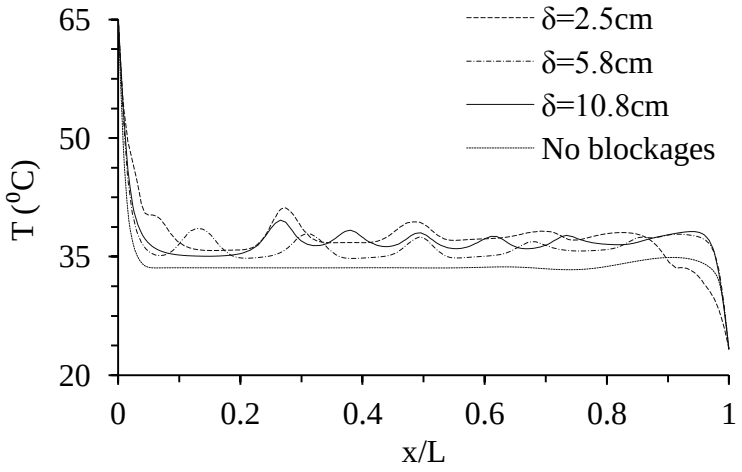

(6-6b)

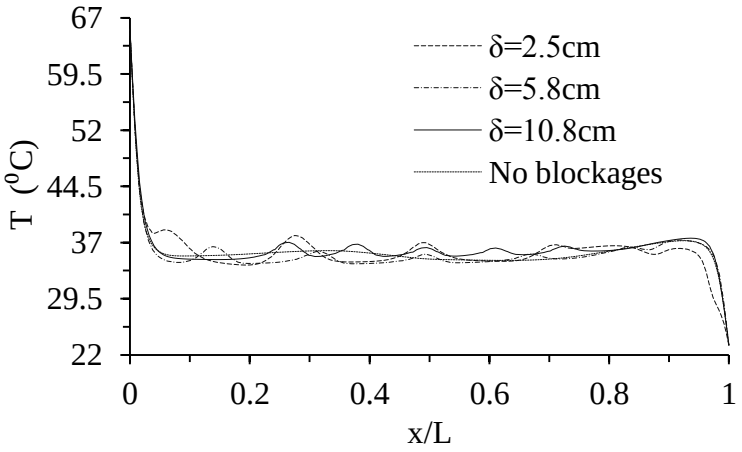

(6-6c)

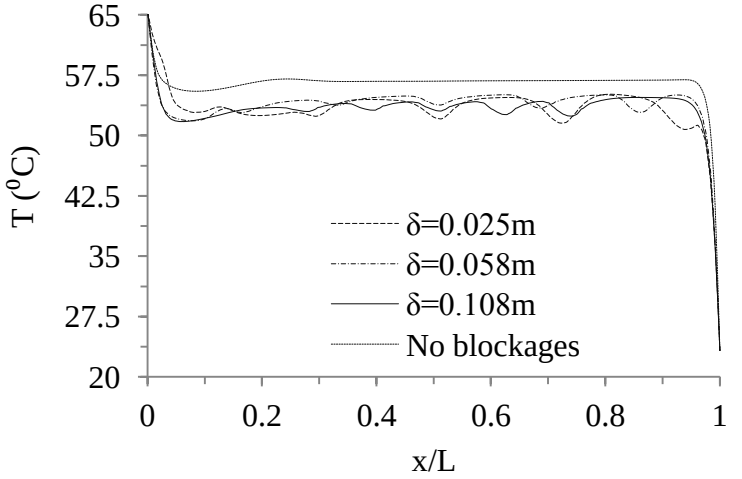

(6-6d)

Figure 6-6: Relative comparison of temperature profiles at (a) mid-height (b) 119.4mm from bottom wall (c) 85.65mm from bottom wall (d) 85.65mm from top wall

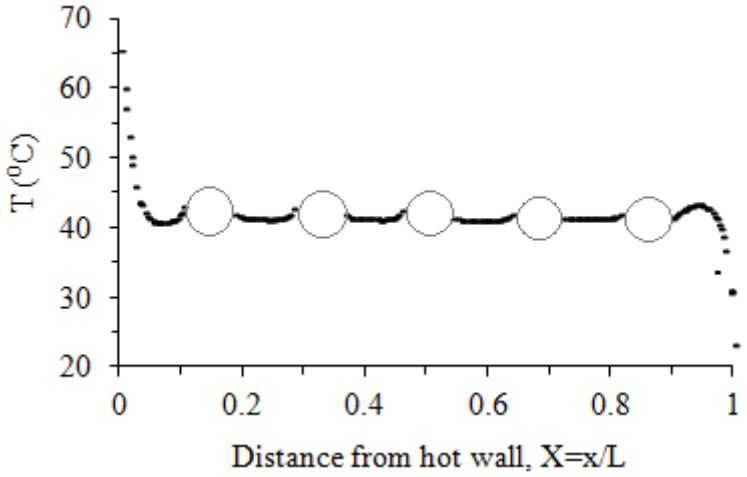

Figure 6-7: Air and cylinder temperature profiles at 0.4425m from bottom wall

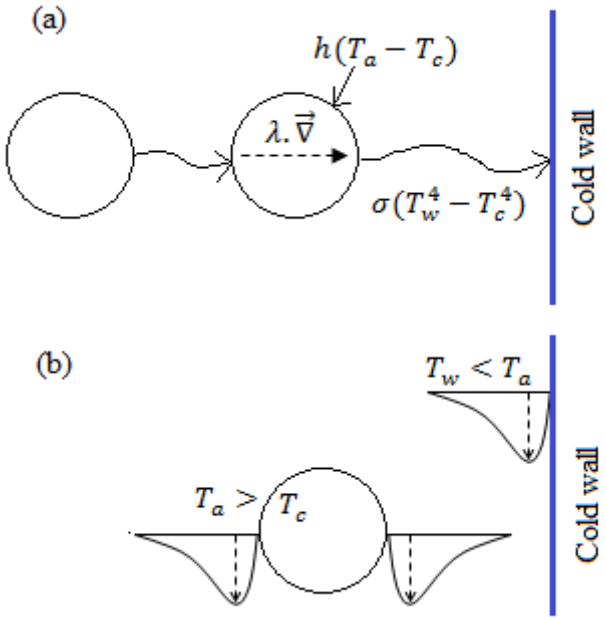

Figure 6-8: Temperature profile of different heat transfer modes near the cold wall; (a) conduction in cylinder, convection between air/cylinder surfaces, radiation between cylinder/cold walls and between two cylinders. (b) Velocity profile near cold and cylinder walls.

As shown in Fig. 6-4b, at the same height, the cylinder temperatures also increase slightly from the cold wall to the hot wall. It can be observed from the numerical results in Fig.6-7, that near the cold wall, the average cylinder temperature is slightly lower than the surrounding air temperature. This difference is due to radiation between cold wall and cylinder surface. The mechanism for this transfer is shown in Figs.6-8a-b. At steady state and without radiation, it is expected that the cylinder temperature should be the same as the surrounding air. There is also a conductive heat flux inside the cylinder (from the hot wall to the cold wall position) and radiative flux

between the cylinders. This explains the small temperature difference between the second column of cylinder and the surrounding air. In addition to the primary natural convection flow near the wall, a secondary natural convection flow around the cylinder exists due to the temperature difference between the cylinder and the surrounding air.

6.3.2 **Influence of blockage proximity on turbulence quantities**

The results presented in this section shows that, Reynolds stresses are generally limited downstream of the boundary layers on the hot and cold walls indicating the development of turbulence in the flow. Turbulence is more intense near the active walls than anywhere else as shown in Fig.6-9. The distribution of the turbulence changes significantly with cylinder proximity, δ, from the active walls. At mid-height of the enclosure, the turbulent viscosity ratio (ratio of turbulent eddy viscosity to the molecular viscosity), the turbulent stresses and kinetic energy are plotted in Fig.6-10a-d. The plots highlight that turbulence is greatly suppressed when the cylinders are closer to the vertical walls and the fact that the core region is an essentially stagnation flow.

It is also observed that the Reynolds stress, turbulent kinetic energy and the turbulent viscosity ratio profiles at mid-height are all symmetric. At 120mm from the active walls the turbulence quantities values are near zero. Their peaks are all located outside the velocity peak (Fig.6-3c) which is about 8mm. It also follows that vertical velocity peak values increase monotonically with increasing cylinders distance from the active walls as shown. In addition to this, Fig.6-11 shows the shear stress along the hot wall as the spiky values are in line with δ=25mm proximity.

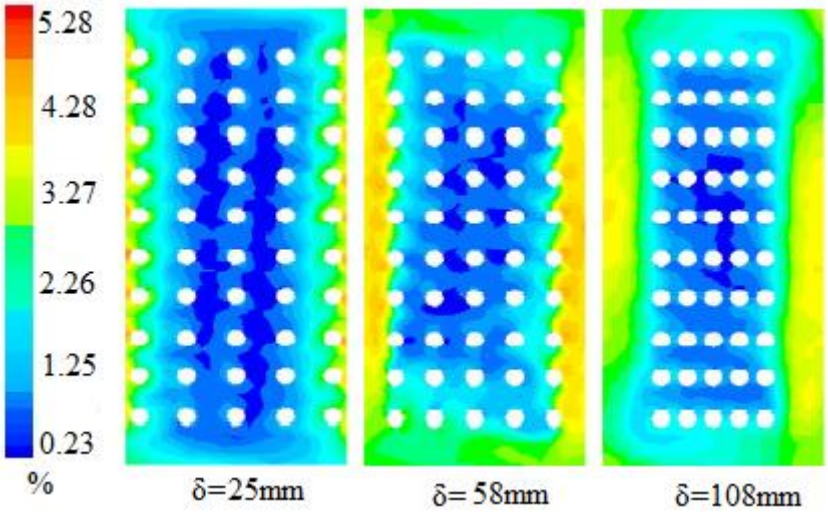

(6-9a)

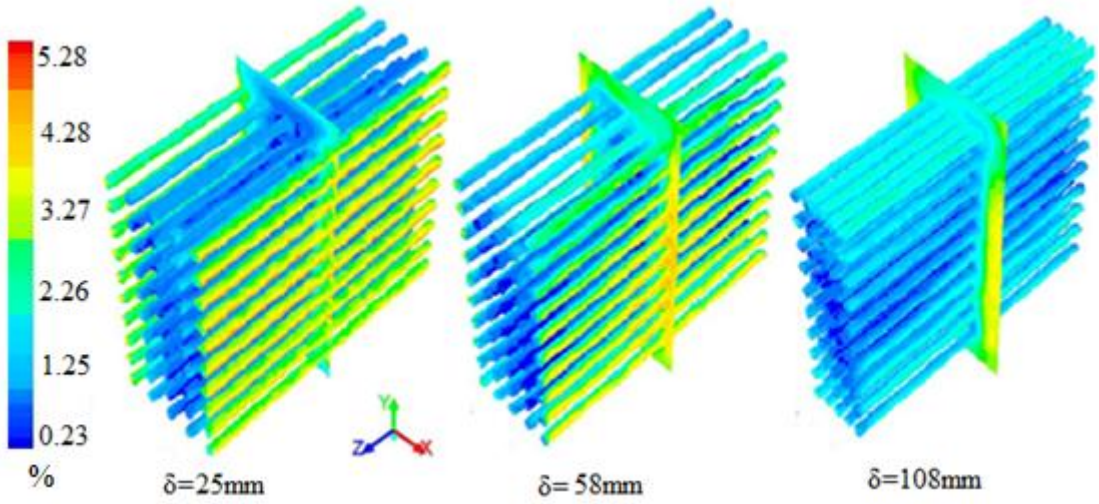

(6-9b)

Figure 6-9: Turbulent intensity field on the (a) symmetry plane of the enclosure (b) cylinders and symmetry plane of the enclosure

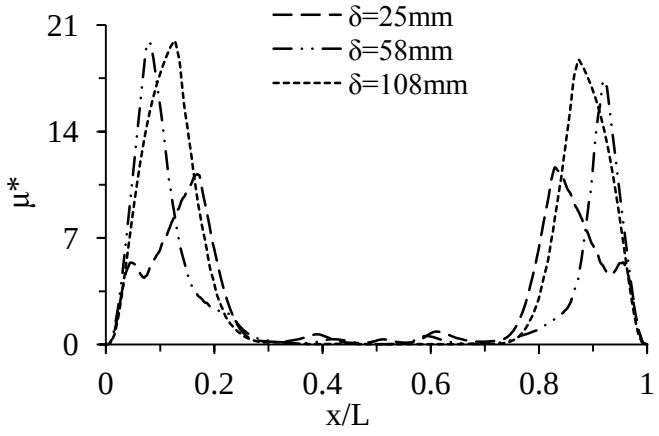

(6-10a)

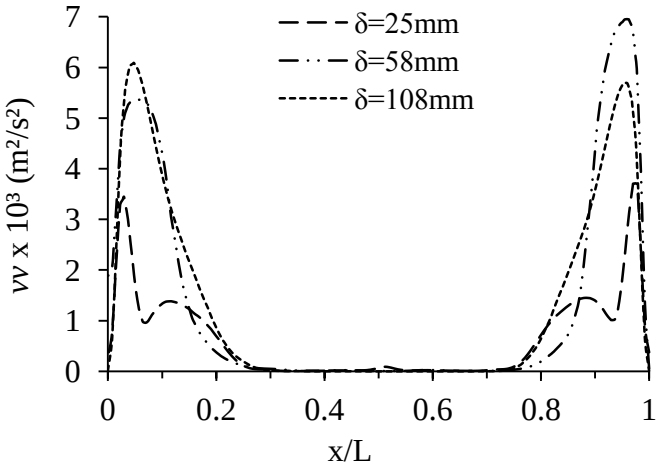

(6-10b)

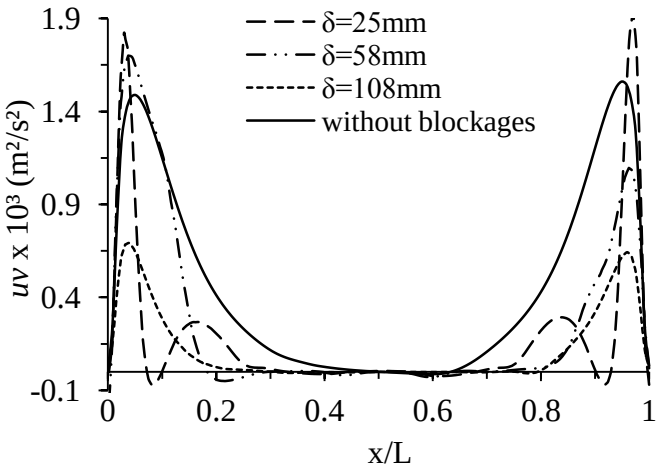

(6-10c)

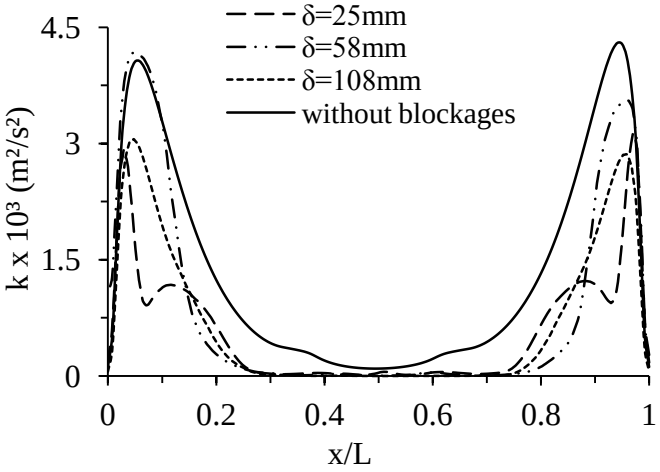

(6-10d)

Figure 6-10: Turbulence quantities profiles at mid-height (a) μ* turbulent viscosity ratio (b) *vv* Reynolds stress (c) *uv* Reynolds stress (d) Turbulent kinetic energy

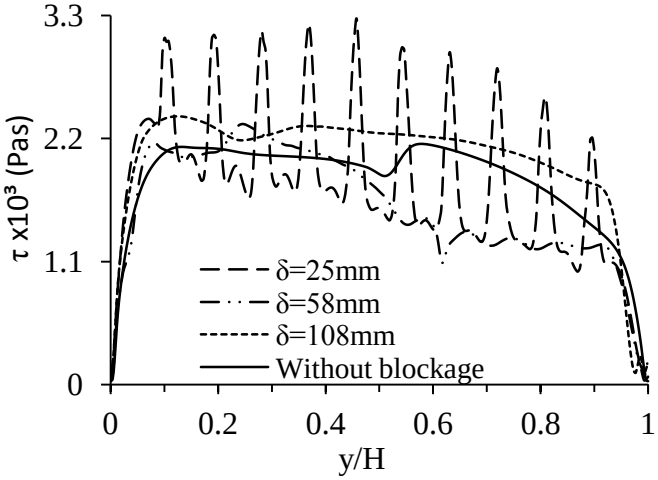

Figure 6-11 Wall shear stress near hot wall

6.3.3 **Influence of blockage proximity on wall heat transfer**

Further exploratory numerical investigation was carried out to quantify the local and average heat transfer on the cavity walls. The average and local heat transfer data were compared in terms of an average Nusselt number and local Nusselt number computed at each wall. The total Nusselt number which is a combination of the heat transfer due to convection and radiation were separately calculated by taking integral average of the fluxes using FLUENT post-processing tools. Similarly the local Nusselt numbers were obtained using the local heat transfer flux at each node. Table 6-4, shows the average Nusselt number for various cylinder proximity and Figs.6-12a-b show the local variations.

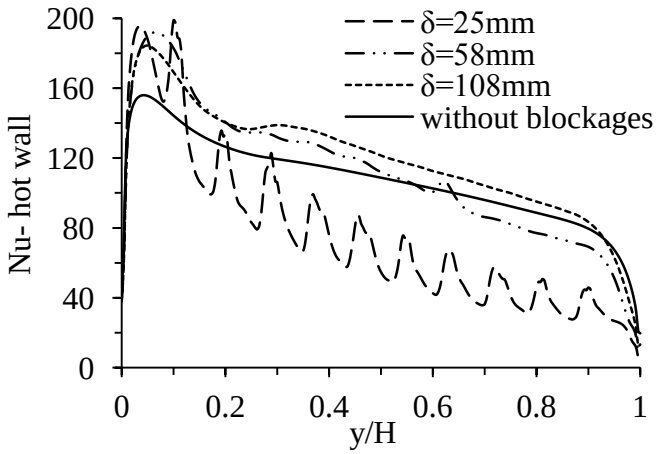

(6-12a)

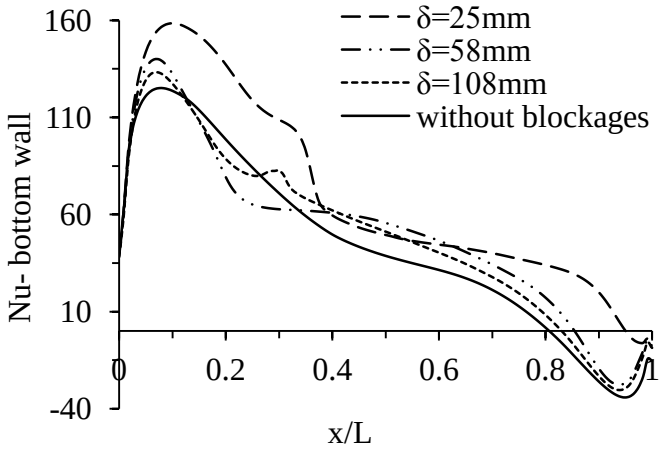

(6-12b)

Figure 6-12: Wall local Nusselt number (a) hot (b) cold (c) bottom (d) top

Table 6-5 shows that the total heat transfer is significantly low for the δ=25mm value. For other values, the average Nusselt number demonstrates a small but monotonic increase of the heat transfer. The local variations of the Nusselt number along the hot wall display the proximity effect very clearly. It also shows that with the cylinder moved further away from the vertical walls, the Nusselt numbers tend to smooth out. The fact that δ=25mm shows markedly small value of heat transfer may be partly related to the fact that turbulence is suppressed due to blockages of the upward and downward flow of the fluids along the hot and cold walls respectively.

Table 6-4: Total Nusselt number for all walls

Surface	δ=25mm	δ=5.8cm	δ=10.8cm	No blockages
Hot wall	76.01	111.23	119.05	107.28
Cold wall	79.15	114.31	122.10	109.38
Top wall	61.74	43.53	42.14	37.88
Bottom wall	69.94	51.21	49.95	44.31

Table 6-5: Average wall radiative Nusselt number

Surface	δ=2.5cm	δ=5.8cm	δ=10.8cm	No blockages
Hot wall	7.67	9.30	9.33	9.55
Cold wall	6.66	8.17	8.17	8.99
Top wall	1.89	2.01	1.52	-0.13
Bottom wall	2.48	2.68	2.22	0.05

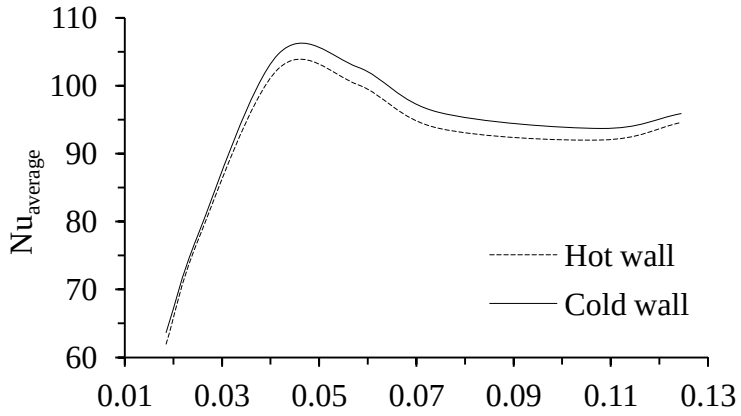

(6-13a)

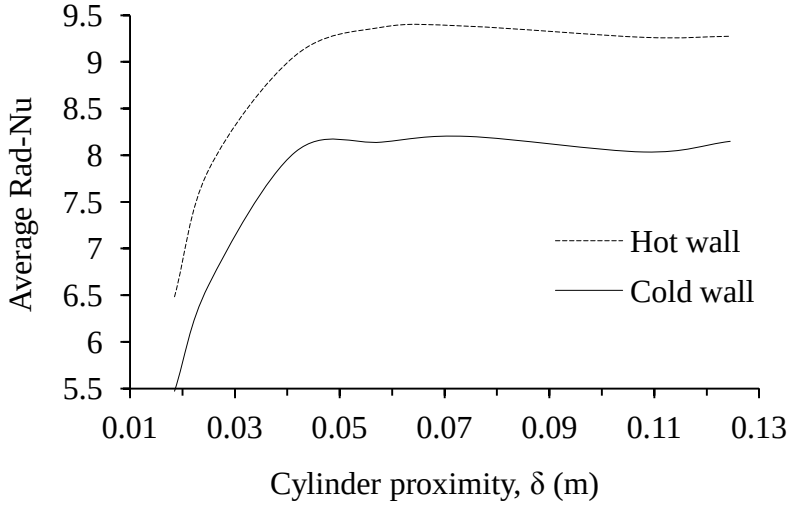

(6-13b)

Figure 6-13: Variation of heat transfer with δ for hot and cold walls (a) average Nu (b) radiative Nu

For the cavity without blockages there seems to be limited flow in the core of a rectangular cavity during natural convection processes but heat conduction takes place within this region, therefore, it does not contribute to the steady state wall-to-wall convection heat transfer. But with the inclusion of the cylindrical objects, it can be observed that secondary flows take place at this region and these flows increase as the cylinders become closer to one another (proximity from the vertical walls increases) leading to a further heat transfer across the confined space.

As the cylinders are closer to each other, the flow in the stagnant fluid core is influenced. The intensity of the flow at the core increases and this behaviour enhanced a larger contribution of lateral conduction from the bottom to the top wall and promoting the fluid motion, thereby, resulting in the gain of a wall-to-wall convection heat gain. The net effect is thus increases in the wall heat transfer as the gaps between the cylinders are smaller. The variation of average heat transfer (Nu) as a function of the cylinder proximity is summarized in Table 6-4 and 6-5 and plotted in Figs.6-13a-b. The curve in Fig.6-13a shows a clear maximum value at a certain δ. In this study, this value corresponds to $\delta_{optimum}$ (= 415mm).

6.3.4 **Validation of experimental data**

The experimental data for the 10x5 blockage arrangement were validated against the numerical results generated in this section. Typical comparisons for various cases studied are shown in Figs.6-14 to 6-16. Agreement with the experiment is generally very good including variation between the top and bottom surface of cylinder. A symmetrical result is possible when the dimensionless temperature is 0.5 at the centre of the cavity. However, our experiments gave a slightly approximate value of 0.51. Figs.6-14 to 6-15 show the core area, the fluid is stratified along the mid-width region and for the most part, the temperature is almost in linear distribution. Following Ziai [71], the stratification parameter mean value is 0.528. Henkes and Hoogendoorn [230] summarised contribution works to the Eurotherm Seminar - 22 to evaluate the range of stratification parameter. The stratification parameter obtained was 0.511–0.572 and the average value was 0.539. Our results lie between these ranges. The temperature distribution along the mid-width is compared in Figs.6-16a-d. Our numerical results are in agreement with the experimental data. The improvement in the accuracy of our numerical results when compared with experimental data is due to the near ideal boundary condition (experimental) that was used in the numerical modelling.

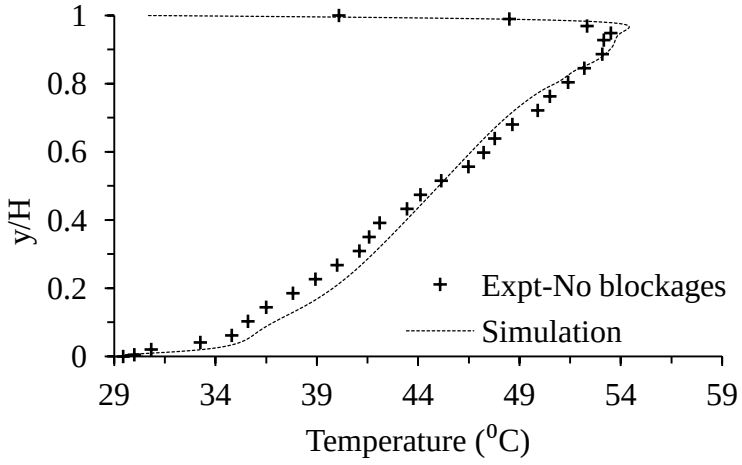

(6-14a)

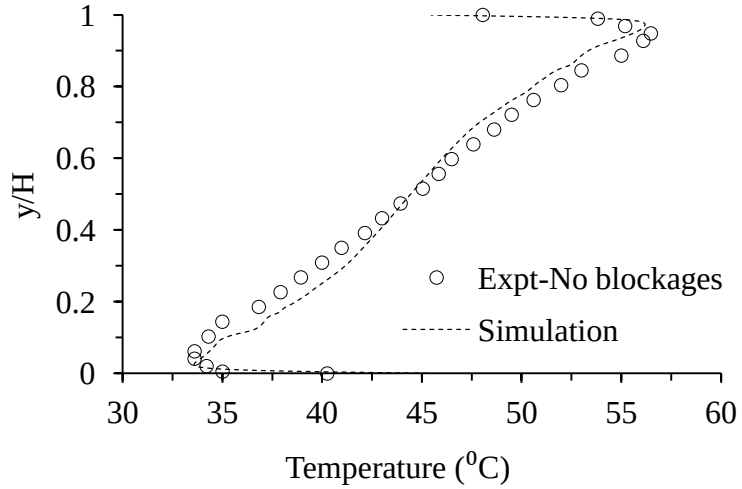

(6-14b)

Figure 6-14: Comparison of temperature profile (a) near cold wall (60mm); (b) at mid-width for cavity without blockages

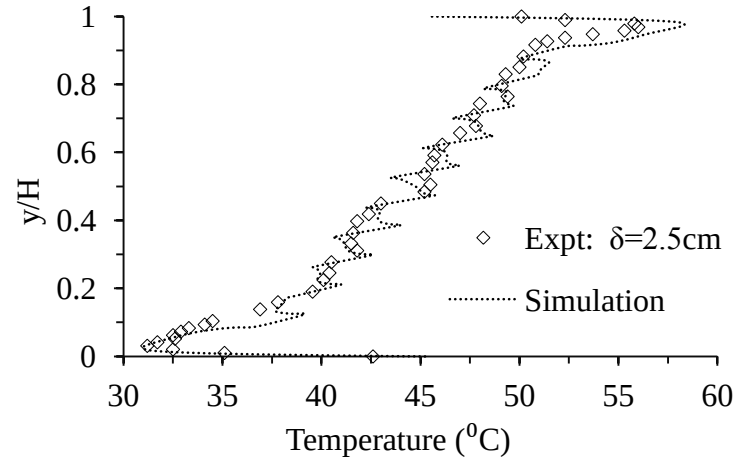

(6-15a)

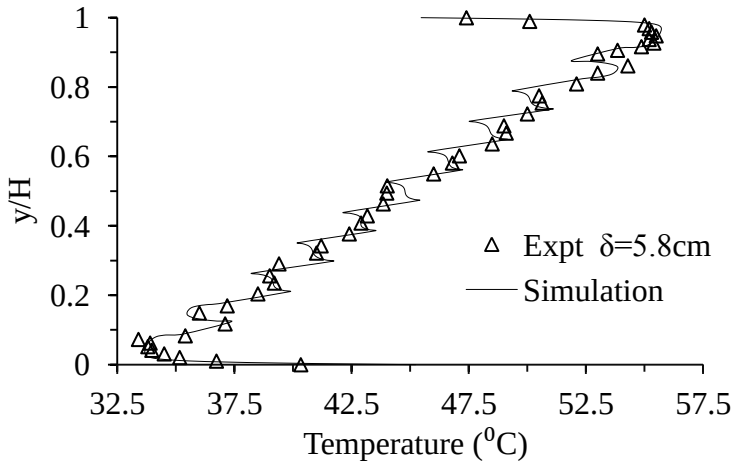

(6-15b)

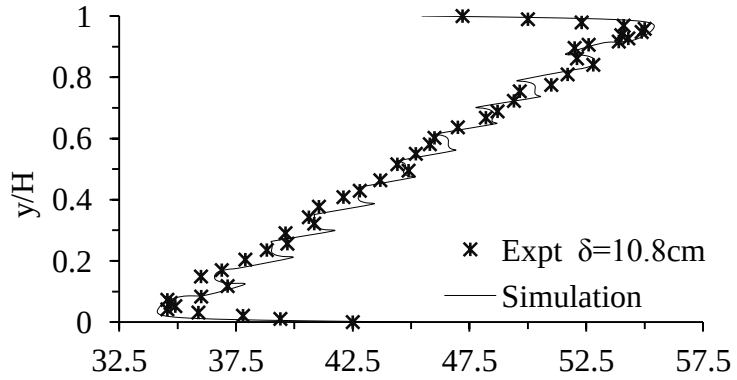

(6-15c)

Figure 6-15: Temperature profile comparison at mid-width (a) δ = 25mm (b) δ = 58mm (c) δ = 10.8cm from the vertical walls – blockages proximity

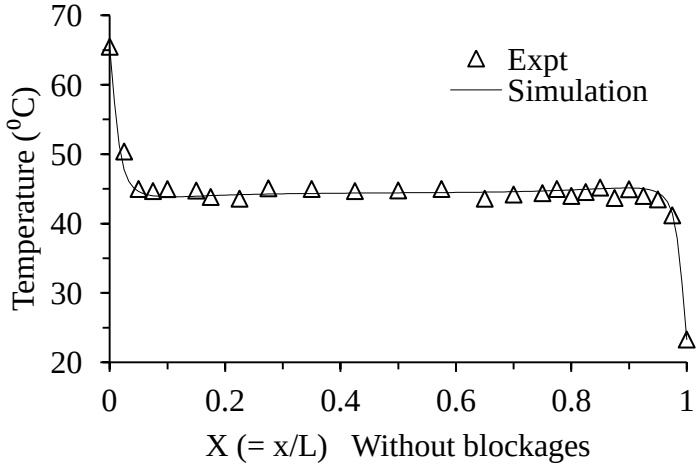

(6-17a)

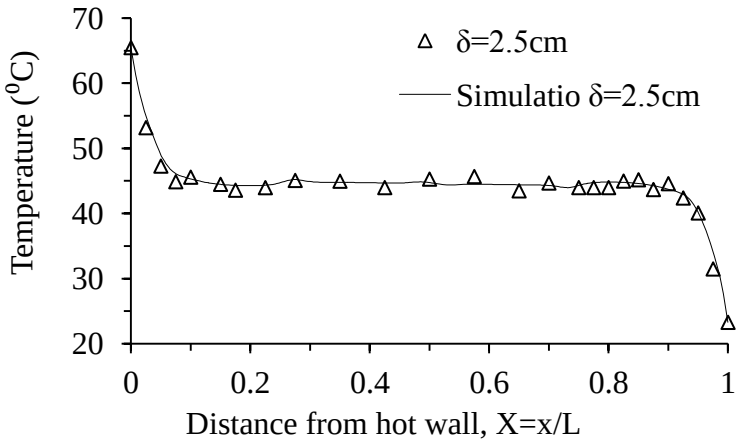

(6-17b)

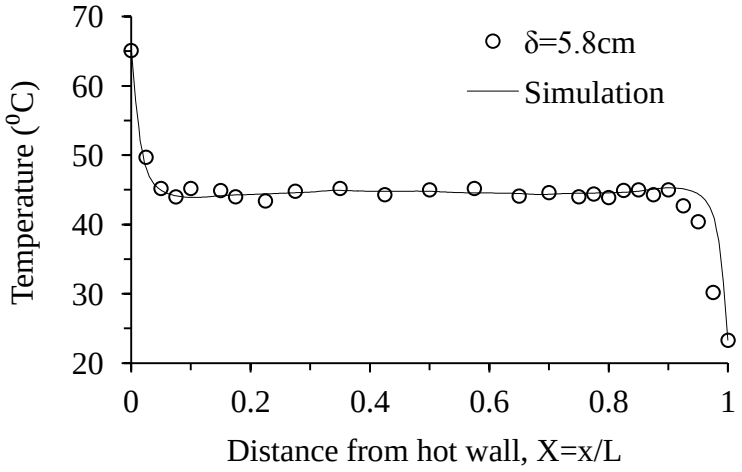

(6-17c)

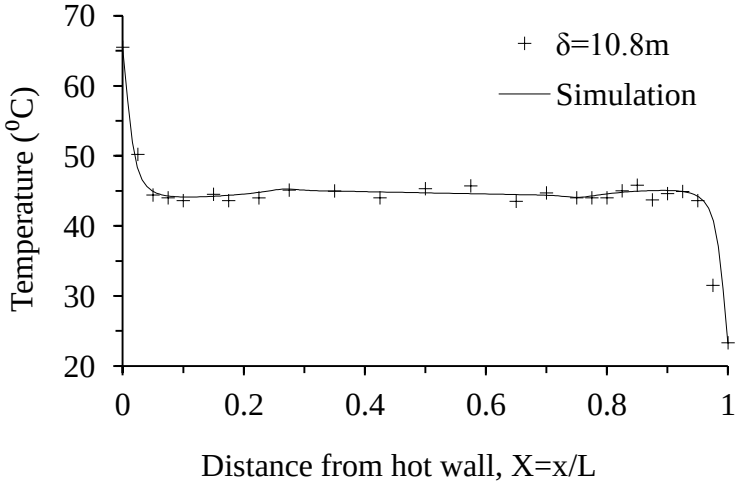

(6-17d)

Figure 6-16: Temperature profile comparison at mid-height with and without blockage, with and without blockages – blockages proximity

6.4 **Blockage proximity from horizontal walls for 10x5 arrangement**

In this section, numerical simulation was conducted to quantify the influence of the blockage proximity from the horizontal walls, δ_v in Fig.6-17, on the wall heat transfer. The average wall Nusselt numbers and wall radiative Nusselt numbers are presented in Table 6-6 and 6-7. Their local counterparts are presented in Figs.6-18a-c. It is observed that very close to the top and bottom walls the heat transfer profile shows a wavy pattern which is due to the blockages of the near wall flow. At δ_v=25mm the thermal boundary layer is compressed thereby blocking most of the flow and hence the heat transfer along the horizontal walls are also reduced.

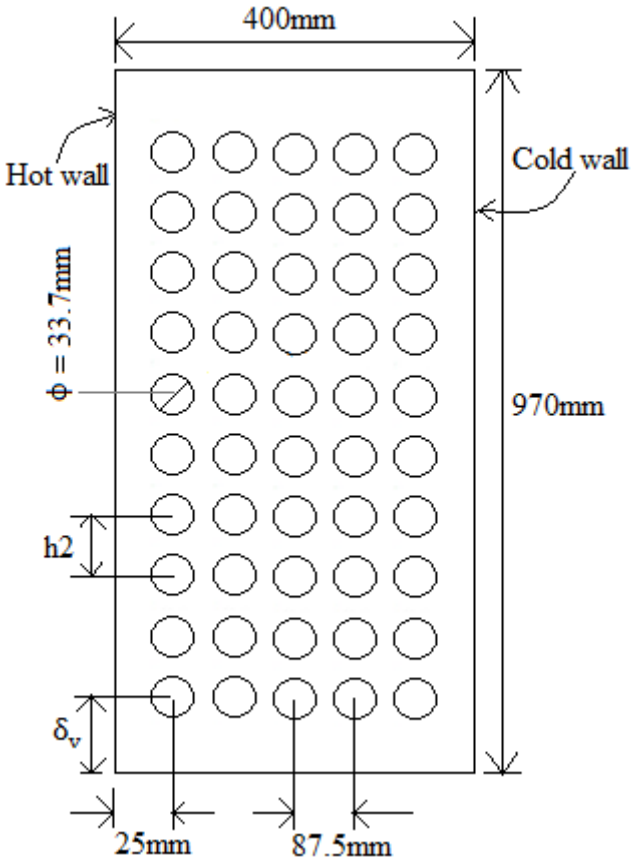

Figure 6-17: Schematic of the geometrical configuration

Table 6-6: Average Nusselt number

δ_v(mm)	Bottom	Cold	Hot	Top
25	32.79	75.48	73.60	29.04
50	34.52	76.76	76.62	41.90
103	34.85	77.40	76.75	30.88

Table 6-7: Average radiative Nusselt number

δ_v(mm)	Bottom	Cold	Hot	Top
0.025	1.81	6.67	7.81	1.53
0.050	1.91	6.11	8.04	12.47
0.103	1.36	6.67	7.87	0.96

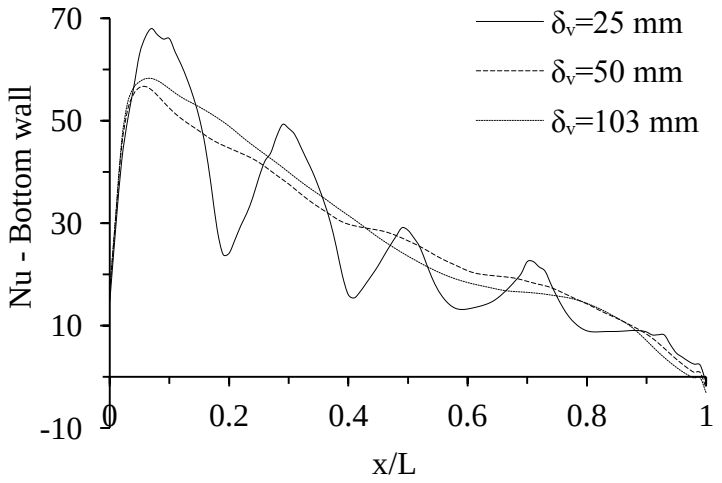

(6-19a)

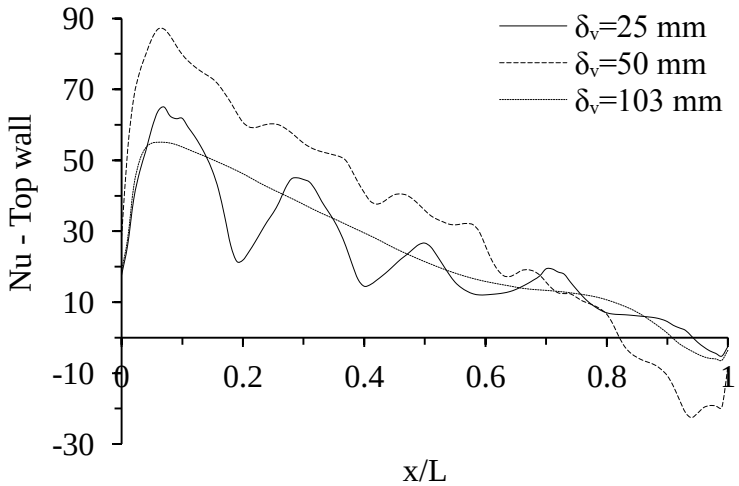

(6-19b)

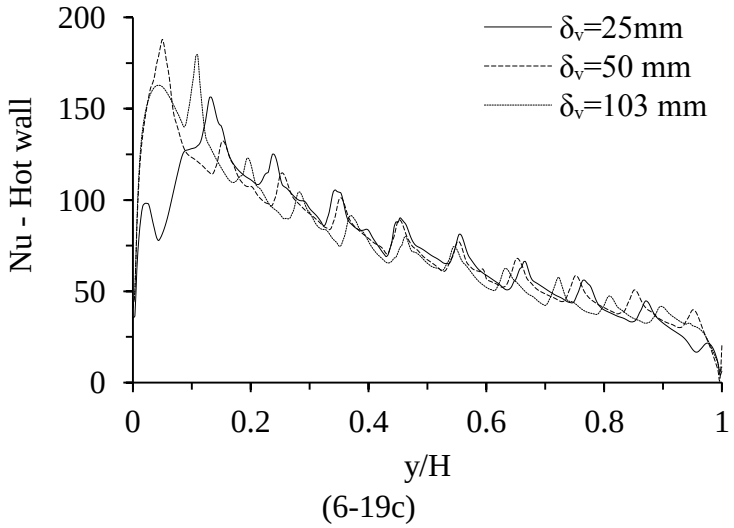

(6-19c)

Figure 6-18: Walls local Nusselt number (a) bottom (b) top (c) hot

6.5 **Effect of blockage for 10x3 arrangement**

The schematic of the arrangements of blockages within the enclosure is shown in Fig.6-19. The blockages are in 10 rows and 3 columns. The first configuration is the arrangement of these blockages near the hot wall: is named as Case-1. The arrangement of the blockages near the cold wall is represented as Case-2, while the arrangement of the blockages at the middle of the enclosure is Case-3.

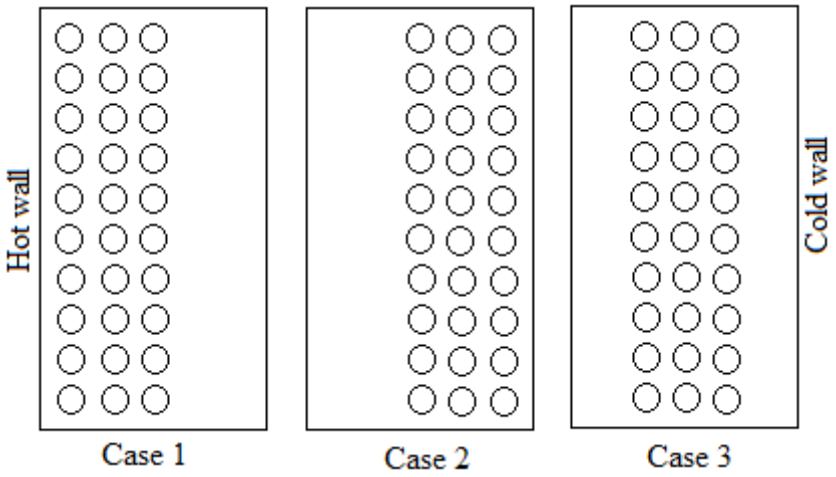

Figure 6-19: Schematic of 10x3 arrangement of blockages

Figs.6-20a-b shows the temperature and turbulent intensity of the flow field. Secondary natural convection flow can be observed at regions near the blockages. As discussed earlier in section 5-10, this effect is due to the multiple radiations at the blockages surface.

It was observed from our experiment study on 10x3 arrangements of blockages that the average temperature was found to be maximum in Case-3 arrangement and a minimum in Case-1, this behaviour was also observed in temperature profiles at the mid-height and mid-width shown in Figs.6-21a-b. There is a relative influence on walls heat transfer within the cavity as shown in Figs.6-23. The average values are shown in Table 6-8 and 6-9 for the total and radiative components respectively. In Fig.6-21a, there is a much temperature variation in the region near the cylinders surface. Blockages arrangement near the hot wall (Case-1) significantly damped turbulence as well as the horizontal convection which caused the temperature to vary. This influence on turbulence is shown in Figs.6-20b and 6-22.

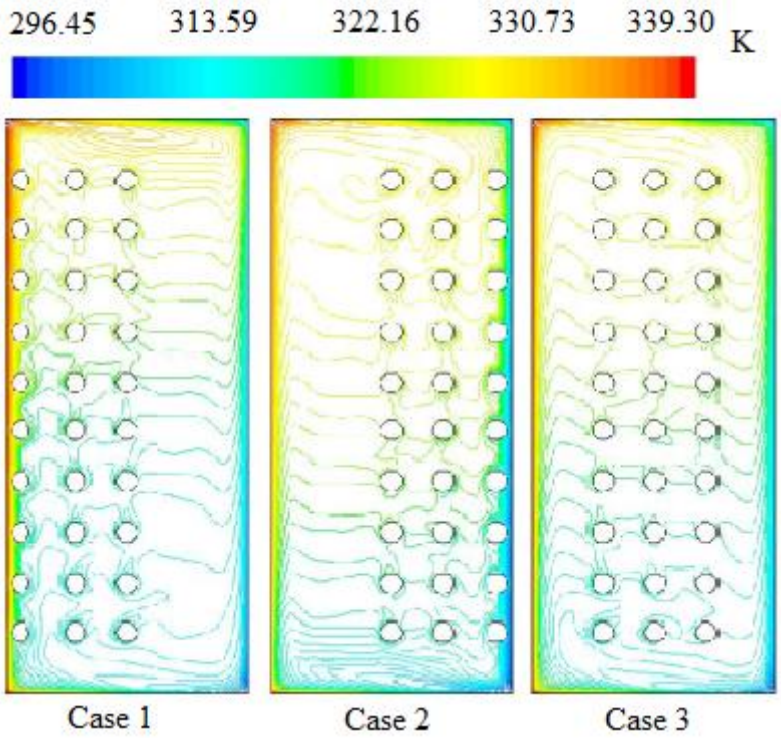

(6-21a)

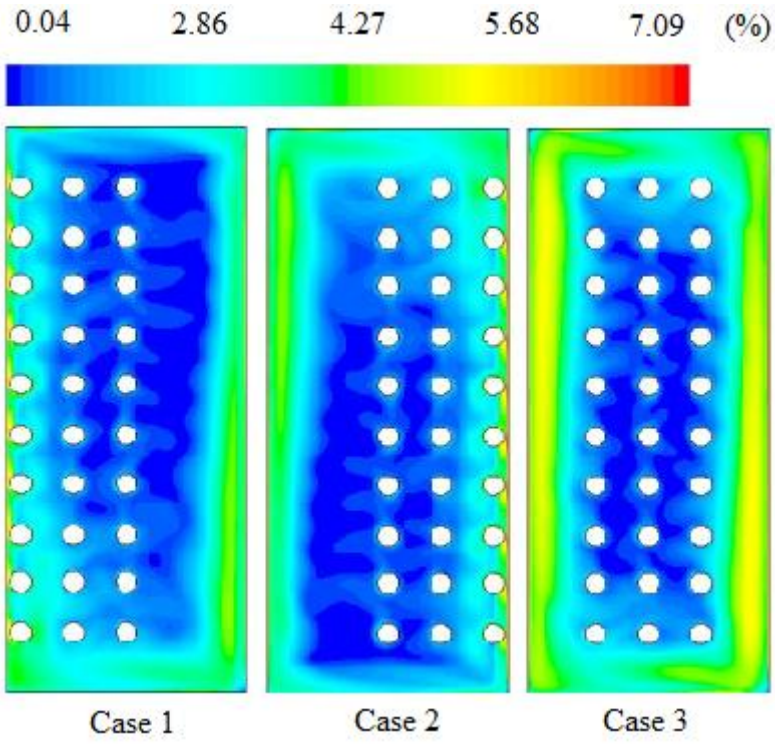

(6-21b)

Figure 6-20: Relative comparison of the flow filed at mid-plane (a) temperature (b) turbulent intensity

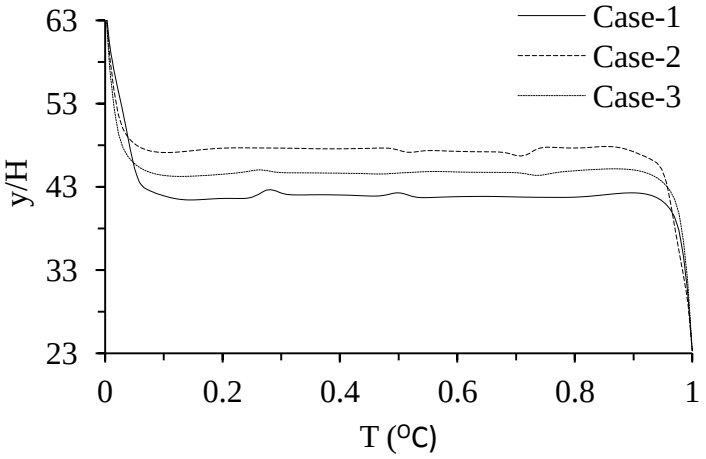

(6-21a)

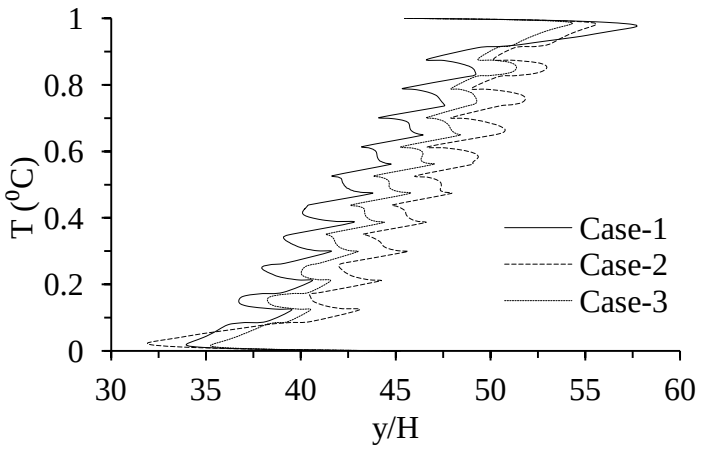

(6-21b)

Figure 6-21: Temperature profile at (a) mid-height (b) mid-width

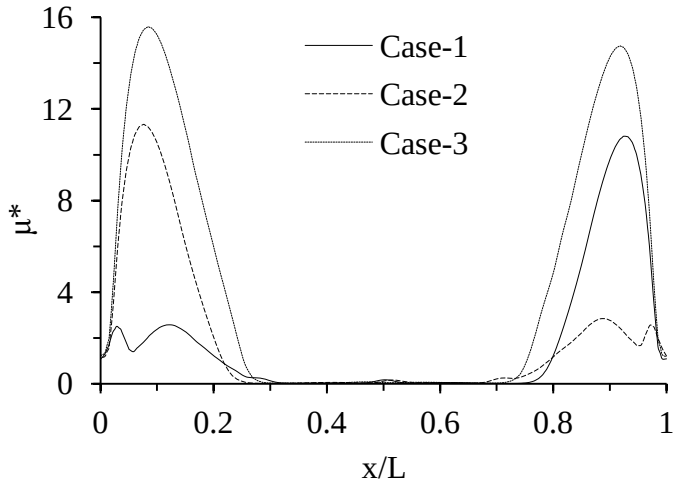

Figure 6-22: Turbulent viscosity ratio at mid-height

Table 6-8: Average walls Nusselt number

Surfaces	Bottom	Cold	Hot	Top
Case-1	32.89	88.14	82.19	29.52
Case-2	33.59	84.36	86.96	28.95
Case-3	30.21	100.24	98.72	26.09

Table 6-9: Average walls radiative Nusselt number

Surfaces	Bottom	Cold	Hot	Top
Case-1	1.17	7.71	8.51	0.38
Case-2	0.79	7.32	8.98	0.74
Case-3	1.12	8.01	9.26	0.70

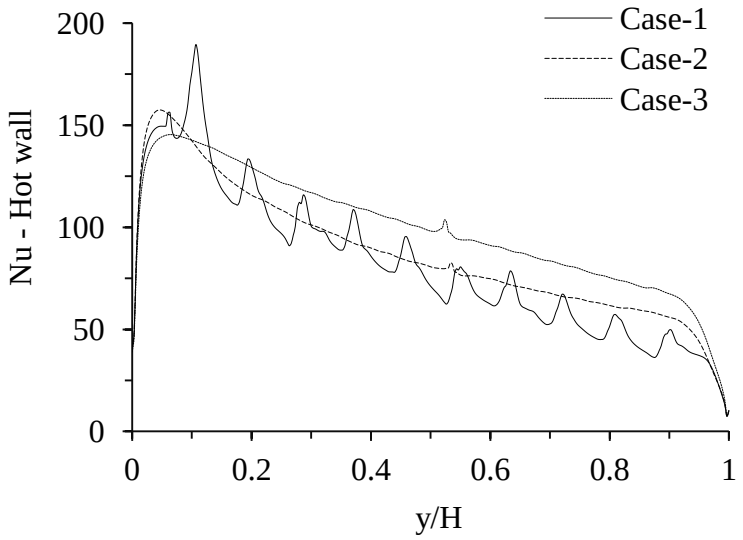

(6-23a)

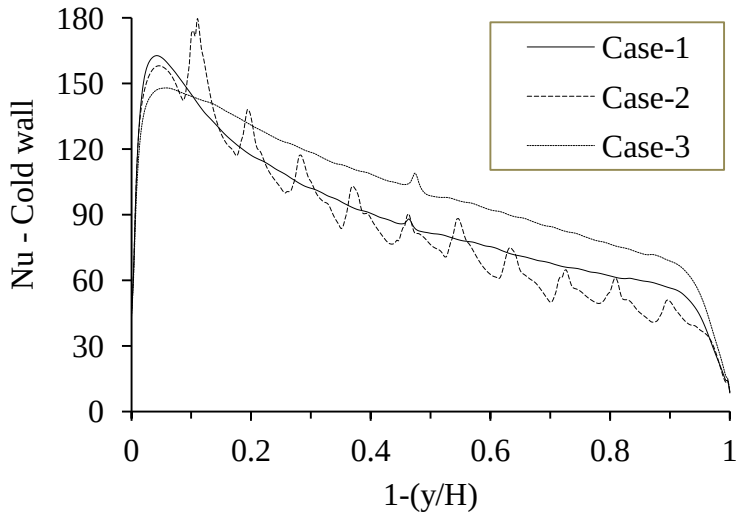

(6-23b)

Figure 6-23: Local Nusselt number (a) hot wall (b) cold wall

6.5.1 **Validation of experimental data**

Numerical and experimental temperature data measured at mid-height and mid-width is compared in the plots shown in Figs. 6-24 and 6-25 respectively. There are general agreements between the results.

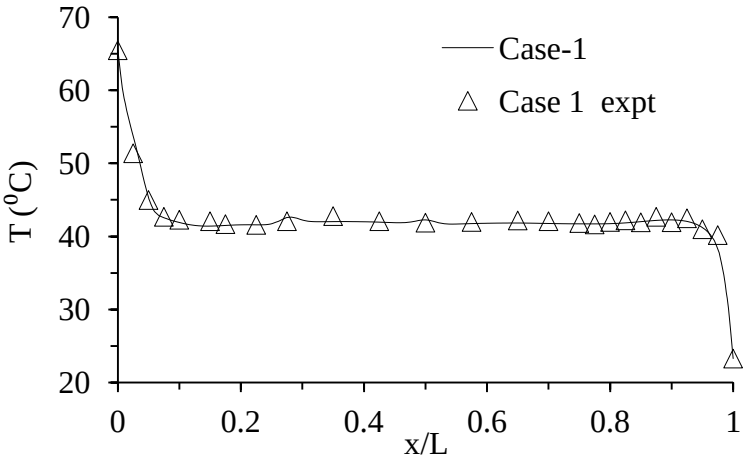

(6-24a)

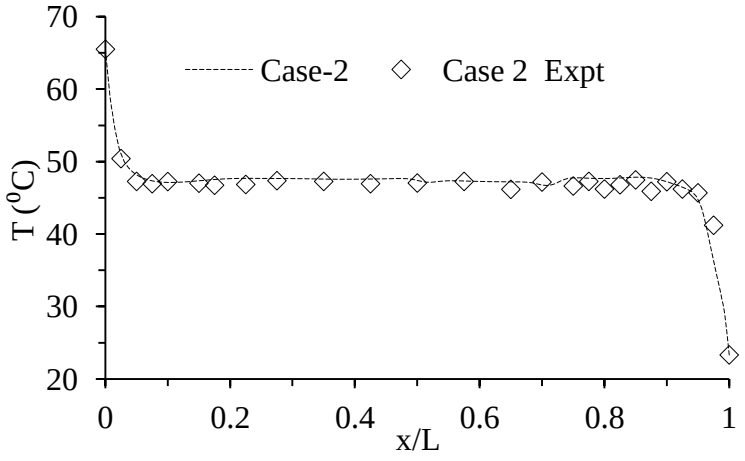

(6-24b)

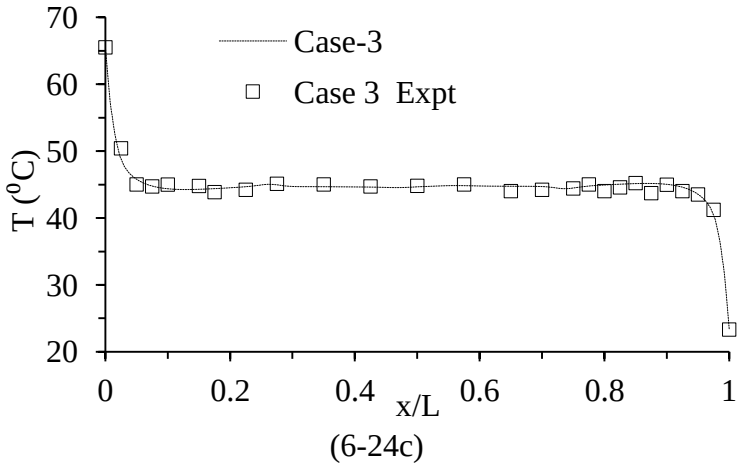

(6-24c)

Figure 6-24: Comparison of CFD and experimental temperature profile at mid-height for; (a) case 1 (b) case 2 (c) case 3

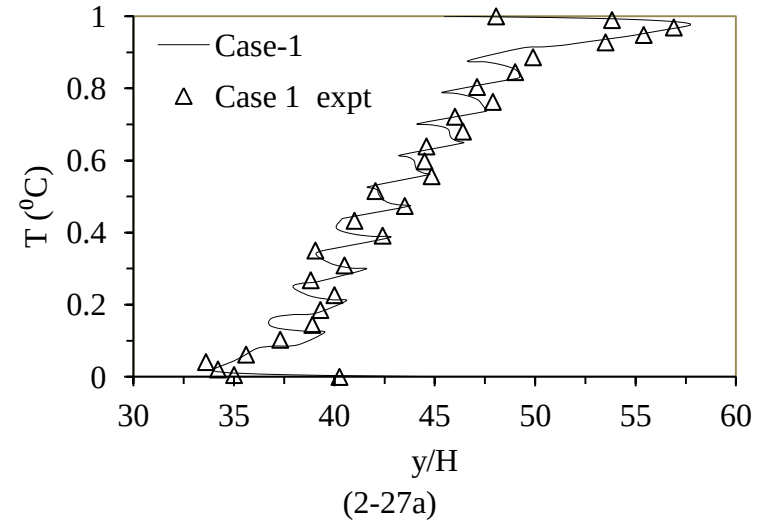

(2-27a)

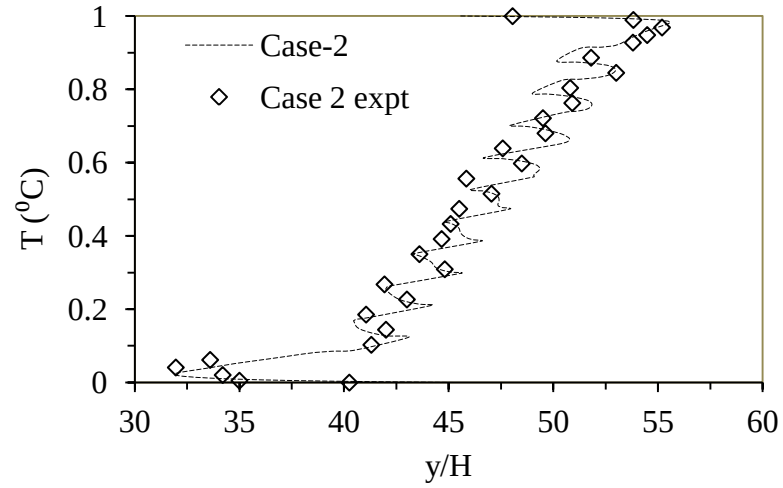

(2-27b)

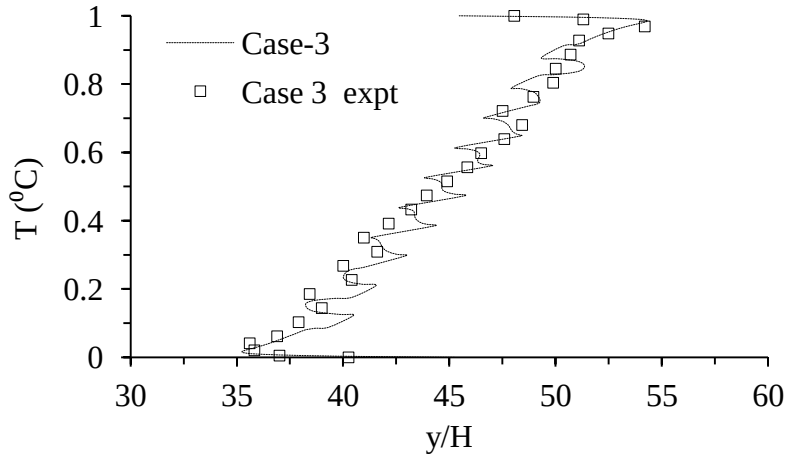

(2-27c)

Figure 6-25: Comparison of CFD and experimental temperature profile at mid-width for; (a) case 1 (b) case 2 (c) case 3

6.6 **Effect of blockage for 5x5 arrangement**

In this section, the influences of 5x5 arrangement of blockages near the top and bottom walls on the flow and heat transfer are investigated. The configuration for the fluid domain arrangement is shown in Fig.6-22. The two cases considered are NTW: (Near Top Wall) and NBW: (Near Bottom).

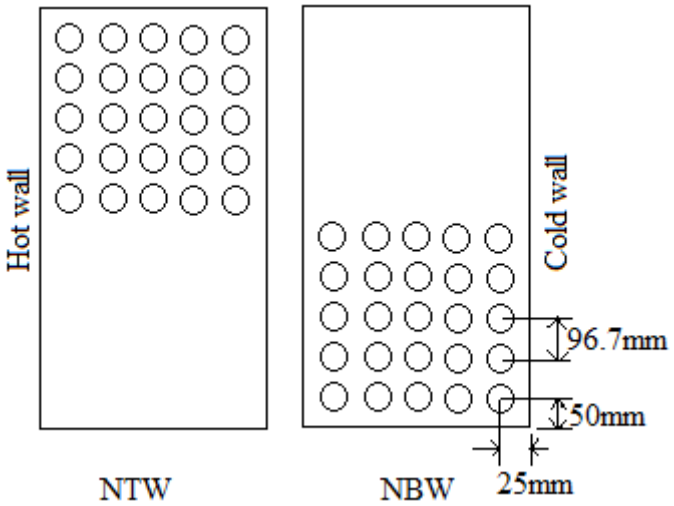

Figure 6-26: Schematic of group arrangement of blockages

The velocity and turbulent field are shown in Figs.6-27a-b respectively. Fig.6-28 shows the temperature profile at the mid-height of the cavity. It can be observed that NTW case shows a slightly higher temperature in relation to that of NBW, with an average of 2.43^0 C temperature difference between the two cases evaluated at the core of the cavity. This behaviour has also been reported in our experimental study. Influences of the 5x5 blockages arrangements on the walls average heat transfer are quantified in Table 6-10 and the local values are plotted in Figs.6-29a-c.

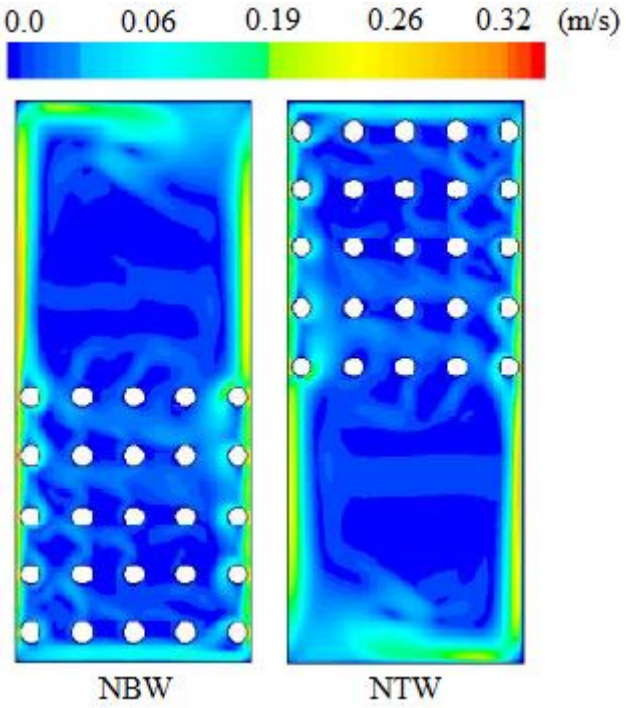

(6-27a)

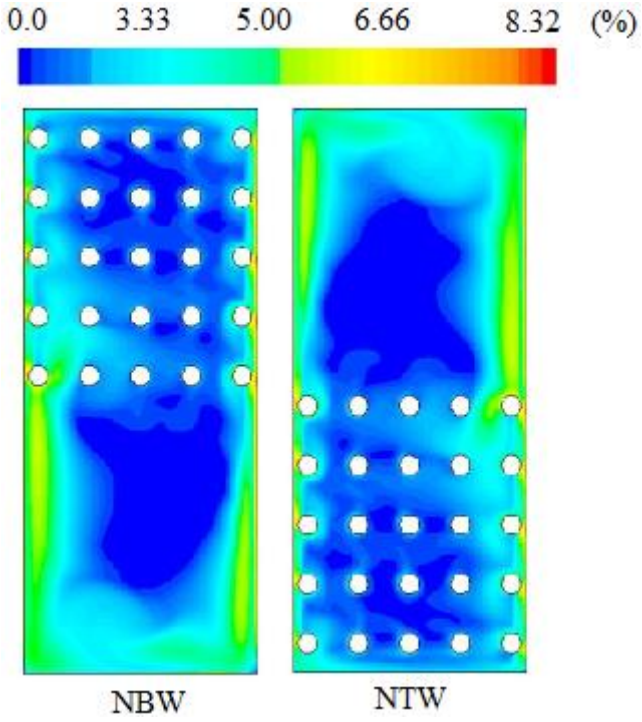

(6-27b)

Figure 6-27: Flow field comparisons; (a) velocity contours (b) turbulent intensity contours

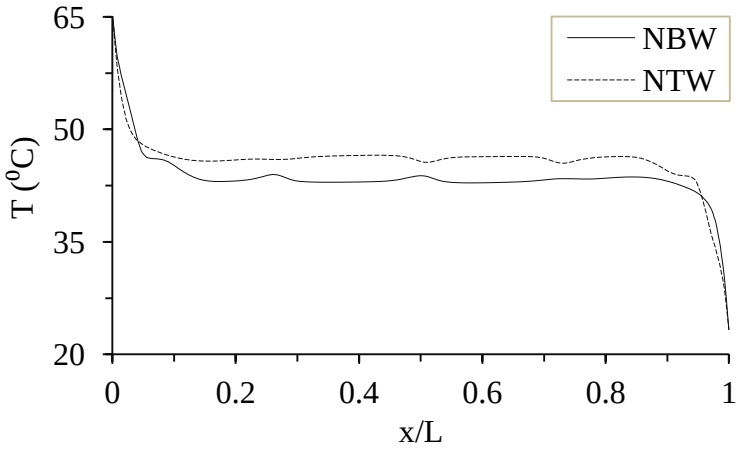

Figure 6-28: Comparison of temperature profile at mid-height

Table 6-10: Average Nusselts number comparisons for different distance from the horizontal walls

Surfaces	Bottom	Cold	Hot	Top
NBW (δ_v=30mm)	110.14	110.57	29.98	24.68
NTW (δ_v=30mm)	25.02	82.78	89.60	22.45
NBW (δ_v=50mm)	26.56	91.94	82.41	22.28
NTW (δ_v=50mm)	25.35	83.82	90.40	23.60

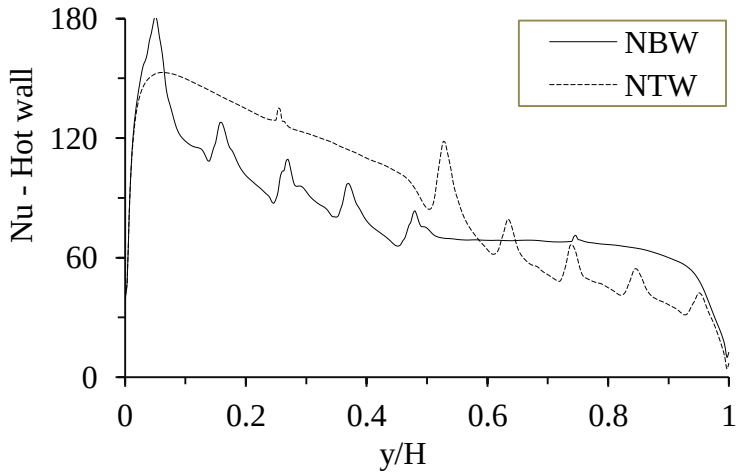

(6-32a)

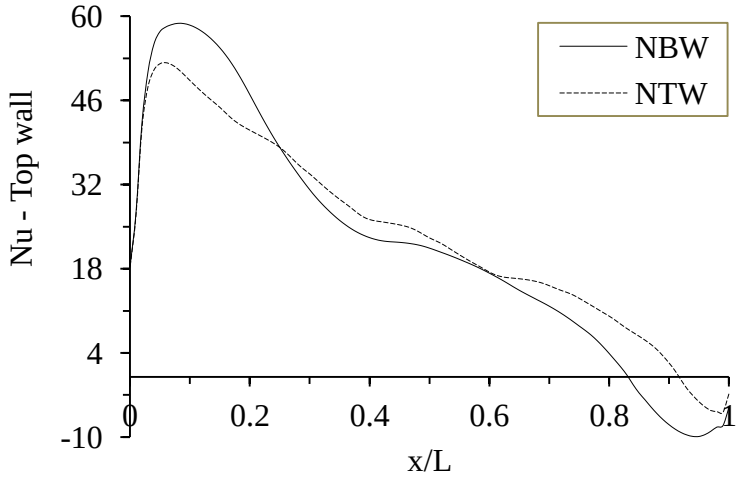

(6-32b)

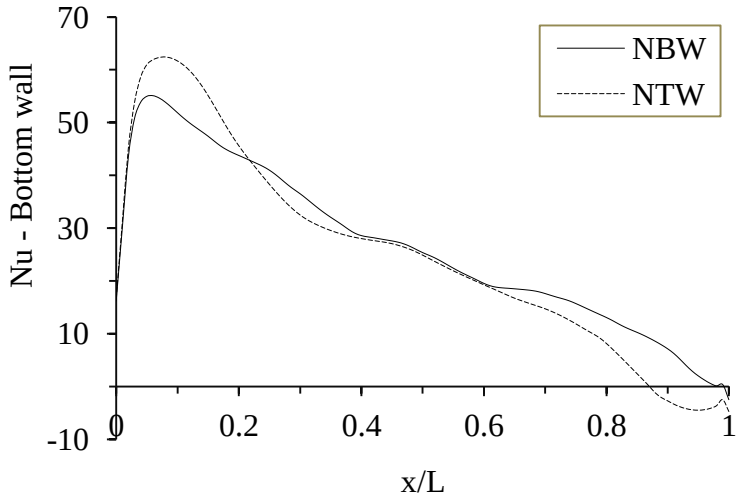

(6-32c)

Figure 6-29: Walls local Nusselt number (a) hot (b) cold (c) bottom

6.6.1 **Validation with experimental data**

The experimental temperature data is compared with numerical computation in Fig.6-30. Excellent agreement can be seen for both situations including the accurate prediction of the thermal boundary layer. These comparisons provide confidence in the predicted flow variables presented in previous section.

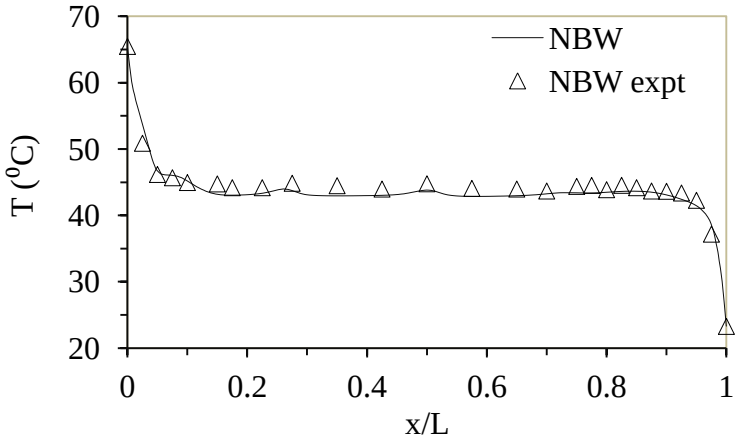

(6-33a)

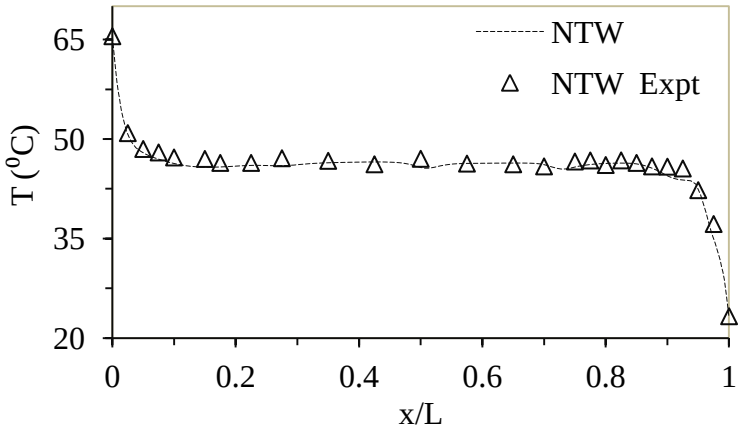

(6-33b)

Figure 6-30: CFD and experimental temperature profile at mid-height for all cases (a) NBW (b) NTW

6.7 **Conclusion**

This study was carried out in order to obtain detailed and accurate numerical results on this topic and allow a better understanding of the interactions between blockages and low turbulent natural convection flow. Some general conclusions are presented below:

a) Temperature stratification was observed in all cases, high temperature at the top and low temperature at the bottom region of the enclosure.

b) Wall proximity can be seen to affect the overall heat transfer via flow field. The effects of turbulence are greatly suppressed as the gap between the walls and the solid objects become smaller.

c) The fact that the variation of the solid object proximity from the vertical walls influences the scenario drastically is vindication that proximity of objects near vertical walls does plays a significant role in apparently low temperature applications. We believe that this may have an important implication in thermal management in built environment applications, cooling of electronic panel and other engineering applications.

d) The influence on fluid flow, heat transfer and turbulence are due to the interaction with the cylindrical objects which was identified and detailed profiles which have been obtained for critical locations and for each δ, there exist optimum average heat transfers at the wall.

e) The experimental data was validated at representative location and there is good agreement between the numerical results and experiments. Additional comparisons are provided in Appendix B, which may be useful for code validation.

Chapter 7 - INFLUENCE OF BLOCKAGES ON HEAT AND MASS TRANSFER IN AN ENCLOSED RECTANGULAR BOX

7.1 Introduction

Previous chapters have dealt with numerical and experimental study of natural convection flow and heat transfer in rectangular enclosures with and without blockage, but without the effect of moisture. This chapter aims to verify and quantify the influence of blockages on the flow, heat and mass transfer for a differentially heated rectangular enclosure partially filled with a disconnected array of blockage. The fluid zone is a mixture of air and water vapour. Different cases of blockage proximity from the active vertical walls were analysed. Different flow and heat transfer quantities were evaluated and the influence on mass transfer due to these blockages have been quantified and analysed.

7.2 Numerical model formulation

Different cases of parametric studies have been reported in this chapter, the enclosure is partially filled with arrays of disconnected cylindrical objects in rows and columns. The basic geometrical configuration considered is that of Laguerre et al., [111] shown in Fig.7-1, where the disconnected cylindrical objects are arranged in 8 rows and 5 columns, the aspect ratio of the rectangular enclosure is 2:1 (H/L). The justification for using this test rig is because it provides humidity data which was used for validation purposes in our study.

7.2.1 Flow problem

As shown in Fig.6-1, the flow problem is a two-dimensional rectangular cavity with aspect ratio of 2:1 (H/L) and contains obstacles which occupy about 15% of the total cavity volume. Laguerre et al., [111] have provided data for temperature profiles along the mid-height (y/H=0.5) and x=66 mm near the cold wall of the cavity. Vertical velocity (V_y) and relative humidity profiles measured at the mid-height and mid-width (x/L=0.5) of the cavity were also reported.

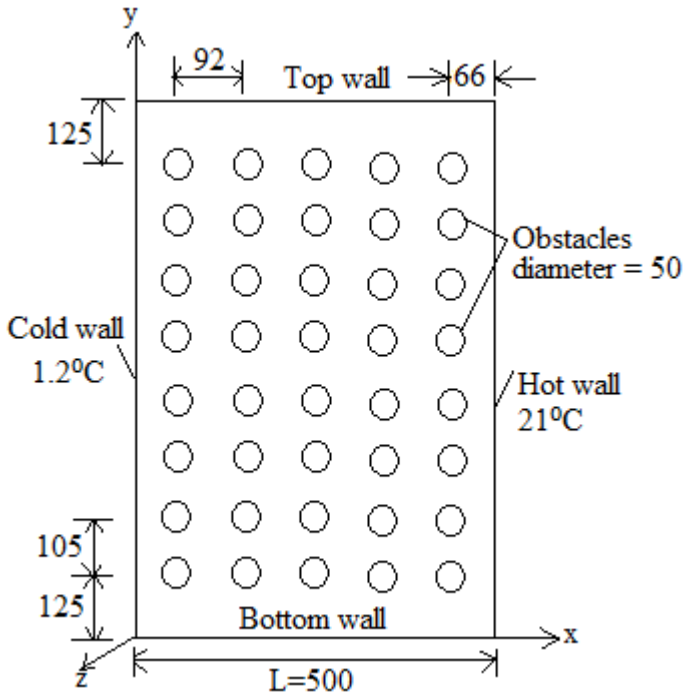

Figure 7-1 Geometry and the coordinates (dimensions are in mm)

Based on the vertical wall temperature difference of 19.8^0 C, the flow Rayleigh number was found to be 1.45 x 10^9. Numerical experiments were conducted for both humidified and un-humidified cases - the former situation was created during experiment done by Laguerre by placing a shallow pan of water (13.7^{0}C) at the bottom surface which acted as the source of water vapour mass flux. Literature suggests that the above Ra implies that the flow is more likely towards the turbulent regime than laminar and hence the flow field in this work is predicted by using Launder-Sharma low-Re k-ε model.

7.2.2 **Numerical procedure**

Calculations were carried out using the FLUENT 13.0. The methodology involves the iterative solution of the Navier-Stokes equations as have been reported in chapter 3. Moisture has been considered as a separate phase and hence another scalar transport equation for species transport has been incorporated. Similarly, we have considered the flow to be turbulent and hence suitable two-equation eddy-viscosity turbulence models have been chosen. More details on turbulence models will be given in the next section. As mentioned before, the accuracy of computations is affected by the choice

of grids, the turbulence models, discretisation schemes and convergence and had been the major concern for numerical scientists [195, 231-234].

These uncertainties that may influence the flow physics were carefully taken into account in the numerical modelling for greater accuracy. For discretisation of the convection terms, second order convection schemes have been followed. Utmost care has been taken to address the issue of grid density and grid quality. The mesh was made up of structured quad mesh near the walls and unstructured near the core region where the flow velocity is very low. In order to capture the sharp gradients the mesh was clustered near the walls where a minimum mesh orthogonal quality is about 1 (value close to zero indicates low quality mesh and value close to one indicates high quality mesh).

Particular attention was given to resolve the boundary layer very close to the walls because the low-*Re* turbulence models have been used for the simulations. The number of cells in the first layer of each cylindrical obstacle was initially 40 which was then raised to 68 corresponding to an overall mesh density of 90, 500. The results were fairly insensitive to the changes of grid density around obstacles, and hence all the calculations reported in this paper were obtained with this mesh. The value of the non-dimensional distance y^+ for the final mesh was found to be just below 1 for all surfaces (cavity and solid obstacles) justifying our use of the low-Re k-ε model (See Appendix D).

It is worthwhile to note that the process of computing a steady-state solution using very fine mesh has been quite challenging because of the oscillations associated with higher-order discretization schemes. As a result, a number of steps were taken to achieve a steady-state solution. Initially, a lower value of Rayleigh number (10^7) was adopted to start the solution with the first-order scheme and the solution was allowed to run to convergence which was typically three orders of magnitude lower than the residual at the start. The resulting data file was then used as an initial guess for the higher Rayleigh number (greater than 10^9) simulation using the higher-order discretization scheme. This method helped to create a more realistic initial field for the low-Re k-ε run. Calculations were performed using a single Intel core 2Duo E6600 2.4 GHz processor and a typical run took about 8 hours of computing time.

The under-relaxation parameters and the discretization scheme used in the simulations are presented in Table 6-1:

Table 7-1: Summary of solver parameters

Parameter	Under-Relaxation Factors	Discretization
Pressure	0.3	PRESTO!
Density	1	-
Body force	1	-
Momentum	0.2	Second Order Upwind
Turbulence kinetic energy	0.3	Second Order Upwind
Turbulence dissipation rate	0.3	Second Order Upwind
Turbulent viscosity	0.5	Second Order Upwind
Water vapour	1	Second Order Upwind
Energy	0.9	Second Order Upwind
Discrete ordinates	0.5	Second Order Upwind

The boundary conditions considered for the simulations are similar to those given in the experimental paper of Laguerre et al., [111] and are summarized in Table 7-2. The constant vapour mass fraction is maintained at the bottom horizontal wall and impermeable conditions assumed for the top and hot vertical walls and for the surfaces of cylindrical obstacles. To conserve the species transport equation, a constant mass fraction equal to the saturation value at the cold wall was specified. The condition of constant mass fraction right on the cold wall is justified because the temperature is constant on that surface. From Eq. 3-27 in section 3.6, S_i is the rate of creation by addition from user-defined source which is solved for N-1 species, where N is the total number of fluid phase species present in the system. In this study the working fluid is a mixture of dry air and water vapour and was treated as a single phase fluid with two component i.e, N=2 (dry air and water vapour). No slip boundary conditions have been imposed for all the solid surfaces.

Table 7-2: Boundary conditions used in the simulations

Wall	Thermal conditions (^{o}C)	Mass fraction (kg water/kg air)	Material, thermal conductivity (W/m-K)
Top	14.4	Zero diffusive flux	Plaster, 0.35
Bottom	13.7	0.00968	Plaster, 0.35
Cold	1.2	0.00407	Aluminium, 202.4
Hot	21	Zero diffusive flux	Glass, 0.75
Obstacles	Zero heat flux	Zero diffusive flux	Plaster, 0.35

In order to calculate the heat transfer due to radiation, the discrete ordinate method [235-238] has been chosen due to its proven superiority in predicting radiative heat

transfer involving a participating medium. Humid air is treated as absorbing-emitting and non-scattering gray medium. The general equation of heat transfer by radiation (in a given $\vec{s}$ direction) for both un-humidified and humidified cavity has been presented in section 3.5.1 of chapter 3:

At the surface of the solid obstacles, thermal boundary condition is presented in equation (7-1):

$$-\lambda\vec{\nabla}T.\vec{n} + \emptyset_{net.rad} = -\lambda\vec{\nabla}T_p.\vec{n} \qquad (7-1)$$

Where $\emptyset_{net.rad}=\emptyset_{in} - \emptyset_{out}$, $\emptyset_{in} = \int_{\vec{s}.\vec{n}>0} I_{in}.\vec{s}.\vec{n}.\mathrm{d}\Omega$ and

$\emptyset_{out} = (1-\varepsilon_r).\emptyset_{in} + \varepsilon_r\sigma T_p^4$.

The walls are all assumed as gray diffuse and 4 angle discretization 2, 4, 16 and 24 were used.

7.3 **Preliminary sensitivity studies**

Preliminary studies were conducted to ascertain the effect of flow regime characteristic (laminar vs turbulent flow regime), low-Re model sensitivity study and 2D simplification of 3D radiation heat transfer modelling for cavity containing obstacles participating in radiation heat transfer.

7.3.1 **Flow regime characteristic**

Double-diffusive phenomenon is governed by the total density stratification consisting of thermal and concentration contributions. Temperature stratification often promotes turbulence, while the stable concentration gradient tends to damped turbulent fluctuations. Specification of the flow regime for such transitional Rayleigh number of 1.45 x 10^9 associated with heat and mass transfer appears to be very confusing.

To resolve this uncertainty surrounding the flow regime characterisation, preliminary numerical investigation was conducted with LRKE model of Launder-Sharma to show if the domain is predominantly laminar or turbulent. The temperature profile near the cold wall (x=66mm) is presented in Fig.7-2, and the relative humidity distribution along the mid-width (x = 0.5L) is represented in Fig.7-3. Both results, laminar and turbulent are plotted against the experimental data which clearly justify our assumption of incorporating a turbulence model in the calculations.

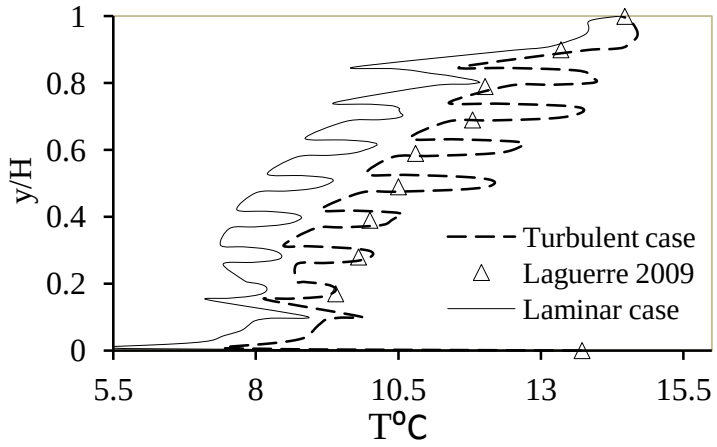

Figure 7-2 Temperature profile near cold wall (x=0.066m)

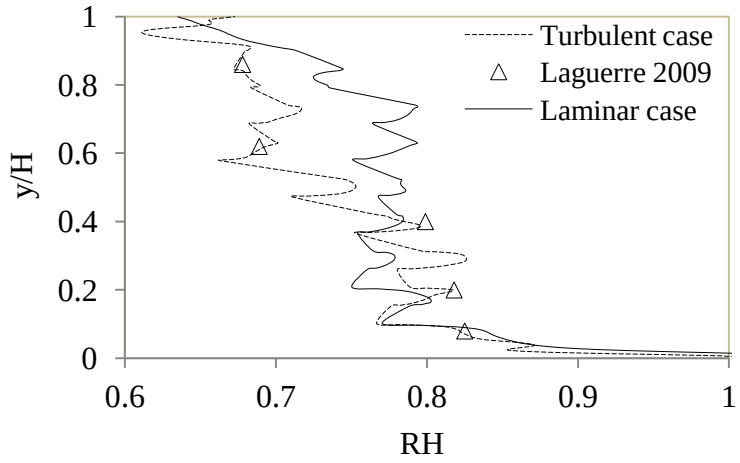

Figure 7-3 Relative humidity profile at mid-width from bottom wall

7.3.2 **Choice of turbulence model and flow characterization**

At the very outset of this research, we were faced with the appropriate characterisation of the flow i.e., whether the flow is to be treated as laminar or turbulent. Bejan [4] and Jaluria [171] have shown that Rayleigh number less than 10^8 indicate a buoyancy-induced laminar flow, with transition to turbulence occurring over the range of $10^8 < Ra < 10^{10}$. Given that the Rayleigh number is 1.45×10^9, which is clearly in the transition zone, and hence we needed to address this issue. While treating the flow to be laminar is rather unambiguous, at least from the viewpoint of viscous models, this is not so for turbulent flows.

It is well known [239-242] that turbulence models play an important role in the predictions of fluid flows. Hence we first checked the turbulence model sensitivity

and later made further comparison to validate our justification for the approach. A total of six eddy-viscosity (EVM) turbulence models (same as that in chapter 4) have been tried. The reason that we restricted ourselves to the EVM is due to the fact that other advanced turbulence modelling such as LES is still very demanding from computation point of view and it is unlikely that it can be applied to practical flows.

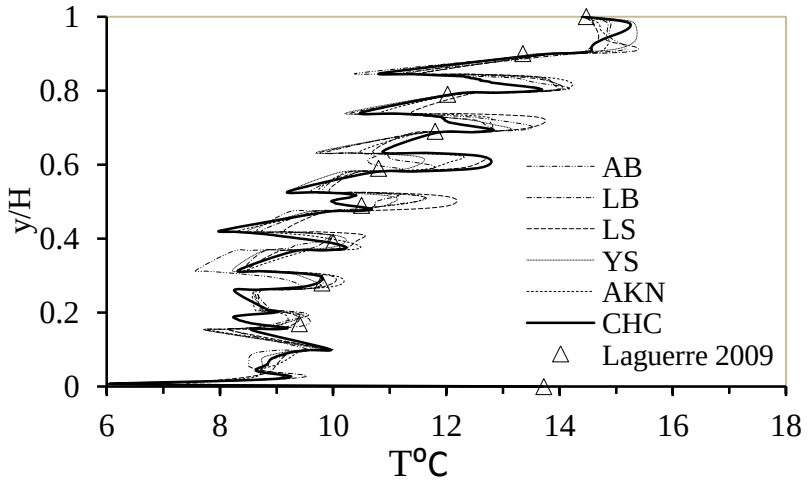

Figure 7-4: Temperature profile near cold wall (x=0.066m)

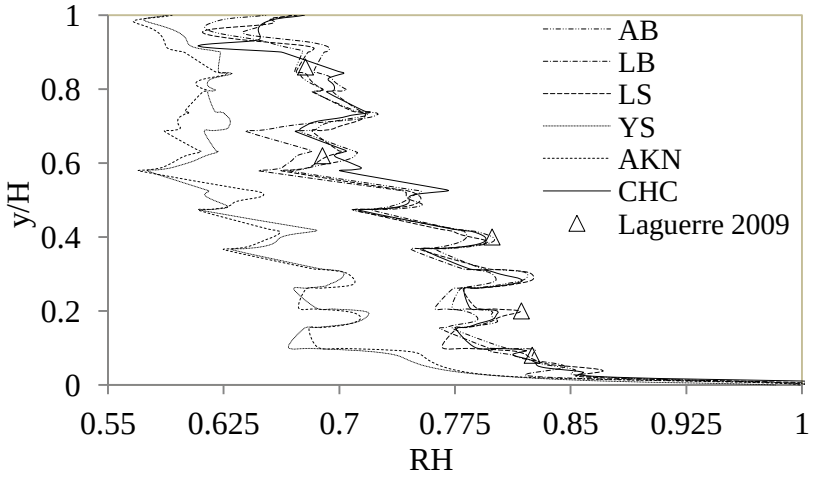

Figure 7-5: Relative humidity profile at mid-width of the cavity

Hence it is much more important to scrutinise the models that are likely to be used from the viewpoint of practitioners. Figs.7-4 and 7-5 show the typical mean quantity profiles predicted by various turbulence models. Table 7-3 presents the average hot wall Nusselt number. A careful look at the plots reveal that while the core region had been predicted well by most of the models, the situation is very different for the near

wall region. For both cases (velocity and temperature), it is clear that the Launder-Sharma model returned the best results. Hence this model has been used for all the calculations reported in this work. It should be noted here that for similar flow without blockage in chapter 4, Y-S model was found to give the best performance unlike L-S for similar flow with blockages. It is clear the uncertainty with the choice of turbulence model varies from one situation to another. From a computational point of view, L-S showed a much more stable solution and hence we restricted ourselves to this model only.

Table 7-3: Average hot wall Nusselt number

LRKE	$Nu_{average}$
Abid (AB)	33.52
Lam & Bremhost (LB)	37.34
Launder & sharma (LS)	41.07
Yang & Shih (YS)	32.60
Abe et al., (AKN)	35.38
Chang et al., (CHC)	34.25

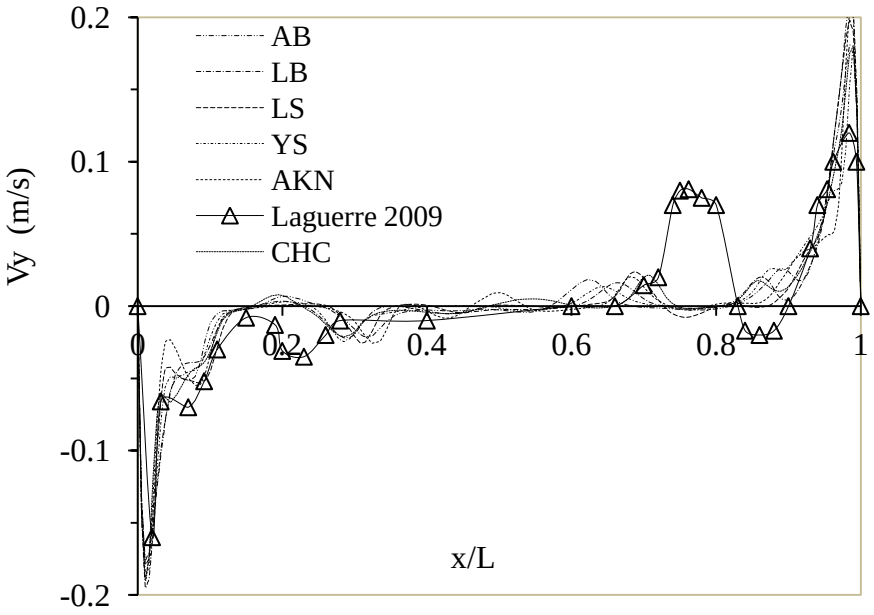

(7-6a)

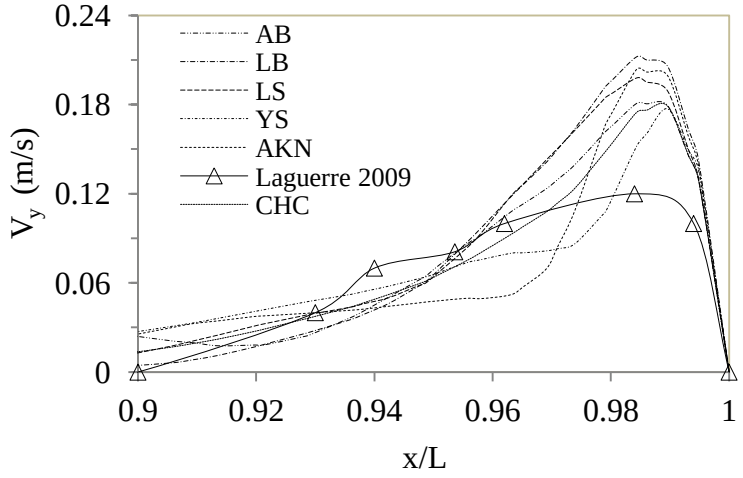

(7-6b)

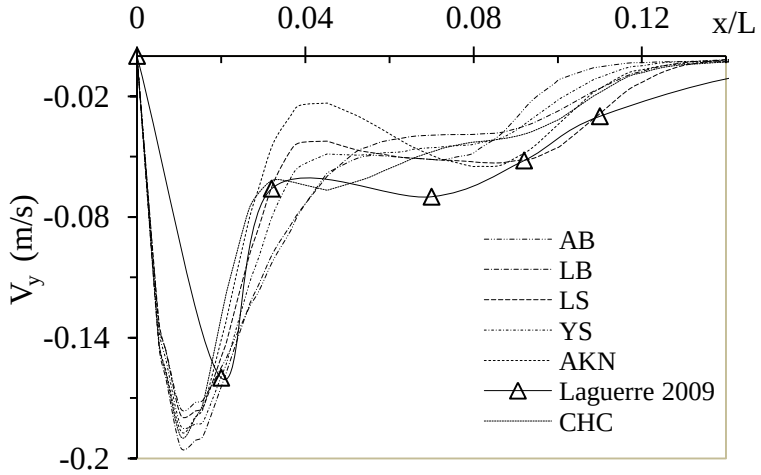

(7-6c)

Figure 7-6: Vertical velocity profile at (a) mid-height (b) near hot wall (c) near cold wall

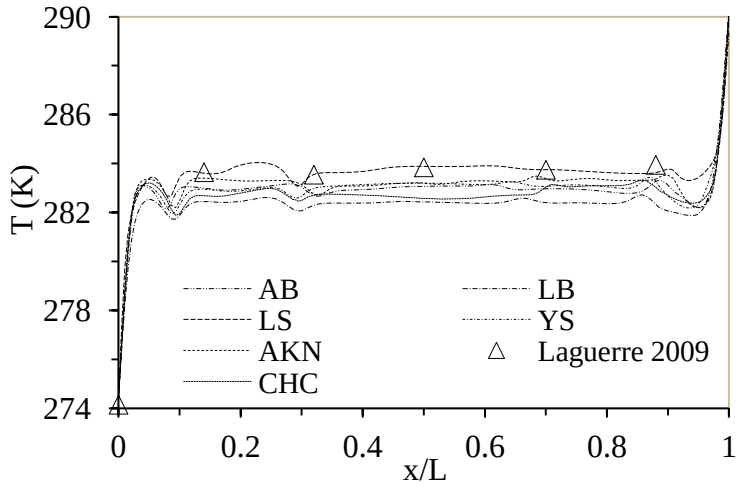

Figure 7-7 Temperature profile at mid-height of the cavity

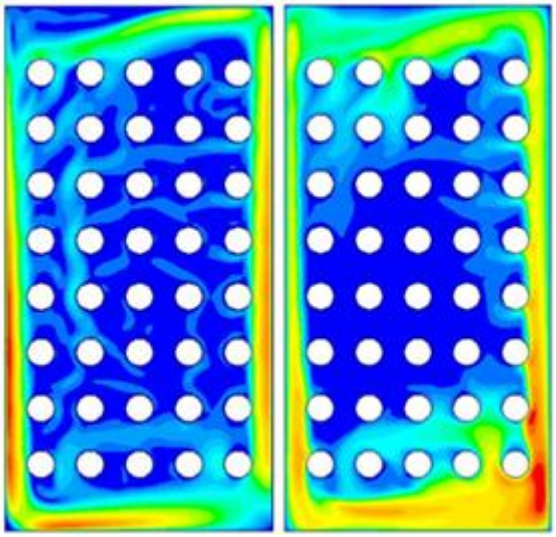

(a) (b)

Figure 7-8: (a) Velocity magnitude and (b) turbulent intensity contours [LS model]

The velocity and turbulent intensity contours shown in Figs.7-8a-b respectively, demonstrate clearly that the main air flow is within the boundary layer so that the obstacles close to the walls interact with the hydrodynamic viscous layer. This observation further highlights the importance of using a low-Re k-ε model. It can also be seen that there are other streams of flow of varying (smaller) magnitude. Such a flow pattern was also verified and reported in the experimental work of Laguerre et al., [111] and can be seen in Fig.7-6.

7.3.3 2D simplification of 3D radiation heat transfer for an enclosure partially filled with blockages

The choice of emissivity is very critical when modelling radiation heat transfer and, even for this type of moderate temperature difference, the effect of radiation has been found to be fairly significant [58, 111]. The 2D simplification of an inherently 3D radiation heat transfer also raises issues with the accuracy of the data produced by 2D simplification of domain. According to Laguerre et al. [111], an equivalent emissivity of ε_{eq}=0.58 can be shown to mimic the radiation heat transfer between three surfaces having emissivity of 0.9 (somewhat similar to the treatment of radiation shield). The radiation flux between two surfaces of emissivity ε_1 and ε_3 when a thin shield of emissivity ε_2 is placed between them is shown in equation (7-2):

$$\varphi_{rad} = \frac{A\sigma(T_1^4 - T_3^4)}{\left(\frac{1}{\varepsilon_1} + \frac{1}{\varepsilon_2} - 1\right) + \left(\frac{1}{\varepsilon_2} + \frac{1}{\varepsilon_3} - 1\right)} \qquad (7-2)$$

If $\varepsilon_1=\varepsilon_2=\varepsilon_3=0.9$. The equivalent radiation flux is presented in equation (7-3):

$$\varphi_{rad}(equivalent) = \frac{A\sigma(T_1^4 - T_3^4)}{\left(\frac{1}{\varepsilon_{eq}} + \frac{1}{\varepsilon_{eq}} - 1\right)} \qquad (7-3)$$

Where, φ_{rad} is the radiative heat flux,

σ = 5.6703 x 10^{-8} (W/m^2k^4) – Stefan-Boltzmann constant,

A = area of emitting surface (m^2)

However, no numerical evidence is provided in support of the above. We have scrutinized this assumption and a comparison of temperature for 2D vs. 3D domain is presented in Figs.7-9a-c. It can be seen that the predicted temperatures for ε= 0.9 (3D) and ε = 0.58 (2D) are in fairly close agreement justifying the 2D treatment.

The ε = 0.9 (2D) is shown for comparison which also highlights the significant influence of radiation for this flow.

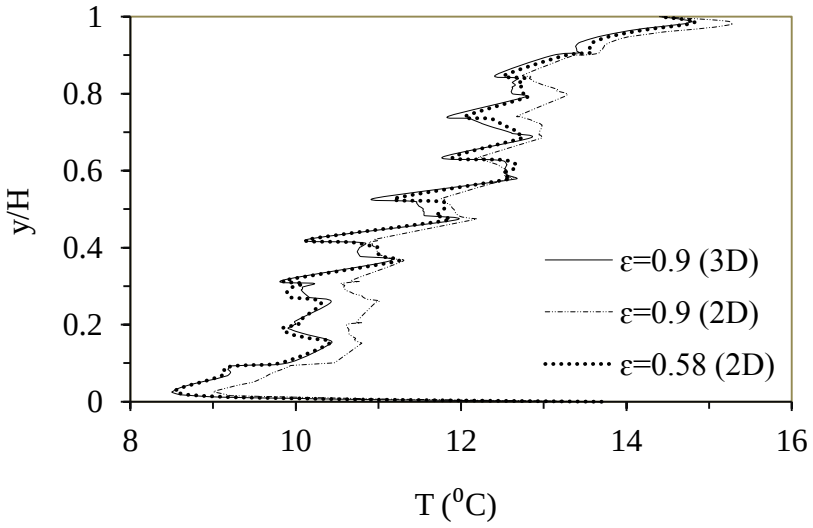

(7-9a)

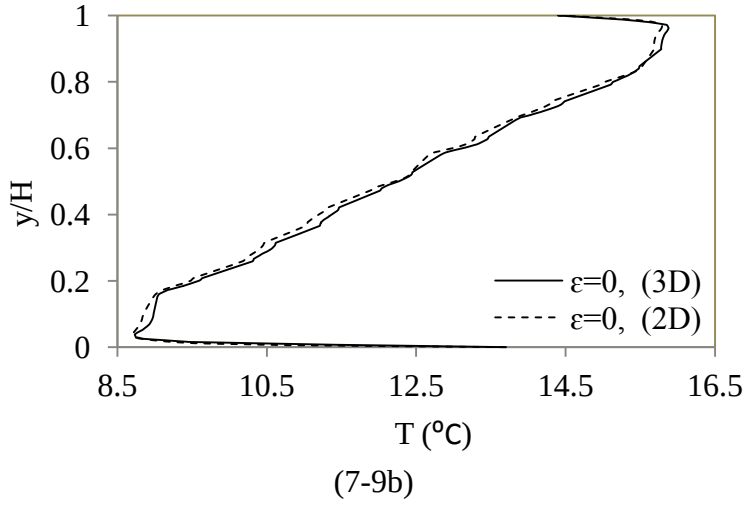

(7-9b)

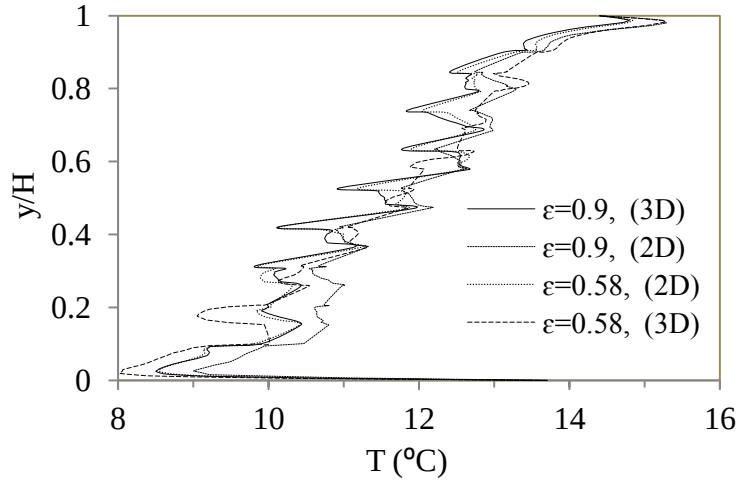

(7-9c)

Figure 7-9: (a) temperature profile at x = 66 mm, (b) temperature profile at mid-width of the cavity for ε=0, (c) temperature profile at mid-width of the cavity

The choice of emissivity is very critical when modelling radiation heat transfer and, even for this type of moderate temperature difference, the effect of radiation has been found to be fairly significant [243]. Therefore, this allows taking approximately into account the 3D radiation effects in 2D simulations.

7.4 **Influence of thermal radiation**

In this section, we present the results for the un-humidified case. Since one of the objectives of this work was to quantify the radiation characteristics for such flows, we varied the surface emissivity for all the surfaces. To model radiation, Discrete Ordinate Model [237, 238] has been selected due to the fact that it allows interaction with participating media such as water vapour [244] as will be presented in a later

section. Four surface emissivity values were specified i.e., ε=0, ε=0.3, ε=0.58, and ε=0.7. The mid-value of ε=0.58 was chosen by reference to Laguerre et al., [111] that it represented the equivalent emissivity value for a two-dimensional treatment of radiation within the cavity. In a nutshell, the effect of treating radiation in 2D fashion means using lower emissivity value than that in the actual 3D geometry. Therefore, to save cost of computations, 2D numerical simulations were conducted and the results shown in the following sections.

7.4.1 **Temperature fields**

The temperature distribution is one of the most critical mean quantities, because the flow develops as a result of buoyancy which is directly dependent on temperature gradient. Figs.7-10a-b, show the plots along the mid-width (x = 0.5L) and near the cold wall (x = 66mm) respectively. From these plots, temperature stratification is low at the bottom wall and high at the top wall for all values of emissivity. Since radiation between all surfaces is taken into account in the simulations, oscillations of the temperature profiles can be very clearly seen in these plots. This is because the fluid temperature further away from the cylinder surface is higher than that very close to its surface - a phenomenon highly influenced by the surface emissivity value.

The temperature profile of the flow domain shows a decrease in temperature distribution with the increase in emissivity of the walls and the obstacles. The temperature field is also highly influenced by the presence of obstacles. In addition to the overall thermal stratification in the cavity, stratification is also observed in each gap between the obstacles. One very important point to note is the fact that the predicted temperature for ε=0 (i.e., without radiation) is very inaccurate, the largest discrepancy being displayed near the top wall. This has also been numerically verified by Laguerre et al., [111]. The fact that the inclusion of radiation improves the scenario drastically is a further vindication that radiation does play a significant role in apparently low temperature applications. We believe that this may have an important implication for built environment applications.

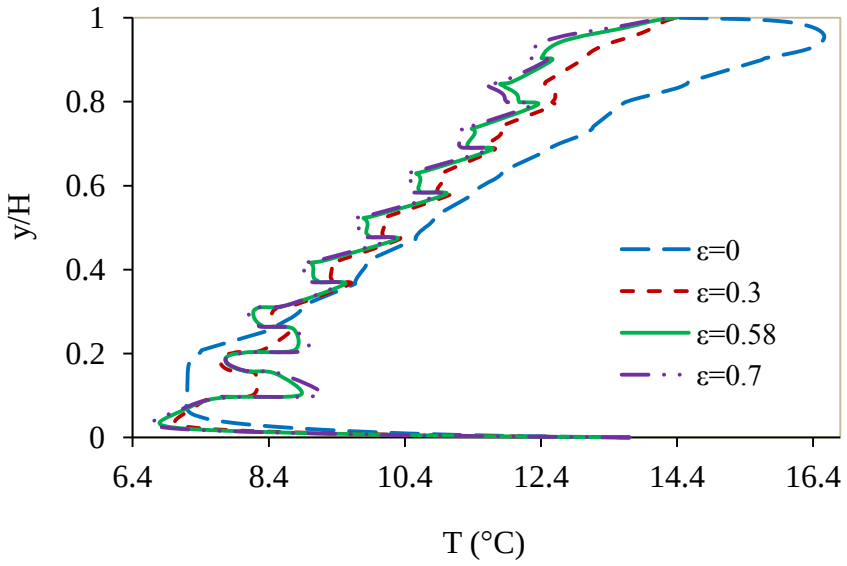

(7-10a)

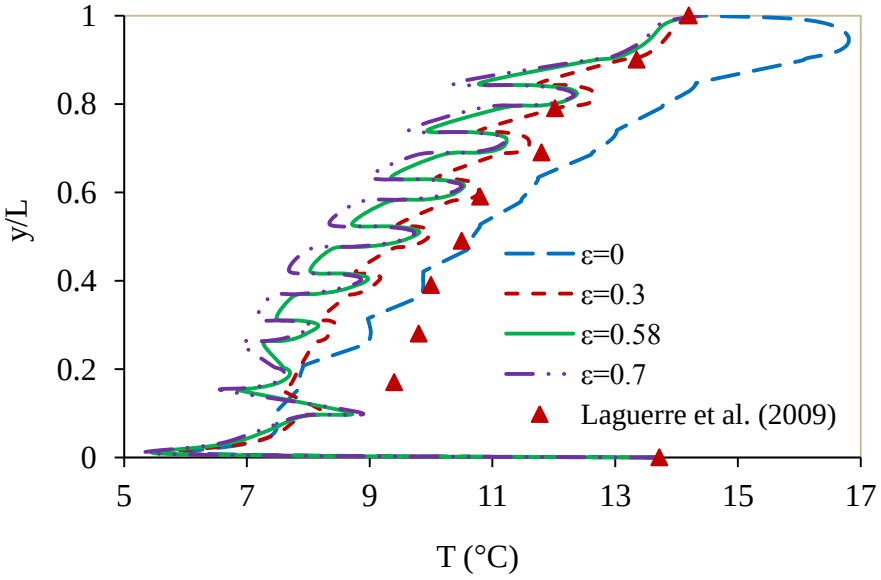

(7-10b)

Figure 7-10: Temperature profile at (a) mid-width (b) near cold wall, x=66mm

7.4.2 **Wall heat transfer**

Average and local heat transfer data are compared in terms of an average Nusselt number and local Nusselt number computed at each wall. The local Nusselt number is given in Figs.7-11a-d and the radiation Nusselt component is shown in Fig.7-12a-b.

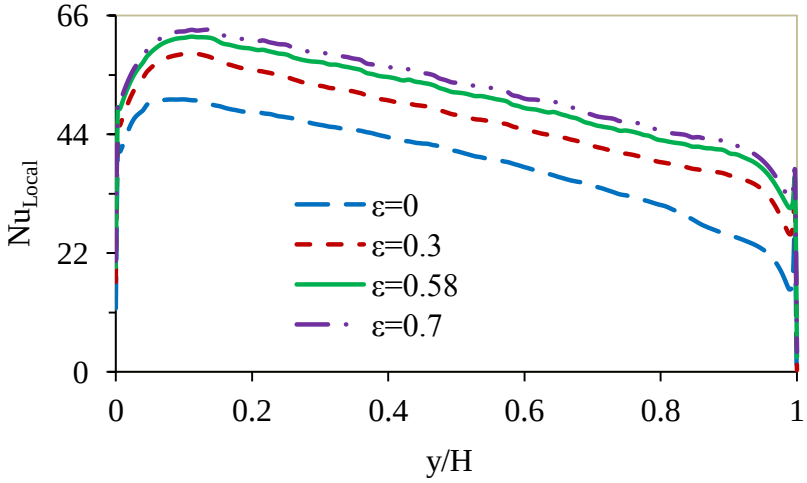

(7-11a)

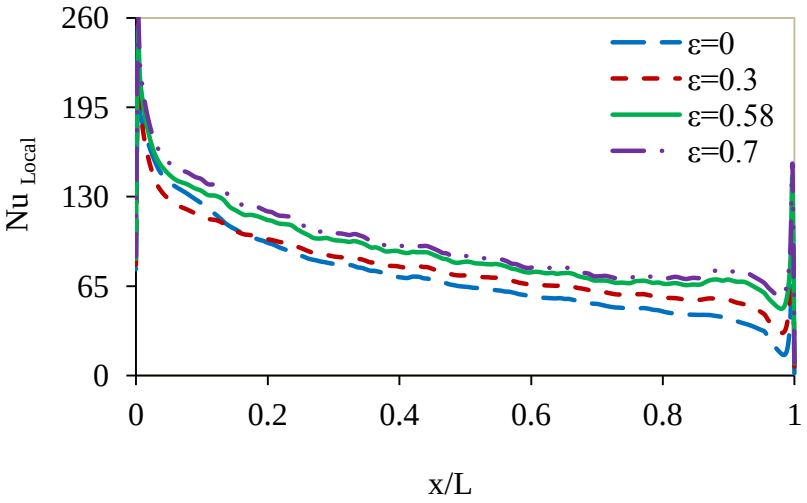

(7-11b)

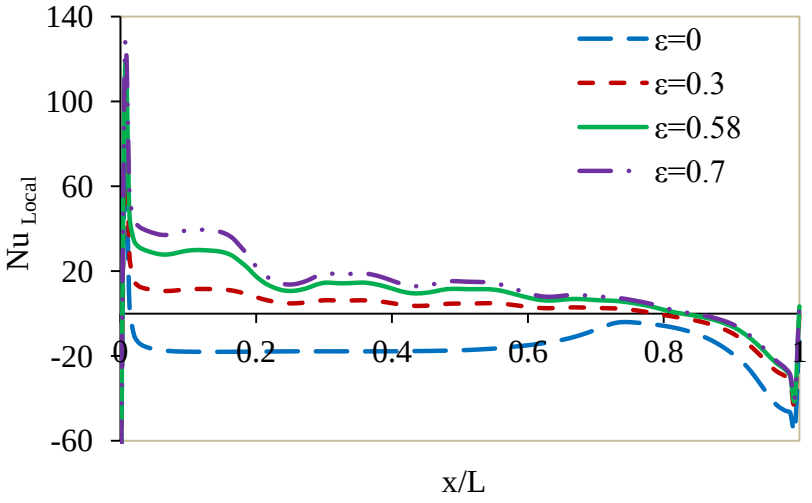

(7-11c)

Figure 7-11: Local Nusselt number along the (a) hot wall (b) cold wall (c) top wall

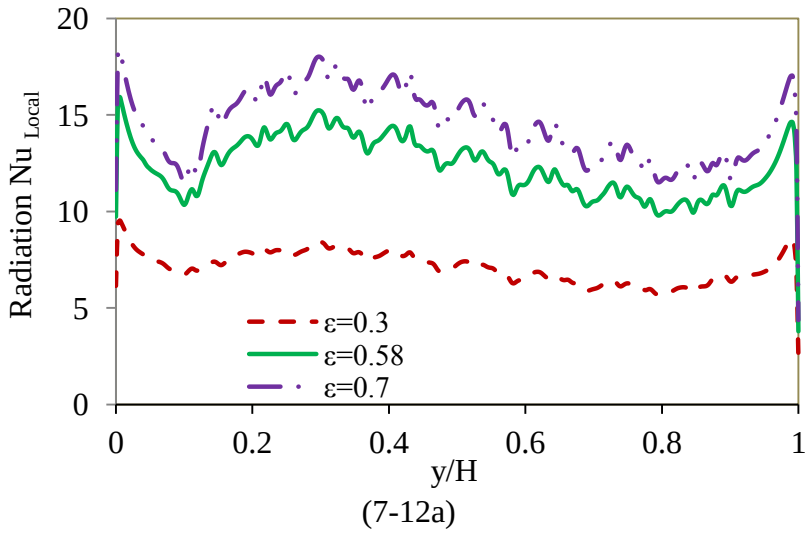

(7-12a)

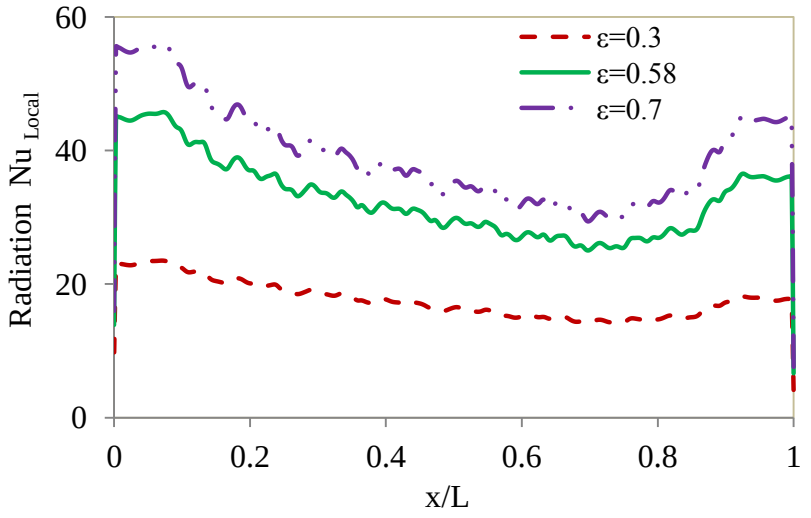

(7-12b)

Figure 7-12: Local radiation Nusselt number along the (a) hot wall (b) cold wall

Table 7-4: Average surface Nusselt number

Test	Hot wall	Bottom wall
ε=0.00	38.98	24.24
ε=0.30	46.78	34.61
ε=0.58	50.81	35.99
ε=0.70	52.47	38.37
ε=0.90	58.18	41.07

Figs.7-11a-c show the local Nusselt number for the hot, cold and the top walls respectively, and the radiative Nusselt number is shown in Fig. 7-12a-b. The average values are given in Table 7-4. As expected, higher surface emissivity is found to

enhance heat transfer which is relatively more prominent for the radiative Nusselt numbers as can be seen in Figs.7-12a-b, these plots also demonstrate fluctuations which are due to the proximity of obstacles.

It can be seen that the average Nusselt number changes with the changes in surface emissivity and their values have significant effect on the heat transfer. Without radiation there is a balance between the conductive and convective heat fluxes at the interfaces of the walls. Radiation causes an additional heat flux towards the interface due to incident radiation and an extra outgoing heat flux associated with emission of radiation. The percentage increment in heat transfer corresponding to these emissivity values are presented in Table 7-5. Since buoyancy-driven flow velocities are small and temperatures are low, the radiative heat fluxes are modest but comparable in size with convective heat fluxes. Therefore, surface emissivity has significant effect on the heat transfer within the cavity.

Table 7-5: Percentage heat transfer increment (%)

Test	Hot wall	Bottom wall
ε=0.30	20.0	42.8
ε=0.58	30.3	48.5
ε=0.70	34.6	58.3
ε=0.90	49.2	69.4

7.4.3 **Stream function**

The measure of circulation rate of the buoyancy driven fluid mixture inside the cavity is represented in Figs.7-13a-b. This is formulated using the stream function Ψ obtained from velocity components u and v. The relationship between stream function, Ψ and velocity components for two dimensional flows as shown in equation (7-8):

$$u = {}^{\partial\Psi}/_{\partial y} \text{ and } v = -{}^{\partial\Psi}/_{\partial x} \qquad (7\text{-}8)$$

As the emissivity value increases, there is a corresponding increment in the value of stream function. Fig.7-13a also displays a stable (rather stagnant) zone in the core areas but shows a 50% increase in circulation rate at the mid-point measured at the mid-height of the cavity. Slightly enhanced perturbations for higher ε values are direct

results of radiation. The stream function profile evaluated at the mid-width of the cavity, Fig.7-13b shows a rather monotonic nature with peaked values near the bottom wall of the cavity. The maximum rise is 35.8% for maximum values of the circulation rate.

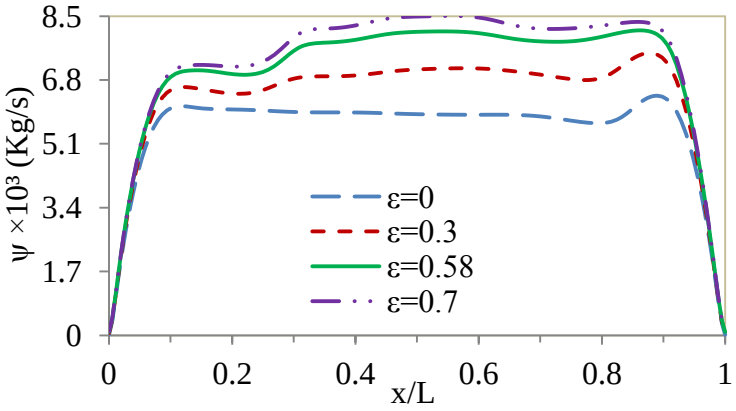

(7-13a)

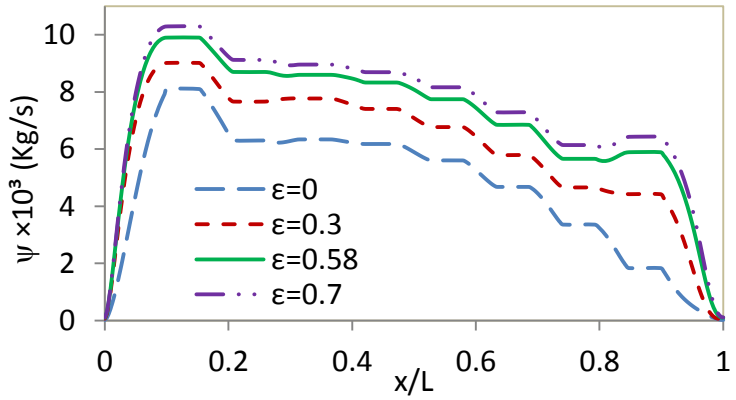

(7-14b)

Figure 7-13: Stream function profile at (a) mid-height (b) mid-width

7.4.4 **Eddy viscosity ratio**

As was shown in Figs.7-8a-b, the flow is characterised by upward and downward boundary layer flows along the hot and cold walls respectively with a rather stagnant region in the central part. Hence the importance of turbulent quantities is also dominant along the two walls. To analyse this effect, we plotted the turbulent viscosity ratio, $\mu^* = \mu_t/\mu$ at the mid-height of the cavity in Fig.7-14.

The ratio represents a relative measure of the diffusive potential of turbulence in the cavity and is seen to decrease with increasing surface emissivity. It is also seen that

the viscous effects are dominated by convection. At higher emissivity, heat transfer is affected more by radiation than by convection. The results also highlight that such flows may be treated as a multi-zone configuration as suggested by Griffiths and Chen [245].

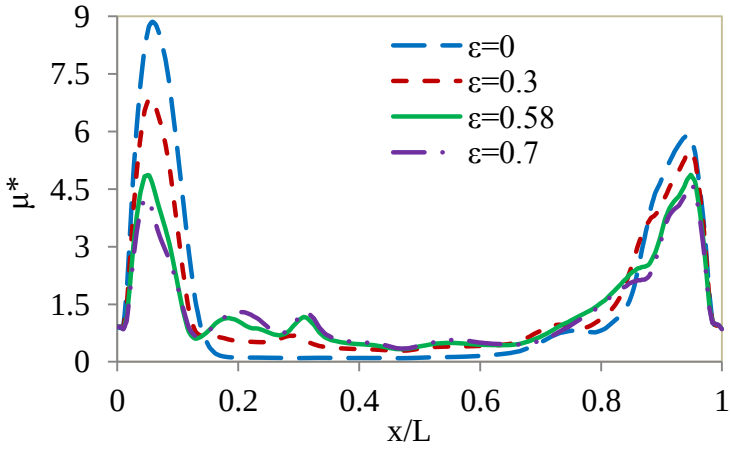

Figure 7-14: Turbulent viscosity ratio at mid-height (Un-humidified cavity)

7.4.5 **Buoyancy effects**

Buoyancy flux, *B* characterises the buoyancy driven flow and is expressed in equation (7-8). In the above equation, β_{mix} represents the combined volumetric expansion coefficient of the air-water vapour mixture. Fig.6-22 shows the buoyancy flux plots at the bottom wall. As the emissivity increase B also increases with minimum value very close to the hot wall and maximum value near the cold. At the bottom edge region of the hot vertical wall, heating rate is gradually decreased due to heat loss to the bottom wall and hence resulting in lesser buoyancy effect.

$$B = {(g\beta_{mix} q_i)}/{\rho c_p} \qquad (7-8)$$

On the other hand, heat loss from the bottom wall is gradually transported to the cold wall, thereby, increasing buoyancy in this area of the cavity. Fig.6-23 shows the buoyancy flux along the hot wall of the cavity where the buoyancy effects due to temperature are maximum and surface emissivity plays an important role especially in temperature induced buoyancy; these effects are found to increase with increasing value of emissivity.

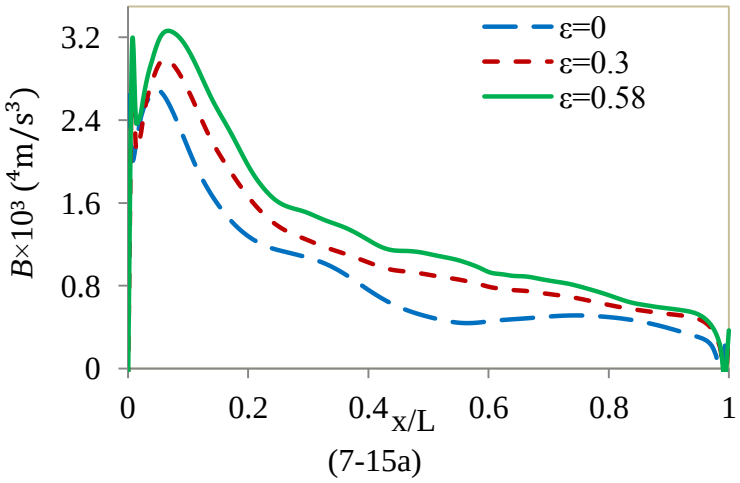

(7-15a)

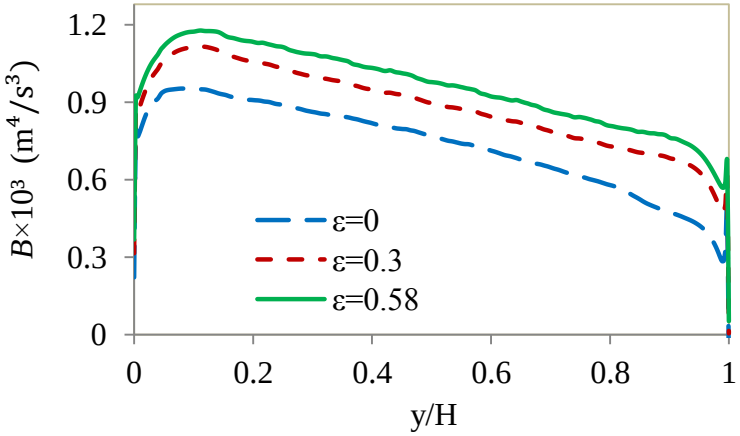

(7-15b)

Figure 7-15: Buoyancy flux near (a) bottom wall (b) hot wall

7.5 **Influence of mass transfer**

In this section we present the results obtained for the situation when the bottom wall acts as a source of mass influx mimicking evaporation in the experimental study where a vat containing water was placed at the bottom wall. In our presentation, we put emphasis on identifying the parameters that were influenced by humidity.

7.5.1 **Heat transfer**

A comparison of the average heat transfer between the temperature induced buoyancy and that due to the combined influence of mass and temperature (doubled-diffusion convection) is shown in Table 7-6. Generally, the data shows heat transfer

enhancement with the addition of water vapour. A modest rise of 5.4% and 5.7% in the heat transfer is observed for the hot and bottom walls respectively.

Figs. 7-16a-b also show some increase in the heat transfer rate due to the combined effects of mass and temperature gradient. Although the effect on the hot wall is only marginal, the effect of humidity can be observed much more prominently for the top wall of the cavity.

Table 7-6: Average Nusselt number

Cases	Hot wall	Bottom wall
Humidified	41.07	25.63
Un-humidified	38.98	24.24

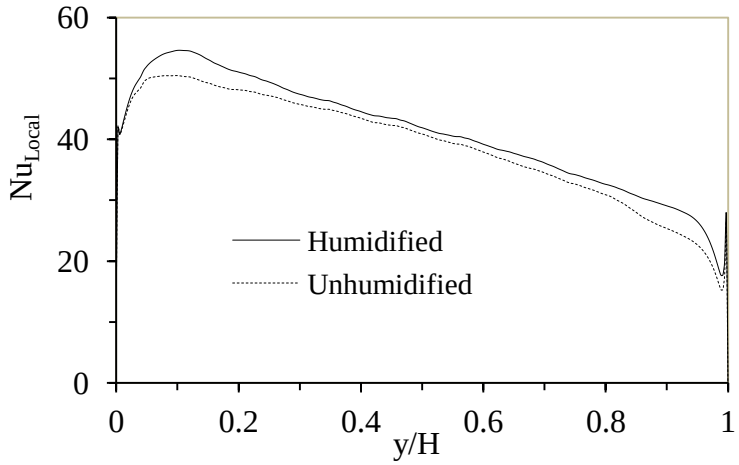

(7-16a)

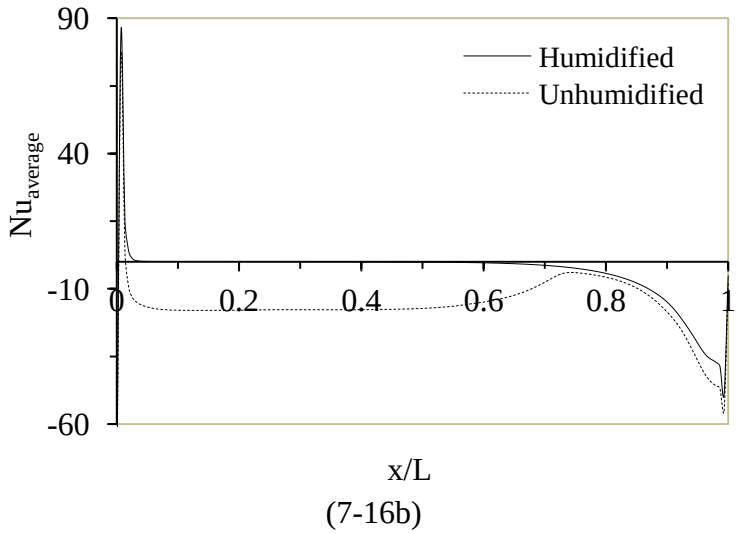

(7-16b)

Figure 7-16: Local Nusselt number near (a) hot wall (b) top wall

7.5.2 **Buoyancy flux**

The buoyancy effects are the results of combined temperature and concentration gradients. The concentration gradient is due to difference in the relative molecular mass between the dry air and water vapour. Figs.7-17a-b, present the buoyancy flux profiles along the bottom and hot walls respectively. The additional contribution due to vapour can be seen clearly in both graphs, although the net values are rather modest which is about 5%. This may prove to be significant in a particularly long exposure situation typical of human comfort studies.

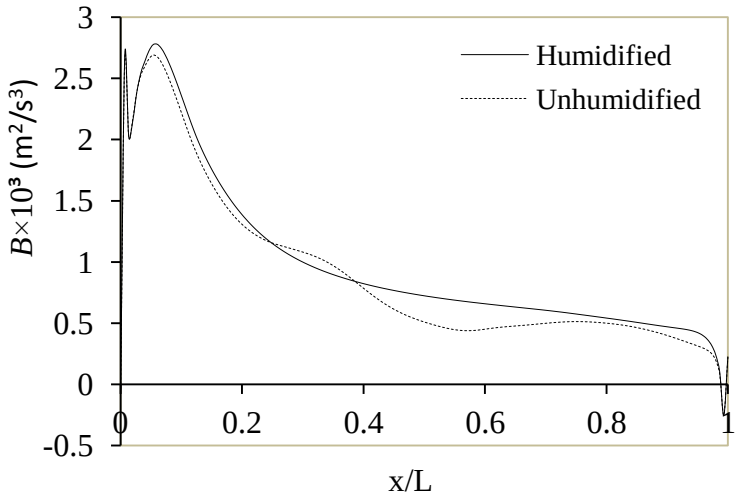

(7-17a)

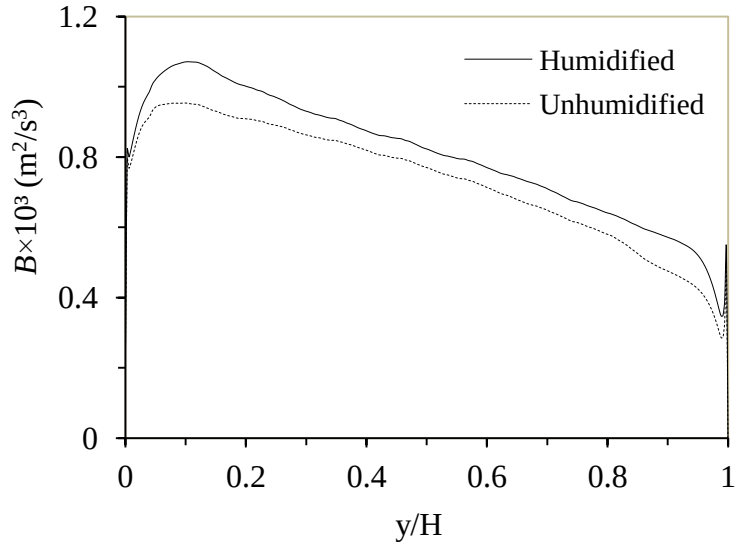

(7-17b)

Figure 7-17: Buoyancy flux near (a) bottom wall (b) hot wall

7.5.3 **Influence of surface radiation on mass transfer**

The earlier section of this thesis, thermal radiation affects the flow and heat transfer in temperature induced natural convection with the influence of obstacles was analysed. However, the results presented here are focused on the influence of thermal radiation on mass transfer. The mass transfer is represented as humidity "m" defined as the ratio of mass of vapour to the total mixture mass.

Figs.7-18a-b show that the mass fraction decreases with increasing surface emissivity which is due to the fact that at low emissivity the vapour mass transfer increases. And as the emissivity increases, the fluid temperature increases leading to a corresponding increase in air flow in the cavity. These phenomena also account for the increment in the profiles of effective diffusion coefficient, $D_{\text{eff,}}$ of vapour at lower values of surface emissivity as shown in Figs.7-19. Further quantitative information is provided in Fig.7-20, where we have plotted the Buoyancy number, "N" which is a ratio of mass to temperature induced buoyancy. This ratio N measures the significance of the contribution to buoyancy of the variation in vapour concentration in the cavity

The effective diffusion coefficient of vapour is also observed to be maximum close to the vertical walls and almost constant at the core of the cavity. The variations and nature of these curves are very similar to the viscosity ratio curves presented in Figure 18, highlighting the fundamental similarity in the diffusive transport mechanism of momentum and concentration.

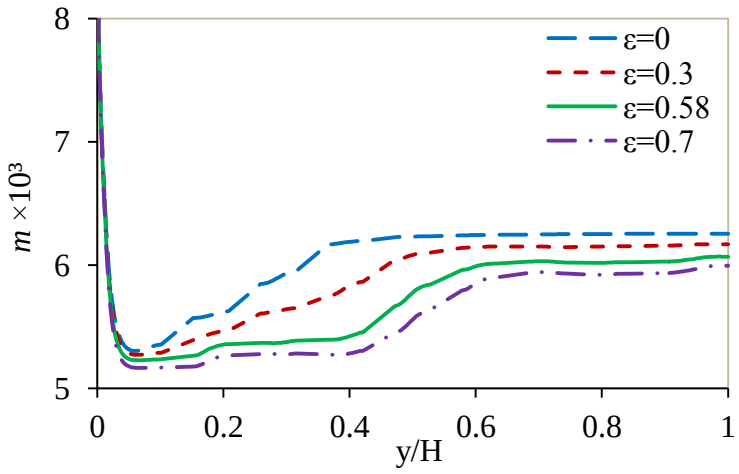

(7-18a)

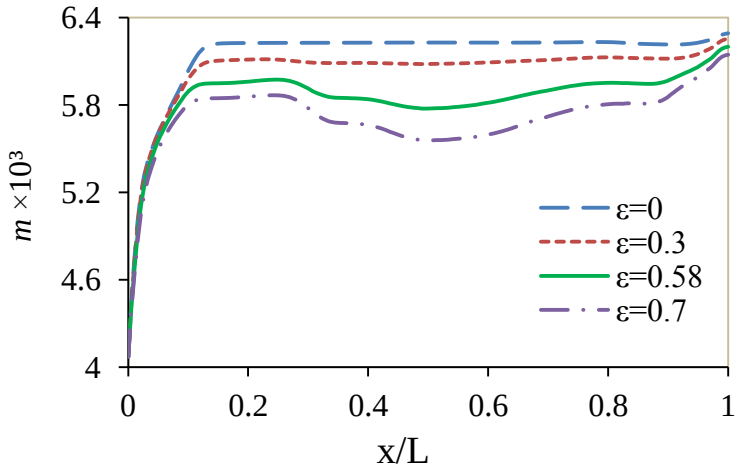

(7-18b)

Figure 7-18: Mass fraction of water vapour along (a) mid-width (b) mid-height

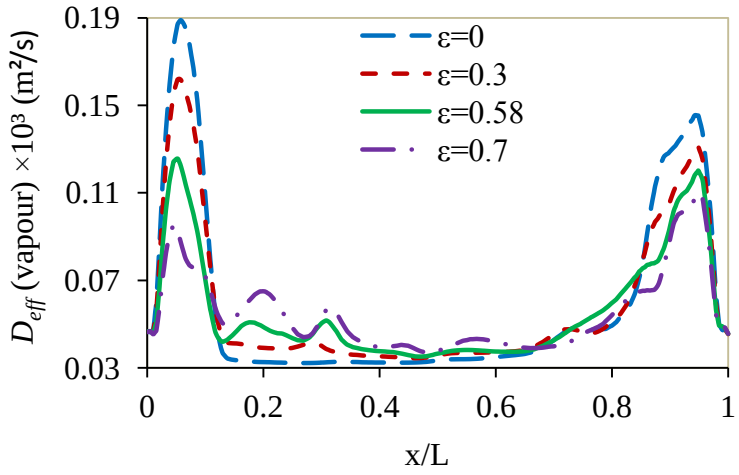

Figure 7-19: Effective diffusion coefficient of water vapour at mid-height

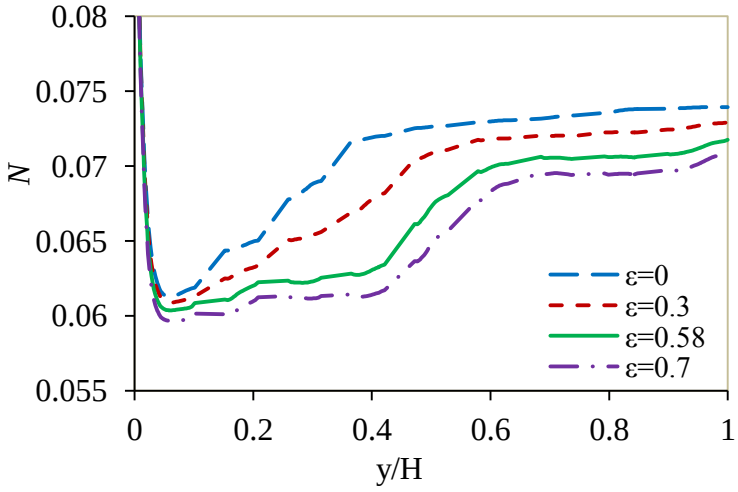

(7-20a)

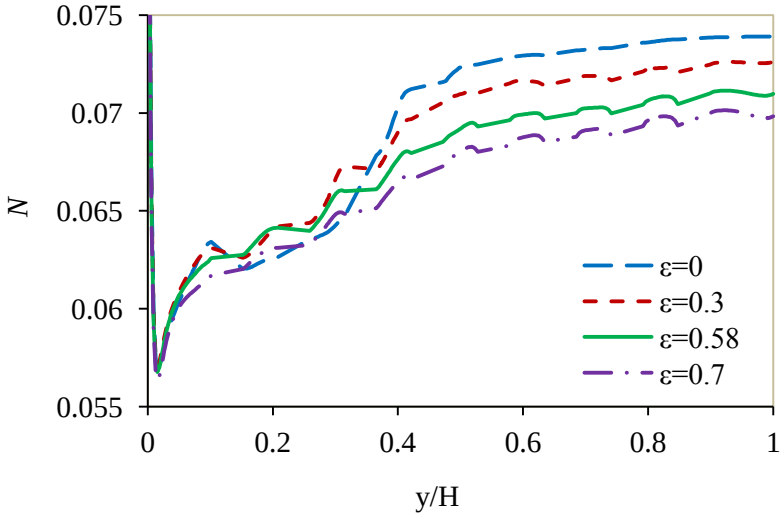

(7-20b)

Figure 7-20: Ratio of mass to temperature induced buoyancy (a) mid-height (b) near cold wall (x=66mm)

7.6 Two-dimensional Simulation of the Influence of Blockage-Active Walls on Mass Transfer

In this section, further numerical study was conducted to ascertain and quantify the effect of blockage proximity on the flow, heat and mass transfer. Detailed analysis was performed on the flow and heat transfer and on the turbulence quantities within the cavity. Profiles of turbulent kinetic energy and turbulent viscosity are studied in detail to observe the net effect on the intensity of turbulence caused by the interactions of these blockages-active walls proximity with double-diffusive natural convection heat and mass transfer. Particular emphasis was placed on quantifying the proximity of the solid objects to the active walls.

The geometrical configuration used in this investigation is similar to that presented in Fig.7-1, and similar numerical procedure and conditions presented in section 7.2.1, were in the simulations. Based on the temperature differentials of the vertical walls the Rayleigh number was kept the same as 1.45×10^9. For this work, the distance of the first column of objects from both the hot and cold walls was varied (δ= 33mm, 50mm, 66mm, 80mm and 120mm). The distance between the other columns, 'c', varies negligibly and hence the effect due to internal re-distribution is ignored.

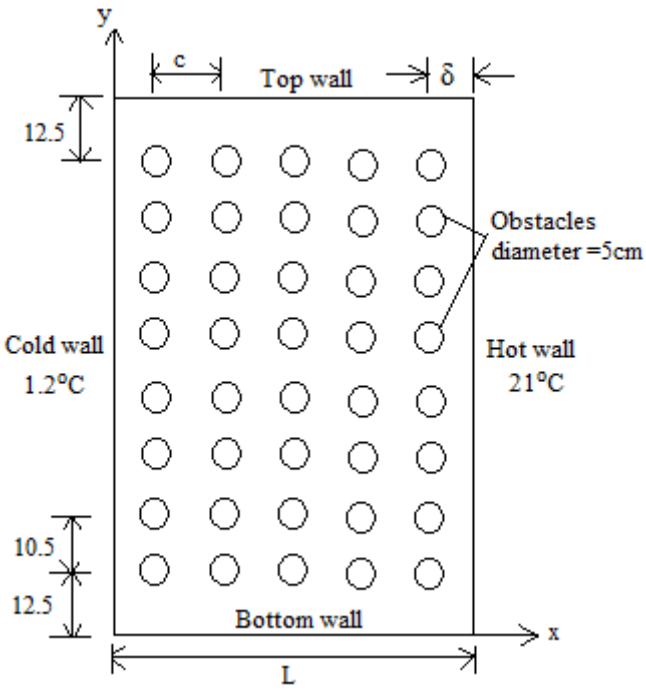

Figure 7-21: Geometry and the coordinates (dimensions are in cm)

7.6.1 **Wall heat transfer**

Average and local heat transfer data are compared in terms of an average Nusselt number and local Nusselt number computed at each wall. The total Nusselt number which is a combination of heat transfer due to convection and radiation were separately calculated by taking integral averages of heat fluxes using FLUENT post-processing tools. Similarly the local Nusselt numbers were obtained using the local heat flux at each node. Table 7-7 shows the average Nusselt number for various walls for various values of δ and Figs.7-22a-b shows the local variations.

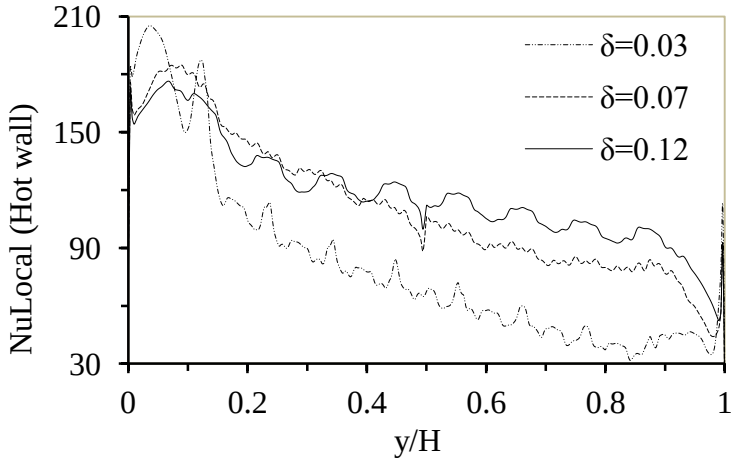

(7-22a)

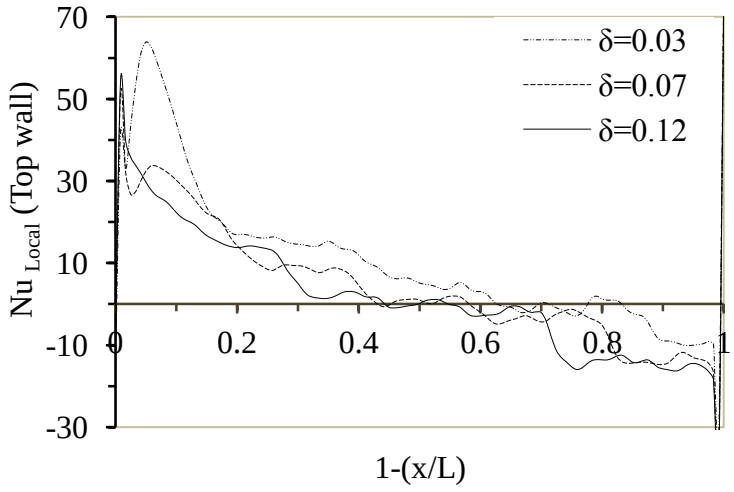

(7-22b)

Figure 7-22: Variation of local Nusselt number near (a) hot wall (b) top wall

Table 7-7: Variation of Average Nusselt Number (Italicised data for δ = 66mm are for coarse mesh of 64,600 cells)

δ (mm)	Bottom wall	Hot wall	Top wall	Cold wall
33	33.8	82	10.4	105.5
50	34.1	105.3	7.3	132.1
66	30.5(*30.4*)	111.6 (*111.3*)	3.9(*3.8*)	138.2(*137.8*)
80	30.4	113.9	2.7	141.5
120	29.1	118.5	1.7	146

The table shows that the total heat transfer is significantly low for the smallest δ value. For other values the average Nu demonstrates a small but monotonic increase of the heat transfer. The local variations of Nu along the hot wall display the proximity effect very clearly. It also shows that with larger δ values, the Nu numbers tend to smooth out. The fact that δ=33mm shows a markedly small value of heat transfer may be partly related to the fact that turbulence is greatly suppressed due to blockage of the upward and downward flow of fluids along the hot and cold walls respectively. The turbulent viscosity ratio, μ* (ratio of turbulent eddy viscosity divided by the molecular viscosity) presented in Figs.7-23a-b, shows that turbulence is greatly reduced as the objects come closer to the walls and supports the multi-zone configuration of flow as suggested by among others, Griffiths and Chen [245] .

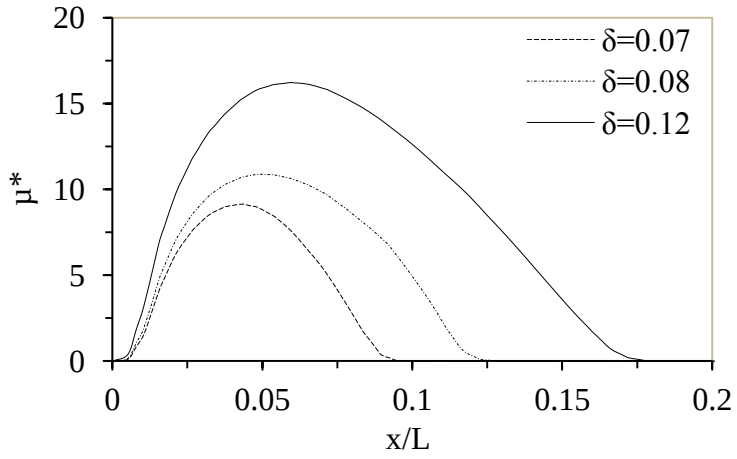

(7-23a)

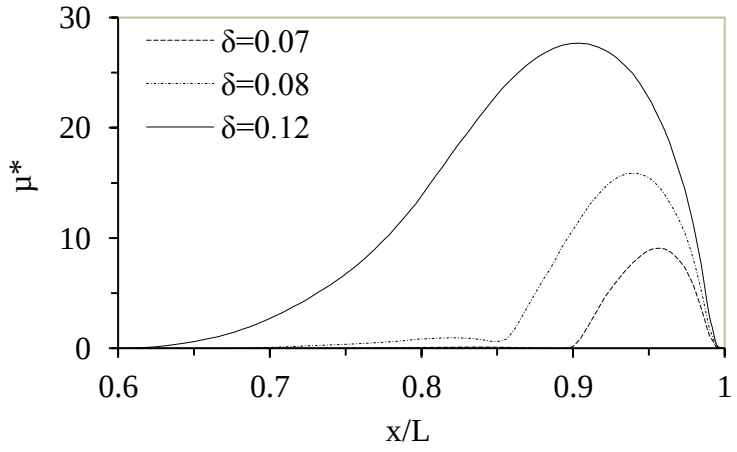

(7-23b)

Figure 7-23: Turbulent viscosity ratio at mid-height and near (a) cold wall (b) hot wall

7.6.2 **Influence of proximity on mass transfer**

Detailed analyses were carried out on the vapour mass flow distributions at various locations of the flow domain. Typical plots of mass fraction, "m" (g/kg) and buoyancy number, "N" defined as the ratio of mass to temperature induced buoyancy is plotted in Fig.7-24 and Fig.7-25. It can be seen that the mass fraction of vapour increases for the smaller δ values. This is due to the smaller gap available for the flow and is essentially a redistribution of the moisture content throughout the flow domain. The buoyancy number "N" measures the contribution to buoyancy of the variation in

vapour concentration. The concentration gradient is due to the difference in the relative molecular mass between the dry air and water vapour. At 20^0C, the relative molecular mass of dry air is 28.97 kg/kg-mol, whilst for saturated air it is 28.71 kg/kg-mol. As expected the effect due to mass induced buoyancy is small and corresponds to the trend in Figs.7-23a-b.

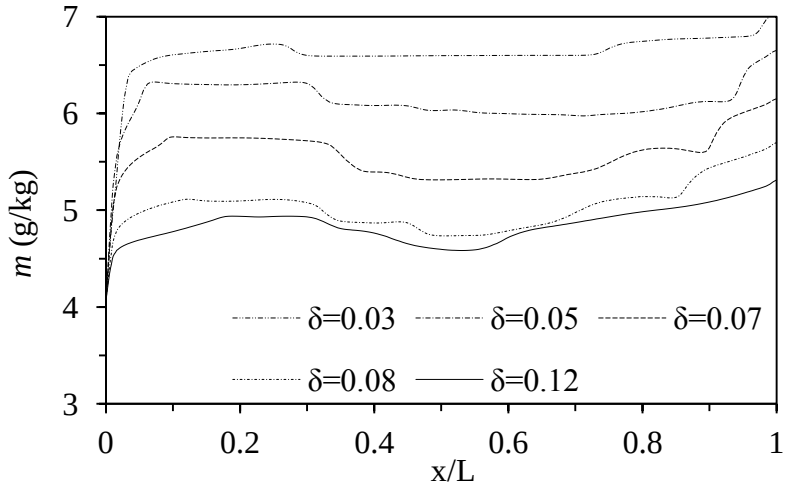

Figure 7-24: Mass fraction along the mid-height

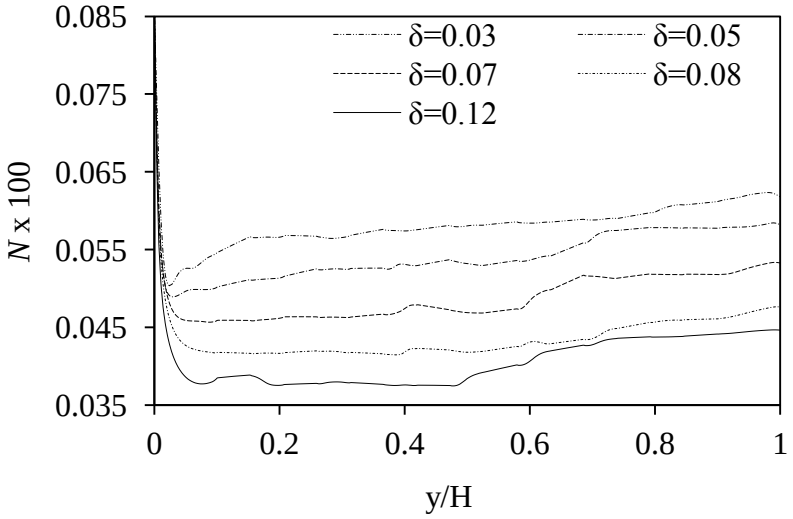

Figure 7-25: Buoyancy number along the mid-height

The effective diffusion coefficient, D_{eff} of vapour shown in Figs.7-26a-b at the mid-height. The variations and nature of these curves are very similar to the viscosity ratio curves presented in Figs.7-23a-b highlighting the fundamental similarity in the diffusive transport mechanisms of momentum and concentration.

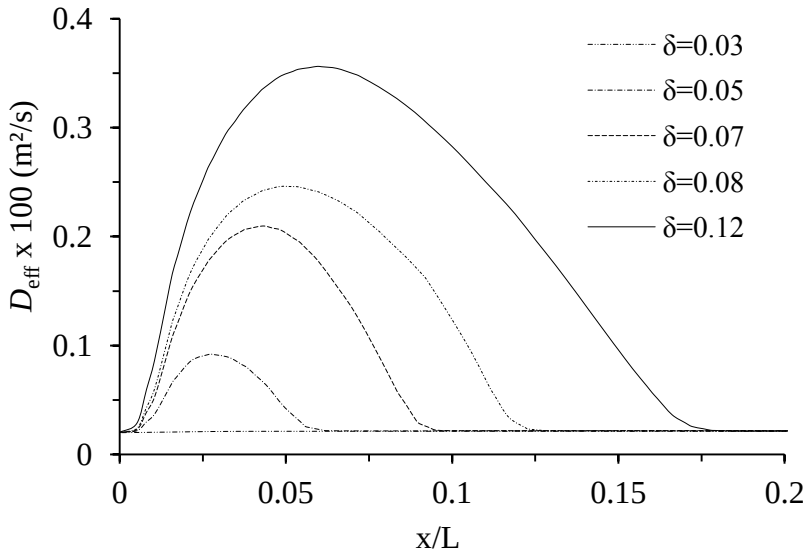

(7-26A)

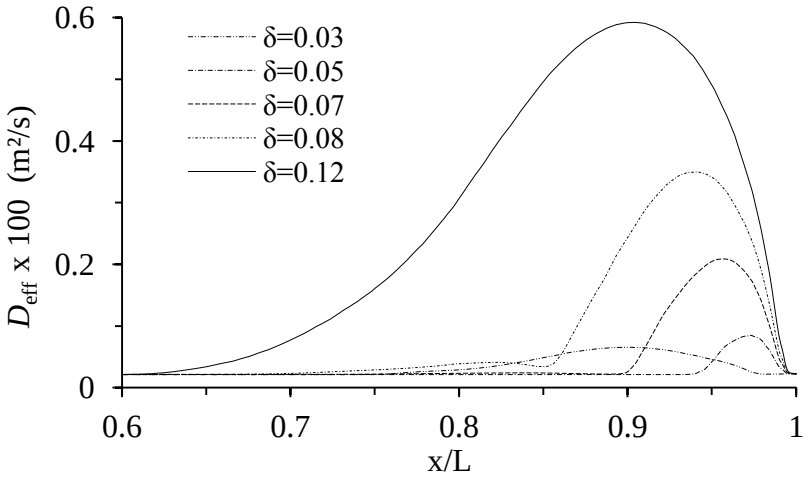

(7-26b)

Figure 7-26: Effective diffusion coefficient of vapour at mid height and near (a) cold wall (b) hot wall

7.7 **Conclusions**

Simultaneous heat and mass transfer due to low turbulent buoyancy driven flows have been numerically scrutinised. From our calculations, the following conclusions can be reached:

- Flow field is characterised by low turbulence near the walls while the core area is essentially a stagnant region; given that an appropriate equivalent emissivity is obtained.
- 2D simplification of a 3D domain is possible to save computational effort.
- Wall proximity can be seen to affect the overall heat transfer via flow field. The effect of turbulence is greatly reduced as the gap between the walls and the solid objects become smaller;
- The flow is sensitive to the appropriate choice of eddy viscosity models and hence a detailed understanding of the performance of EVM is required. For the EVMs tested in this work, the Launder-Sharma low-Re k-ε model gave the best performance.
- The flow field is dominated by low turbulence near the walls while the core area is essentially a stagnant region highlighting the fact that a multi-zone approach may be applicable.
- Radiation has been found to influence the flow and the rate of heat and mass transfer within the cavity especially for higher emissivity values (the implication is that by a careful selection of material, heat transfer may be passively influenced);
- The influence on fluid flow, heat and mass transfer due to the interaction with the obstacles was identified and detailed profiles have been obtained for critical locations.

Chapter 8 - PRACTICAL CASE STUDY: FLOWS AND HEAT DOUBLE SKIN FACADES WITH VENETIAN BLIND

8.1 Introduction

The potential to reduce building cooling load and annual energy consumption is widely recognized in the use of devices to control solar energy gain. Double-skin facades (DSF) are getting more and more attention and are widely used in commercial buildings. In hot summer and cold winter regions, a naturally ventilated external DSF with venetian blinds is the most common type, due to the simple control strategy and good energy performance, compared with mechanically ventilated DSF. In order to save air-conditioning energy and to guarantee indoor thermal comfort, the performance of shading, ventilation and heat transfer in naturally ventilated DSF buildings should be analyzed and optimized.

Although the concept is not new, its complexity and adaptability to different climatic conditions increase the need for further careful analysis. The fact that DSF are often influenced by aesthetics, their design is highly variable; hence the classification and the design parameters are very important. The accuracy of numerical modelling of the flow and heat transfer predictions in the facade will lead to less uncertainty in the design and construction by better adapting to the performance requirements of the designer.

Our research findings as presented in previous chapters provide a detailed knowledge base and numerical skills to fully describe the complex interaction between glaze/blockages with airflow and heat transfer system in the context of building energy simulation to accurately quantify this potential. This chapter focuses on the application of the research findings in the numerical analysis of heat and airflow in a double skin facade with integrated solar blockage system called venetian blinds.

The work is structured into various sections. Firstly, a detailed literature review which aims to highlight major factors that influence the flow and heat transfer in DSF systems in line with our previous investigation is presented. Secondly, a comprehensive numerical analysis of various aspects of facades and some parametric evaluation are presented. Finally, a discussion and conclusions section highlights some of the limitations found in the literature and recommendation for further

research and development needed in order to enhance the flow and heat transfer in Double Skin Facades.

8.2 **The concept of DSF**

In recent years, new building envelope systems have been developed in order to improve thermal insulation, shade solar radiation and provide suitable thermal and visual comfort conditions. One of these special types of envelopes is the double skin facade. The DSF is an arrangement with a pair of glass skins separated by an air corridor in front of the actual building facade [246-249]. Solar control devices are placed in the cavity between these two skins, which protect them from the influences of the weather and air pollution- a factor of particular importance in high rise buildings or ones situated in the vicinity of busy roads [250, 251]. A typical example is shown in Fig.8-1 below.

Figure 8-1: Schematic of DSF flow with solar blind

The concept of facades consists of an external screen, a ventilated cavity and an internal screen. Solar shading is positioned in the ventilated cavity gap, which influences the heat transfer and airflow due to strong buoyancy effect [252, 253]. The external and internal screens can be single glass or double glazed units and the depth of the cavity and the type of ventilation depend on environmental conditions, the

desired envelope performance and the overall design aesthetics of the buildings [14, 254-256].

The principal distinction between a DSF and a multiple glazing unit, integrating or not a solar protection in the cavity, lies in the possibility of controlled ventilation of the DSF [257]. In a traditional building the effective control of the solar gain via the usual outdoor blinds is in general difficult because of the interaction between the weather and the equipment. The additional external glazing, protecting these blinds from bad weather, thus creating a double-skin facade, makes it possible to solve this difficulty. This double layer envelope also allows the opening of the internal window and to carry out natural ventilation of the space. Fig.8-2 shows pictures of buildings with DSF system.

Figure 8-2: Examples of buildings with DSF system

8.2.1 **Useful classification of facade configurations**

The Belgian Building Research Institute Study (BBRI, 2002) [258] has developed a classification system to describe different double-skin facade configurations. This will be useful for facade selection in this study. BBRI classified facades according to: (a) ventilation type (b) partitioning of air cavity and (c) ventilation mode.

a) **Ventilation type:** this relates to the ventilation in the air cavity situated between the two glazed facades which can consist of; natural ventilation and mechanical ventilation
b) **Partitioning of the air cavity:** this refers to the physical division of the air cavity where distinction is made to separate windows from facades; air-flow windows and double-Skin Facades (DSF)

The Double Skin Facades are sub-classified into:

- One storey height façade modules – the air cavity is divided horizontally and vertically at the level of each facade module. Naturally ventilated double skin facades with one storey-height façade modules are also known as a 'Box window'.
- Corridor façades – are characterized by a wide air cavity partitioned at the level of each storey.
- Multiple storey façade – are not partitioned vertically or horizontally. The air cavity extends to a large height with metallic maintenance grids at the level of each storey allowing circulation.
- Shaft-box façade – are very similar in nature to the one-storey height module. However, the modules are linked with building high vertical shaft by means of a bypass opening. The stack effect draws the air from the box windows into the vertical shafts and from there up to the top, where it is emitted.

c) **Ventilation mode:** this classification relates to the origin and the destination of the air circulating in the cavity. Sub-classification of the ventilation mode are shown in Fig.8-3:

- Exhaust air
- Supply air
- Static air buffer
- External air curtain
- Internal air curtain

Choosing what appropriate facade classification to model is important by taking into account what needs to be accounted for in different configurations. Blind representation (positional sense) is a feature that is important in all common double-skin facades.

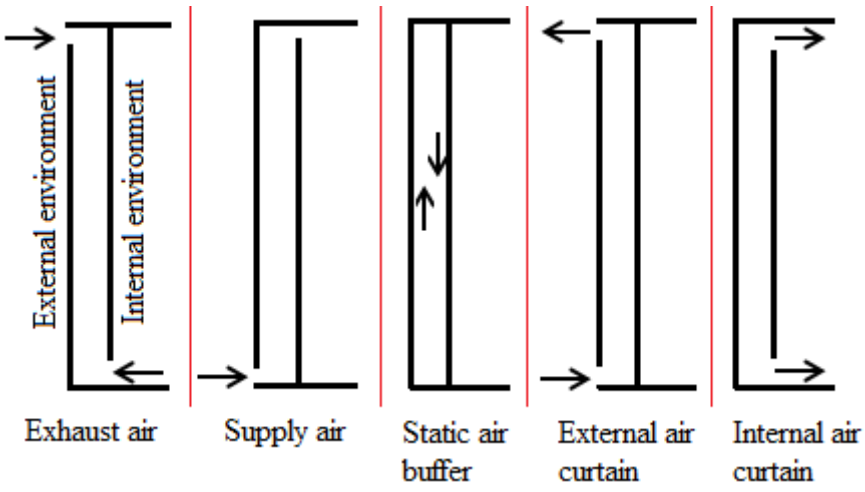

Figure 8-3: Schematic of the BBRI facade classification - ventilation mode

8.2.2 **Design aspect of DSF**

The geometry and type of double skin facades are crucial for the fluid dynamics and heat transfer characteristics of the air inside the cavity, hence such classification is a guide for initial design parameters. Fig.10-4 shows the path of air ingress and egress. The function of the facade and the HVAC strategy is closely dependent on the temperature and air flow of the air between the glass layers [259-262]. The main characteristics that influence the properties of the air in the cavity are the cavity depth, pane type, type and position of shading devices, size and position of the inlet and outlet openings of the cavity and the ventilation strategy.

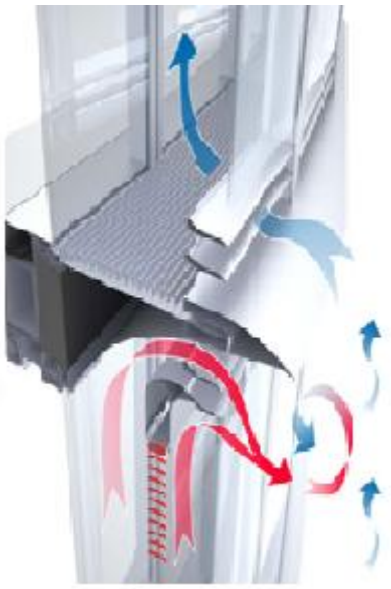

Figure 8-4: Air ingress and egress to and from the DSF channel

8.2.3 **Literature review on DSF modeling approaches**

Although DSF are already extensively used, their thermal performance is not well understood [256, 259-266]. The modelling and simulation of the Double Skin Facade Cavity is a complicated task, since different elements interact with each other influencing the function of the cavity. Efforts to model the cavity are focused mostly on air flow simulations, calculation of the temperature at different heights and daylight simulations. Airflow simulations are necessary in order to predict more accurately the temperature at different heights in the cavity. The temperature is also critical when deciding the design, types and ways of ventilation and materials.

Different modelling approaches have been adopted by different researchers in modelling the airflow and heat transfer within the cavity [132, 267-273].

Three methods are normally used for investigating the performances of DSFs. Research using field experiments has shown that the use of a DSF may lead to a reduction in energy usage in summer of up to 15% by using natural ventilation and up to 30% in winter by using passive solar heating [274]. Zollner et al. [263] conducted parametric studies of DSFs by varying the cavity depth in a full scale experiment. The work indicated that the buoyant air flow inside the façade cavity induced by solar radiation strongly depends on the ratio of the façade height to depth and the sizes of the ventilation opening into and out of the façade. Smaller scale DSF experiments by Ding et al. [275] also demonstrated the energy saving potential of using DSFs. Other researchers have used mathematical analysis to study the performance of DSFs, for example, the thermal network model used by Paassen et al. [276, 277] and the component-based nodal model developed by Hanby et al. [270] were used to simulate heat transfer mechanisms through DSFs.

Traditional experimental studies often lack flexibility to conduct parametric studies and the level of detail from the simple network models is limited. CFD modelling can potentially overcome these shortcomings, although the resources needed for detailed 3D simulations can be significant. Most of the CFD simulations work conducted to investigate façades with venetian blinds has been 2D (e.g. Shahid & Naylor [278] and Naylor & Collins [279]). 3D CFD simulation was conducted by Safer et al. [266] in which the venetian blinds were treated as porous media and the glazing elements as semi-transparent surfaces in order to reduce the mesh size. Marjanovic et al. [280] made other simplifications, such as reducing the façade width and height and increasing the thickness of the blind slats, in order to perform 3D simulations.

The approaches for numerical modelling of the air flow and heat transfer as classified by Djunaedy et al. [281] are:

- Building energy balance (BEB) models that basically rely on airflow estimation.
- Zonal airflow network (AFN) models that are based on (macroscopic) zone mass balance and inter-zone flow-pressure relationships; typically for a whole building.

- CFD that is based on energy, mass and momentum conservation in all (minuscule) cells that make up the flow domain; typically a single building zone.

Although airflow is an important aspect of thermal performance of building, its treatment in facade systems has been limited [282] due to inherent computational difficulties and lack of sufficient data. Recently, researchers [266, 283-285] are increasing the use of CFD approaches in modelling the air flow and heat transfer, since the conservation of momentum, mass and energy are solved for all nodes of the grid in the facade.

Ventilated facades are already a common feature of architectural competitions in Europe; but there are still relatively few buildings in which they have actually been realized, and there is still too little experience of their behaviour in operation as reported by Gratia et al. [131, 286-288], Zollner et al. [263] and Pasquay T., [289]. For this reason the CFD analysis could be one of the most important tools to predict the behaviour of DSF and help architects and engineers make decisions during the design process.

8.2.4 **DSF with blind**

The recent trend in the research community for the numerical modelling of flow and heat transfer in double skin facades is focused on facades with interaction of obstacles with the flow and heat transfer within the cavity. These obstacles are in the form of venetian blinds for solar shielding and building construction elements.

Mei et al. [290] , Safer et al. [266] and Ye et al. [291] conducted 2D numerical simulation to investigate coupled convective and radiative heat transfer through the DSF with venetian blinds inside the facade cavity. They investigated the influence of the blind angle in the range of 0 - 80° on the air flow and heat transfer within the cavity and their modelling results were validated with the measurement from a section of facade tested within a solar simulator, and with predictions from a component based nodal model. Agreement between experiment and numerical results was generally good and any discrepancies were caused by the implication of the CFD model resulting in less turbulence mixing within the facade cavity. Their results have shown that the presence of the venetian blinds has led to 35 percent enhancement in

natural ventilation flow and 75 percent reduction in heat loads for the internal environment and also the changes of the convective heat transfer coefficient on the glazing surfaces was caused by the venetian blinds with different angles.

Wilmer Pasut and Michele De Carli [292] of the University of California at Berkeley investigated the performance of the two most commonly used turbulence models (k-ε and k-ω) for simulating the naturally ventilated DSF and results validated against experimental data from literature. Nassim et al. [293] conducted a comprehensive numerical modelling of radiative and convective heat transfer of a compact double-skin facade equipped with venetian blind and concluded that the convective heat transfer coefficients found were weak and only little influenced by slat tilt angles, but its effects on radiative heat transfer was very important, since it regulated the solar radiation transmitted to the inside.

Neveen et al. [294] compared the performance of three different double skin facades configurations in prevailing summer conditions in a temperate climate. Their interest was on a possibility of air flowing from one level to the other and increasing the contaminant level on subsequent floors. They performed CFD simulation and compared cavity air velocity and temperature profiles to examine the potential for natural ventilation. Their results indicated that with almost similar air volumes inside the double skin cavity, the air velocities inside the cavity and into the rooms are unaffected by the changes in the outer skin configuration, and also, staggering the inlets and outlets of the internal skin lead to a negligible amount of return air entering into subsequent floors.

Fuliotto et al. [295] used a decoupling method to evaluate thermal performances and analysed fluid phenomena in a DSF. Solar radiation effects were evaluated with an analytical model, while complex flow and thermal effect were simulated using CFD. The numerical results agreed well with experimental data collected on a full scale test room with a ventilated DSF. Mei et al. [290] investigated the effects of external conditions, solar irradiation and exterior air temperature on double skin facade with differing internal characteristics. The effect of blind blade angle on cavity temperatures and air flow were reported.

Zhu et al. [296], developed a simplified mathematical model of heat transfer process in double skin facade to analyze the effect of outside environmental parameters and dimension of facade on the temperature of the interior and facade. Their results show that the main factor affecting facade temperature is solar irradiance and that the temperature of the interior and exterior facade would be lowered by using glazing with low absorption coefficient to decrease the effect of solar irradiance on indoor environment. Also, the temperature of the interior and exterior facade could be lowered by increasing the depth of facade gap, but the effect of lowering temperature by increasing the gap by a large amount was not obvious.

Behzad et al. [297], evaluated the effect of DSF's air-gap size on the amount of solar heat transferred through the façade envelope. They used a CFD tool to simulate six different strategies. Analysis of their results shows that the DSF air-gap size is an important factor in order to reduce solar heat gains and temperature reduction of up to 3^0C by well designed gap size.

Teshome et al. [298], investigated the airflow and heat transfer for a DSF system equipped with a venetian blind using the RNG turbulence model for a three-level combination of slat tilt angle and blind position. The prediction was validated using experimental data collected for a mechanically ventilated DSF equipped with venetian blinds. The predicted trends in glass and blind surface temperatures of the CFD model are compared well with the experimental measurements. Their results show that the presence of venetian blinds influences the surface heat transfer coefficients and the temperature and the air distribution in the DSF system. Also, the changes in the position of the blinds (outer, middle, and inner) have more effect on the distribution of temperature, velocity, and heat transfer compared to the changes in the slat angles (0◦, 45◦, 90◦).

Wong et al. [299] investigated the effects of double glazed facade with ventilation system on the energy consumption, thermal comfort and condensation and compared results with a single glazed system. Their simulated results showed that double glazed facades with natural ventilation are able to minimize energy consumption as well as to enhance the thermal comfort, and that turning the mechanical fans on could also solve the condensation problem due to high humidity. Mona et al. [300], investigates the

energy performance of a high-rise office building equipped with convectional insulated glazing using Energy Plus and CFD software Fluent to evaluate various thermal comfort parameters for the new configurations and their results show that the new configuration had a major impact on enhancing natural ventilation and hence a reduction in energy consumption.

8.3 Limitations from the literatures

The brief literature presented above highlight some of the research done on the flow and heat transfer in double Skin Facade. These studies have shown that the classifications are commonly based on geometrical parameters and channel ventilation strategies. Some of the limitations identified from the literature are highlighted below:

- Accurate and detailed CFD modelling of a full scale DSF for the turbulent air flow along with solar radiation heat transfer and the interaction of construction materials with the flow and heat transfer has not been reported. A thorough analysis will lead to less uncertainty in the design and construction by better adaptation to the performance requirements of the designers.

- The effects of blinds (position sense) on the flow dynamics and heat transfer to the indoor space have not been quantified.

- There is discrepancy on the choice of geometrical configuration for numerical modelling. Parametric studies on different coupling approaches will be a useful tool for saving computational cost and effort.

- The influence of outdoor air temperature and solar irradiation on various parameters of the indoor space has not been quantified in detail.

8.4 Parametric study of DSF with venetian blinds

The facade systems of commercial buildings are the main component of the building envelope that receives external heat gains such as solar irradiance transmitted directly through the facade or indirectly as secondary heat flux from absorbed irradiance. The temperature increase through absorption on shading devices inside such a double facade depends on air volume flow rates and the optical characteristics. The effects of external conditions, such as solar-irradiation and outdoor air temperature were

investigated with differing internal characteristics which are presented and analysed. In particular, the effect of the solar-blockage angles and its positioning within the DSF channel on the airflow and thermal performances of the cavity and the indoor space is reported. The quantified values will serve as an outline and guidance to assist designers of such facades.

The objective of this study is to perform a detailed numerical model for the airflow and heat transfer phenomena in the DSF system to study the influence of the location of the blinds and the slat angle on the temperature and air distribution in the air cavity and on the glass surfaces. Also investigated is the influence of external environment temperature and solar irradiation. The result of the research is an improved understanding of the thermal and air flow behaviour of such ventilated double skin facades.

8.4.1 **Case description**

In this study we are interested in a compact one floor DSF geometry similar to the test case used in the experimental study of Mei et al. [290]. Apart from aesthetic considerations, the main reason for using the configuration is summarised as follow:

- High level of natural lighting and sound insulation contribution.
- Increase of natural ventilation contribution.
- The internal environment is protected from wind and pollutants.
- Cooling load reductions if a solar blockage system is installed.
- Low risk of condensation on transparent surfaces because of the continuous air movement.

The test facility (Fig.8-5) is located in an environmental chamber and consists of a solar generator, a DSF and controlled internal environment located behind the inner glazing. The DSF consists of a single outer glazing element; venetian blinds were situated at one-third of the facade. Solar heat flux is generated from a full-scale solar generator which is located at the front of the facade. Only direct solar radiation is considered in the CFD model as the diffuse effects were expected to be negligible. The Rayleigh numbers based on the channel height for all the cases investigated are in the order of 10^9 to 10^{10} which is within the range of flows addressed in this thesis. The

primary input data are the outdoor/indoor air temperature, solar irradiation from the solar generator and heat transfer coefficient of the facade walls.

The main dimensions of a double skin were taken from the experimental work of Mei et al. [290], as shown in fig.8-6. The external environment dimensions are 3.8m high by 0.6m wide and 1.28m depth. The outer skin of the facade is a single 12mm thick clear glass pane. The external glass area is 1.28m and 1.91m high. Both the air intake and exhaust of the DSF are designed as a commercial grille arrangement to permit air flow through the cavity. The grilles are 0.24m high and 1.45m wide. Each grille (inclined at 30^0 to the horizontal line) has three 0.045m high spaces for air ingress and egress. The inner glass area is 1.28m by 2.44m high.

The sun-shading blind is a Venetian type blind (solar-blockages). The blind is made of aluminium and is 2.1m high and 1.45m wide. The blind blades are 80mm wide and the blind is located at one third of the cavity width as measured from the outer skin of the external glaze. The cavity formed by the outer and inner layer is ventilated and frequently contained a blind. This blind, together with the cavity ventilation, provides a means to control the heat transfer across the facade, in terms of solar gain transmission and recovery of heat lost from the interior.

Figure 8-5: Test chamber showing solar generator and DSF , Mei et al. [290]

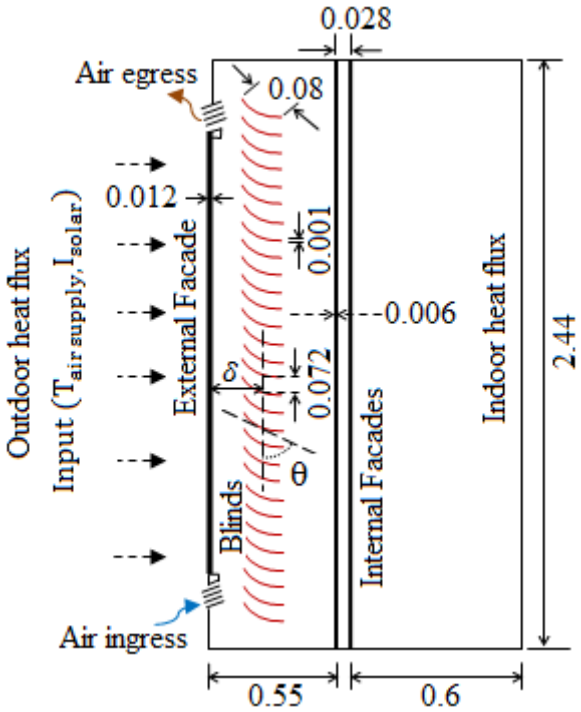

Figure 8-6: Schematic description of the model (δ=blind proximity from external glaze)

The current study addresses the limitations from the literature findings as reported earlier. Numerical parametric studies are done for the heat transfer problem in order to fully describe the gain to the indoor space. The convective and long-wave radiation fluxes were modelled in addition to the transmitted solar flux. A parametric study was conducted to quantify the influence of several factors of the air flow and heat transfer by the DSF. The factors investigated are;

1. Modelling strategies
2. Solar irradiation
3. Solar blockages
   I. Solar blockages proximity from the external glazing
   II. Solar blockages inclination angle from the vertical centre-line
4. Environmental air temperature influence.

Fig. 8-7(a-b) gives the schematic of the facade with the external and the internal environment and the DSF ventilation pots (air ingress and egress)

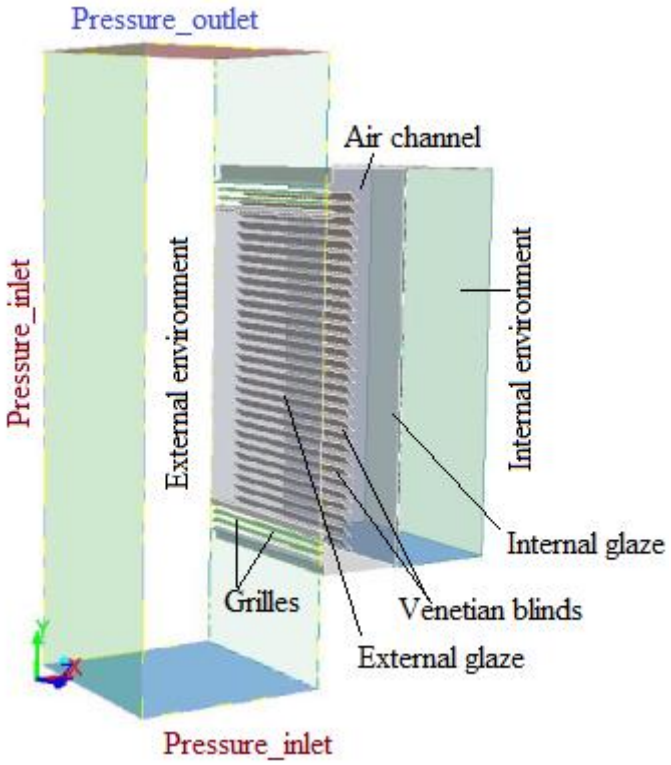

(8-7a)

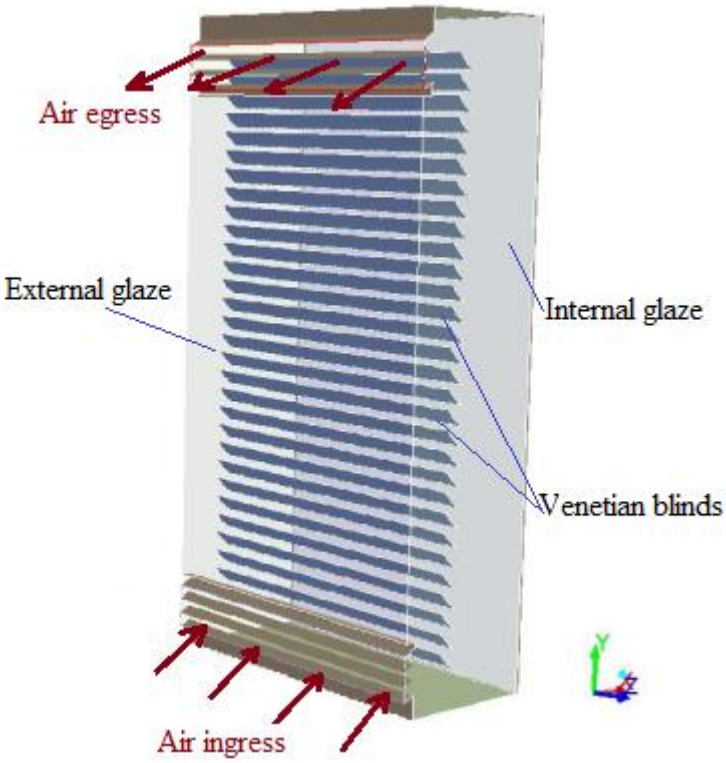

(8-7b)

Figure 8-7: Schematic diagram: (a) computational domain, (b) ventilation of the DSF geometry

8.4.2 **Modeling strategies**

Several solution techniques exist for the numerical modelling of DSF system in the open literature. There seem to be no studies to evaluate the influence of the different modelling strategies based on coupling and/or decoupling of the external and/or internal environmental conditions with the DSF channel flow and heat transfer. This current study aims to resolve this uncertainty by quantifying the influence of different modelling approaches for the airflow and heat transfer. Four different cases of modelling strategies were considered as shown in Fig.8-8a-d. These are (a) DSF channel + outdoor fluid + indoor fluid, Case 1., (b) DSF channel + outdoor fluid, Case 2., (c) decoupling the DSF flow with the internal and external environments, Case 3., and (d) DSF channel + indoor fluid, Case 4. For simplicity, the outdoor environment wind speed is not considered. For the investigation into the influence of solar blockages inclination and proximity, the configuration used is that of the DSF cavity coupled with the internal environment (heat output) only. This arrangement was used for the studies (solar irradiation, solar blind and outdoor temperature influence) because of our interest in evaluating some key parameter in the indoor environmental.

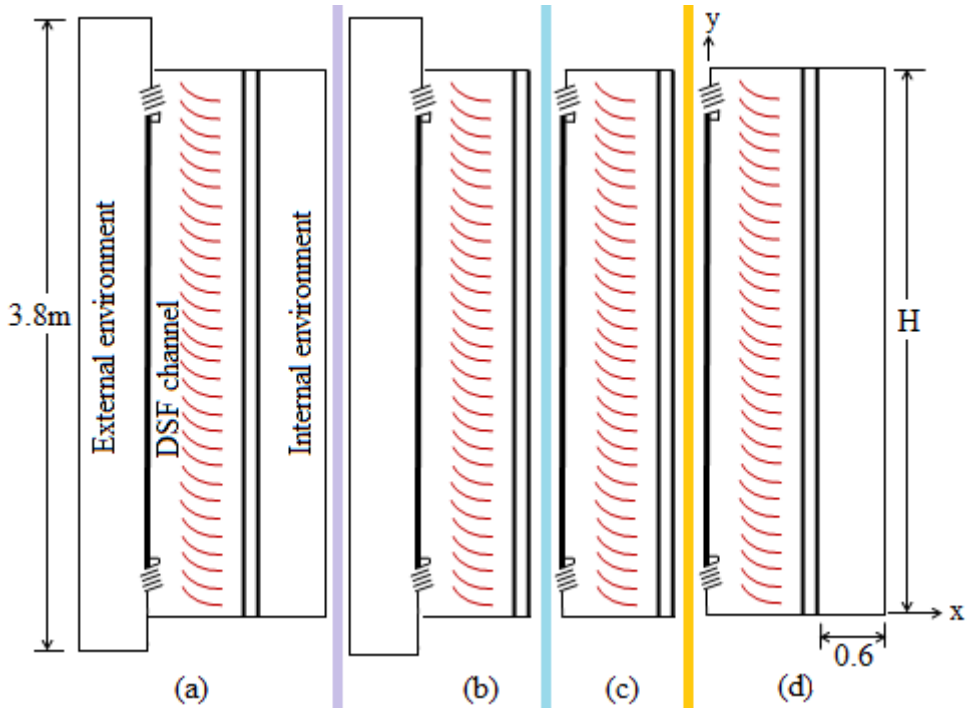

Figure 8-8: Modelling geometrical cases (a) case 1 (b) case 2 (c) case 3 (d) case 4

8.4.3 **Solar irradiation and blockage influence**

The solar blockages angle and solar irradiation are very important, since they regulate the amount of radiation transmitted to the indoor environment. Heat exchange between the glazing elements and the surrounding occurs by conduction, convection and radiation. The solar irradiance values used in this investigation range from 120W/m² to 715W/m² BBRI, 2002 [258]. Parametric study on the influence of the solar blockages on the airflow and heat transfer to the indoor space, in particular the effects of different blockages location/inclination within the DSF channel on energy transfer are studied.

It is important to quantify the airflow and thermal behaviour of the indoor environment due to the blockages inclination angle since it regulates the amount of solar heat and visible solar flux transmitted to the indoor space. This parametric study is aimed at finding the optimal location of the solar blockages devices in order to achieve a high air flow within the DSF channel. If this can be guaranteed, the risk of an undesirable facade overheating can be avoided. It is assumed that the angles of inclination (θ in Fig.8-6) which the solar-blockages make with the vertical axes can be adjusted to achieve a series of blockage inclination angles from the vertical centre-line (15^0, 30^0, 45^0, 60^0 and 75^0). Also the proximity of blinds, δ also shown in Fig.8-6, the external glazing can be varied for values of 0.104m, 0.195m, 0.287m, 0.379m and 0.470m. The outdoor and indoor air temperature is fixed at 20^0C for all solar irradiance values used in the simulation.

8.4.4 **Outdoor temperature influence**

The air flow and heat transfer of the facade are evaluated by carrying out a detailed numerical study on the external environmental temperature variation ranging from 10^0C to 40^0C at an inlet velocity set at 0.15m/s. The tests for the influence of solar blockage, modelling strategies and environmental influences were carried out at fixed conditions of 715W/m² irradiance and 20^0C temperature for both indoor and outdoor environments.

8.5 Solution method for coupled DFS Flow with solar irradiation

In this section the issues of airflow and irradiation modeling are discussed in some detail in order to highlight the specific matters in the context of DSF. The fundamental methodology and the governing equations are mostly the same as given in Chapter 3.

8.5.1 Airflow modeling

A comprehensive numerical modelling of solar radiation and convection heat transfer of a compact DSF equipped with solar blockages is carried out. Calculations were performed using the commercial CFD package FLUENT 14.0. Turbulence was modelled using the Launder-Sharma low Reynolds number of the k-ε model. In the 3D full scale coupled DSF model a non-uniform structured and unstructured mesh density of about 6million was used. $y^+$for the final mesh was found to be 1 for all surfaces.

As mentioned before, the process of computing a steady-state solution using a very fine mesh has been quite challenging as a result, a number of steps were taken to achieve the solution as described in section 4.3. Briefly, the energy and the radiation equation were decoupled from the momentum equation and were solved first. When the temperature on the components developed sufficiently, the flow equations were then solved together with the radiation equation and iterated to convergence. The large difference in the thermal conductivity between the air and the aluminium blinds may result in numerical round-off error, which caused global imbalances of energy as oscillation. Therefore, the simulation was run in double-precision to overcome this problem. All simulation cases used the second-order upwind scheme for all the variables except for pressure. The pressure discretization used the Body Force Weighted scheme. Table 8-1 shows the values of the Under-Relaxation factors.

Table 8-1: Under-Relaxation parameters used in the simulation

Pressure	0.3
Density	0.8
Body Force	0.8
Momentum	0.3
Turbulence kinetic energy	0.5
Turbulence dissipation rate	0.5
Turbulence viscosity	0.8
Energy	0.9
Discrete Ordinate	0.8

The calculations were started with reduced under relaxation factor for energy and discrete ordinate and gradually increased to the final values as shown in Table 8-1 to keep the residuals stable. All calculations are done with a steady state formulation of the numeric solver, as additional transient investigations did not achieve higher accuracy. The angular discretization used in the DO modelling for the localized heat source is 6x6 divisions. A sensitivity study of the angular discretization was performed by starting with 2x2, then 4x4, and so forth until there is no considerable change in maximum temperature at 6x6 divisions.

8.5.2 **Delimitations**

Some delimitation had to be made in order to focus the work on the essentials and to be able to make appropriate simplifications, the delimitations are: (a) Only one double skin facade geometry is considered. (b) The only heat source is from the beam from the solar generator. (c) Boundary condition will represent one specific point in time. (d) The external and internal glazing is modelled as a semi-transparent material. (e) The solar blockages are modelled as opaque walls, and the scattering in the glazing surface are assumed to be neglected. (f) The thermal conductivity of the glazing material is assumed to be constant and independent of its temperature. (g) air inside the double-skin and the air of the double glazing are modelled as a transparent material. (h) Only the inside face of the interior glazing communicates convectively with the indoor space, as opposed to both glazing and solar-blockage surfaces.

8.5.3 **Solar irradiation modeling**

Solar ray tracing options of the solar load model [301] (FLUENT 14.0) were employed to calculate radiation effects that enter the computational domain. The ray tracing approach is highly efficient and a practical means of applying solar loads as heat sources in the energy equations and it provides a practical tool for determining the solar heating effect inside a building. The solar load model of the ray tracing algorithm is used to predict the direct illumination energy source that results from incident solar radiation. It takes a beam that is modelled using the incident solar radiation position vector and illumination parameters and applies it to any or all wall or inlet/outlet boundary zones, performs a face-by-face shading analysis to determine

well-defined shadows on all boundary faces and interior walls, and computes the heat flux on the boundary faces that results from the incident radiation.

Solar Ray Tracing is not a participating radiation model. It does not deal with emission from the surfaces. The reflecting component of the primary incident load is distributed uniformly across all surfaces rather than being local to the surfaces reflected to. Surface emission is an important factor in our study; therefore we implement a radiation model (Discrete Ordinates method) in conjunction with the Solar Ray Tracing. The discrete radiation model is coupled with the solar ray tracing model to deal with emission from surfaces, and the reflecting component of the primary incident load through the computational domain.

Direct solar irradiation from a solar generator is transmitted by radiation and some by natural convection through the glazing elements of the DSF to the temperature controlled internal environment located behind the inner glazing. Some of the radiation emitted by the solar simulator is transmitted through the glazing elements, while some is reflected and some is absorbed. The flow iterations per radiation iteration were specified as 5(since radiation is the dominant mode of heat transfer in the computational domain). For the angular discretization parameters, the value 3 was used for Theta Divisions and Phi Divisions and 6 for Theta Pixels and Phi Pixels.

8.5.4 **Conduction model of the glass wall**

In order to obtain the temperature profile at the glass wall, FLUENT uses a differential energy balance equation to determine the conductive heat flux. The heat transfer equation for the differential element of the glass wall in two dimensions is given by;

$$\frac{\partial}{\partial x}\left[\frac{k_g}{Cp_g}\frac{\partial T_g}{\partial x}\right]+\frac{\partial}{\partial y}\left[\frac{k_g}{Cp_g}\frac{\partial T_g}{\partial y}\right]+\frac{1}{Cp_g}\frac{d\emptyset}{dx}=0 \qquad (10-1)$$

Where $\emptyset$ is the attenuation energy function by absorption and scattering, which depends on the extinction coefficient (s_g) as shown in equation (10-2) [302].

$$\emptyset(x)=I\,exp\left[-s_g(L_g-x)\right] \qquad (10-2)$$

Where I is the solar radiation, L_g is the thickness of the glass.

The boundary condition for the glass walls is expressed in equation (10-3) [$x=W+L_g$]:

$$-k_g \frac{\partial T_g}{\partial x} = h_{ext}\left[T_g - T_{amb}\right] + \sigma \varepsilon_g^* \left[T_g^4 - T_{amb}^4\right] \qquad (10-3)$$

Where T_{amb} is the outdoor ambient are temperature

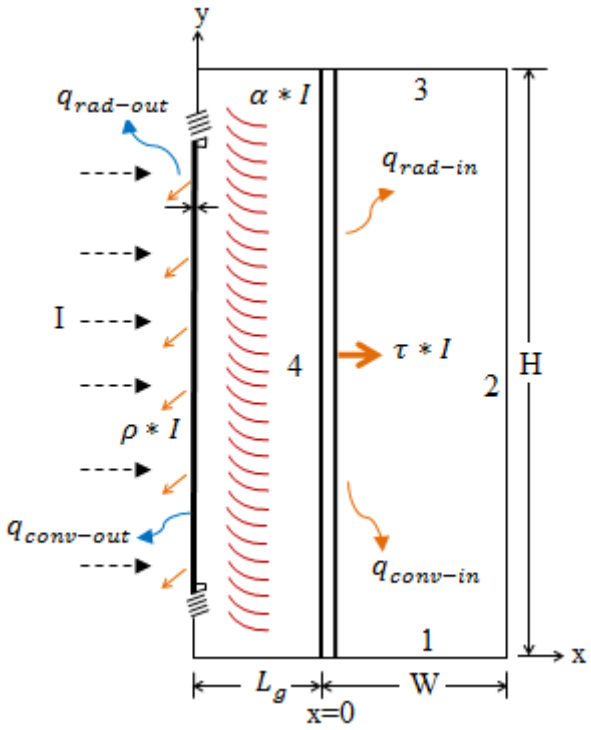

Figure 8-9: Schematic representation of the heat transfer analysis.

The velocity boundary conditions on the walls are zero and temperature boundary conditions are set as: Bottom adiabatic wall (wall 1): $q_{cond-1} = -q_{rad-1}$

Isothermal vertical wall (wall 2): $T(0, y, t) = T_2$

Top adiabatic wall (wall 3): $q_{cond-3} = -q_{rad-3}$

Glass vertical wall (wall 4): $q_{cond-g-4} = q_{cond-4} + q_{rad-4}$

Where q_{cond-1}, q_{cond-3} and q_{cond-4} are the conduction heat fluxes for wall 1, 3 and 4 respectively.

8.5.5 **Thermal parameters**

The total heat transfer across the glass wall is given by the Nusselt numbers. The total heat transfer involves the contribution of the convective and radiative Nusselt numbers which can be expressed as:

$$Nu_{total} = Nu_{conv} + Nu_{rad} \qquad (10-4)$$

Where:

$$Nu_{conv} = \frac{k}{q_{cond}} \int_0^H \frac{\partial T}{\partial x} dy \qquad (10-5)$$

$$Nu_{rad} = \frac{1}{q_{cond}} \int_0^H q_{rad}\, dy \qquad (10-5)$$

8.5.6 **Numerical modeling parameters**

The materials used for the simulations are transparent media (air), semi-transparent solids (glazing) and opaque solids (venetian blinds). The key parameters of these materials for air flow and heat transfer are shown in Tables 10-2 and 10-3. The air density is set as a function of temperature using the Boussinesq approximation method. This method treats density as a constant value in all solved equations, except for the buoyancy term in the momentum equation (equation (3-3).

Table 8-2: Thermo-physical properties of air at 20^0C

Property	Dry-air at 20^0 C
Density (kg/m^3)	1.2047
Specific heat (J/kg-K)	1006.1
Thermal conductivity (w/m-)	0.0256
Absorption coefficient (1/m)	0.01
Refractive index	1
Dynamic Viscosity (kg/m-s)	1.821 x 10^{-5}
Thermal diffusivity (m^2/s)	2.112 x 10^{-5}
Thermal expansion coefficient (1/K)	3.411 x 10^{-3}
Prandtl number	0.7156

Table 8-3: Thermo-physical properties of the material used in the simulations

Property	Single glazing	Double glazing	Venetian blinds	Passive walls
Density (kg/m^3)	2500	2500	2719	10
Specific heat (J/kg-k)	840	840	871	830
Thermal conductivity (w/m-k)	1.7	1.7	202.4	0.1
Absorption coefficient (1/m)	30* 3000*	30* 1285.7**	-	-
Refractive index	1.5	1.5	1.44	1
Emissivity	0.84	0.84	0.7	0.58

**** For wavelength 0–2.7 micrometers and * for wavelength 2.7–1000 micrometers

The external glazing element whose outer surface is exposed to ambient air is modelled as an internal wall with cells on both sides, so that there is also a shadow zone corresponding to it. The shadow is facing the fluid zone. The inner and the outer surface of the glazing elements are set to semi-transparent conditions. This allows radiation to be transmitted through the wall between the adjacent participating cell zones. It also calculates the effect of reflection and refraction at the interface. These effects occur because of the change in refractive index (set through the material properties) and are a function of the incident angle of the radiation and the surface finish. In our case, the glazing element is assumed to have a very smooth surface so the diffuse fraction is set to 0.

The DFS cooling mechanism on the outer surface of the glaze is by natural convection and radiation. The convective heat transfer is taken as 25 W/m²k following BBRI, 2002 [258]. It is worthwhile to mention that the effect of environmental condition and wind speed can be partially modelled via the heat transfer coefficient.

8.5.7 **Boundary conditions**

In the computational domain, glazing elements are modelled as semi-transparent solids and venetian blinds as opaque solids. The semi-transparent glazing elements are spectrum selective of radiation transfer, i.e., short wave radiation (solar) has a very high transmittance while long wave (thermal) radiation has a very low transmittance. These have been modelled using a 'two-band' spectrum model (ANSYS FUENT-14). The solar band corresponds to wavelengths smaller than 2.7 micrometers, and the thermal band to wavelength larger than 2.7 micrometers. All glazing materials are considered as participating in radiation, which enables transmission and absorption of radiation inside the DSF.

The surface of the external glazing element is mainly cooled by natural convection to the surrounding. As these walls are transparent it must also lose radiation to the surroundings, while the surroundings will supply a small source of background radiation associated with the temperature. Therefore a mixed thermal condition was applied to provide the source of background radiation as well as to calculate the convective cooling on the external glazing. The source of the background radiation is added directly to the discrete ordinate (DO) radiation equation. The background

radiation was supplied from the thermal conditions. An external emissivity of 1 is used, in keeping with the assumption of a small object in a large enclosure [303]. For a semi-transparent wall the internal emissivity has no effect as there is no absorption or emission of the surface.

It is assumed that the glazing elements are clean and there are no particles in the air to scatter the radiation in different directions, the scattering coefficient is set to zero (assuming zero humidity). Conduction in the solar blockage thickness (0.001m) is modelled as a thin wall by using the shell conduction thermal condition and with the help of text user interface to achieve robustness; the command ignores the secondary gradient for highly skewed shell conduction cells. This allows the solver to grow layers of prism to model conduction in the planar direction according to the specified thickness. The absorptivity and transmissivity of all glazing and opaque material is given the Table 8-4. This applies to the long wave (infrared) and short wave (visible) bands. These radiant properties are obtained from ASHRAE fundamentals handbook 2010 [304].

The spectral transmission and absorption behaviour of glass was considered in the definition of material properties and especially in the implementation of the radiation model. Glass has a high transparency for visible light, but it is nearly impermeable for infrared radiation with a wavelength beyond 2.5 micrometers.

Table 8-4: Solar radiance properties of materials used

Surface	Material	Radiant properties
External glass	Single glazed clear glass	$\alpha_v = 0.09, \alpha_{IR} = 0.09, \alpha_D = 0.1$ $\tau_v = 0.83, \tau_{IR} = 0.83, \tau_D = 0.75$
Internal glass	Double glazed coated glass	$\alpha_v = 0.49, \alpha_{IR} = 0.49, \alpha_D = 0.49$ $\tau_v = 0.3, \tau_{IR} = 0.3, \tau_D = 0.32$
Venetian blind	Aluminium	$\alpha_v = 0.5, \alpha_{IR} = 0.75$

Were,α represents absorptivity τ represents transmissivity. The transcripts v, IR and D represents visible, infrared and diffuse hemispherical components respectively.

The external wall is exchanging heat with a convection coefficient "h" chosen according to the European standards for building design [305]: the convective heat transfer coefficient of the external glazing is 25.0 W/m²-k, and that of the internal glazing is 7.7 W/m²-k. The external and internal temperatures were both fixed at

20ºC. The upper and lateral walls are considered adiabatic and they do not participate in the solar ray tracing. Surfaces outside the double skin and the air ingress and egress are modelled as a pressure inlet and pressure outlet with the same gauge total pressure of 0. The boundary of the air ingress and egress are modelled as a pressure inlet and pressure outlet with the same gauge total pressure of 0, and in order to improve the result quality an angle the same as the ingress grille angle (30^{O}) was used for the air direction in the ingress boundary condition. For the modelling strategies study, the boundary conditions used for the external and internal boundaries are represented in Fig. 8-7a-b.

8.6 **Results and discussions**

Fig.8-10 shows the schematic where all parameters were evaluated.

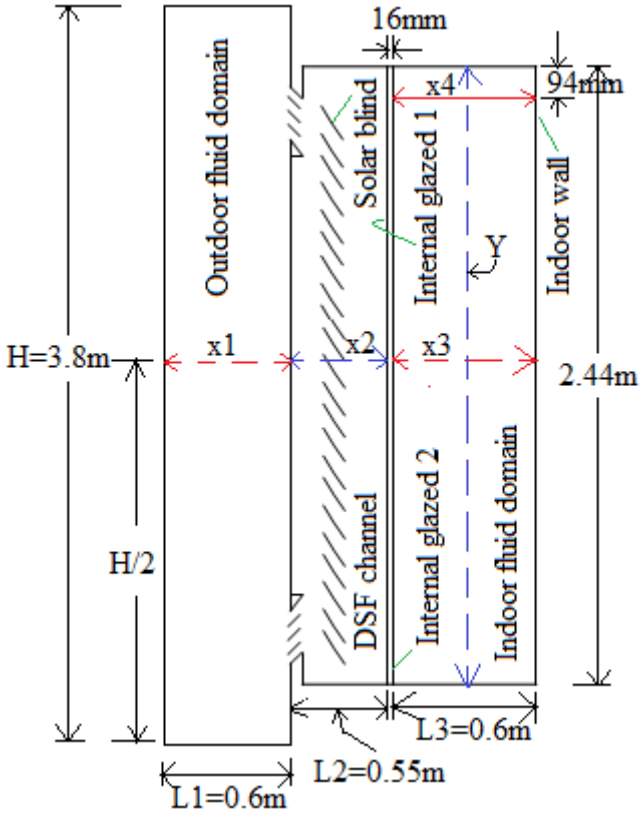

Figure 8-10: Schematic showing lines along the central plane were parameters are evaluated.

Convective and solar heat transfer were evaluated at the internal glazed (1 & 2) and indoor wall surfaces. The domain widths are the outdoor (x1), DSF channel (x2) and indoor domain (x3 and x4). The horizontal temperature profile near the top wall of the

indoor space was also compared for different parametric study. "Y" represents vertical line at mid-width of the indoor fluid domain. The solar flux field has also been presented for the investigation of the influence of a solar blind on heat transfer. Numerical results for the geometrical modelling strategies have been presented first followed by the results on solar irradiation. Solar blind positioning and inclination angle within the DSF channel are then presented, along with variation of outdoor air temperature.

8.6.1 **Modeling strategies**

As stated earlier, the modelling approach cases used in this study are: Case 1 (DSF channel + outdoor + indoor fluid zone), Case 2 (DSF channel + outdoor fluid zone), Case 3 (DSF channel only) and Case 4 (DSF channel + Indoor fluid zone) as shown in Fig.8-8. The mesh density and computational effect are presented in Table 8-5.

Table 8-5: Computational efforts for all modelling strategies studied

Cases	Number of cells (Million)	Time (hours) to reach converged solution
Case 1(DSF)	4	96
Case 2 (DSF + indoor)	5	120
Case 3 (outdoor + DSF)	5	120
Case 4 (outdoor + DSF + Indoor)	6	I44

The predicted temperatures are plotted in Figs.8-11a-d along chosen lines x1, x2, x3, x4 and Y as shown in Fig.8-10.

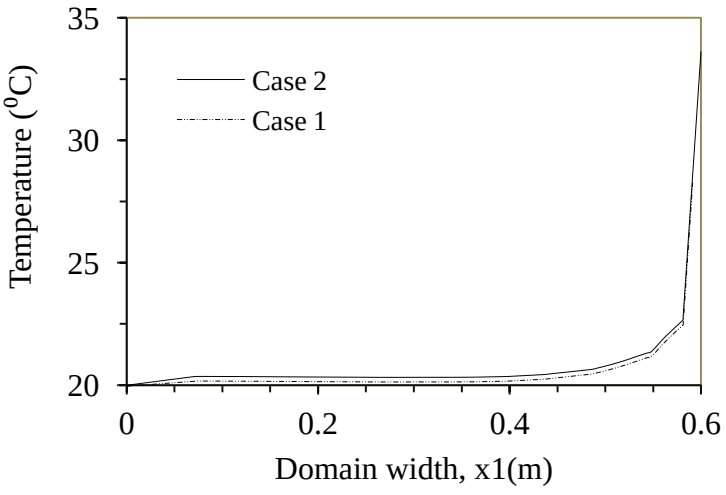

(8-11a)

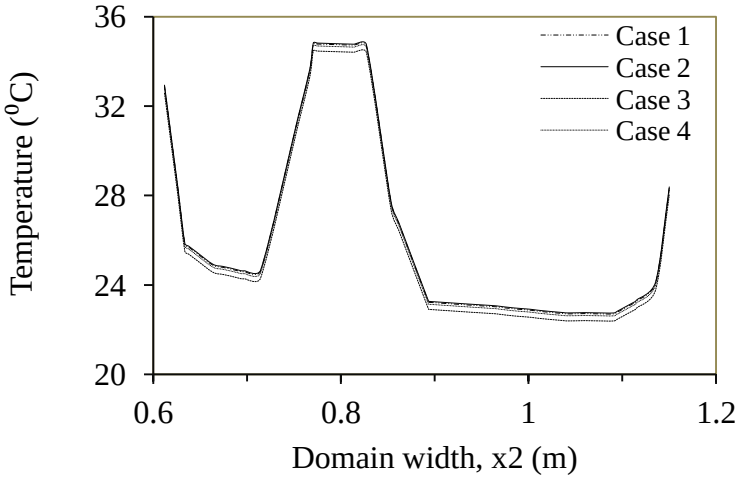

(8-11b)

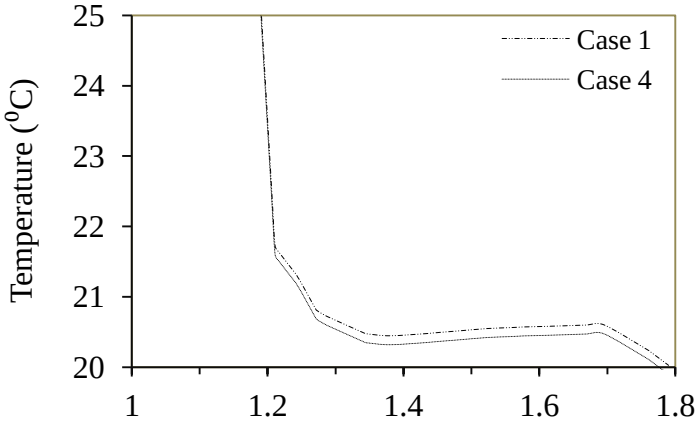

(8-11c)

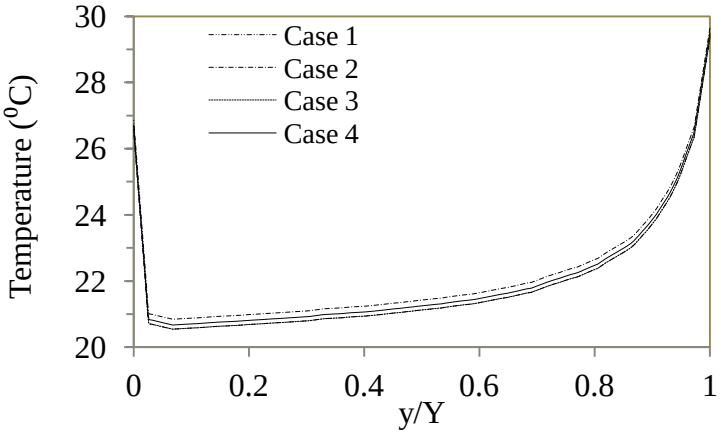

(8-11d)

Figure 8-11: Temperature profile at (a) at mid-height of the outdoor environment (b) mid-height of the DSF channel (c) mid-height of the indoor environment (d) mid-width of the DSF channel (=H/2)

Table 8-6: Average surface heat flux

Surface	Average Wall Heat Flux (W/m²)			
	Case 1	Case 2	Case 3	Case 4
Internal glaze 1	40.7	40.59	40.88	41.01
Internal glaze 2	35.61	35.97	35.69	35.74

Table 8-7: Average solar heat flux

Surface	Average Solar Heat Flux (W/m²)			
	Case 1	Case 2	Case 3	Case 4
Internal glaze 1	61.03	60.9	60.88	60.57
Internal glaze 2	32.85	32.66	33.14	32.91

Fig.8-11a shows the temperature profiles at the mid-height of the DSF cavity for all cases tested; it can be observed that the maximum average temperature difference between all cases is about 0.4^0C. Also, the temperature profile of the indoor environment (case 2 and 4) at the mid-height is presented in Fig.8-11b and again there is no significant temperature difference between the two cases. Finally, Fig.8-11d shows the temperature profile at the mid-width of the DSF channel for all cases and Tables 8-6 and 8-7 show the average wall and solar heat fluxes at the double-glazing and internal glazed-1 is facing the DSF channel zone and internal glazed-2 facing the indoor zone respectively. It is observed that the relative difference in the results is not very significant compared to the average temperature and heat fluxes (wall and solar). Therefore, for all four modelling strategies employed in the study, there appears to be no significant difference in the key parameters responsible for the heat transfer which eventually determine the performance of the DSF, provided all indoor and outdoor boundary conditions are determined accurately. However, inclusion of external and internal environments can be useful if there is a need to investigate the behaviour of these environments. But, it will be less cost effective and also save computational effort by not including these domains in computations if the primary need is to numerically model the DSF channel only as is evident from Table 8-5. It is also clear that case-4 allows freedom in simulating complex environment scenarios.

8.6.2 **Influence of solar irradiation**

Solar irradiation measures the total amount of solar radiation which is transmitted to the surface of the external glass and then transmitted through the DSF to the indoor environment. The values of irradiation employed for the analysis ranged from 120 to 715W/m². For all results presented in this section the internal facade is closed with no free window ventilation, and the computational domain involves coupling the DSF domain with the indoor domain (case-2). Angle of inclination of the solar blockage and the indoor wall temperature are fixed at 45^0 and 20^0C respectively. Therefore, the heat transfer to or from the indoor space are due to the combined effects of radiation, conduction and natural convection on the internal glazing surface.

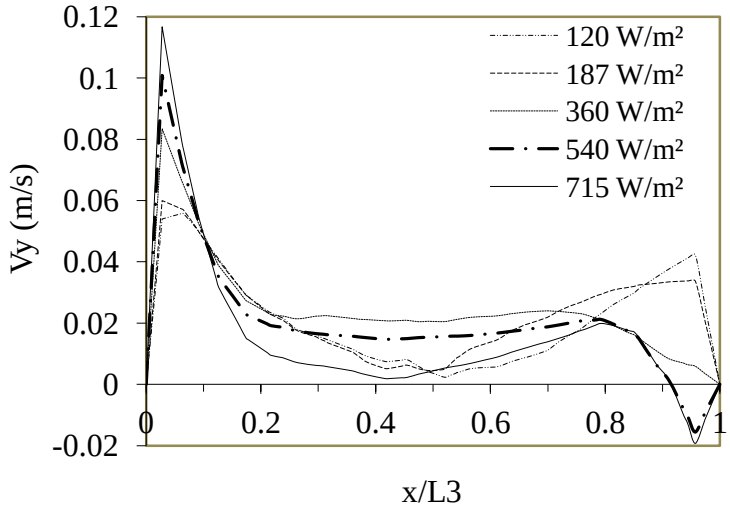

Figure 8-12: Horizontal velocity profile at mid-height of the internal wall

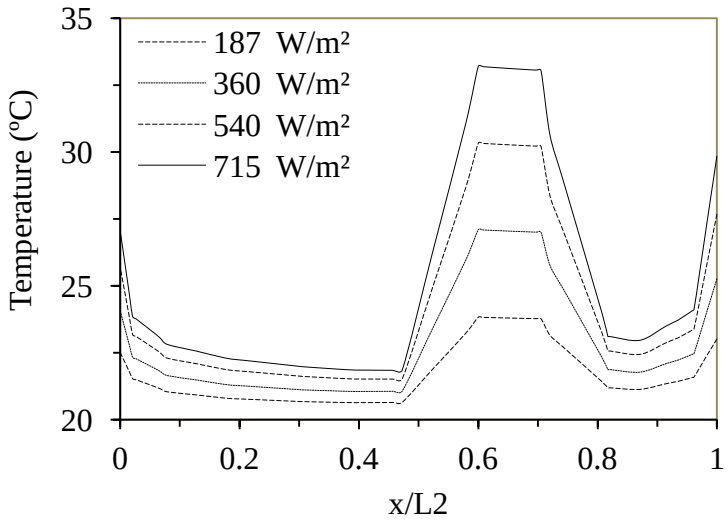

Figure 8-13: Horizontal temperature profile at mid-height of DSF channel

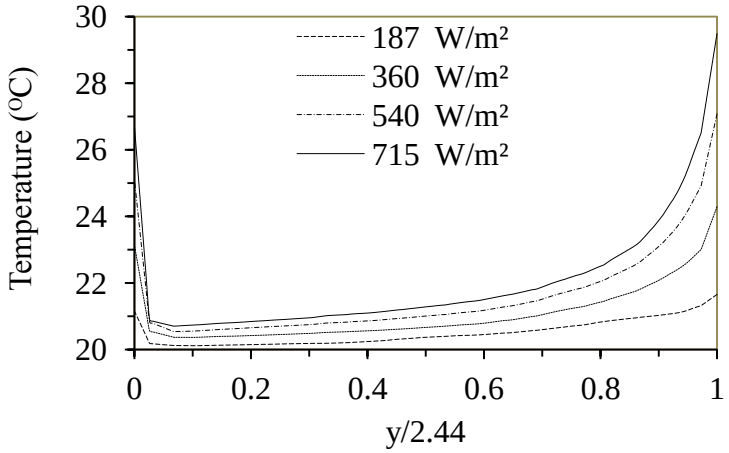

(8-14a)

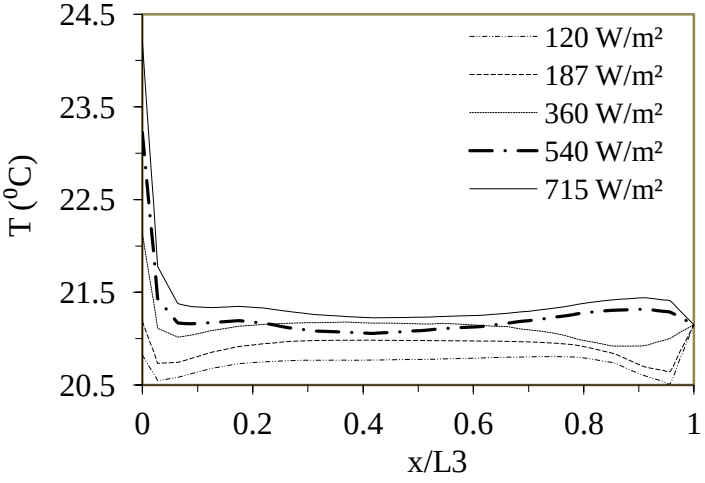

(8-14b)

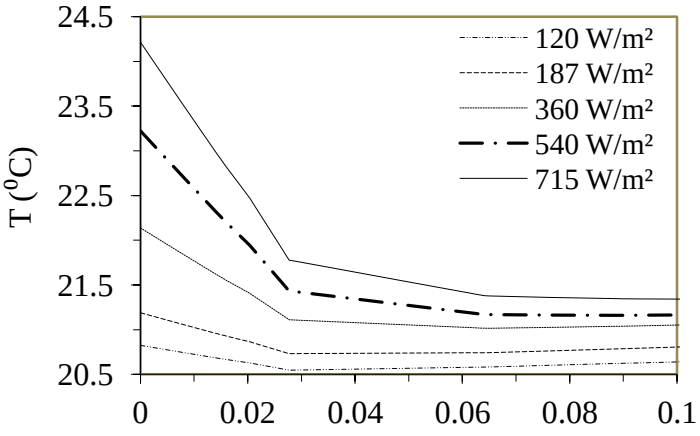

(8-14c)

Figure 8-14: Internal environment temperature profile at (a) mid-width (b) mid-height (c) at mid-height - near internal glaze

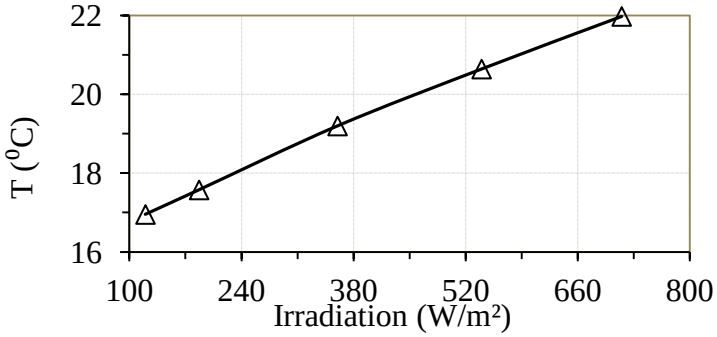

(8-15a)

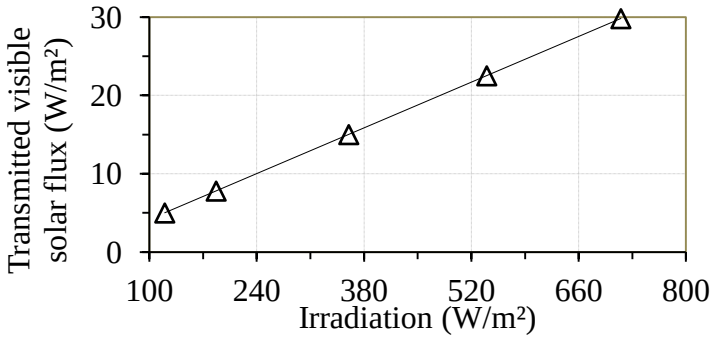

(8-15b)

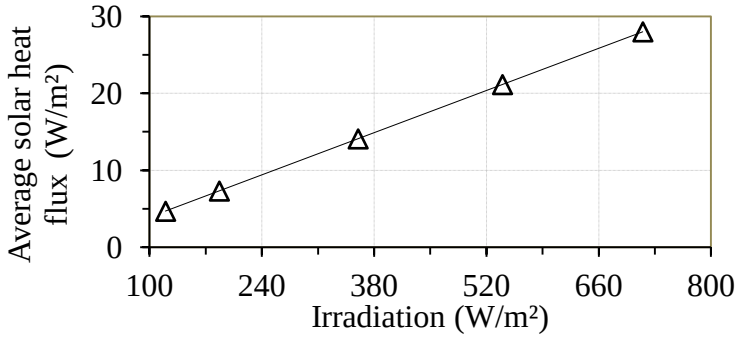

(8-15c)

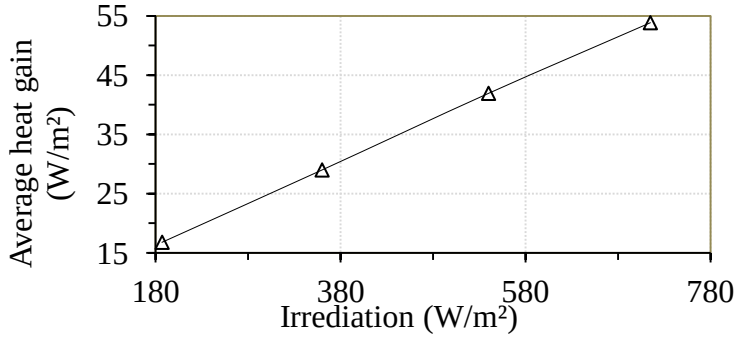

(8-15d)

Figure 8-15: Average values of (a) temperature - internal glaze-2 (b) transmitted visible solar flux - internal glaze-2 (c) solar heat flux at the indoor wall (d) surface heat flux at indoor wall

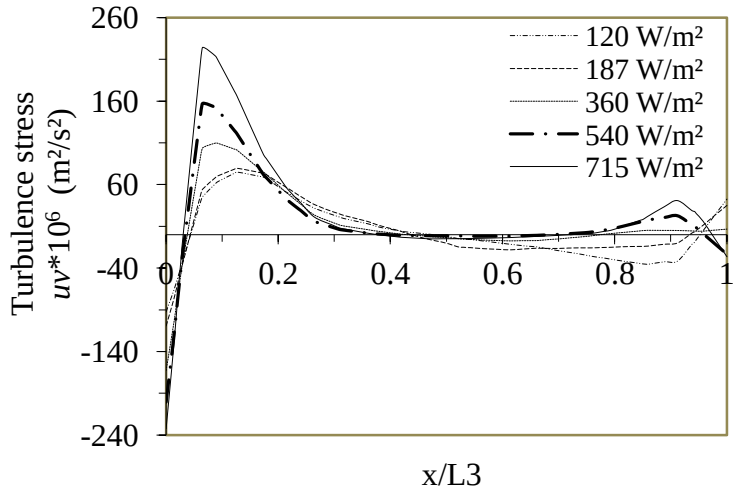

(8-16a)

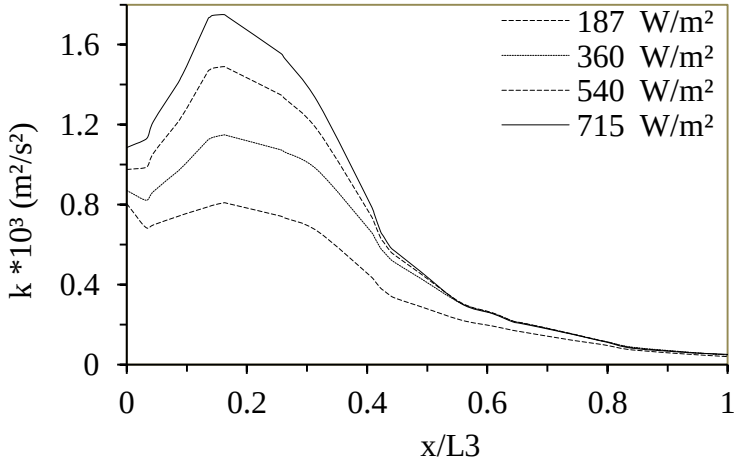

(8-16b)

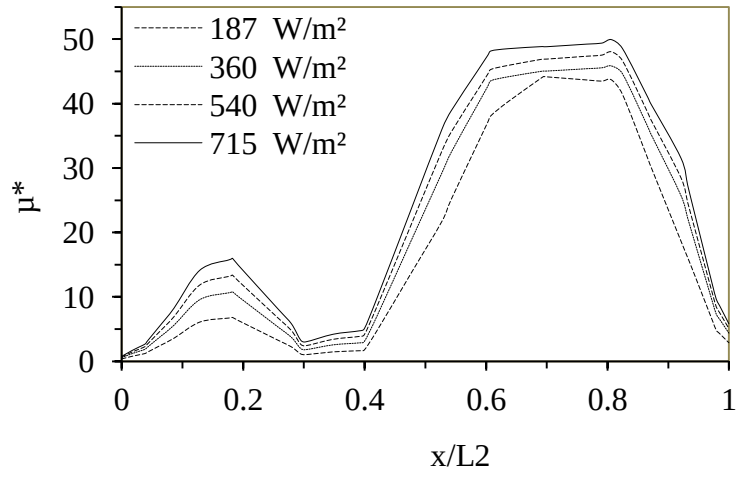

(8-16c)

Figure 8-16: Turbulence quantity profiles (a) Reynolds stress ($\overline{uv}$)at mid-height - x3 (b) kinetic energy at mid-height – x3 (c) viscosity ratio at mid-height DSF – x2

In order to quantify the effects of varying irradiation, air velocity, temperature and average heat fluxes are plotted in Figs.8-12 - 16. It appears that the increase of the air velocity, local temperature and average wall and transmitted heat fluxes are more or less directly proportional to the irradiance.

Fig.8-12 shows the velocity profile at the mid-height of the indoor space, the maximum airflow for all cases is close to the surface of the internal glazing and their peaks are at 0.03m from the glazing element. The highest velocity is 0.12m/s corresponding to the 715W/m² and the lowest peak of 0.06m/s corresponds to 120W/m². This pattern is typical of buoyancy driven convection which is influenced by the rate of heat transfer.

The temperature profiles at the mid-height of the DSF channel are presented in Fig.8-13, and as expected, the air temperature at the surface of the solar blockages gives a slightly different gradient which is due to the large difference in the thermal conductivity between the solid surface of the solar blockage and the air (about 4688:1). The highest temperature corresponds to 715W/m² irradiance, while the lowest corresponds to the lowest solar irradiance (120W/m²). A maximum temperature difference of about 10^0 C at the surface of the solar blockage is observed. The temperature profiles at the mid-height and mid-width of the indoor space follow similar trends as shown in Fig.8-15a- c.

Figs.8-15a-d show the average surface temperature, transmitted visible solar heat flux, average solar heat flux and average surface heat flux profiles for the internal glazing element for all values of solar irradiance. The heat fluxes display a linear relation with irradiation. Furthermore, the turbulent quantities at the mid-height of the indoor space were quantified by plotting the turbulence quantities of Reynolds stress, kinetic energy, and viscosity ratio as a function of the solar irradiance, shown in Figs.8-17a-c respectively. All plots show that the turbulent quantities increase with increases in the solar irradiance.

8.6.3 **Influence of solar blind positioning from the external facade**

As already mentioned, one of the main advantages of the DSF is that it allows the possibility of installing an integrated solar blockage system which is protected from

wind and weather. Its heating behaviour due to the incident solar irradiation contributes significantly to the development of a free convection air flow. This is important to quantify the optimal location of the solar blockages to achieve a high airflow rate within the DSF channel. Hence, the risk of an undesirable facade overheating can be avoided. Different blockage locations have been modelled and results presented in Figs.8-17- 19. The distance between the solar blockage and the external glazing element (δ in Fig.8-6) was varied from 0.104m to 0.379m.

It can be observed that the total solar transmission is relatively unaffected by the changes in the blind position within the DSF channel. However, the scattering effect of the solar blockages relative to its location in the glazing/shading array can become important. The results presented in Figs.8-17- 18 shown that at certain distance from the external glazing in the DSF channel, the temperature and heat transfer to the internal environment can be maximized. Therefore, optimised DSF channel ventilation can be achieved if the solar blind is located at about 0.195m from the external facade.

With this configuration, slightly higher air flow rates in the facade channel can be obtained as can be seen in Fig.8-20. Also, high air temperatures appear between the solar blockage and external facade. The heating of the solar blockages element is the driving mechanism for the DSF channel ventilation, air flow rate through the channel will rise with increasing irradiation. Thus, it is possible to transfer heat of up to 19% of the incident solar irradiation. This effect is shown in the plots of the local temperature and heat transfer as a function of δ values (Figs.8-18a- b). The final effect is evident through the temperature difference between the DSF channel and the internal environment as shown in Figs.8-16- 17.

Turbulent kinetic energy profiles are shown in Fig.8-19, demonstrating that turbulence is generally suppressed due to the blockage proximity which was also observed in chapter 6 (section 6.3.2). For the case where the solar-blockages are much closer to the glazing layers the heat transfer is enhanced. This is believed to be due to the location of the blockages closer to the glazing surface which means that the turbulent boundary layer caused by the blockages is sufficiently thin so that it overlaps with the thermal boundary layer of the glazing surfaces.

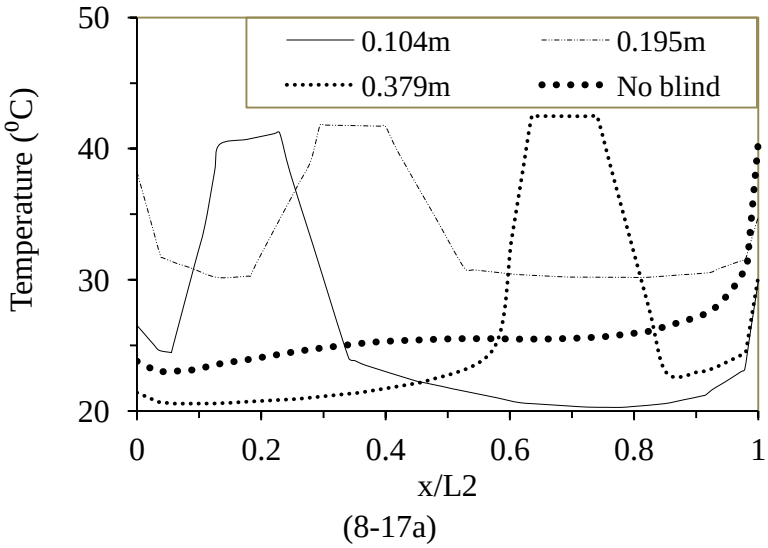

(8-17a)

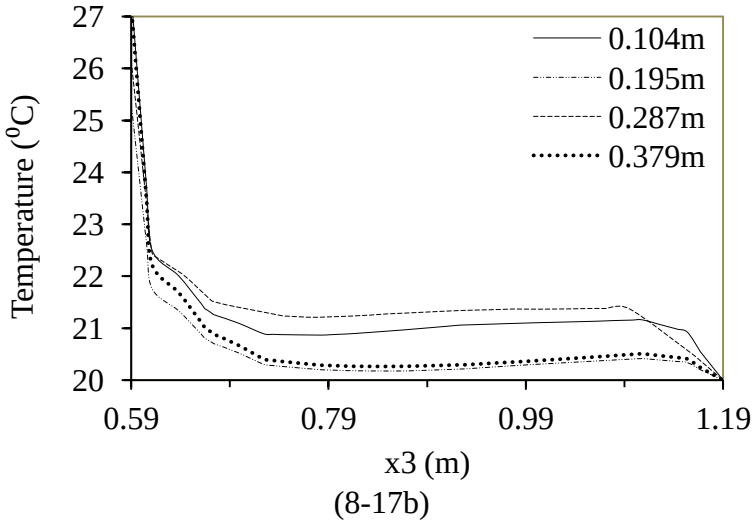

(8-17b)

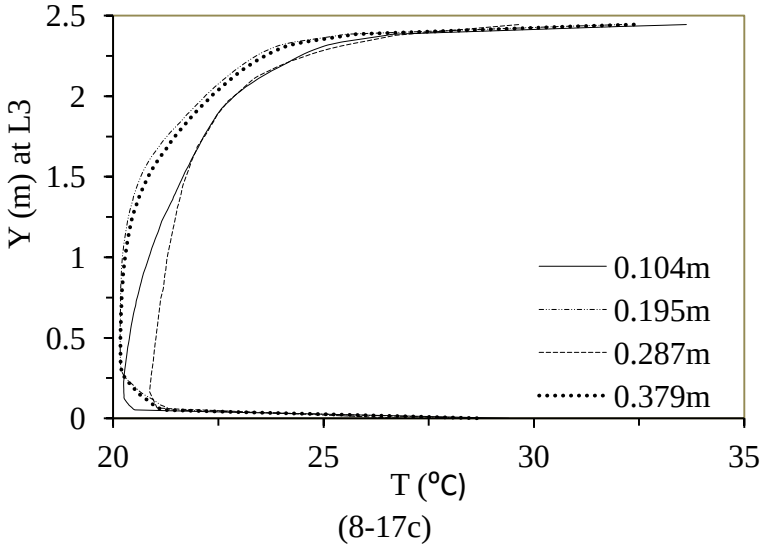

(8-17c)

Figure 8-17: Temperature profile at (a) mid-height of DSF channel (b) mid-height of the indoor environment (c) mid-width of the indoor environment, L3.

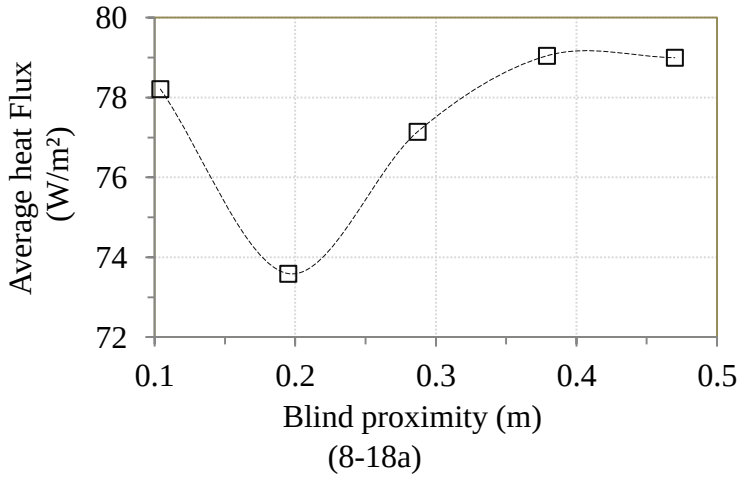

(8-18a)

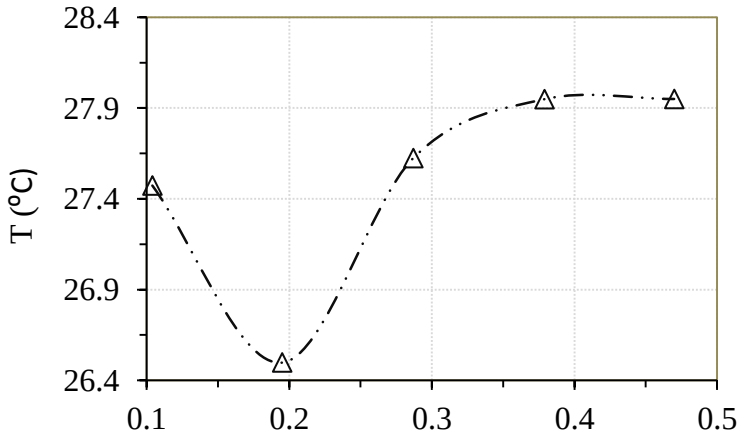

(8-18b)

Figure 8-18: (a) Average surface heat flux at indoor wall (b) average temperature at the internal glaze-2

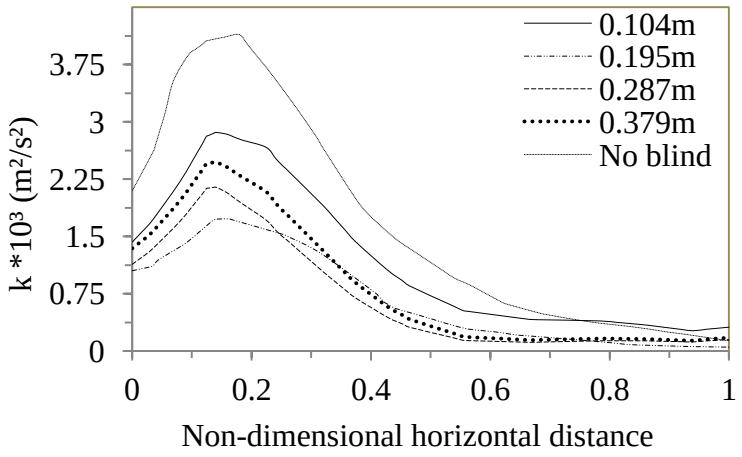

Figure 8-19: Turbulent kinetic energy profile measured at mid-height of the indoor environment

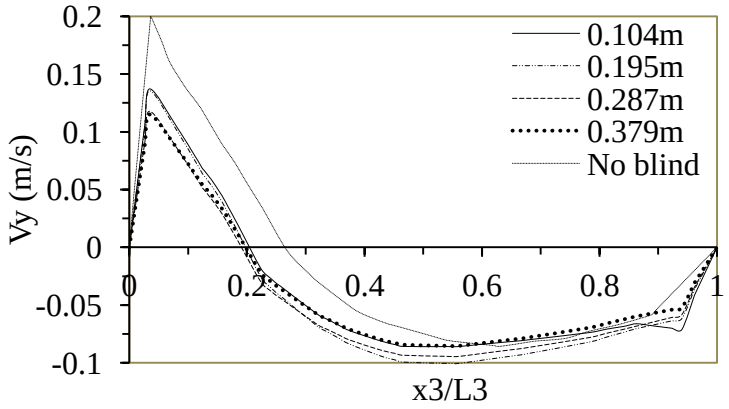

Figure 8-20: Vertical velocity profile at mid-height of the indoor environment

8.6.4 **Influence of solar blind inclination angle**

The ability to quantify both solar and thermal aspects of energy transfer in glazing/blockage systems allows us to investigate the effects of solar blockage angle on the different components. Calculations were carried out for a fixed solar irradiance of 715W/m² and the thermal condition of indoor and outdoor environment were both fixed at 20^0C. The solar blockages as shown in Fig.8-6 were set at 30^0, 45^0, 60^0 and 75^0, where 30^0 and 75^0 relate to almost fully closed and almost fully opened respectively. The thermal behaviour of the indoor environment as a result of varying the solar blockage angle is presented in Figs.8-21- 25 and the average values of heat flux and temperature are shown in Table 8-8.

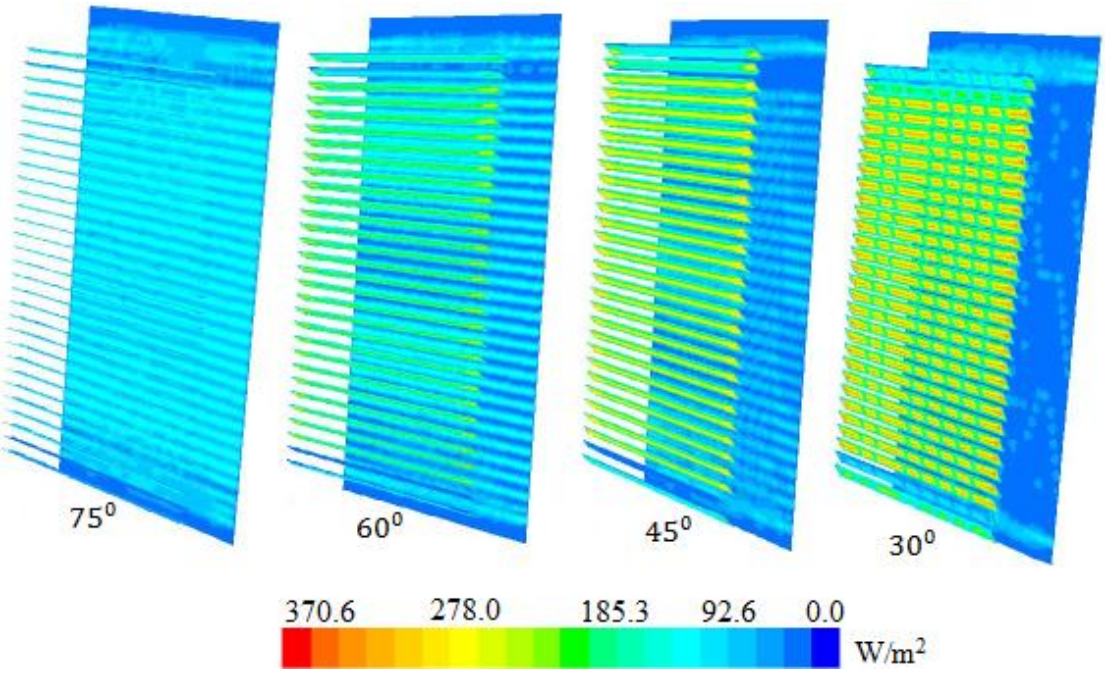

(8-21a)

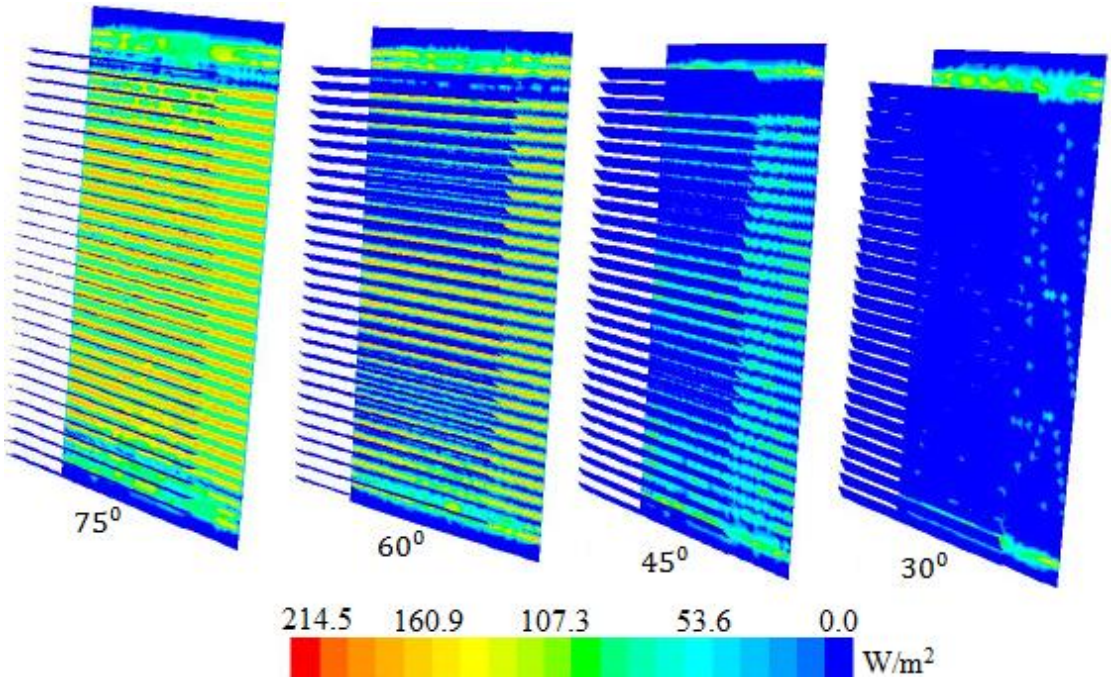

(8-21b)

Figure 8-21: (a) Contour of solar heat flux at the surface of the internal glaze-1 and the blinds (b) contour of transmitted visible solar flux at the surface of the internal glaze-1 and the blind.

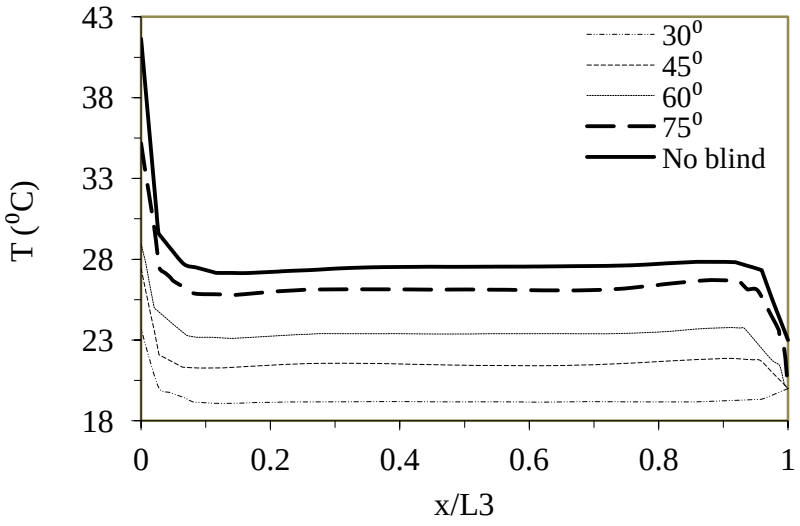

(8-22a)

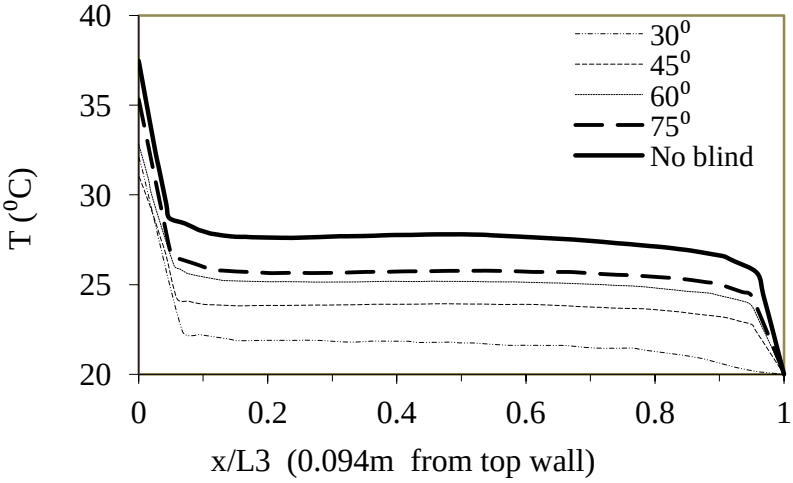

(8-22b)

Figure 8-22: Temperature profile at (a) mid-height of the indoor space (b) near the top wall (0.094 from top wall) of the indoor space

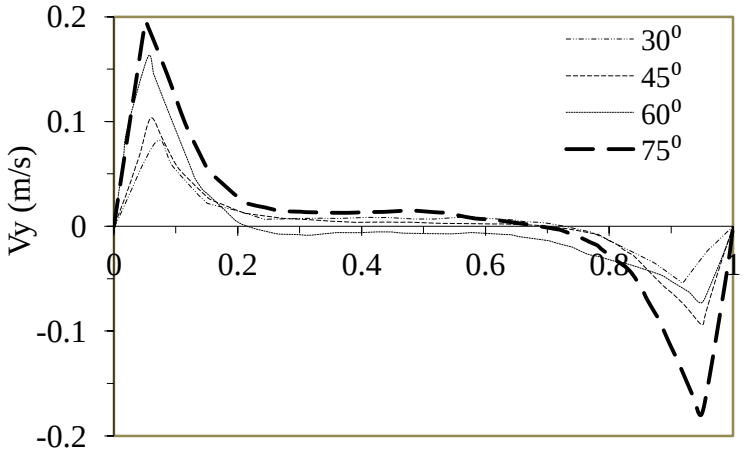

Figure 8-23: Velocity profile near the top wall of the indoor space

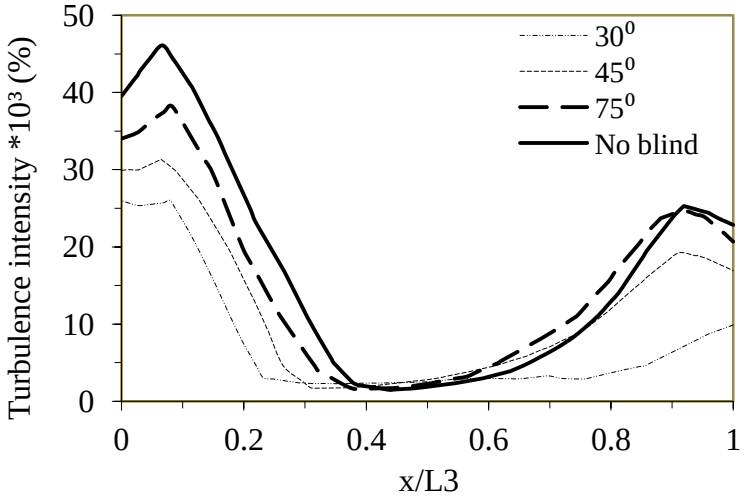

Figure 8-24: Turbulence intensity at mid-height of the indoor space

Table 8-8: Average parameters evaluated at internal glaze–2

Blind angles (^{0})	Temperature (^{0}C)	Heat flux (W/m²)	solar heat flux (w/m²)	Transmitted visible solar heat flux (w/m²)
30	25.25	14.35	18.79	6.99
45	28.28	16.95	23.22	29.80
60	30.15	21.86	28.58	57.67
75	33.51	26.67	34.80	89.80
No blind	39.33	37.77	45.80	124.20

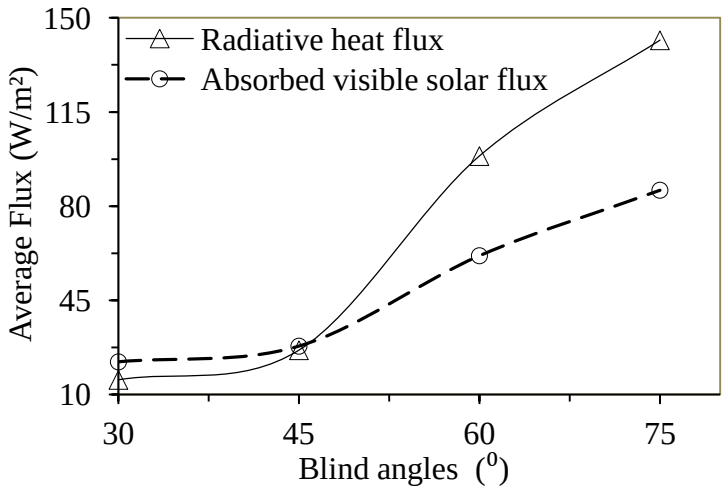

Figure 8-25: indoor wall average surface heat flux as a function of blind angle

There appears to be a direct relationship between incident solar irradiation transmitted to the indoor space and the inclination angles of the solar blockage as can be seen from Figs.8-21a- b. As the solar blockage angle increases (opening), solar irradiance transmitted to the indoor space also increases. This behaviour is further evidenced in the plots of the flow velocity and turbulence intensity as shown in Fig.8-23- 24.

Figs.8-21a –b show contours of solar heat flux and transmitted visible solar flux for the surface of internal glazing-1and the blinds. The results demonstrate that there is a direct relationship between the blind inclination angles and the transmitted solar heat flux and the visible solar heat flux. The solar heat and visible solar fluxes transmitted are higher with increased solar blind angle, as a result, the radiative and convective gains to the indoor space are noticeably higher (Fig.8-25). Similar behaviour is also

observed with the average temperature distribution at the internal glaze-2 and the average heat flux of the internal glaze-2, average solar heat flux of the internal glaze surface and the transmitted visible solar heat flux (Table 8-8). The blind angle also affects the turbulence level of the indoor air as shown in Fig.8-24.

8.6.5 **Influence of outdoor air temperature**

In order to quantify the influence of the outdoor air temperature on the thermal behaviour of the indoor space, different outdoor temperatures were tested (10^0C, 20^0C, 30^0C and 40^0C) and their influence on the indoor space were evaluated. All tests were done at a fixed solar irradiance of 715W/m². The effects of outdoor temperature on the indoor temperature and air flow are shown in Figs.8-26 and 27 respectively. There seems to be a direct relationship between outdoor temperature and the indoor flow and temperature plots as a function of outdoor temperature.

Fig.8-27 shows the comparison of the air velocity at mid-height of the indoor space (L3) and Fig.8-26a- b are the temperature profiles evaluated at mid-height (x3) and mid-width (Y) of the indoor space respectively. It is observed that, the outdoor air temperature influences the indoor air temperature and flow. The maximum increase of indoor air temperature corresponds with the optimal outdoor air temperature (40^0C) used in this investigation. Similarly, the turbulent kinetic energy profile (Fig.8-27) displays similar variation to the change in the outdoor temperature.

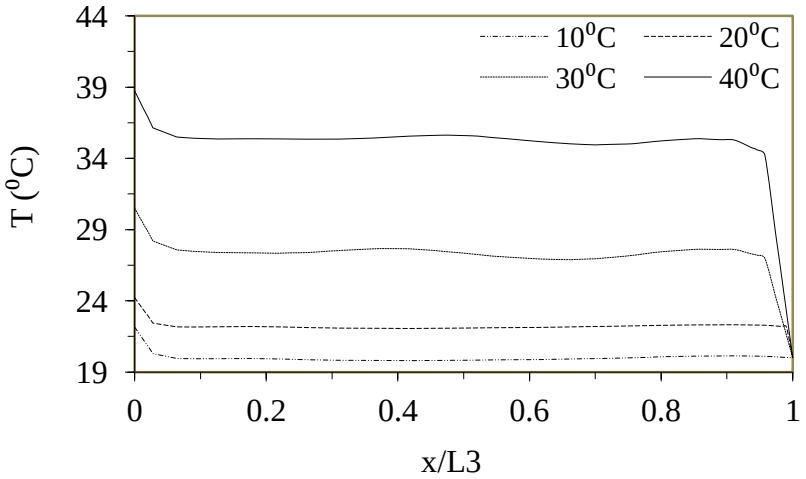

(8-26a)

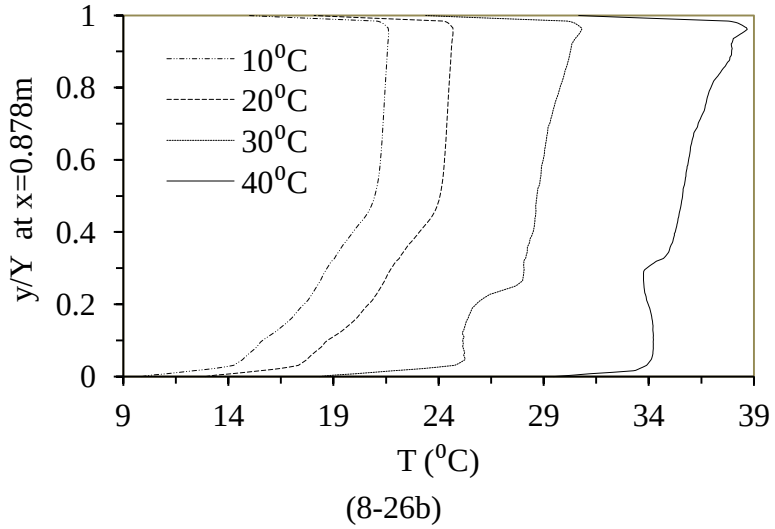

(8-26b)

Figure 8-26: Indoor temperature profile at (a) mid-height (b) mid-width

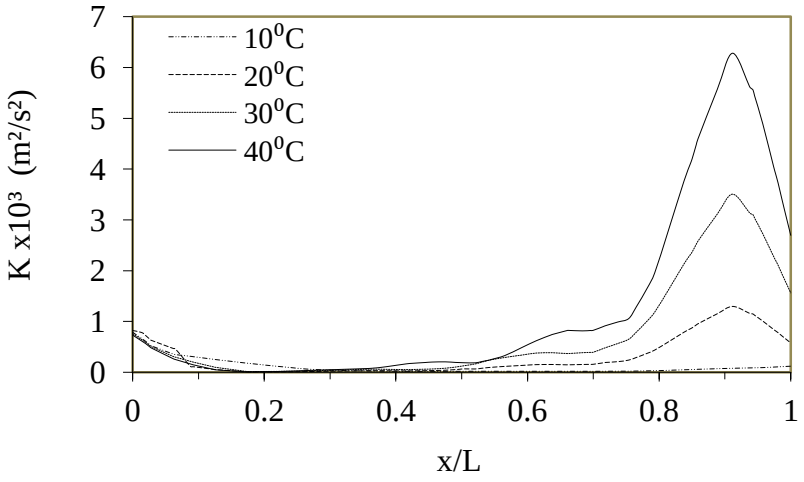

Figure 8-27: Turbulent kinetic energy at mid-height of the internal environment

8.7 **Conclusion**

The need to fully describe the solar and thermal characteristics of complex glazing/blockages systems is critical for providing the necessary inputs into building energy simulations to assess the potential in energy saving. The correct behaviour of a DSF is the key to increasing energy savings and hence requires the structure to be carefully designed. In this study, detailed CFD results of a DSF system are presented. The current study complements previous study of Mei et al. [306] by addressing the detailed heat transfer due to the influence of solar radiation intensity, influence of solar blockages and influence of external environment thermal condition and provides

a comparative analysis of the net heat gain to the indoor environment and the relative magnitude of its components.

Sensitivity analysis for different numerical modelling strategies has been conducted for four different cases which include: channel, outdoor-channel, channel-indoor and then outdoor-channel-indoor fluid domains. It was observed that there is no significant difference in the quantification of the thermal behaviour for tested configuration. Therefore, it is recommended to model the DSF channel in isolation if the outdoor or indoor spaces are not key factors for the airflow and heat transfer. However, the outdoor and the indoor thermal boundary conditions must be well defined.

Solar irradiance and outdoor air temperature were shown to affect the airflow and heat transfer in the indoor environment. It is evident from the results that the airflow, temperature and heat transfer to the indoor space increase with increasing values of the irradiance. The effects of the solar blockage inclination angles located in the DSF channel were analysed. Heat gain into the indoor space and its components are moderated by the solar blockages device.

The solar blockages device within the cavity can be considered to separate the cavity into two vertical chambers, in front of and behind the blockages. It is concluded that the blockages have a significant influence on the thermal and airflow performance of the facade. If the solar blockage device is almost fully closed (30^0 inclination), the 'front chamber' of the cavity and the blockage element itself will have higher temperatures than if it was opened. In contrast, the temperature behind the solar-blockage device will be higher if the solar-blockage device is almost fully opened (75^0 inclination). The net heat gain to the indoor space is dominated by transmitted solar radiation, with a small contribution from the radiative and convective fluxes. This is the expected result with a non-shaded glazing which does little to block the solar radiation. With closing the solar blockages (30^0), heat transfer to the building can be minimized to about 85% of the incoming solar energy.

In general, the net heat gain to the indoor environment can be reduced considerably with solar blockage devices (venetian blinds) in place. The energy efficiency of the DSFs can be enhanced by controlling the slat angle of the solar-blockage device. The

optimum solar blockages position in terms of energy saving is 0.195m where the heat transfer to the indoor space is minimum.

The influence of outdoor air temperature on the indoor temperature should be carefully taken into consideration for an optimum thermal performance of the DSF system. The overheating effect that could arise in summer conditions inside the DSF with closed configurations can be avoided by the communication between the gap and the external environment air. Solar gains in buildings are desirable in winter-time, but problematic in summer, as they may cause overheating and discomfort; for this reason the external layer should remain open in the hot season, this will give the air the possibility to escape from the channel.

Chapter 9 - CONCLUSIONS AND FUTURE WORK

9.1 Summary of the Research Work

Over the last three decades, researches on natural convection flows and heat transfer in an enclosed environment has experienced rapid growth due to the growing demand for detailed quantitative knowledge of the transfer processes and also due to its relevance in many practical applications. The basic set up for such flows, which has attracted most attention from researchers, is an air-filled rectangular cavity whose vertical walls are heated differentially. In recent years the trend in buoyancy driven flow research has shifted to the examination of cavity flow with blockages which are disconnected. Most of the studies in this category are concentrated on steady state laminar flow with a very limited number of works on higher range. An important aspect of this type of flow which has not been investigated in detail is the effect of wall proximity of blockages on the flow and heat/mass transfer. This issue has many practical applications such as natural drying of wood stacks, cold storage (refrigerators), and location of solar blinds in double skin facade (DSF) and in the location of electronics panel for effective thermal management.

The goal of the work presented in this thesis has been to assess and quantify the challenges associated with the numerical modelling of low turbulence natural convection flow and heat transfer in confined spaces with or without blockages. The challenges include the following: (a) selection of eddy viscosity models to give the best numerical prediction (b) specification of passive thermal boundary conditions (c) influence of emissivity on double diffusion buoyancy driven turbulent flow in an enclosure partially filled with solid objects (d) limited experimental data for the validation of CFD codes (e) interaction between turbulence buoyancy flows with blockages. The motivation behind this research is to overcome the above highlighted challenges.

A comprehensive study has been conducted to investigate and analyse the relative performance of low Reynolds number k-epsilon models in quantifying the flow and heat transfer within an enclosure with and without blockages. The search for a realistic boundary condition specification at the passive walls was considered by performing numerical analysis and quantifying the influence of three possible used

boundary conditions. Different parametric studies were conducted to investigate the influence of emissivities of the solid surface on the flow and heat transfer for enclosed space with and without blockages. Choice of equivalent emissivity was investigated by performing a numerical study to justify 2D simplification of an inherently 3D radiation heat transfer in a rectangular enclosure partially filled with blockages.

To be able to obtain reliable temperature data, an experimental set up capable of establishing low Rayleigh number buoyancy driven flow in a rectangular enclosure with and without blockages was designed and fabricated. The skills and concepts that enabled us to design the thermal test rig were acquired from literature and complemented by preliminary CFD simulation studies. Temperature data of air and for all walls (including the blockage surfaces) were recorded at steady state using k-type thermocouples. This data has also been validated using the results from the numerical simulations. It has been shown that these results compare very well with the numerical results.

The interactive influence between turbulent buoyancy flows and heat transfer with disconnected blockages was investigated by conducting numerical calculations on blockage proximity from the active vertical walls and passive horizontal walls. A further numerical study was done for group blockages located within the rectangular enclosed space. As an application of the research methodology, a comprehensive investigation was conducted on a double skin facade (DSF) partially filled with disconnected solar blinds (solar blockages), whose detailed flow and heat transfer mechanism is yet to be established. The current methodology has been applied to establish a number of parameters in connection with the design and performance of DSF which are believed to be useful to the practitioners.

9.2 **Summary of the research work findings**

The research findings from the study are highlighted below:

- For the Rayleigh numbers considered in this study, the flow field for an empty cavity is characterised by low turbulence near the walls while the core area is essentially a stagnant region. The presence of blockages initiates secondary flows at the core of the cavity and especially close to the surface of solid blockages.

- Our parametric study has shown that the experimental temperature profile (ETP) is a more realistic thermal boundary condition in contrast to the adiabatic wall condition normally used in numerical studies by most researchers on natural convection flow and heat transfer in an enclosed space. However, in the absence of ETP, the LTP should be use as the passive wall thermal boundary condition.
- The flow is sensitive to the appropriate choice of eddy viscosity models and hence a detailed understanding of the performance of eddy viscosity models (EVMs) is required. For the EVMs tested in this work, the Launder-Sharma low-*Re* k-ε model gave the best performance for double diffusive natural convection and the heat transfer in an enclosure partially filled with blockages. Whereas, for a cavity without blockages, the validated results show that the Yang-Shih model is the most accurate in predicting the flow and especially the heat transfer closed to the walls of the cavity. Hence the need for turbulence model sensitivity studies remaining to be a priority for practitioners.
- Radiation has been found to influence the flow, heat and mass transfer within the cavity. The implication of this influence is that by a careful selection of material, heat transfer and humidity distribution may be passively influenced. Given that an appropriate equivalent emissivity is obtained, a 2D simplification of a radiative surface in a 3D domain is possible to save computational effort.
- The influence on fluid flow, heat and mass transfer due to the interaction with the obstacles was identified and detailed profiles have been obtained for critical locations. Blockages proximity can be seen to affect the overall heat transfer via flow field. Turbulence is greatly suppressed as the gap between the walls and the solid objects become smaller. At a certain blockage location from the vertical walls the wall heat transfer is found to be the optimum. This finding may be valuable for practitioners in built environment design.
- Ranges of experimental temperature data have been generated and some of them were validated. Data generated for various blockage arrangements and wall proximity may act as a benchmark data for future CFD code validation.

- Detailed analysis of double skin facade highlights the relative merits of commonly adopted numerical modelling approaches and shows that significant computational saving is possible considering a simple domain. The positioning of Venetian

blinds and, in particular, their proximity from the glazing is a very critical parameter that needs to be given serious consideration. The proposed methodology establishes an accurate and fundamental approach on how solar irradiation can be modelled within a CFD package.

9.3 **Recommendations for future work**

Although the objectives listed in chapter one of this thesis have been mostly achieved, the work was never envisaged to be fully comprehensive to cover all indoor natural convection systems. Since the amount of work and time required to do so is beyond the scope of this thesis, the author recommends further works, which can be carried out to extend the work reported here.

- Double diffusion buoyancy driven flow with multi-component fluid (more than two phase) with larger relative molecular mass should be investigated to evaluate the level of their interactions. Also, it will be interesting to investigate the interaction with the flow and heat transfer using different geometric shapes relevant to electronic components and agricultural produces cooling.
- Further research on the blockages should consider the blockages on a number of factors, such as different predetermined temperature to investigate the influence of blockages heat transfer on the flow and total heat transfer in the enclosed space, and effects of blockages surface roughness.
- More detailed experimental studies on the air flow velocity and turbulence are needed for CFD code validation for such a complex natural convection flow domain with blockages. The developed experimental rig may be modified to allow optical access for non-invasive measurement of the flow variables. It will be interesting to investigate the influence of inclination angles on the flow and heat transfer and produce correlations for the various cases of arrangement of blockages within the enclosed space.
- The analysis of flow and heat transfer for DSF may be extended to accommodate daily and seasonal variations of solar radiation.

9.4 References

[1] Y. Jaluria, "Introduction of Disturbances in a Natural-Convection Flow," *International Journal of Heat and Mass Transfer,* vol. 19, pp. 1057-1063, 1976.

[2] Y. Jaluria and B. Gebhart, "Experimental Study of Nonlinear Disturbance Behavior in Natural-Convection," *Journal of Fluid Mechanics,* vol. 61, pp. 337-365, 1973.

[3] Y. Jaluria, *Natural Convection Heat and Mass Transfer* vol. 5: Pergamon Press, 1980.

[4] A. Bejan, *Heat Transfer*. New York: John Wiley and Sons, Inc., 1993.

[5] J. P. Holman, *Heat Transfer*: McGraw-Hill, 1992.

[6] Y. A. Cengel, *Heat Transfer*: McGraw-Hill, 2003.

[7] T. Aihara, "Natural Convective Heat Transfer in Vertical Parallel Fins of Rectangular Profile," *Japan Society of Mechanical Engineering,* pp. 915-926, 1968.

[8] L. S. W. Aung, "Developing Laminar Free Convection between Vertical Flat Plates with Asymmetric Heating," *Int. J. Heat and Mass Transfer(15),* pp. 2293-2308, 1972.

[9] R. F. Bergholz, "Natural Convection of a Heat Generating Fluid in a Closed Cavity," *J. Heat Transfer (102),* pp. 242-247, 1980.

[10] E. A. H. Davis, "Transmission of Heat by Radiation and Natural Convection," Food Investigation Board: Special Report No.91922.

[11] S. Kadem, A. Lachemet, R. Younsi, and D. Kocaefe, "3d-Transient modeling of heat and mass transfer during heat treatment of wood," *International Communications in Heat and Mass Transfer,* vol. 38, pp. 717-722, Jul 2011.

[12] O. Laguerre, S. Ben Amara, M. C. Charrier-Mojtabi, B. Lartigue, and D. Flick, "Experimental study of air flow by natural convection in a closed cavity: Application in a domestic refrigerator," *Journal of Food Engineering,* vol. 85, pp. 547-560, Apr 2008.

[13] O. Laguerre, S. Ben Amara, and D. Flick, "Experimental study of heat transfer by natural convection in a closed cavity: application in a domestic refrigerator," *Journal of Food Engineering,* vol. 70, pp. 523-537, 2005.

[14] Q. Y. Chen, "Ventilation performance prediction for buildings: A method overview and recent applications," *Building and Environment,* vol. 44, pp. 848-858, Apr 2009.

[15] S. A. V. Ramalingam, "Thermal Management of Electronics: A Review of Literature," p. Vol.2, 2008.

[16] A. Bejan and G. A. Ledezma, "Thermodynamic optimization of cooling techniques for electronic packages," *International Journal of Heat and Mass Transfer,* vol. 39, pp. 1213-1221, Apr 1996.

[17] I. C. H. Buchberg, "Natural convection in enclosed spaces: a review of application to solar energy collection," *J. Heat Transfer,* pp. 182-188, 1976.

[18] M. R.J. Kee, "Natural convection of a heat-generating fluid within closed vertical cylinders and spheres," *Journal Name: J. Heat Transfer,* pp. 55-61, 1976.

[19] D. Siano, M. Costa, and F. Bozza, "Prediction and enhancement of the acoustic performance of a spark ignition engine intake air filter box,"

Proceedings of the Institution of Mechanical Engineers Part D-Journal of Automobile Engineering, vol. 227, pp. 591-604, 2013.

[20] J. A. Cronin, M. I. Frecker, and A. Mathew, "Design of a Compliant Endoscopic Suturing Instrument," *Journal of Medical Devices-Transactions of the Asme*, vol. 2, Jun 2008.

[21] R. F. Abrahao, E. Correia, and B. J. Teruel, "Computational simulation for the development of packages for bananas," *Revista Brasileira De Fruticultura*, vol. 30, pp. 79-87, Mar 2008.

[22] C. Flores, H. Juarez, M. A. Nunez, and M. L. Sandoval, "Algorithms for Vector Field Generation in Mass Consistent Models," *Numerical Methods for Partial Differential Equations*, vol. 26, pp. 826-842, Jul 2010.

[23] A. Joann Gonchar. (July 2010). Luminous library - An integrated facade strategy helps designers create more comfortable and better-performing glass buildings.Accessed 16 Januray 2013 Avialable at: *http://continuingeducation.construction.com/article_print.php?C=685&L=5*.

[24] *M. N. Solution. (2013). Accessed 16 Januray 2013 Avialable at: http://modular-solution.com/*

[25] *A. Reporter. (July 15, 2012). Integrated fridge/freezers. Accessed 16 Januray 2013 Avialable at*: *http://www.punchng.com/spice/gadgets/its-so-cool-here/*

[26] D. F. P. Incropera, T. L. Bergman and A. S Lavine, *Principles of Heat and Mass Transfer*. London: John Wiley and Sons, 2013.

[27] J. R.A. Pitarma, M.E. Ferreira and M.G. Carvalho, "An advanced active tool in environmental management and education," *Management of Environmental: An International Journal*, pp. 102-110, 2004.

[28] D. J. Sheridan, "Natural Convection in Enclosures Filled with a Vapoure and a Non-condensing Gas," *Int. J. Heat Mass Transfer*, pp. 855-862, 1989.

[29] L. D. Shia-Hui Peng, "International Journal of Heat and Fluid Flow," *Computation of turbulent buoyant flows in enclosures with low-Reynolds-number k-w models*, vol. 20, pp. 172-184, 1999.

[30] F. E. Ham, "Towards the large-eddy simulation of complex turbulent flows," Ph.D thesis, University of Waterloo, Waterloo Canada, 2002.

[31] E. H. Ridouane and A. Campo, "Compounded heat transfer enhancement in enclosure natural convection by changing the cold wall shape and the gas composition," *Journal of Heat Transfer-Transactions of the Asme*, vol. 129, pp. 827-834, Jul 2007.

[32] A. Barletta, E. Nobile, F. Pinto, E. Rossi di Schio, and E. Zanchini, "Natural convection in a 2D-cavity with vertical isothermal walls: Cross-validation of two numerical solutions," *International Journal of Thermal Sciences*, vol. 45, pp. 917-922, Sep 2006.

[33] G. S. Barozzi and M. A. Corticelli, "Natural convection in cavities containing internal sources," *Heat and Mass Transfer*, vol. 36, pp. 473-480, Nov 2000.

[34] M. Song and R. Viskanta, "Natural-Convection Flow and Heat-Transfer within a Rectangular Enclosure Containing a Vertical Porous Layer," *International Journal of Heat and Mass Transfer*, vol. 37, pp. 2425-2438, Nov 1994.

[35] J. C. DeBlois, M. M. Bilec, and L. A. Schaefer, "Design and zonal building energy modeling of a roof integrated solar chimney," *Renewable Energy*, vol. 52, pp. 241-250, Apr 2013.

[36] M. A. Izquierdo-Barrientos, J. F. Belmonte, D. Rodriguez-Sanchez, A. E. Molina, and J. A. Almendros-Ibanez, "A numerical study of external building walls containing phase change materials (PCM)," *Applied Thermal Engineering,* vol. 47, pp. 73-85, Dec 5 2012.

[37] M. M. Rahman, H. F. Oztop, A. Ahsan, and J. Orfi, "Natural convection effects on heat and mass transfer in a curvilinear triangular cavity," *International Journal of Heat and Mass Transfer,* vol. 55, pp. 6250-6259, Oct 2012.

[38] C. Sanjuan, M. J. Suarez, M. Gonzalez, J. Pistono, and E. Blanco, "Energy performance of an open-joint ventilated facade compared with a conventional sealed cavity facade," *Solar Energy,* vol. 85, pp. 1851-1863, Sep 2011.

[39] X. L. Xu and Z. Yang, "Natural ventilation in the double skin facade with venetian blind," *Energy and Buildings,* vol. 40, pp. 1498-1504, 2008.

[40] A. Suleiman, A. Trombe, Y. Le Maoult, and S. Monteix, "Experimental and numerical analysis of building boundary conditions," *Experimental Heat Transfer,* vol. 17, pp. 1-18, Jan-Mar 2004.

[41] I. Tari and M. Mehrtash, "Natural convection heat transfer from inclined plate-fin heat sinks," *International Journal of Heat and Mass Transfer,* vol. 56, pp. 574-593, Jan 1 2013.

[42] K. Kota, P. Hidalgo, Y. Joshi, and A. Glezer, "Hybrid Liquid Immersion and Synthetic Jet Heat Sink for Cooling 3-D Stacked Electronics," *Ieee Transactions on Components Packaging and Manufacturing Technology,* vol. 2, pp. 817-824, May 2012.

[43] V. Panthalookaran, "CFD-Assisted Optimization of Chimneylike Flows to Cool an Electronic Device," *Journal of Electronic Packaging,* vol. 132, Sep 2010.

[44] M. B. Dogruoz and M. Arik, "On the Conduction and Convection Heat Transfer From Lightweight Advanced Heat Sinks," *Ieee Transactions on Components and Packaging Technologies,* vol. 33, pp. 424-431, Jun 2010.

[45] J. Petroski, M. Arik, and M. Gursoy, "Optimization of Piezoelectric Oscillating Fan-Cooled Heat Sinks for Electronics Cooling," *Ieee Transactions on Components and Packaging Technologies,* vol. 33, pp. 25-31, Mar 2010.

[46] A. Hamouche and R. Bessaih, "Mixed convection air cooling of protruding heat sources mounted in a horizontal channel," *International Communications in Heat and Mass Transfer,* vol. 36, pp. 841-849, Oct 2009.

[47] M. J. Marongiu, M. K. Berhe, and G. S. Fallon, "Thermal management of IC's and microprocessor using heat sinks (pin fin and channel) incorporating phase change materials (PCM) for transient operation," *1999 International Symposium on Microelectronics, Proceedings,* vol. 3906, pp. 789-794, 1999.

[48] E. C. Yu and Y. K. Joshi, "Natural convection air cooling of electronic components in partially open compact horizontal enclosures," *Itherm '98: Sixth Intersociety Conference on Thermal and Thermomechanical Phenomena in Electronic Systems,* pp. 51-57, 1998.

[49] B. Calcagni, F. Marsili, and M. Paroncini, "Natural convective heat transfer in square enclosures heated from below," *Applied Thermal Engineering,* vol. 25, pp. 2522-2531, Nov 2005.

[50] A. Koonsrisuk, S. Lorente, and A. Bejan, "Constructal solar chimney configuration," *International Journal of Heat and Mass Transfer,* vol. 53, pp. 327-333, Jan 15 2010.

[51] F. Ampofo and T. G. Karayiannis, "Experimental benchmark data for turbulent natural convection in an air filled square cavity," *International Journal of Heat and Mass Transfer,* vol. 46, pp. 3551-3572, 2003.

[52] S. Lorente, A. Koonsrisuk, and A. Bejan, "Constructal Distribution of Solar Chimney Power Plants: Few Large and Many Small," *International Journal of Green Energy,* vol. 7, pp. 577-592, 2010.

[53] A. A. DafaAlla and P. L. Betts, "Experimental study of turbulent natural convection in a tall air cavity," *Experimental Heat Transfer,* vol. 9, pp. 165-194, Apr-Jun 1996.

[54] J. Wasilewski, K. Mirota, S. Peryt-Stawiarska, A. Nowakowski, L. Polonski, and M. Zembala, "An introduction to computational fluid dynamics based on numerical simulation of pulsatile flow in the left coronary artery," *Kardiochirurgia I Torakochirurgia Polska,* vol. 9, pp. 366-374, Sep 2012.

[55] J. A. Weaver and R. Viskanta, "Natural-Convection Due to Horizontal Temperature and Concentration Gradients .1. Variable Thermophysical Property Effects," *International Journal of Heat and Mass Transfer,* vol. 34, pp. 3107-3120, Dec 1991.

[56] H. S. Yoon, D. H. Yu, M. Y. Ha, and Y. G. Park, "Three-dimensional natural convection in an enclosure with a sphere at different vertical locations," *International Journal of Heat and Mass Transfer,* vol. 53, pp. 3143-3155, Jul 2010.

[57] D. A. Iyi, R. Hasan and R. Penlington, "Numerical Analysis of the Influence of Thermal Boundary Condition and Surface Emissivity on the Flow and Heat Transfer in Turbulent Buoyancy Driven Flow," presented at: The Third Asian Symposium on Computational Heat Transfer and Fluid Flow, Kyoto, Japan, 2011.

[58] D. A. Iyi, R. Hasan and R. Penlington., "Interaction effects between surface radiation and double-diffusive turbulent natural convection in an enclosed cavity filled with solid obstacles," *Begell House Journals,* vol. 0, July 1-6, 2012 2012.

[59] C. Aharoni, "Effect of the energy of adsorption at the pore wall surface on capillary condensation," *Langmuir,* vol. 18, pp. 7441-7446, Oct 1 2002.

[60] D. Saury, N. Rouger, F. Djanna, and F. Penot, "Natural convection in an air-filled cavity: Experimental results at large Rayleigh numbers," *International Communications in Heat and Mass Transfer,* vol. 38, pp. 679-687, Jul 2011.

[61] Kutatela.Ss, Kirdyash.Ag, and V. P. Ivakin, "Turbulent Natural-Convection on a Vertical Plate and in a Vertical Layer," *International Journal of Heat and Mass Transfer,* vol. 15, pp. 193-&, 1972.

[62] P. F. W. Giel, "An Experimental Study of High Rayleigh Number Natural Convection in an Enclosure," presented at the International Heat Transfer Conference, San Francisco., 1986.

[63] H. Han and T. H. Kuehn, "Double Diffusive Natural-Convection in a Vertical Rectangular Enclosure .1. Experimental-Study," *International Journal of Heat and Mass Transfer,* vol. 34, pp. 449-459, Feb 1991.

[64] K. J. King, *Turbulent natural convection in rectangular air cavities*. Queen Mary College: London, UK., 1989.

[65] A. T. Kirkpatrick and M. Bohn, "An Experimental Investigation of Mixed Cavity Natural-Convection in the High Rayleigh Number Regime," *International Journal of Heat and Mass Transfer,* vol. 29, pp. 69-82, Jan 1986.

[66] K. K. J. Cheesewrite R., and Ziai S, "Experimental data for the validation of computer codes for the prediction of two-dimensional buoyant cavity flows," presented at the Procs ASME Meeting HTD, 1986.

[67] A. Z. S. Cheesewright R., "Distribution of temperature and local heat transfer rate in turbulent natural convection in a large rectangular cavity," in *8th Interna-tional Heat Transfer Conference*, 1986.

[68] A. C. R. Bowles A., "Direct measurements of the turbulence heat flux in a large rectangular air cavity," presented at the Experimental Heat Transfer, 1989.

[69] A. M. Lankhorst, D. Angirasa, and C. J. Hoogendoorn, "LDV measurements of buoyancy-induced flows in an enclosure at high rayleigh numbers," *Experimental Thermal and Fluid Science,* vol. 6, pp. 74-79, 1993.

[70] P. L. Betts and I. H. Bokhari, "Experiments on turbulent natural convection in an enclosed tall cavity," *International Journal of Heat and Fluid Flow,* vol. 21, pp. 675-683, Dec 2000.

[71] Y. S. Tian and T. G. Karayiannis, "Low turbulence natural convection in an air filled square cavity: Part I: the thermal and fluid flow fields," *International Journal of Heat and Mass Transfer,* vol. 43, pp. 849-866, 2000.

[72] F. Ampofo, "Turbulent natural convection in an air filled partitioned square cavity," *International Journal of Heat and Fluid Flow,* vol. 25, pp. 103-114, 2004.

[73] W. Chen and W. Liu, "Numerical and experimental analysis of convection heat transfer in passive solar heating room with greenhouse and heat storage," *Solar Energy,* vol. 76, pp. 623-633, 2004.

[74] B. Xu, B. Li, and D. Stock, "An experimental study of thermally induced convection of molten gallium in magnetic fields," *International Journal of Heat and Mass Transfer,* vol. 49, pp. 2009-2019, 2006.

[75] O. Laguerre, S. Benamara, D. Remy, and D. Flick, "Experimental and numerical study of heat and moisture transfers by natural convection in a cavity filled with solid obstacles," *International Journal of Heat and Mass Transfer,* vol. 52, pp. 5691-5700, 2009.

[76] Y. Shu, B. Li, and B. Ramaprian, "Convection in modulated thermal gradients and gravity: experimental measurements and numerical simulations," *International Journal of Heat and Mass Transfer,* vol. 48, pp. 145-160, 2005.

[77] N. Z. Ince and B. E. Launder, "On the computation of buoyancy-driven turbulent flows in rectangular enclosures," *International Journal of Heat and Fluid Flow,* vol. 10, pp. 110-117, 1989.

[78] W. P. Jones and B. E. Launder, "The calculation of low-Reynolds-number phenomena with a two-equation model of turbulence," *International Journal of Heat and Mass Transfer,* vol. 16, pp. 1119-1130, 1973.

[79] R. A. W. M. Henkes, F. F. Vandervlugt, and C. J. Hoogendoorn, "Natural-Convection Flow in a Square Cavity Calculated with Low-Reynolds-Number Turbulence Models," *International Journal of Heat and Mass Transfer,* vol. 34, pp. 377-388, Feb 1991.

[80] K. Y. Chien, "Predictions of Channel and Boundary-Layer Flows with a Low-Reynolds-Number Turbulence Model," *Aiaa Journal,* vol. 20, pp. 33-38, 1982.

[81] V. Vivek, A. K. Sharma, and C. Balaji, "Interaction effects between laminar natural convection and surface radiation in tilted square and shallow enclosures," *International Journal of Thermal Sciences,* vol. 60, pp. 70-84, 2012.

[82] C. Balaji and S. Venkateshan, "Interaction of radiation with free convection in an open cavity," *International Journal of Heat and Fluid Flow,* vol. 15, pp. 317-324, 1994.

[83] S. Mahapatra, S. Sen, and A. Sarkar, "Interaction of surface radiation and variable property natural convection in a differentially heated square cavity–a finite element analysis," *International Journal of Numerical Methods for Heat & Fluid Flow,* vol. 9, pp. 423-443, 1999.

[84] M. Akiyama and Q. Chong, "Numerical analysis of natural convection with surface radiation in a square enclosure," *Numerical Heat Transfer, Part A Applications,* vol. 32, pp. 419-433, 1997.

[85] K. Velusamy, T. Sundararajan, and K. N. Seetharamu, "Interaction effects between surface radiation and turbulent natural convection in square and rectangular enclosures," *Journal of Heat Transfer-Transactions of the Asme,* vol. 123, pp. 1062-1070, Dec 2001.

[86] G. Colomer, M. Costa, R. Consul, and A. Oliva, "Three-dimensional numerical simulation of convection and radiation in a differentially heated cavity using the discrete ordinates method," *International Journal of Heat and Mass Transfer,* vol. 47, pp. 257-269, 2004.

[87] M. Hasnaoui, E. Bilgen, and P. Vasseur, "Natural convection heat transfer in rectangular cavities partially heated from below," *Journal of Thermophysics and Heat Transfer,* vol. 6, pp. 255-264, 1992/04/01 1992.

[88] A. K. Sharma, K. Velusamy, C. Balaji, and S. Venkateshan, "Conjugate turbulent natural convection with surface radiation in air filled rectangular enclosures," *International Journal of Heat and Mass Transfer,* vol. 50, pp. 625-639, 2007.

[89] A. Andreozzi, B. Buonomo, and O. Manca, "Thermal and fluid dynamic behaviors in symmetrical heated channel-chimney systems," *International Journal of Numerical Methods for Heat & Fluid Flow,* vol. 20, pp. 811-833, 2010.

[90] A. Ben-Nakhi and M. A. Mahmoud, "Conjugate natural convection in the roof cavity of heavy construction building during summer," *Applied Thermal Engineering,* vol. 27, pp. 287-298, Feb 2007.

[91] C. Bonnebat and L. Dehbi, "Design of double skin metallic roofing for the protection of buildings against the thermal effects of sun radiation," *Steel in Sustainable Construction: Iisi World Conference 2002, Conference Proceedings,* pp. 153-162, 2002.

[92] C. Bouden, "Influence of glass curtain walls on the building thermal energy consumption under Tunisian climatic conditions: The case of administrative buildings," *Renewable Energy,* vol. 32, pp. 141-156, Jan 2007.

[93] J. A. Castillo and R. Tovar, "Transient cooling of a room with a chilled ceiling," *Solar Energy,* vol. 86, pp. 1029-1036, Apr 2012.

[94] E. Dascalaki, M. Santamouris, C. A. Balaras, and D. N. Asimakopoulos, "Natural-Convection Heat-Transfer Coefficients from Vertical and Horizontal Surfaces for Building Applications," *Energy and Buildings,* vol. 20, pp. 243-249, 1994.

[95] G. Desrayaud and G. Lauriat, "A numerical study of natural convection in partially open enclosures with a conducting side-wall," *Journal of Heat Transfer-Transactions of the Asme,* vol. 126, pp. 76-83, Feb 2004.

[96] A. Sharma, C. R. Chen, and N. V. Lan, "Solar-energy drying systems: A review," *Renewable & Sustainable Energy Reviews,* vol. 13, pp. 1185-1210, Aug-Sep 2009.

[97] R. Hu and J. L. Niu, "A review of the application of radiant cooling & heating systems in Mainland China," *Energy and Buildings,* vol. 52, pp. 11-19, Sep 2012.

[98] X. Q. Zhai, Z. P. Song, and R. Z. Wang, "A review for the applications of solar chimneys in buildings," *Renewable & Sustainable Energy Reviews,* vol. 15, pp. 3757-3767, Oct 2011.

[99] K. C. Ng, M. A. A. Aziz, and E. Y. K. Ng, "On the effect of turbulent intensity towards the accuracy of the zero-equation turbulence model for indoor airflow application," *Building and Environment,* vol. 46, pp. 82-88, Jan 2011.

[100] H. Liu and H. B. Awbi, "Performance of phase change material boards under natural convection," *Building and Environment,* vol. 44, pp. 1788-1793, Sep 2009.

[101] M. Omri and N. Galanis, "Evaluation of confined natural and forced convection predictions by different turbulence models," *International Journal of Numerical Methods for Heat & Fluid Flow,* vol. 19, pp. 5-24, 2009.

[102] M. Tencer, "Deposition of aerosol ("hygroscopic dust") on electronics - Mechanism and risk," *Microelectronics Reliability,* vol. 48, pp. 584-593, Apr 2008.

[103] A. Pasupathy, R. Velraj, and R. V. Seeniraj, "Phase change material-based building architecture for thermal management in residential and commercial establishments," *Renewable & Sustainable Energy Reviews,* vol. 12, pp. 39-64, Jan 2008.

[104] L. Goossens, J. Vanderoost, S. V. N. Jaecques, G. H. van Lenthe, G. Van der Perre, S. Boonen, J. D'hooge, S. V. N. Jaecques, and W. Lauriks, "Microstructural simulation of ultrasonic wave propagation through vertebral bone samples," *2008 Ieee Ultrasonics Symposium, Vols 1-4 and Appendix,* pp. 142-145, 2008.

[105] A. Rebora, M. Senarega, and L. A. Tagliafico, "Influence of some design parameters on the thermal performance of domestic refrigerator appliances," *Heat and Mass Transfer,* vol. 42, pp. 803-811, Jul 2006.

[106] A. H. Abib and Y. Jaluria, "Generation of stable thermal stratification in a partially enclosed space due to a room fire," *International Journal of Numerical Methods for Heat & Fluid Flow,* vol. 6, pp. 31-52, Dec 1996.

[107] M. Behnia, J. A. Reizes, and G. D. Davis, "Combined Radiation and Natural-Convection in a Rectangular Cavity with a Transparent Wall and Containing a Non-Participating Fluid," *International Journal for Numerical Methods in Fluids,* vol. 10, pp. 305-325, Feb 1990.

[108] N. P. Moshkin, "Numerical model to study natural convection in a rectangular enclosure filled with two immiscible fluids," *International Journal of Heat and Fluid Flow,* vol. 23, pp. 373-379, Jun 2002.

[109] G. D. McBain, "Natural convection with unsaturated humid air in vertical cavities," *International Journal of Heat and Mass Transfer,* vol. 40, pp. 3005-3012, Sep 1997.

[110] M. K. Das and K. S. K. Reddy, "Conjugate natural convection heat transfer in an inclined square cavity containing a conducting block," *International Journal of Heat and Mass Transfer*, vol. 49, pp. 4987-5000, Dec 2006.

[111] O. Laguerre, S. Benamara, D. Remy, and D. Flick, "Experimental and numerical study of heat and moisture transfers by natural convection in a cavity filled with solid obstacles," *International Journal of Heat and Mass Transfer*, vol. 52, pp. 5691-5700, Dec 2009.

[112] T. Ait-Taleb, A. Abdelbaki, and Z. Zrikem, "Numerical simulation of coupled heat transfers by conduction, natural convection and radiation in hollow structures heated from below or above," *International Journal of Thermal Sciences*, vol. 47, pp. 378-387, Apr 2008.

[113] A. Capriccioli and P. Frosi, "Multipurpose ANSYS FE procedure for welding processes simulation," *Fusion Engineering and Design*, vol. 84, pp. 546-553, Jun 2009.

[114] A. A. Dehghan and M. Behnia, "Combined natural convection-conduction and radiation heat transfer in a discretely heated open cavity," *Journal of Heat Transfer-Transactions of the Asme*, vol. 118, pp. 56-64, Feb 1996.

[115] P. Kumar and V. Eswaran, "A Numerical Simulation of Combined Radiation and Natural Convection in a Differential Heated Cubic Cavity," *Journal of Heat Transfer-Transactions of the Asme*, vol. 132, Feb 2010.

[116] M. J. Jonsson, A. Foetzki, M. Kalberer, T. Lundstrom, W. Ammann, and V. Stockli, "Root-soil rotation stiffness of Norway spruce (Picea abies (L.) Karst) growing on subalpine forested slopes," *Plant and Soil*, vol. 285, pp. 267-277, Jul 2006.

[117] A. Mezrhab, D. Lemonnier, S. Meftah, and A. Benbrik, "Numerical study of double-diffusion convection coupled to radiation in a square cavity filled with a participating grey gas," *Journal of Physics D-Applied Physics*, vol. 41, Oct 7 2008.

[118] A. Mezrhab, M. A. Moussaoui, and H. Naji, "Lattice Boltzmann simulation of surface radiation and natural convection in a square cavity with an inner cylinder," *Journal of Physics D-Applied Physics*, vol. 41, Jun 7 2008.

[119] P. J. Ming and W. P. Zhang, "Numerical Simulation of Natural Convection and Radiation Heat Transfer in Two-Dimensional Enclosure on Hybrid Grids," *Numerical Heat Transfer Part B-Fundamentals*, vol. 61, pp. 505-520, 2012.

[120] F. Moufekkir, M. A. Moussaoui, A. Mezrhab, D. Lemonnier, and H. Naji, "MRT-lattice Boltzmann computations of natural convection and volumetric radiation in a tilted square enclosure," *International Journal of Thermal Sciences*, vol. 54, pp. 125-141, Apr 2012.

[121] F. Moufekkir, M. A. Moussaoui, A. Mezrhab, H. Naji, and D. Lemonnier, "Numerical prediction of heat transfer by natural convection and radiation in an enclosure filled with an isotropic scattering medium," *Journal of Quantitative Spectroscopy & Radiative Transfer*, vol. 113, pp. 1689-1704, Sep 2012.

[122] S. VijayaVenkataRaman, S. Iniyan, and R. Goic, "A review of solar drying technologies," *Renewable & Sustainable Energy Reviews*, vol. 16, pp. 2652-2670, Jun 2012.

[123] F. D. Costa and D. Sandberg, "Mathematical model of a smoldering log," *Combustion and Flame*, vol. 139, pp. 227-238, Nov 2004.

[124] Y. Jaluria, "Study of Transient Heat-Transfer in Long Insulated Wires," *Journal of Heat Transfer-Transactions of the Asme,* vol. 98, pp. 127-132, 1976.

[125] S. C. Haldar, K. Manohar, and G. S. Kochhar, "Conjugate conduction-convection analysis of empty freezers," *Energy Conversion and Management,* vol. 49, pp. 783-790, Apr 2008.

[126] M. K. Chourasia and T. K. Goswami, "CFD simulation of effects of operating parameters and product on heat transfer and moisture loss in the stack of bagged potatoes," *Journal of Food Engineering,* vol. 80, pp. 947-960, Jun 2007.

[127] M. K. Chourasia and T. K. Goswami, "Simulation of transport phenomena during natural convection cooling of bagged potatoes in cold storage, part 1: Fluid flow and heat transfer," *Biosystems Engineering,* vol. 94, pp. 33-45, May 2006.

[128] Y. Yamashita, Y. Hirata, Y. Iwata, K. Yamazaki, and Y. Ito, "Performance and heat transfer characteristics of a latent heat storage unit with finned tubes: Experimental study on liquefaction of LNG Boil-off Gas by melting n-pentane as a phase-change material," *Kagaku Kogaku Ronbunshu,* vol. 30, pp. 399-406, Jul 2004.

[129] D. L. James and S. Stevkovski, "Thermal analysis of the ALR8(SI) plutonium storage container," *Journal of Thermophysics and Heat Transfer,* vol. 16, pp. 575-586, Oct-Dec 2002.

[130] M. A. Cotter and M. E. Charles, "Transient Cooling of Petroleum by Natural-Convection in Cylindrical Storage Tanks - a Simplified Heat-Loss Model," *Canadian Journal of Chemical Engineering,* vol. 70, pp. 1090-1093, Dec 1992.

[131] E. Gratia and A. De Herde, "The most efficient position of shading devices in a double-skin facade," *Energy and Buildings,* vol. 39, pp. 364-373, Mar 2007.

[132] K. C. Lin and A. Violi, "Natural convection heat transfer of nanofluids in a vertical cavity: Effects of non-uniform particle diameter and temperature on thermal conductivity," *International Journal of Heat and Fluid Flow,* vol. 31, pp. 236-245, Apr 2010.

[133] C. Teodosiu, R. Hohota, G. Rusaouen, and M. Woloszyn, "Numerical prediction of indoor air humidity and its effect on indoor environment," *Building and Environment,* vol. 38, pp. 655-664, May 2003.

[134] D. J. Close and J. Sheridan, "Natural-Convection in Enclosures Filled with a Vapor and a Non-Condensing Gas," *International Journal of Heat and Mass Transfer,* vol. 32, pp. 855-862, May 1989.

[135] G. Desrayaud and G. Lauriat, "Heat and mass transfer analogy for condensation of humid air in a vertical channel," *Heat and Mass Transfer,* vol. 37, pp. 67-76, Jan 2001.

[136] N. Laaroussi and G. Lauriat, "Conjugate thermosolutal convection and condensation of humid air in cavities," *International Journal of Thermal Sciences,* vol. 47, pp. 1571-1586, 2008.

[137] E. J. Braga and M. J. S. de Lemos, "Laminar natural convection in cavities filled with circular and square rods," *International Communications in Heat and Mass Transfer,* vol. 32, pp. 1289-1297, 2005.

[138] K. Hooman and A. A. Merrikh, "Theoretical Analysis of Natural Convection in an Enclosure Filled with Disconnected Conducting Square Solid Blocks," *Transport in Porous Media,* vol. 85, pp. 641-651, Nov 2010.

[139] A. K. A. Shati, S. G. Blakey, and S. B. M. Beck, "An empirical solution to turbulent natural convection and radiation heat transfer in square and rectangular enclosures," *Applied Thermal Engineering,* vol. 51, pp. 364-370, 2013.

[140] S. K. Jena and S. K. Mahapatra, "Numerical modeling of interaction between surface radiation and natural convection of atmospheric aerosol in presence of transverse magnetic field," *Applied Mathematical Modelling,* vol. 37, pp. 527-539, Jan 2013.

[141] A. Shaija and G. S. V. L. Narasimham, "Effect of surface radiation on conjugate natural convection in a horizontal annulus driven by inner heat generating solid cylinder," *International Journal of Heat and Mass Transfer,* vol. 52, pp. 5759-5769, Dec 2009.

[142] A. K. Sharma, K. Velusamy, and C. Balaji, "Interaction of turbulent natural convection and surface thermal radiation in inclined square enclosures," *Heat and Mass Transfer,* vol. 44, pp. 1153-1170, Aug 2008.

[143] H. M. Duwairi, "Radiation effects on mixed convection over a nonisothermal cylinder and sphere in a porous media," *Journal of Porous Media,* vol. 9, pp. 251-259, 2006.

[144] E. H. Ridouane, M. Hasnaoui, A. Amahmid, and A. Raji, "Interaction between natural convection and radiation in a square cavity heated from below," *Numerical Heat Transfer Part a-Applications,* vol. 45, pp. 289-311, Feb 2004.

[145] N. Ramesh and S. P. Venkateshan, "Effect of surface radiation and partition resistance on natural convection heat transfer in a partitioned enclosure: An experimental study," *Journal of Heat Transfer-Transactions of the Asme,* vol. 121, pp. 616-622, Aug 1999.

[146] M. A. Hossain and M. A. Alim, "Natural convection-radiation interaction on boundary layer flow along a thin vertical cylinder," *Heat and Mass Transfer,* vol. 32, pp. 515-520, Aug 1997.

[147] C. Balaji and S. P. Venkateshan, "Combined Conduction, Convection and Radiation in a Slot," *International Journal of Heat and Fluid Flow,* vol. 16, pp. 139-144, Apr 1995.

[148] Z. Zhao, D. Poulikakos, and Z. Ren, "Combined Natural-Convection and Radiation from Heated Cylinders inside a Container," *Journal of Thermophysics and Heat Transfer,* vol. 6, pp. 713-720, Oct-Dec 1992.

[149] S. S. Kutateladze, A. G. Kirdyashkin, and V. P. Ivakin, "Turbulent natural convection on a vertical plate and in a vertical layer," *International Journal of Heat and Mass Transfer,* vol. 15, pp. 193-202, 1972.

[150] P. Filis and D. Poulikakos, "An experimental study of the effect of wall temperature nonuniformity on natural convection in an enclosure heated from the side," *International Journal of Heat and Fluid Flow,* vol. 7, pp. 258-265, 1986.

[151] H. Han and T. H. Kuehn, "Double diffusive natural convection in a vertical rectangular enclosure—I. Experimental study," *International Journal of Heat and Mass Transfer,* vol. 34, pp. 449-459, 1991.

[152] K. J. King, "Turbulent Natural Convection In Rectangular Air Cavities.," Ph.D. thesis, Queen Mary College London, UK., 1989

[153] A. T. Kirkpatrick and M. Bohn, "An experimental investigation of mixed cavity natural convection in the high Rayleigh number regime," *International Journal of Heat and Mass Transfer,* vol. 29, pp. 69-82, 1986.

[154] R. Cheeswright, King, K.J. and Ziui, S., "Experimental Data for the Validation of Computer Codes for the Prediction of Two-Dimensional Buoyant Cavity Flows," *in: ASME Winter Annual Meeting, Anaheim, HTD-60,,* December 1986.

[155] A. A. Dafa'Alla and P. L. Betts, "Experimental study of turbulent natural convection in a tall air cavity," *Experimental Heat Transfer An International Journal,* vol. 9, pp. 165-194, 1996.

[156] P. Betts and I. Bokhari, "Experiments on turbulent natural convection in an enclosed tall cavity," *International Journal of Heat and Fluid Flow,* vol. 21, pp. 675-683, 2000.

[157] Y. S. Tian and T. G. Karayiannis, "Low turbulence natural convection in an air filled square cavity: Part II: the turbulence quantities," *International Journal of Heat and Mass Transfer,* vol. 43, pp. 867-884, 2000.

[158] Y. Tian and T. Karayiannis, "Low turbulence natural convection in an air filled square cavity: part I: the thermal and fluid flow fields," *International Journal of Heat and Mass Transfer,* vol. 43, pp. 849-866, 2000.

[159] B. Xu and B. Q. Li, "Hot-film measurement of temperature gradient induced natural convection in liquid gallium," *Experimental Thermal and Fluid Science,* vol. 29, pp. 697-704, 2005.

[160] Y. Shu, B. Q. Li, and B. R. Ramaprian, "Convection in modulated thermal gradients and gravity: experimental measurements and numerical simulations," *International Journal of Heat and Mass Transfer,* vol. 48, pp. 145-160, 2005.

[161] R. A. W. M. Henkes, F. F. Van Der Vlugt, and C. J. Hoogendoorn, "Natural-convection flow in a square cavity calculated with low-Reynolds-number turbulence models," *International Journal of Heat and Mass Transfer,* vol. 34, pp. 377-388, 1991.

[162] C. Balaji and S. P. Venkateshan, "Interaction of surface radiation with free convection in a square cavity," *International Journal of Heat and Fluid Flow,* vol. 14, pp. 260-267, 1993.

[163] K. S. Velusamy, T; Seetharamu, KN., "Interaction effects between surface radiation and turbulent natural convection in square and rectangular enclosures," *J. Heat Transfer,* vol. 123, pp. 1062-1070, 2001.

[164] E. H. M. Hasnaoui, "Effect of Surface Radiation on Multiple Natural Convection Solutions in a Square Cavity Partially Heated from Below," *J. Heat Transfer* vol. 128, pp. 1012-1021, 2006.

[165] A. K. Sharma, K. Velusamy, C. Balaji, and S. P. Venkateshan, "Conjugate turbulent natural convection with surface radiation in air filled rectangular enclosures," *International Journal of Heat and Mass Transfer,* vol. 50, pp. 625-639, 2007.

[166] E. Sparrow, L. Azevedo, and A. Prata, "Two-fluid and single-fluid natural convection heat transfer in an enclosure," *Journal of heat transfer,* vol. 108, pp. 848-852, 1986.

[167] O. Laguerre, S. Benamara, D. Remy, and D. Flick, "Experimental and numerical study of heat and moisture transfers by natural convection in a cavity filled with solid obstacles," *International Journal of Heat and Mass Transfer,* vol. 52, pp. 5691-5700, 2009.

[168] C. Teodosiu, R. Hohota, G. Rusaouën, and M. Woloszyn, "Numerical prediction of indoor air humidity and its effect on indoor environment," *Building and Environment*, vol. 38, pp. 655-664, 2003.
[169] H. S. Yoon, D. H. Yu, M. Y. Ha, and Y. G. Park, "Three-dimensional natural convection in an enclosure with a sphere at different vertical locations," *International Journal of Heat and Mass Transfer*, vol. 53, pp. 3143-3155, 2010.
[170] D.F.P. Incropera, T.L. Bergman and A.S. Lavine, *Principles of Heat and Mass Transfer*. Danvers: John Wiley and Sons, Inc., 2013.
[171] Y. Jaluria, *Natural Convection Heat and Mass Transfer* vol. 5. London: William Clowes Limited, 1980.
[172] F. M. White, *Heat and Mass Transfer*. Canada: Addison-Wesley, 1988.
[173] H. K. V. W. Malalasekera, *An Introduction to Fluid Dynamics : The Finite Volume Method*. London: Pearson Education Limited, 2007.
[174] X. Z. Wang, K. J. Roberts, and C. Ma, "Crystal growth measurement using 2D and 3D imaging and the perspectives for shape control," *Chemical Engineering Science*, vol. 63, pp. 1173-1184, Mar 2008.
[175] G. Adomian, "Solution of the Navier Stokes Equation .1.," *Computers & Mathematics with Applications-Part A*, vol. 12, pp. 1119-1124, Nov 1986.
[176] R. G. Deissler, "Derivation of Navier-Stokes Equation," *American Journal of Physics*, vol. 44, pp. 1128-1130, 1976.
[177] M. F. Modest, *Radiation Heat Transfer*. United State: McGraw-Hill, 1993.
[178] Z. Uddin and S. Harmand, "Natural convection heat transfer of nanofluids along a vertical plate embedded in porous medium," *Nanoscale Research Letters*, vol. 8, pp. 1-19, Feb 7 2013.
[179] H. J. Kim, B. H. An, J. Park, and D. K. Kim, "Experimental study on natural convection heat transfer from horizontal cylinders with longitudinal plate fins," *Journal of Mechanical Science and Technology*, vol. 27, pp. 593-599, Feb 2013.
[180] A. Horibe, R. Shimoyama, N. Haruki, and A. Sanada, "Experimental study of flow and heat transfer characteristics of natural convection in an enclosure with horizontal parallel heated plates," *International Journal of Heat and Mass Transfer*, vol. 55, pp. 7072-7078, Nov 2012.
[181] G. Nardini and M. Paroncini, "Heat transfer experiment on natural convection in a square cavity with discrete sources," *Heat and Mass Transfer*, vol. 48, pp. 1855-1865, Nov 2012.
[182] S. Grafsronningen and A. Jensen, "Natural convection heat transfer from two horizontal cylinders at high Rayleigh numbers," *International Journal of Heat and Mass Transfer*, vol. 55, pp. 5552-5564, Oct 2012.
[183] K. S. Reddy and N. S. Kumar, "Combined laminar natural convection and surface radiation heat transfer in a modified cavity receiver of solar parabolic dish," *International Journal of Thermal Sciences*, vol. 47, pp. 1647-1657, Dec 2008.
[184] S. Kiwan and M. Khodier, "Natural convection heat transfer in an open-ended inclined channel-partially filled with porous media," *Heat Transfer Engineering*, vol. 29, pp. 67-75, 2008.
[185] E. Baez and A. Nicolas, "Natural convection fluid flow and heat transfer in porous media," *Journal of Mechanics of Materials and Structures*, vol. 2, pp. 1571-1584, Oct 2007.

[186] H. K. Versteeg and W. Malalasekera, *An introduction to computational fluid dynamics : the finite volume method*. Harlow, Essex, England Longman Scientific & Technical ;: New York : Wiley, 1995.
[187] H. C. Chen and V. C. Patel, "Near-Wall Turbulence Models for Complex Flows Including Separation," *Aiaa Journal,* vol. 26, pp. 641-648, Jun 1988.
[188] F. R. Menter, "2-Equation Eddy-Viscosity Turbulence Models for Engineering Applications," *Aiaa Journal,* vol. 32, pp. 1598-1605, Aug 1994.
[189] S. K. Choi and S. O. Kim, "Computation of a turbulent natural convection in a rectangular cavity with the elliptic-blending second-moment closure," *International Communications in Heat and Mass Transfer,* vol. 33, pp. 1217-1224, Dec 2006.
[190] S. Kenjeres and K. Hanjalic, "Prediction of Turbulent Thermal-Convection in Concentric and Eccentric Horizontal Annuli," *International Journal of Heat and Fluid Flow,* vol. 16, pp. 429-439, Oct 1995.
[191] A. J. N. Khalifa, "Natural convective heat transfer coefficient - a review II. Surfaces in two- and three-dimensional enclosures," *Energy Conversion and Management,* vol. 42, pp. 505-517, Mar 2001.
[192] R. Martinuzzi and A. Pollard, "Comparative study of turbulence models in predicting turbulent pipe flow. I-Algebraic stress and k-epsilon models," *Aiaa Journal,* vol. 27, pp. 29-36, 1989.
[193] V. C. Patel, W. Rodi, and G. Scheuerer, "Turbulence models for near-wall and low Reynolds number flows-a review," *Aiaa Journal,* vol. 23, pp. 1308-1319, 1985.
[194] C. Hrenya, E. Bolio, D. Chakrabarti, and J. Sinclair, "Comparison of low Reynolds number turbulence models in predicting fully developed pipe flow," *Chemical Engineering Science,* vol. 50, pp. 1923-1941, 1995.
[195] S. J. Wang and A. S. Mujumdar, "A comparative study of five low Reynolds number k-epsilon models for impingement heat transfer," *Applied Thermal Engineering,* vol. 25, pp. 31-44, Jan 2005.
[196] R. Abid, "Evaluation of 2-Equation Turbulence Models for Predicting Transitional Flows," *International Journal of Engineering Science,* vol. 31, pp. 831-840, Jun 1993.
[197] C. K. G. Lam and K. Bremhorst, "A Modified Form of the K-Epsilon Model for Predicting Wall Turbulence," *Journal of Fluids Engineering-Transactions of the Asme,* vol. 103, pp. 456-460, 1981.
[198] B. E. Launder and B. I. Sharma, "Application of the energy-dissipation model of turbulence to the calculation of flow near a spinning disc," *Letters in Heat and Mass Transfer,* vol. 1, pp. 131-137, 1974.
[199] Z. Yang and T. Shih, "New time scale based k-epsilon model for near-wall turbulence," *Aiaa Journal,* vol. 31, pp. 1191-1198, 1993.
[200] K. Abe, T. Kondoh, and Y. Nagano, "A New Turbulence Model for Predicting Fluid-Flow and Heat-Transfer in Separating and Reattaching Flows .1. Flow-Field Calculations," *International Journal of Heat and Mass Transfer,* vol. 37, pp. 139-151, Jan 1994.
[201] K. C. Chang, W. D. Hsieh, and C. S. Chen, "A modified low-Reynolds-number turbulence model applicable to recirculating flow in pipe expansion," *Journal of Fluids Engineering-Transactions of the Asme,* vol. 117, pp. 417-423, Sep 1995.

[202] J. Kim, P. Moin, and R. Moser, "Turbulence Statistics in Fully-Developed Channel Flow at Low Reynolds-Number," *Journal of Fluid Mechanics,* vol. 177, pp. 133-166, Apr 1987.
[203] S. A. P. Hassid, M., "A Turbulent Energy Dissipation Model for Flows Drag Reduction," *J. Fluid Engng,* vol. 100, pp. 107-112, 1978.
[204] K. Hanjalic and B. E. Launder, "Contribution Towards a Reynolds-Stress Closure for Low-Reynolds-Number Turbulence," *Journal of Fluid Mechanics,* vol. 74, pp. 593-610, 1976.
[205] G. Batchelor and A. Townsend, "Decay of isotropic turbulence in the initial period," *Proceedings of the Royal Society of London. Series A. Mathematical and Physical Sciences,* vol. 193, pp. 539-558, 1948.
[206] G. Batchelor and A. Townsend, "Decay of turbulence in the final period," *Proceedings of the Royal Society of London. Series A. Mathematical and Physical Sciences,* vol. 194, pp. 527-543, 1948.
[207] A. V. Appalaswamy and Y. Jaluria, "Axisymmetric Plume Flow in a Vertical Uniform Free Stream," *Journal of Applied Mechanics-Transactions of the Asme,* vol. 47, pp. 667-669, 1980.
[208] S. Hussain and P. H. Oosthuizen, "Validation of numerical modeling of conditions in an atrium space with a hybrid ventilation system," *Building and Environment,* vol. 52, pp. 152-161, Jun 2012.
[209] S. Dembele, K. L. M. Lima, and J. X. Wen, "Assessment of an unstructured exponential scheme discrete ordinates radiation model for non-gray media," *Heat and Mass Transfer,* vol. 47, pp. 1349-1362, Nov 2011.
[210] R. Henkes and C. Hoogendoorn, "Comparison of turbulence models for the natural convection boundary layer along a heated vertical plate," *International Journal of Heat and Mass Transfer,* vol. 32, pp. 157-169, 1989.
[211] W. Wu, D. Ewing, and C. Ching, "The effect of the top and bottom wall temperatures on the laminar natural convection in an air-filled square cavity," *International Journal of Heat and Mass Transfer,* vol. 49, pp. 1999-2008, 2006.
[212] Y. Jaluria, *Natural convection*: Pergamon Press Oxford, 1980.
[213] A. Gerasimov, "Modelling Turbulence Flows with Fluent," *Europe ANSYS Inc. ,* 2006.
[214] F. Ampofo and T. Karayiannis, "Experimental benchmark data for turbulent natural convection in an air filled square cavity," *International Journal of Heat and Mass Transfer,* vol. 46, pp. 3551-3572, 2003.
[215] Fluent, "User's Guide Fluent 13.0, Fluent Incorporated, 2011.
[216] B. E. Launder and D. B. Spalding, "The numerical computation of turbulent flows," *Computer Methods in Applied Mechanics and Engineering,* vol. 3, pp. 269-289, 1974.
[217] T.-H. Shih, W. W. Liou, A. Shabbir, Z. Yang, and J. Zhu, "A new< i> k</i>-ϵ eddy viscosity model for high reynolds number turbulent flows," *Computers & Fluids,* vol. 24, pp. 227-238, 1995.
[218] V. Yakhot and S. A. Orszag, "Renormalization group analysis of turbulence. I. Basic theory," *Journal of scientific computing,* vol. 1, pp. 3-51, 1986.
[219] K. Abe, T. Kondoh, and Y. Nagano, "A new turbulence model for predicting fluid flow and heat transfer in separating and reattaching flows—I. Flow field calculations," *International Journal of Heat and Mass Transfer,* vol. 37, pp. 139-151, 1994.

[220] N. D. Francis, *Characterization of Fuego for Laminar and Turbulent Natural Convection Heat Transfer*: United States. Department of Energy, 2005.
[221] K. Lari, M. Baneshi, S. A. Gandjalikhan Nassab, A. Komiya, and S. Maruyama, "Combined heat transfer of radiation and natural convection in a square cavity containing participating gases," *International Journal of Heat and Mass Transfer,* vol. 54, pp. 5087-5099, 2011.
[222] Charnwood. 20012). Digital thermometers.
[223] A. Chunovkina and A. Chursin, ""Guide to the Expression of Uncertainty in Measurement" (GUM) and "mutual recognition of national measurement standards and of calibration and measurement certificates issued by national metrology institutes" (MRA): Some problems of data processing and measurement uncertainty evaluation," *Advanced Mathematical and Computational Tools in Metrology V,* vol. 57, pp. 55-66, 2001.
[224] F. Penot and A. Ndame, "Successive Bifurcations of Natural-Convection in a Vertical Enclosure Heated from the Side," *Heat Transfer, Vols 1 and 2,* vol. 129, pp. 507-513, 1992.
[225] R. Capdevila, O. Lehmkuhl, G. Colomer, and C. D. Perez-Segarra, "Study of turbulent natural convection in a tall differentially heated cavity filled with either non-participating, participating grey and participating semigrey media," *6th European Thermal Sciences Conference (Eurotherm 2012),* vol. 395, 2012.
[226] H. X. Yang and Z. J. Zhu, "Numerical study of three-dimensional turbulent natural convection in a differentially heated air-filled tall cavity," *International Communications in Heat and Mass Transfer,* vol. 35, pp. 606-612, May 2008.
[227] S. Lorente, J. Lee, and A. Bejan, "The "flow of stresses" concept: The analogy between mechanical strength and heat convection," *International Journal of Heat and Mass Transfer,* vol. 53, pp. 2963-2968, Jul 2010.
[228] K. M. Wang, S. Lorente, and A. Bejan, "Vascular structures for volumetric cooling and mechanical strength," *Journal of Applied Physics,* vol. 107, Feb 15 2010.
[229] L. Davoust, M. D. Cowley, R. Moreau, and R. Bolcato, "Buoyancy-driven convection with a uniform magnetic field. Part 2. Experimental investigation," *Journal of Fluid Mechanics,* vol. 400, pp. 59-90, Dec 10 1999.
[230] R. A. W. M. Henkes and C. J. Hoogendoorn, "Comparison Exercise for Computations of Turbulent Natural-Convection in Enclosures," *Numerical Heat Transfer Part B-Fundamentals,* vol. 28, pp. 59-78, Jul-Aug 1995.
[231] D. A. Iyi, R. Hasan and R. Penlington, "Numerical Simulation of 2D Turbulent Natural Convection of Humid Air in a Cavity Filled with Solid Objects," *Procedia Engineering,* vol. 56, pp. 538-543, 2013.
[232] D. A. Iyi, R. Hasan, and R. Penlington, "Numerical Analysis of the Influence of Thermal Boundary Condition and Surface Emissivity on the Flow and Heat Transfer in Turbulent Buoyancy Driven Flow," in *The Third Asian Symposium on Computational Heat Transfer and Fluid Flow, 22-26 September, Kyoto*, 2011.
[233] D. A. Iyi, R. Hasan and R. Penlington, "Numerical Simulation of 2D Turbulent Natural Convection of Humid Air in a Cavity Filled with Solid Objects," *Procedia Engineering,* vol. 56, pp. 538-543, 2013.

[234] R. Hasan, J. McGuirk, D. Apsley, and M. Leschziner, "A turbulence model study of separated 3D jet/afterbody flow," *Aeronautical Journal,* vol. 108, pp. 1-14, 2004.
[235] S. Chandrasekhar, *Radiation Transfer*. Dover, New York, 1960.
[236] D. J. T. Hyde, J.S, "The Discrete Ordinates Approximation for Multidimensional Radiation Heat Transfer in Furnances," Technical Report, UKAEA No. AERE-R-8502, AERE Harwell1977.
[237] W. A. Fiveland, "Three-dimensional Radiative Heat Transfer Solutions by the Discrete-ordinates Method," *J. Thermophys. Heat Transfer,* vol. 2, pp. 309-316, 1988.
[238] W. A. Fiveland, "A Discrete Ordinates Method for Predicting Radiation Heat Transfer in Axisymmetric Enclosures, ASME Paper 82-HT-20," 1982.
[239] Y. Kamotani, L. W. Wang, and S. Ostrach, "Experiments on Natural-Convection Heat-Transfer in Low Aspect Ratio Enclosures," *Aiaa Journal,* vol. 21, pp. 290-294, 1983.
[240] B. Wang, J. F. Mao, and L. J. Wang, "2-D Numerical Analysis of Combined Heat and Mass Transfer in Straight Rectangular Fin with Natural Convection," *Key Engineering Materials and Computer Science,* vol. 320, pp. 651-656, 2011.
[241] Z. T. Yu, W. Wang, X. Xu, L. W. Fan, Y. C. Hu, and K. F. Cen, "A numerical investigation of transient natural convection heat transfer of aqueous nanofluids in a differentially heated square cavity," *International Communications in Heat and Mass Transfer,* vol. 38, pp. 585-589, May 2011.
[242] Y. L. Zhang, Z. H. Rao, S. F. Wang, H. Zhang, L. J. Li, and M. L. Zhang, "Natural Convection Heat Transfer of the PCM Microcapsule Slurry for a Solid Phase State in a Horizontal Rectangular Enclosure," *Manufacturing Science and Technology, Pts 1-3,* vol. 295-297, pp. 1393-1396, 2011.
[243] S. Kim, S. Lorente, and A. Bejan, "Transient behavior of vascularized walls exposed to sudden heating," *International Journal of Thermal Sciences,* vol. 48, pp. 2046-2052, Nov 2009.
[244] J. R. Howell, "Thermal Radiation in Participating Media: The past, the present and some possible future," *Journal of Heat and Fluid Flow,* vol. 25, pp. 659-670, 1988.
[245] B. Griffith and Q. Y. Chen, "Framework for coupling room air models to heat balance model load and energy calculations (RP-1222)," *Hvac&R Research,* vol. 10, pp. 91-111, 2004.
[246] J. Winter, "Intelligent glass facades," *Architectural Review,* vol. 207, pp. 97-97, Jan 2000.
[247] B. Bielek, M. Bielek, and D. Szabo, "New Knowledge About Regime of Natural Physical Cavity of Double-Skin Transparent Facade under Windless Climate Conditions - Long Term in-Situ Experimental Research," *Cesb 10: Central Europe Towards Sustainable Building - from Theory to Practice,* pp. 77-80, 2010.
[248] Y. Takemasa, M. Hiraoka, M. Katoh, K. Miura, S. Kasai, and T. Oya, "Natural Ventilation with Dynamic Facades," *International Journal of Ventilation,* vol. 8, pp. 287-298, Dec 2009.
[249] K. Roth, T. Lawrence, and J. Brodrick, "Double-skin facades," *Ashrae Journal,* vol. 49, pp. 70, Oct 2007.
[250] A. Compagno, "Intelligent Glass Facades ", Berlin: Birkhäuser, 2002.

[251] K. Harrison, and Meyer-Boake, T, "The Tectonics of the Environmental Skin," University of Waterloo, School of Architecture, 2003.

[252] G. Ballestini, M. De Carli, N. Masiero, and G. Tombola, "Possibilities and limitations of natural ventilation in restored industrial archaeology buildings with a double-skin facade in Mediterranean climates," *Building and Environment,* vol. 40, pp. 983-995, Jul 2005.

[253] D. C. M. Ballestini G., Masiero N., and Tombola G. , "Possibilities and limitations of natural ventilation in restored industrial archaeology buildings with a doubled-skin facade in Mediterranean climates," presented at the Building and Environment 2005.

[254] M. Kragh, "Mechanically ventilated double skin facades," *Advances in Building Technology, Vols I and Ii, Proceedings,* pp. 1233-1240, 2002.

[255] S. K. Chou, K. J. Chua, and J. C. Ho, "A study on the effects of double skin facades on the energy management in buildings," *Energy Conversion and Management,* vol. 50, pp. 2275-2281, Sep 2009.

[256] N. Hamza, "Double versus single skin facades in hot and areas," *Energy and Buildings,* vol. 40, pp. 240-248, 2008.

[257] M. W. Valentin G., and Jean-Jacques R, "An Investigation into the Effect of Ventilated Double-Skin Facade with Venetian Blinds: Global Simulation and Assessment of Energy Performance," in *Proc. Building Simulation*, 2007.

[258] I. C. B. Belgian Building Research Institute (BBRI) (2002). Source book for a better understanding of conceptual and operational aspects of active facades. Department of Building Physics.

[259] M. A. Haggag, "Building skin and energy efficiency in a hot climate with particular reference to Dubai, UAE," *Energy and Sustainability,* vol. 105, pp. 287-297, 2007.

[260] G. Q. He, L. F. Shu, and S. M. Zhang, "Double skin facades in the hot summer and cold winter zone in China: Cavity open or closed?," *Building Simulation,* vol. 4, pp. 283-291, Dec 2011.

[261] M. G. Ignjatovic, B. D. Blagojevic, B. V. Stojanovic, and M. M. Stojiljkovic, "Influence of Glazing Types and Ventilation Principles in Double Skin Facades on Delivered Heating and Cooling Energy during Heating Season in an Office Building," *Thermal Science,* vol. 16, pp. S461-S469, 2012.

[262] W. J. Stec and A. H. C. van Paassen, "Symbiosis of the double skin facade with the HVAC system," *Energy and Buildings,* vol. 37, pp. 461-469, May 2005.

[263] A. Zollner, E. R. F. Winter, and R. Viskanta, "Experimental studies of combined heat transfer in turbulent mixed convection fluid flows in double-skin-facades," *International Journal of Heat and Mass Transfer,* vol. 45, pp. 4401-4408, Oct 2002.

[264] M. Fossa, C. Menezo, and E. Leonardi, "Experimental natural convection on vertical surfaces for building integrated photovoltaic (BIPV) applications," *Experimental Thermal and Fluid Science,* vol. 32, pp. 980-990, Feb 2008.

[265] C. Menezo, M. Fossa, and E. Leonardi, "An experimental investigation of free cooling by natural convection of vertical surfaces for building integrated photovoltaic (BIPV) applications," *2007 International Conference on Thermal Issues in EmergingTechnologies - Theory and Applications,* pp. 119-125, 2007.

[266] N. Safer, M. Woloszyn, and J. J. Roux, "Three-dimensional simulation with a CFD tool of the airflow phenomena in single floor double-skin facade equipped with a venetian blind," *Solar Energy*, vol. 79, pp. 193-203, 2005.

[267] A. S. Andjelkovic, T. B. Cvjetkovic, D. D. Djakovic, and I. H. Stojanovic, "Development of Simple Calculation Model for Energy Performance of Double Skin Facades," *Thermal Science*, vol. 16, pp. S251-S267, 2012.

[268] J. Boyer and A. Dang, "Designing for performance: A case study in the applied science of an environmentally responsive high-rise design," *Building Simulation 2007, Vols 1-3, Proceedings*, pp. 1720-1725, 2007.

[269] Daryanto, "Comparative Study of Heat Transfer in Double Skin Facades On High-Rise Office Building in Jakarta Daryanto," *Progress in Civil Engineering, Pts 1-4*, vol. 170-173, pp. 2751-2755, 2012.

[270] V. I. Hanby, M. J. Cook, D. G. Infield, Y. Ji, D. L. Loveday, L. Mei, and M. J. Holmes, "Nodal network and CFD simulation of airflow and heat transfer in double skin facades with blinds," *Building Services Engineering Research & Technology*, vol. 29, pp. 45-59, 2008.

[271] T. E. Jiru and F. Haghighat, "Modeling ventilated double skin facade - A zonal approach," *Energy and Buildings*, vol. 40, pp. 1567-1576, 2008.

[272] E. Oesterle, Lieb, R-D., Lutz, M., & Heusler, W. , "Double Skin Facades – Integrated Planning," Prestel Verlag: Munich, Germany, 2001.

[273] A. Reith, A. Gelesz, and G. Pultz, "Evaluation and optimization of a double skin facade with the help of computational simulations," *Bauphysik*, vol. 33, pp. 111-117, Apr 2011.

[274] L. Xu and T. Ojima, "Field experiments on natural energy utilization in a residential house with a double skin facade system," *Building and Environment*, vol. 42, pp. 2014-2023, May 2007.

[275] W. T. Ding, Y. J. Hasemi, and T. Yamada, "Natural ventilation performance of a double-skin facade with a solar chimney," *Energy and Buildings*, vol. 37, pp. 411-418, Apr 2005.

[276] F. Di Maio and A. H. C. van Paassen, "Integration of double facades and ventilation systems in buildings," *Advances in Building Technology, Vols I and Ii, Proceedings*, pp. 1225-1232, 2002.

[277] P. D. V. MVD, "Development of simplified tools for evaluation energy performance of double façades," presented at the The International Building Physics Conference, Eindhoven, September 2002.

[278] H. Shahid and D. Naylor, "Energy performance assessment of a window with a horizontal Venetian blind," *Energy and Buildings*, vol. 37, pp. 836-843, Aug 2005.

[279] D. Naylor and M. Collins, "Evaluation of an approximate method for predicting the U value of a window with a between-panes blind," *Numerical Heat Transfer Part a-Applications*, vol. 47, pp. 233-250, Feb 9 2005.

[280] C. M. Marjanovic L, Hanby VI, and Rees S, "CFD modelling of convective heat transfer from a window with adjacent venetian blinds," presented at the The Ninth International IBPSA Conference, Montreal, Canada, 2005.

[281] E. Djunaedy, Hensen, J.L.M., & Loomans, M.G.L.C, "Towards a Strategy for Airflow Simulation in Building Design," presented at the Centre for Building & Systems TNO - TU/e. Technische Universiteit Eindhoven, Netherlands, 2002.

[282] J. L. M. Hensen, Bartak, M., & Drkal, F, "Modelling and simulation of double-skin facade systems," presented at the ASHRAE Transactions, Atlanta, GA, 2002.

[283] M. Bhamjee, A. Nurick, and D. M. Madyira, "An experimentally validated mathematical and CFD model of a supply air window: Forced and natural flow," *Energy and Buildings,* vol. 57, pp. 289-301, Feb 2013.

[284] Z. Zeng, X. F. Li, C. Li, and Y. X. Zhu, "Modeling ventilation in naturally ventilated double-skin facade with a venetian blind," *Building and Environment,* vol. 57, pp. 1-6, Nov 2012.

[285] A. Guardo, M. Coussirat, C. Valero, E. Egusquiza, and P. Alavedra, "CFD assessment of the performance of lateral ventilation in Double Glazed Facades in Mediterranean climates," *Energy and Buildings,* vol. 43, pp. 2539-2547, Sep 2011.

[286] E. Gratia and A. De Herde, "Guidelines for improving natural daytime ventilation in an office building with a double-skin facade," *Solar Energy,* vol. 81, pp. 435-448, 2007.

[287] E. Gratia and A. De Herde, "Are energy consumptions decreased with the addition of a double-skin?," *Energy and Buildings,* vol. 39, pp. 605-619, May 2007.

[288] E. Gratia and A. De Herde, "Greenhouse effect in double-skin facade," *Energy and Buildings,* vol. 39, pp. 199-211, Feb 2007.

[289] T. Pasquay, "Natural ventilation in high-rise buildings with double facades, saving or waste of energy," *Energy and Buildings,* vol. 36, pp. 381-389, Apr 2004.

[290] L. D. L. Mei L, Infield DG, Hanby V, Cook M, Li Y, Holmes M, Bates J., "The Influence of Blinds on Temperatures and Air Flows within Ventilated Double-Skin Facades," presented at the Proceedings of Clima 2007 Well Being Indoors.

[291] P. Ye, S. J. Harrison, P. H. Oosthuizen, and D. Naylor, "Modelling of convective heat transfer from a window glass adjacent to a venetian blind," *Heat Transfer 1998, Vol 3,* pp. 195-200, 1998.

[292] W. Pasut and M. De Carli, "Evaluation of various CFD modelling strategies in predicting airflow and temperature in a naturally ventilated double skin facade," *Applied Thermal Engineering,* vol. 37, pp. 267-274, May 2012.

[293] M. W. Nassim Safer, Jean-Jacques R., Gilles R., and Frederic K, "Modelling of Double-Skin Facades for Building Energy Simulations: Radiative and Convective Heat Transfer," presented at the Ninth International IBPSA Conference, Montreal, Canada, August 15-18, 2005.

[294] M. C. Neveen H, and Paul C, "Comparative Analysis of Natural Ventilation performance in Non-Uniform Double Skin Facades in Temperature Climates," in *12th Proc. Of Building Simulation 2011, International Conference of Building Performance Simulation Association Sydney*, Sydney, 2011.

[295] R. Fuliotto, F. Cambuli, N. Mandas, N. Bacchin, G. Manara, and Q. Y. Chen, "Experimental and numerical analysis of heat transfer and airflow on an interactive building facade," *Energy and Buildings,* vol. 42, pp. 23-28, Jan 2010.

[296] X. Zhu, Fu, J., and Yi, X, "A Simplified mathematical model of heat transfer process in Doubles Skin Facade," presented at the Int. Conf, on Computer Distributed Control and Intelligent Environmental Monitoring, 2012.

[297] M. Z. K. Behzad R., and Parisa R, "How Double Skin Façade's Air-Gap Sizes Effect on Lowering Solar Heat Gain in Tropical Climate," *World Applied Sciences Journal 18*, vol. 6, pp. 774-778 2012.

[298] Y. X. T. Teshome E.J., and Fariborz H, "Airflow and heat transfer in double skin facades," *Energy and Buildings*, vol. 43, pp. 2760–2766, 2011.

[299] W. L. Wong N. H., Aida N. C., Anupama R. P., and Wei X, "Effects of double glazed facade on energy consumption, thermal comfort and condensation for a typical office building in Singapore," *Energy and Buildings* vol. 37, pp. 563-572, 2005.

[300] J. A. Mona A., "CFD Modelling of a New Natural Ventilated Double Skin Facade Configuration in a Chicago High-Rise Office Building," presented at the Fourth National Conference of IBPSA-USA, New York, 2010.

[301] R. F. WARD G., and CLEAR R., "A ray tracing solution for diffuse interreflection," *Comp. Graphics*, vol. 4, p. 8592, 1988.

[302] M. M., *Radiation Heat Transfer, .* New York: McGraw-Hill, 1993.

[303] S. H. Jang and M. W. Shin, "Thermal analysis and modeling of led arrays for automotive headlamp," *Proceedings of the Asme International Mechanical Engineering Congress and Exposition 2007, Vol 5*, pp. 247-250, 2008.

[304] American Society of Heating Refrigerating and Air-Conditioning Engineers., "ASHRAE handbook. Fundamentals," Inch-pound ed. Atlanta, Ga.: American Society of Heating, Refrigerating, and Air-Conditioning Engineers, 1985, p. v.

[305] P. Y. Ni, L. T. I. Jonsson, and P. G. Jonsson, "Simulations of the Ladle Teeming Process and Verification With Pilot Experiment," *Steel Research International*, vol. 84, pp. 276-287, Mar 2013.

[306] Y. Ji, M. J. Cook, V. I. Hanby, D. G. Infield, D. L. Loveday, and L. Mei, "CFD modelling of Double-Skin Facades with venetian blinds," *Building Simulation 2007, Vols 1-3, Proceedings*, pp. 1491-1498, 2007.

APPENDIX A: UDF - THERMAL BOUNDARY CONDITIONS AT PASSIVE WALLS

```
/************************************************************************
   UDF HORIZONTAL-WALLS for specifying steady-state LINEAR temperature
profile boundary
   condition
   Draco Aluya Iyi
************************************************************************
/

#include "udf.h"

DEFINE_PROFILE(Top_temperature_profile, t, i)
{
  real x[ND_ND];                /* this will hold the position vector */
  real y;
  face_t f;

  begin_f_loop(f, t)
    {
      F_CENTROID(x,f,t);
      y = x[0];
      F_PROFILE(f, t, i) = 283.15 + 40*(1-y/0.75);
    }
  end_f_loop(f, t)
}
DEFINE_PROFILE(Bottom_temperature_profile, t, i)
{
  real x[ND_ND];                /* this will hold the position vector */
  real y;
  face_t f;

  begin_f_loop(f, t)
    {
      F_CENTROID(x,f,t);
      y = x[0];
      F_PROFILE(f, t, i) = 283.15 + 40*(1-y/0.75);
    }
  end_f_loop(f, t)
}
```

```
/************************************************************************
*
   UDF HORIZONTAL-WALL for specifying steady-state EXPERIMENTAL
temperature profile boundary
   condition
   Draco Aluya Iyi
************************************************************************
*/

#include "udf.h"

DEFINE_PROFILE(Top_temperature_profile, t, i)
{
  real x[ND_ND];                /* this will hold the position vector
*/
  real y;
  face_t f;

  begin_f_loop(f, t)
    {
      F_CENTROID(x,f,t);
      y = x[0];
      F_PROFILE(f, t, i) = 283.15 + 40*(-
2.458*(y*y*y*y/(0.75*0.75*0.75*0.75))+1.686*(y*y*y/(0.75*0.75*0.75))+1.
211*(y*y/(0.75*0.75))-1.44*(y/0.75)+1);
    }
  end_f_loop(f, t)
}
DEFINE_PROFILE(Bottom_temperature_profile, t, i)
{
  real x[ND_ND];                /* this will hold the position vector
*/
  real y;
  face_t f;

  begin_f_loop(f, t)
    {
      F_CENTROID(x,f,t);
      y = x[0];
      F_PROFILE(f, t, i) = 283.15 +
40*(2.458*(y*y*y*y/(0.75*0.75*0.75*0.75))-
8.146*(y*y*y/(0.75*0.75*0.75))+8.477*(y*y/(0.75*0.75))-
3.789*(y/0.75)+1);
    }
  end_f_loop(f, t)
}
```

```
/************************************************************************
  UDF HORIZONTAL-WALLS for specifying steady-state LINEAR temperature profile boundary
  condition
  Draco Aluya Iyi
  Northumbria University
************************************************************************/

#include "udf.h"

DEFINE_PROFILE(Top_temperature_profile, t, i)
{
 real x[ND_ND];              /* this will hold the position vector */
 real y;
 face_t f;

 begin_f_loop(f, t)
  {
   F_CENTROID(x,f,t);
   y = x[0];
   F_PROFILE(f, t, i) = 296.45 + 42.2*(1.0253-y/0.4);
  }
 end_f_loop(f, t)
}
DEFINE_PROFILE(Bottom_temperature_profile, t, i)
{
 real x[ND_ND];              /* this will hold the position vector */
real y;
 face_t f;

 begin_f_loop(f, t)
  {
   F_CENTROID(x,f,t);
   y = x[0];
   F_PROFILE(f, t, i) = 296.45 + 42.2*(1.0203-(1.001*(y/0.4)));
  }
 end_f_loop(f, t)
}
```

APPENDIX B: ADDITIONAL VALIDATION RESULTS

Experimental temperature results comparison at mid-width of the cavity (10x5 arrangements of blockages)

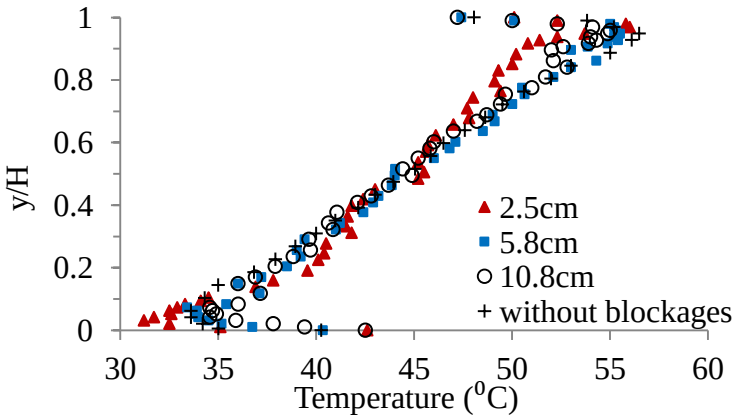

Proximity effects on temperature profile at mid-width

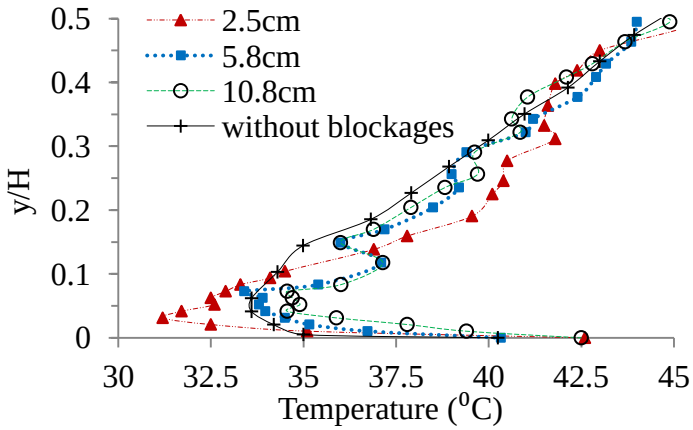

Proximity effects on temperature profile at mid-width (Near bottom wall)

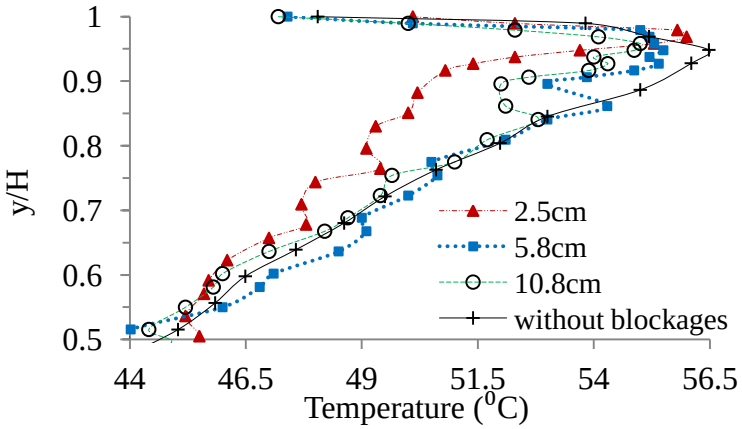

Proximity effects on temperature profile at mid-width (Near top wall)

Temperature data comparison at y=8.6 mm from bottom wall (near top wall)

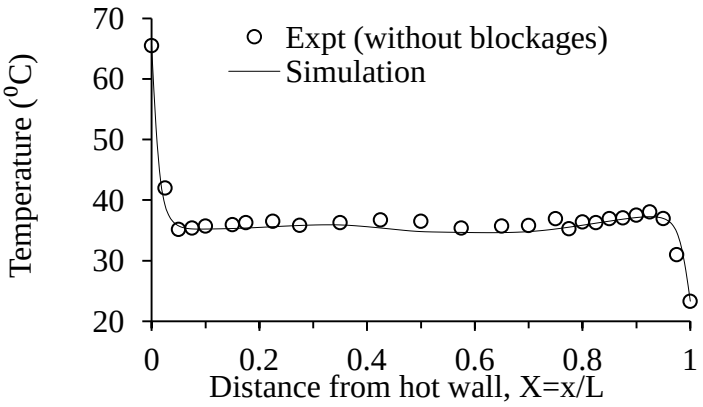

Temperature profile near bottom wall comparison with CFD data (No blockages)

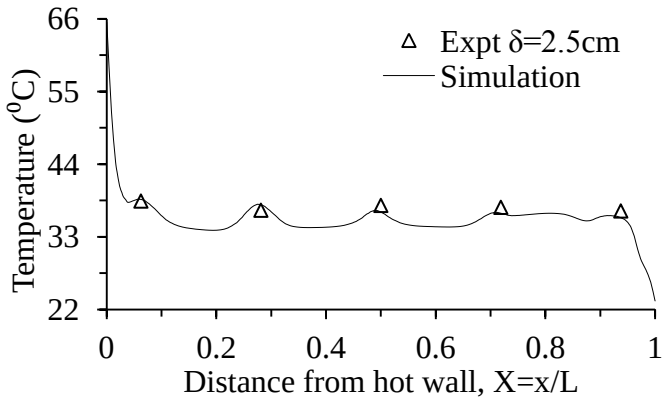

Temperature profile near bottom wall comparison with CFD data; δ=2.5cm

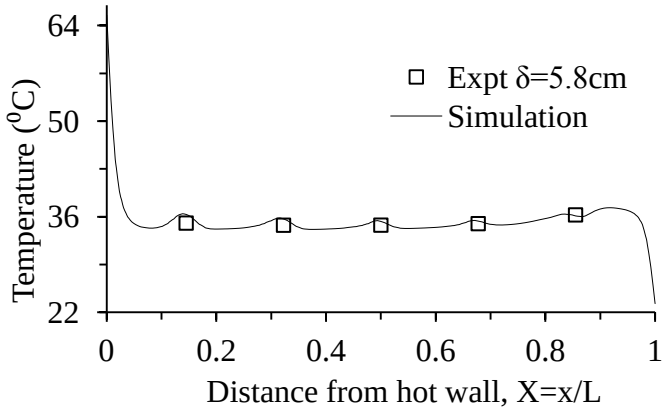

Temperature profile near bottom wall comparison with CFD data; δ=5.8cm

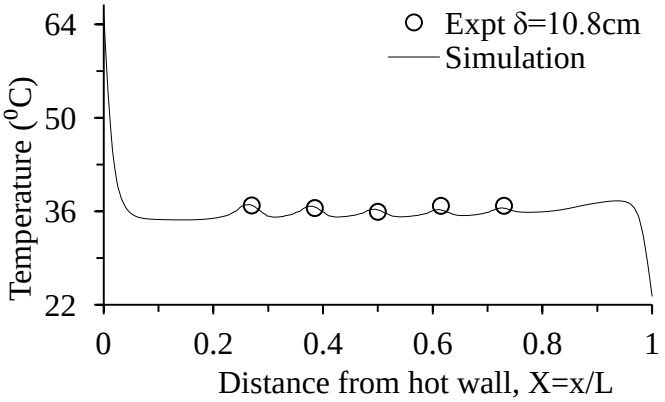

Temperature profile near bottom wall comparison with CFD data; δ=10.8cm

Temperature data comparison at y=884.35mm from bottom wall (near top wall)

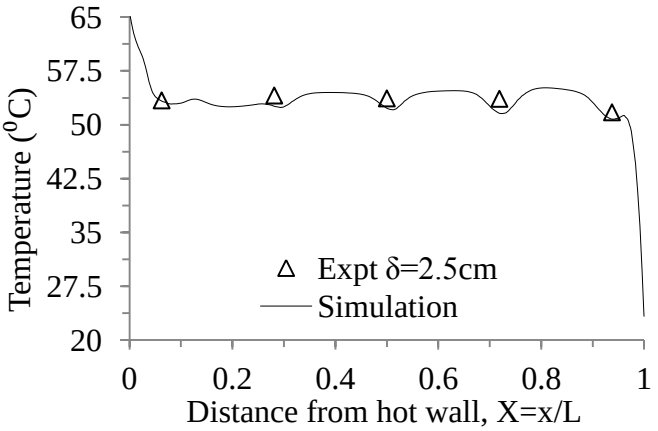

Temperature profile near top wall comparison with CFD data (δ=2.5cm); 88.435cm from bottom wall

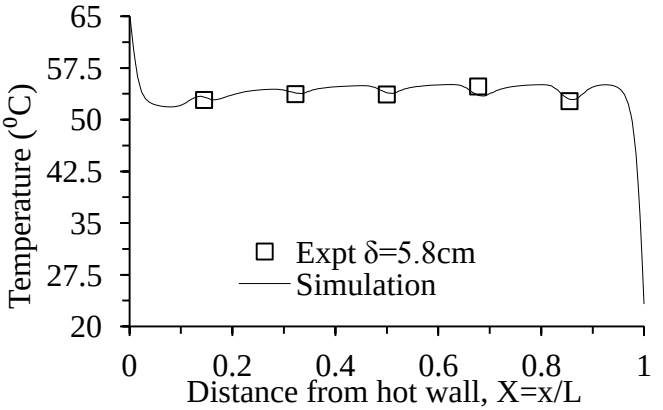

Temperature profile near top wall comparison with CFD data (δ=5.8cm); 88.435cm from bottom wall

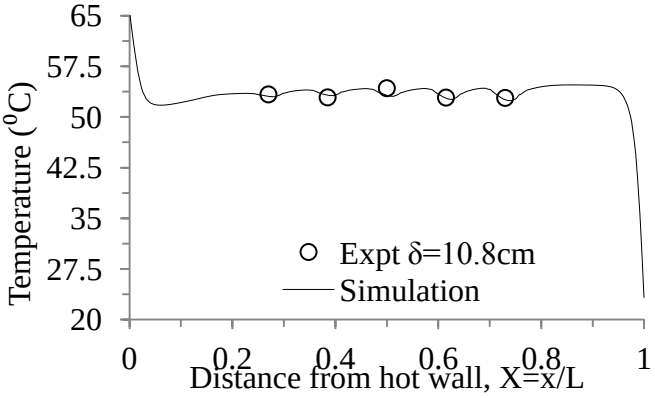

Temperature profile near top wall comparison with CFD data (δ=10.8cm); 88.435cm from bottom wall

Blockages proximity influence (10x5 configuration

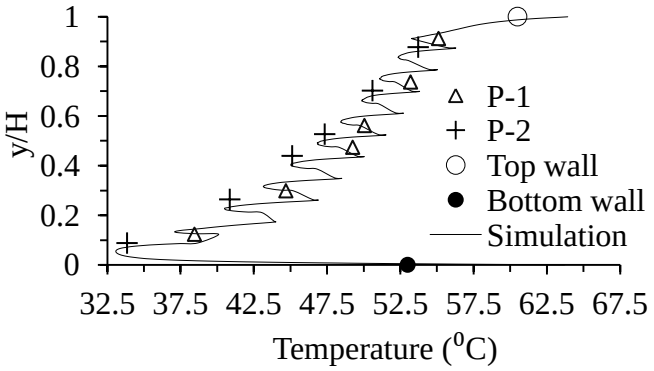

(6-16a)

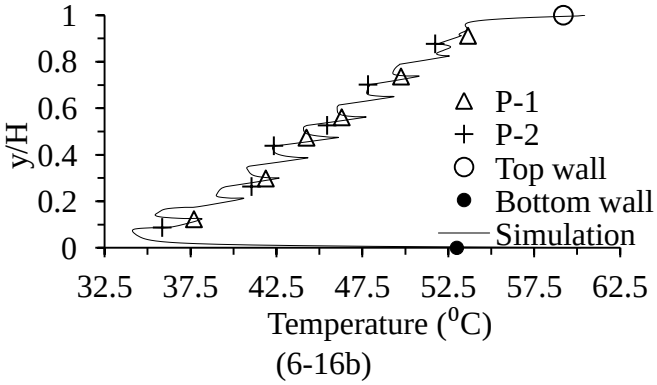

(6-16b)

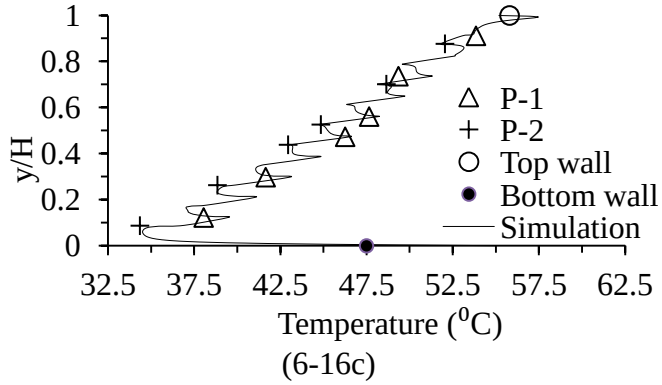

(6-16c)

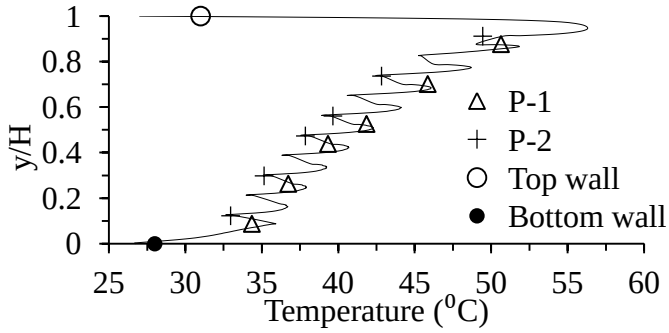

(6-16d)

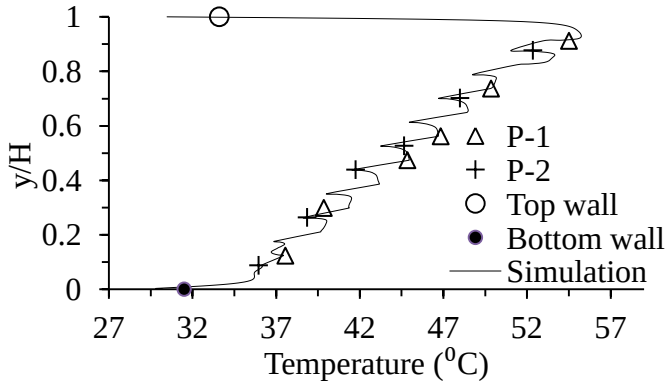

(6-16e)

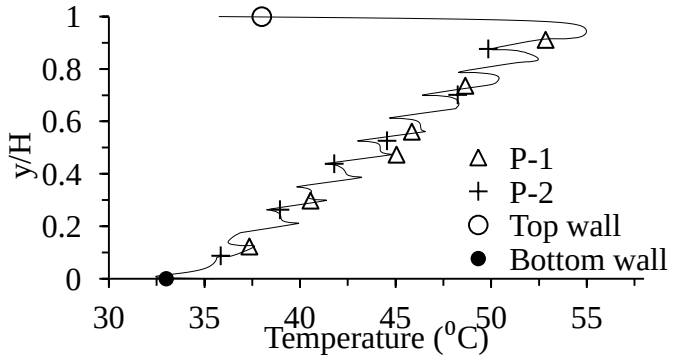

(6-16f)

Figure 0-1: Cylinder temperature data comparison (a) δ=25mm at x=25mm (b) δ=58mm at x=58mm (c) δ=108mm at x=108mm (d) δ=25mm at x=375mm (e) δ=58mm at x=342mm (f) δ=108mm at x=108mm from hot wall

APPENDIX C: ADDITIONAL EXPERIMENTAL RESULTS

Horizontal temperature data at the cylinder surface near bottom wall and top wall of the cavity

The cylinder surface temperature data measured at the horizontal plane and 85.65mm from the bottom and top walls respectively are shown in Figs.8-16 to 8-21.

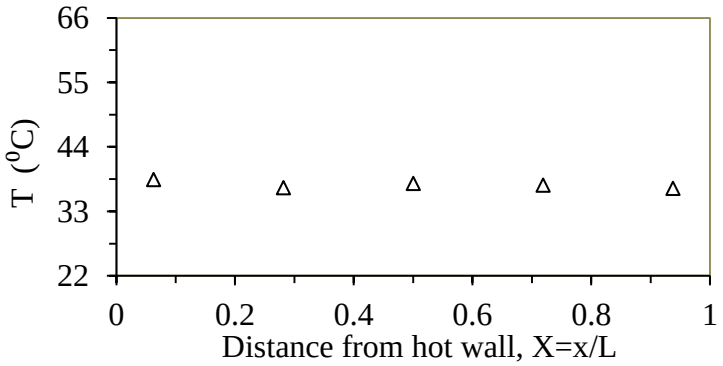

Temperature profile of cylinders near bottom wall (y=85.65mm) for δ=25mm

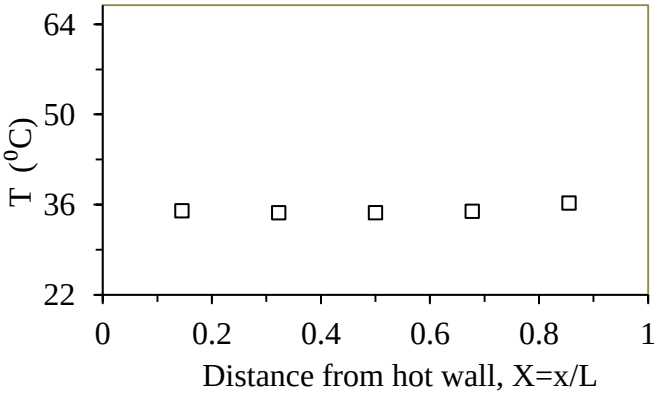

Temperature profile near bottom wall (y=85.65mm) for δ=58mm

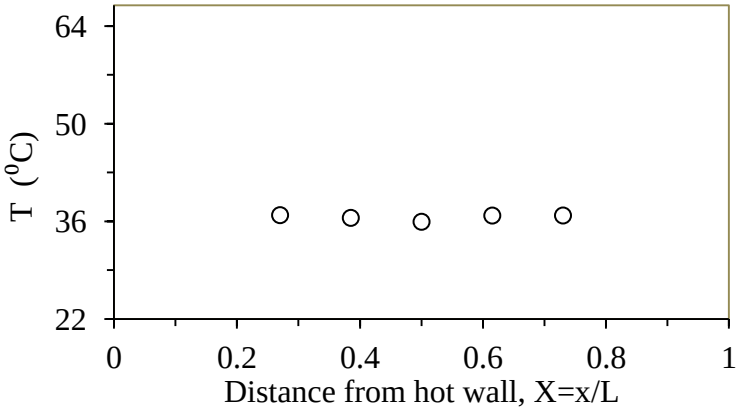

Temperature profile near bottom wall (y=85.65mm) for δ=108mm

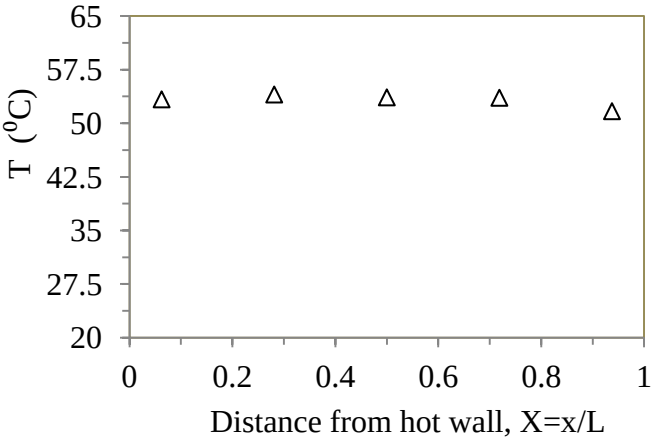

Temperature profile near top wall for δ=25mm (884.35mm from bottom wall)

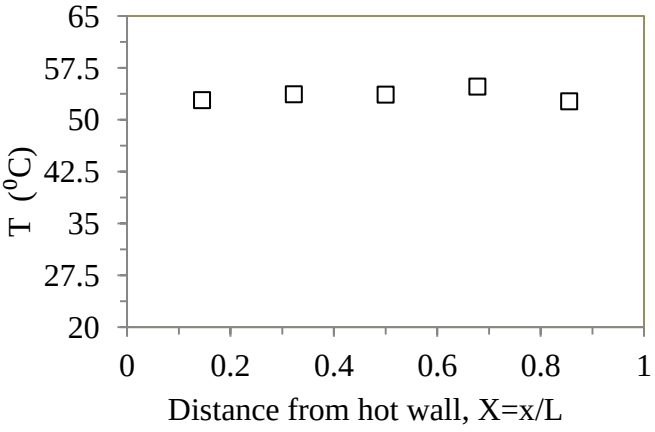

Temperature profile near top wall for δ=58mm (884.35mm from bottom wall)

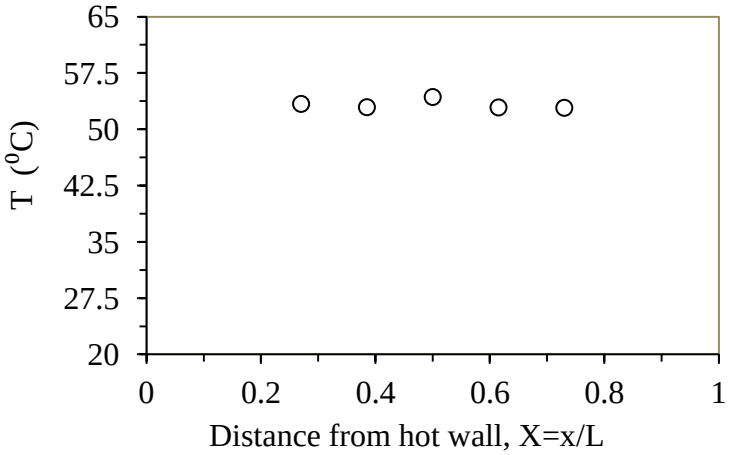

Temperature profile near top wall for δ=108mm (884.35mm from bottom wall)

APPENDIX D: MESH SENSITIVITY STUDY

The slant $Y^{+} \approx 1$ and minimum mesh orthogonal quality is 1

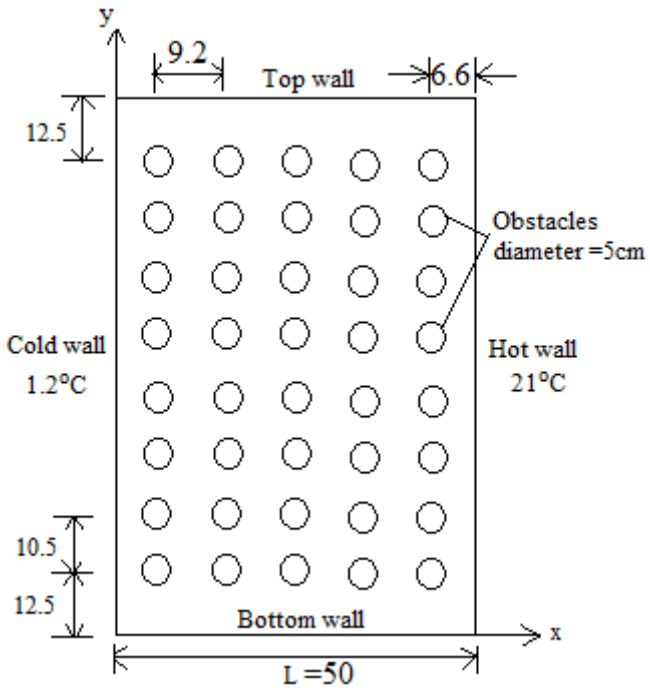

Figure B-1: Schematic of the flow domain

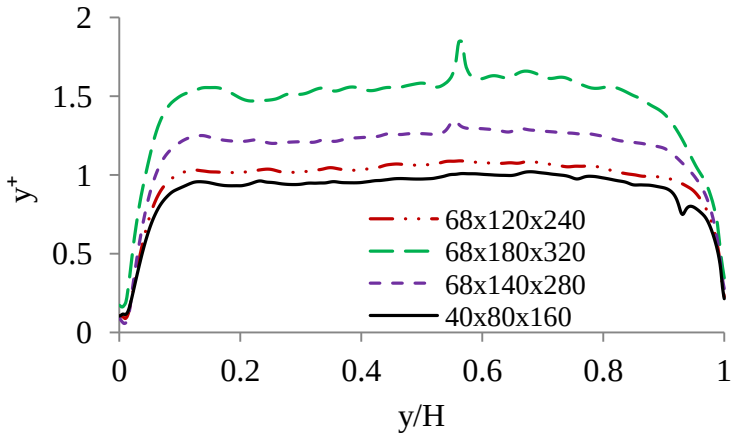

Figure B-2: Non-dimensional normal distance (y^{+}), cold wall

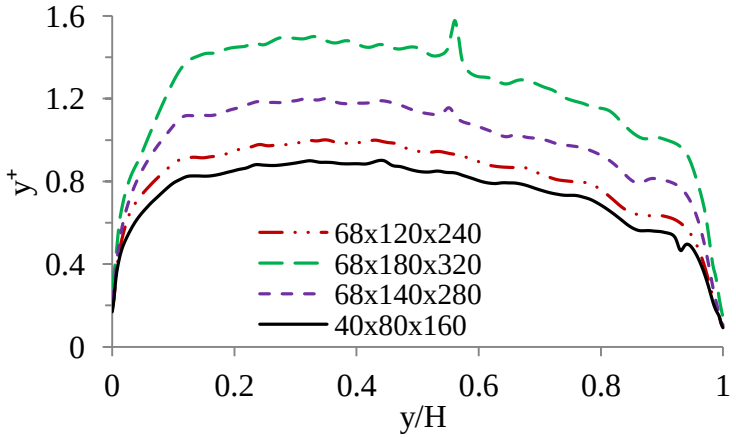

Figure B-3: Non-dimensional normal distance (y^+), hot wall

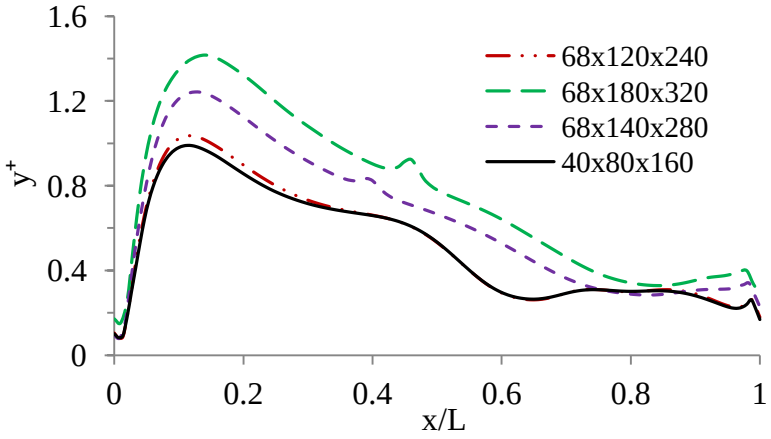

Figure B-4: Non-dimensional normal distance (y^+), bottom wall

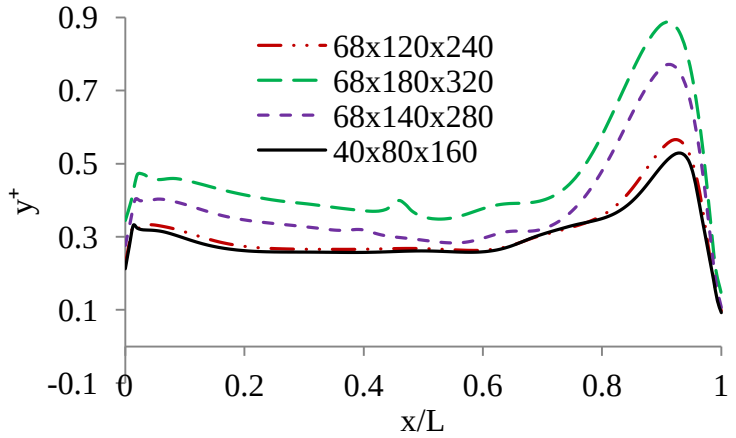

Figure B-5: Non-dimensional normal distance (y^+), top wall

APPENDIX E: TOTAL UNCERTAINTY CALCULATION

The total uncertainty in temperature measurement is the positive square root of the combined variance, which is given by

$$U_R = \left[\sum_{i=1}^{n}\left[\left(\frac{\partial R}{\partial X_i}\right)^2 {u_{X_i}}^2\right]\right]^{1/2}$$

Where U_R and are u_{X_i} the uncertainties of R and, X_i respectively [223], R is a measurand determined from a set of independent quantities, X_1, X_2, X_3,.. ....X_n measured in an experimental study, therefore, R=R(X_1, X_2, X_3,....X_n)

Therefore, the uncertainty in the measured experimental temperature data is 0.51^0 C. $[(0.1^2 + 0.5^2)^{0.5} = 0.51^0\text{C}]$.